Exploration Of Biomedically Relevant Spectroscopic Techniques For Potential Clinical Diagnostic And Therapeutic Procedures

THESIS

SUBMITTED FOR THE DEGREE OF

DOCTOR OF PHILOSOPHY (TECH.)

IN

APPLIED OPTICS AND PHOTONICS

BY

NABARUN POLLEY

DEPARTMENT OF APPLIED OPTICS AND PHOTONICS
UNIVERSITY OF CALCUTTA
INDIA
2016

To My Parents
and Sister

Acknowledgements

Undertaking this PhD has been a truly life-changing experience for me and it would not have been possible to do without the support and guidance that I received from many people.

First of all I take this opportunity to express my sincere gratitude to my advisor Dr. Samir Kumar Pal, whom I am extremely grateful for being an exceptional mentor for me. His instrumental expertises, insight into various experimental problems, wisdom, and inspiration have allowed my research skills to develop, my creativity to flourish along with getting shaped as a working researcher. He has provided me with many opportunities to gain scientific experience, allowing me to explore new areas of research, interact and collaborate with talented researchers from a number of different national and international institutes. If it weren't for his ideas, constant support, guidance, motivation and patience, none of this work would have been possible. He has taught me so much, inspired me to work hard, always taken time to listen to my crazy ideas, and made these years so enjoyable. I could not have wished for a better advisor. Thank you Sir, for everything you have done for me.

I have enjoyed fruitful collaborations of Prof. Peter Lemmens of Institute for Condensed Matter Physics, Technical University of Braunschweig, Germany , Dr. Bhaskar Roy Chowdhury of Calcutta Medical Research Centre, , Professor Sukhen Dac of Jadavur University and Dr. Soumendra Darbar of Dey's Medical. I am thankful to the lab members of my collaborating research groups: Prasanna Kumar Mondal , Srimoyee Saha, Somtirtha Banerjee for insightful discussions. Great appreciation is extended to SNBNCBS staffs and faculty members for their assistances in my research career. I owe a special thanks to the Department of Science and Technology (DST), India for my research fellowship (INSPIRE fellowship), and for projects.

I'd like to express my sincere thanks to all my seniors and colleagues for providing a stimulating and enriching environment. Special thanks to Dr. Anupam Grir for helping me at the initial stage of my research work. I am grateful to samim and susobhan for helping me out from many difficulties during my research works. Special thanks to Aniruddha and Probir for their assistance in formatting and proof-reading my thesis. My sincere appreciation goes to all my seniors: Dr. Abhinandan Makhal, Dr. Subrata Batabyal, Dr. Nirmal Goswami, Dr. Ranajay Saha, Dr. Tanumay Mondal, Dr. Surajit Rakshit, Dr. Anupam Giri, Dr. Soma Banerjee, Dr. Prasanna Kumar Mondal and all the present group members: Animesh Da, Siddhi di, Samim, Susobhan, Prasenjit, Damayanti, Priya, Paulomi, Dr. Shreyasi Dutta, Tuhin, Jayita, Aniruddha, Probir, Ramesh and Soumendra da for providing a homely and a cheerful environment, and also for assisting me in research. I would like to mention Aniruddha and Probir's name for their immense cooperation and help in my research.

My time at S. N. Bose Centre was made enjoyable in large part due to the friends and groups that became a part of my life. Very special thanks to Samim and Susobhan with whom I shared many glorious moments over a long period of time, supported my work annoyances, and also for the good moments of fun! I will always miss their company in future. I also want to thank subrata Da, Ranajay da, for the good times I shared with them. I pay tribute to all my teachers throughout my life.

Finally, I would like to express my gratitude to my family who supports me through thick and thin, with loves and affections. I want them to know that I love them cordially. Without their sacrifices, moral supports and blessings the thesis would not have taken its shape.

Dated:

Department of Chemical, Biological and Macromolecular Sciences,
S. N. Bose National Centre for Basic Sciences,
Salt Lake, Kolkata 700106, India *(Nabarun Polley)*

Contents

Page No.

Chapter 1

Introduction

1.1. Background

Interaction of light with matter always fascinates human since ancient times. Despite the understanding of colour generation upon interaction of light with the matter, the term 'spectroscopy' was originated in the 17th century through the study of visible light dispersed according to its wavelength, by a prism. Spectroscopy in the medical science is popularised in the early 20th century. However, its glorious presence in the diagnosis of diseases is still evident since the earliest times. Primitive medical diagnoses made by ancient physicians were based on what they could observe with their eyes and ears, which sometimes also included the examination of human specimens. The ancient Greeks attributed all disease to disorders of bodily fluids called humors, and during the late medieval period, doctors routinely performed uroscopy. Later, the microscope revealed not only the cellular structure of human tissue, but also the organisms that cause disease. More sophisticated diagnostic tools and techniques such as the thermometer for measuring temperature and the stethoscope for measuring heart rate were not in widespread use until the end of the 19th century. The clinical laboratory would not become a standard fixture of medicine until the beginning of the 20th century [1].

On the other hand the therapeutic application of medicinal drugs has been established much later on in 19th century. The development of small molecule therapeutic agents for the treatment and prevention of diseases has played a critical role in the practice of medicine for many years. In fact, the use of natural extracts for medicinal purposes goes back thousands of years; however, it has only been in the past half century or so that searching for new drugs has found itself in the realm of science. In 1900, one-third of all deaths in the U.S. were from three general causes that are rare today because they are preventable and/or treatable: pneumonia, tuberculosis, and diarrhea. By 1940, the chance of dying from these three causes was 1 in 11; by 2000, the odds were down to 1 in 25. This is one of the exemplary evidences where, development of new therapeutic strategies becomes the life saver of millions and millions of people all over the world.

Optical spectroscopy holds promise as clinical tool for diagnosing at the early stage of carcinomas and other diseases by combining with available photonic technology and has been utilised throughout this thesis work. Whereas, continuous improvement in the pharmacological and therapeutic properties of drugs driving the revolution in development of novel drugs. In fact, a wide spectrum of therapeutic nano-carriers has been extensively investigated to address this emerging need. In this thesis work, we have utilised the catalytic degradability upon surface modification of a 3d transition metal oxide nano particles as a therapeutic drug.

1.2. Introduction

Recent developments of small light sources, detectors, and fiber optic probes provide opportunities to quantitatively measure interactions, which yield information for diagnosis at the biochemical, structural, or (patho) physiological level within intact tissues [2]. The basic changes are in the way or the technique of measuring parameters with medical relevance [3]. The interaction of light with biological medium covers the general field of biomedical optics which has its own role in developing different modern clinical diagnostic techniques. Not only diagnosis, therapeutic (usually, followed by diagnosis) aspect of diseases has also improved a lot due to the development of novel drug delivery systems. In the following section we have discussed biomedically relevant spectroscopic techniques with potential application in medical diagnosis and therapy.

1.2.1. Spectroscopy in Medical Diagnosis: Application of spectroscopy in diagnosis covers broad field of application from pulse oximetry to non-invasive optical biopsy. In this section we have represented the state of the art diagnostic strategies based on different spectroscopic techniques. Ultraviolet/visible (UV/Vis) absorption spectroscopy has been used in the clinical laboratory for many years. The technique has appeal, as it is almost universal in its application. Absorption spectroscopy is usually performed with molecules dissolved in a transparent solvent, such as aqueous buffers. The absorbance of a solute depends linearly on its concentration and, therefore, absorption spectroscopy is ideally suited for quantitative measurements. The wavelength of absorption and the strength of absorbance of a molecule depend not only on the chemical nature but also on the molecular environment of its chromophores. Absorption spectroscopy is therefore an excellent technique for following

ligand-binding reactions, enzyme catalysis, and conformational transitions in proteins and nucleic acids [4]. In this category the most popular diagnostic tool used in day to day basic for the measurement of oxygen saturation (SpO_2) is pulse oximetry. A blood-oxygen monitor displays the percentage of blood that is loaded with oxygen. More specifically, it measures what percentage of haemoglobin, the protein in blood that carries oxygen, is loaded. Acceptable normal ranges for patients without pulmonary pathology are from 95 to 99 percent. For a patient breathing room air at or near sea level, an estimate of arterial pO_2 can be made from the blood-oxygen monitor "saturation of peripheral oxygen" (SpO_2) reading. Pulse oximeter works based on the Beer–Lambert law. It utilizes an electronic processor and a pair of small light-emitting diodes (LEDs) facing a photodiode through a translucent part of the patient's body, usually a fingertip or an earlobe. One LED is red, with wavelength of 660 nm, and the other is infrared with a wavelength of 940 nm. Absorption of light at these wavelengths differs significantly between blood loaded with oxygen and blood lacking oxygen. Oxygenated haemoglobin absorbs more infrared light and allows more red light to pass through. Deoxygenated haemoglobin allows more infrared light to pass through and absorbs more red light. The ratio of the red light measurement to the infrared light measurement is then calculated by the processor (which represents the ratio of oxygenated haemoglobin to deoxygenated haemoglobin), and this ratio is then converted to SpO_2 by the processor via a lookup table [5]. Absorbance spectroscopy has also been employed for the estimation of glycated hemoglobin in hemolysate samples of normal individuals and diabetic patients, which does not involve the use of external dyes or reagents. The optic fiber based instrument used for recording absorption spectra in the spectral range 200–850 nm of glycated hemoglobin (HbA1c). The parameter “area under the curve” of each baseline corrected absorption spectrum was used for the estimation of HbA1c (%). The glycated hemoglobin values obtained by this spectroscopic method were compared with the values reported by the standard ion exchange HPLC method. It has been observed the aforementioned technique may be employed as a supplementary technique to other techniques that already exist [4].

Fluorescence spectroscopy is a complementary technique of absorption spectroscopy which analyzes fluorescence from a sample. It is primarily concerned with electronic and vibrational states of the fluorophores. Fluorescence spectroscopy is being used in many medical subspecialties as a diagnostic tool which extends from diagnostic studies for the

determination of skin cancers to atheromatic plaques detection in coronary arteries. There are three main types of fluorophores used for cancer diagnostic studies: exogenous fluorophores, endogenous fluorophores, and fluorophores synthesized in the tissue from a precursor molecule that is given externally [6, 7]. Endogenous fluorophores give rise to autofluorescence phenomenon. Examples of endogenous fluorophores include collagen, elastin, nicotinamide adenine dinucleotide (NADH), tryptophan, porphyrins, and flavin adenine dinucleotide (FAD) [8]. Collagen and elastin are mainly responsible for spectral changes associated with structural changes within the tissues and cells [8]. Other fluorophores like FAD, NADH, tryptophan, and porphyrins are mainly responsible for spectral changes associated with changes in cellular metabolism and functional processes [7]. Steady-state ultraviolet (UV) fluorescence spectroscopy can be utilised to separate malignant tumors from benign and normal breast, cervical, ovarian, and uterus tissues and tumors [7-9]. Upon exiting the tissue samples at 300 nm using a lamp-based spectrometer the emission can be recorded from 320 nm to 550 nm. The ratios of fluorescence intensities at 340 nm to 440 nm for cancerous breast tissues were found to be different from that of normal and benign tissues. In order to obtain further information on the chromophores responsible for the emission and to have a better physics picture of the heterogeneous nature of tissue fluorescence in cancerous and normal tissue, the kinetics of the physical processes occurring in tissues can be studied using time-resolved fluorescence. The key fluorescence relaxation decay parameters can be determined from the time-resolved fluorescence spectroscopic data of photo-excited tissues. The fluorescence kinetics from malignant and non-malignant breast tissues upon excitation at 310 nm and 353 nm, exhibit different double exponential decay profiles consisting of slow and fast components. Typical time-resolved fluorescence profiles at 340 nm emission band from a benign breast tissue, a benign tumor and a malignant tumor, photoexcited at 100 fs 310 nm pulse contain one slow and one fast component of fluorescence decay. The profiles for non-malignant (benign and normal) and malignant samples show a marked difference. The fast component seems to be more dominant in non-malignant tissues than in malignant tissues. The fluorescence decay curves for 440 nm band appear to contain one slow and one fast component of fluorescence lifetime. Unlike the 340 nm band, there is no marked dominance of either component for 440 nm [8]. Which further shows that the time resolved fluorescence is a novel way to obtain fundamental information on cancer. On the other hand, laser-induced fluorescence spectroscopy, a noninvasive real-time technique for evaluating

neoplasia, measures the auto-fluorescence of tissue based on the amounts of naturally occurring fluorophores present. With fluorescence spectroscopy, diagnostic algorithms can be derived that allow reasonable sensitivity and specificity for the diagnosis of squamous intraepithelial lesions (SILs) and work without a priori information about the abnormalities of the cervix [9]. New medical technologies can be evaluated using several measures, including sensitivity, specificity, positive and negative predictive values, receiver operating characteristic (ROC) curves, and areas under ROC curves. The ROC curve has the advantage of comparing test performance over several thresholds and can be used both in diagnostic settings, in which the prevalence of disease is high, and in screening settings, in which the prevalence of disease is low. Furthermore, fluorescence dye based detection of different diseases has also been reported. For an instance, fluorescence lifetime imaging of 4',6-diamidino-2-phenylindole (DAPI) stained nuclei has been utilised as a novel diagnostic tool for the detection and classification of B-cell chronic lymphocytic leukemia [10]. Conversely, the use of different dyes for the detection of cellular reactive oxygen species by fluorescence assay has also been reported [11].

Raman spectroscopy represents a molecular fingerprint of the sample and provides quantitative information regarding its chemical makeup. It is a powerful analytical technique that can measure the chemical composition of complex biological samples, such as biofluids, cells and tissues. Biochemical changes in cells and tissues, that may either be caused or are the cause of a disease, can lead to significant changes in the Raman spectra. The potential of Raman spectroscopy arises from its ability to detect such biochemical changes at a molecular level, and therefore, can be used for diagnostics, prognostics or as a tool for evaluating new therapies. Raman spectroscopy has several features that are advantageous for medical diagnostics. It has high chemical specificity and molecular information that can be obtained without any staining or labelling. Changes in the molecular composition of biological samples as measured by Raman spectroscopy can be used to build multivariate calibration and classification models, which allow quantitative and objective diagnosis for independent patients. Raman spectroscopy relies on scattering of light by molecules and information regarding the vibrational modes of the molecules can be obtained using visible or near-infrared lasers. Thus, Raman spectroscopy can take advantage of the advanced optical microscopy technologies, optical fibres, miniaturised lasers and other photonic devices, to improve diagnostic performance and speed. Often the measurements are carried out in

backscattering geometry without requiring transmission of light through the specimen. This feature is useful in particular for *in vivo* diagnostic and for examination of thick tissue specimens (e.g. surgical resections), without requiring micro-sectioning. The use of visible or near-infrared light for excitation also reduces the absorption effects of water, allowing measurements of body fluids or cells within water environments. Similar to other optical techniques, Raman spectroscopy can provide real-time (or near real-time) molecular information and high resolution imaging at relatively low cost compared to other well established medical imaging techniques (e.g. ultrasound, magnetic resonance imaging, etc.). This is an important feature as often the clinical implementation and translation of technologies are limited by practical, logistical and financial factors [12]. The application of Raman spectroscopy in medical diagnosis includes invasive detection of cancer (brain, barest, lung, skin, prostate, Colorectal); minimally invasive bio fluid analysis for the detection of asthma, inflammatory response, coagulant and anti-coagulant factors in human blood, malaria etc.

1.2.2. Spectroscopy in Medical Therapy: Application of spectroscopy in medical science in not limited to medical diagnosis only. Spectroscopy has significant role in therapeutic applications including photodynamic therapy, atmospheric pressure plasma therapy even evaluating the action of a targeted cancer drug through magnetic resonance spectroscopy has also been reported.

Photo dynamic therapy (PDT) is a treatment that uses a drug, called a photosensitizer or photosensitizing agent, and a particular type of light. When photosensitizers are exposed to a specific wavelength of light, they produce a reactive form of oxygen that kills nearby cells. Each photosensitizer is activated by light of a specific wavelength. This wavelength determines how far the light can travel into the body. Thus, doctors use specific photosensitizers and wavelengths of light to treat different areas of the body with PDT. In the first step of PDT for cancer treatment, a photosensitizing agent is injected into the bloodstream. The agent is absorbed by cells all over the body but stays in cancer cells longer than it does in normal cells. Approximately 24 to 72 hours after injection, when most of the agent has left normal cells but remains in cancer cells, the tumor is exposed to light. The photosensitizer in the tumor absorbs the light and produces an active form of oxygen that destroys nearby cancer cells. In addition to direct killing of cancer cells, PDT appears to

shrink or destroy tumors in two other ways. Firstly, the photosensitizer can damage blood vessels in the tumour, thereby preventing the cancer from receiving necessary nutrients. Secondly, PDT also may activate the immune system to attack the tumour cells. The light used for PDT can come from a laser or other sources. Laser light can be directed through fiber optic cables (thin fibers that transmit light) to deliver light to areas inside the body. For example, a fiber optic cable can be inserted through an endoscope (a thin, lighted tube used to look at tissues inside the body) into the lungs or esophagus to treat cancer in these organs. Other light sources include light-emitting diodes (LEDs), which may be used for surface tumors, such as skin cancer. PDT is usually performed as an outpatient procedure. PDT may also be repeated and may be used with other therapies, such as surgery, radiation therapy, or chemotherapy. Extracorporeal photopheresis (ECP) is a type of PDT in which a machine is used to collect the patient's blood cells, treat them outside the body with a photosensitizing agent, expose them to light, and then return them to the patient. The U.S. Food and Drug Administration (FDA) has approved ECP to help lessen the severity of skin symptoms of cutaneous T-cell lymphoma that has not responded to other therapies. Studies are under way to determine if ECP may have some application for other blood cancers, and also to help reduce rejection after transplants.

Plasma medicine is an innovative and emerging field combining plasma physics, life sciences and clinical medicine to use physical plasma for therapeutic applications. Plasma, described as the fourth state of matter, comprises charged species, active molecules and atoms and is also a source of UV-photons[13]. These plasma-generated active species are useful for several bio-medical applications such as sterilization of implants and surgical instruments as well as modifying biomaterial surface properties. Sensitive applications of plasma, like subjecting human body or internal organs to plasma treatment for medical purposes, are also possible. Initial experiments confirm that plasma can be effective in *in vivo* antiseptics without affecting surrounding tissue and, moreover, stimulating tissue regeneration [13]. Based on sophisticated basic research on plasma-tissue interaction, first therapeutic applications in wound healing, dermatology and dentistry will be opened [13].

Though nanoparticles are not directly related to the spectroscopic studies but the working of the nanoparticles can be confirmed by means of spectroscopic methods only. Hence, the application of the nanoparticles for drug delivery agent or as drug is indirectly

related to the spectroscopy. However, in some cases the effective application of the nanoparticles could be enhanced through the application of external light or magnetic field which is in the domain of spectroscopy [14]. Nanometer-sized colloidal particles with small size and large surface area have many superior properties when used as magnetic resonance imaging (MRI) contrast agents, such as their ability to carry large payloads of active magnetic centers, easy penetration of biological membranes, long blood circulation times, and efficient conjugation to affinity molecules. Thus, they have the potential to allow us to visualize targets at low imaging-agent concentration with high sensitivity and specificity [15]. Furthermore, nanoparticles can be used in combination with therapeutic agents as bifunctional medical systems that enable simultaneous MRI diagnosis and drug treatment [16]. For example, superparamagnetic iron oxide nanoparticles have been developed as efficient T2 contrast agents and employed to image tumors, stem cell migration, and cancer metastases. Some colloidal nanoparticles containing gadolinium (III) or manganese(II) have recently been reported as potent T1 MRI contrast agents [17]. Very recently, reports on MnO nanoparticles as T1 contrast agents for MRI signal enhancement of the anatomic brain structure can also be found [17]. Conversely, manganese oxides have been widely exploited because of their promising applications in many fields, such as catalysis [18], molecular adsorption [19], [20], ion exchange [21], supercapacitors [22], magnetic applications [23], and secondary batteries. Among the manganese oxides, the hausmannite Mn_3O_4 is the most stable oxide at high temperature relative to other manganese oxides, such as MnO_2 and Mn_2O_3. The compound is known to be an active catalyst for the oxidation of methane and carbon monoxide [24], decomposition of waste gases, the selective reduction of nitrobenzene [25], and the combustion of organic compounds at temperatures of the order of 373-773 K. These catalytic applications provide a powerful method of controlling air pollution. Most recently, hollow Mn_3O_4 nanoparticles have been utilized as positive MRI contrast agent (exploiting their room temperature paramagnetism) with enhanced relaxivity attributed to an increased water-accessible surface area and the flexibility of further functional surface modifications [26, 27].

Thus, spectroscopy can offer the necessary tools to investigate the relevant structure and function, but the size and complexity of biological systems is beyond that usually encountered in the physical and chemical sciences and therefore poses a particular challenge. This challenge is met by extraordinary efforts to extend the sensitivity, specificity, information

content, and in some cases spatial resolution of spectroscopic methods. Goal of this thesis is to exploit modern instrumentation and spectroscopic tools for the betterment of human life by developing novel diagnostic and therapeutic strategies which can further help to shape our understanding of living systems. The thesis also aims to give an overview about the spectroscopic and analytic tools, and to assess how novel developments may promise unprecedented insight into biomedical procedures.

1.3. Scope and Objective

Spectroscopic investigation has taken an important role in diagnosis of different diseases including hypoxia [32], anemia, jaundice [33] and even cancer [34]. Despite the development of novel diagnostic techniques, very few of them can replace existing conventional biochemical or other lab based techniques. For instance, the possible alternative for invasive blood sampling is transcutaneous bilirubinometer (BiliChek and JM-103 are the commercial version of the device) that provides instantaneous cutaneous bilirubin concentration (TcB). The method is based on optical spectroscopy that relates the amount of light absorption by bilirubin (yellow skin) to the concentration of bilirubin in the skin. Since the discovery of the method in 1980 [33] , several more devices have been developed in order to improve the accuracy of the device. However, even after 30 years of development [35], no subcutaneous bilirubinometer can replace blood sampling. In one of our study we have addressed this issue by collecting the spectroscopic signal from the vascular bed of bulbar conjunctiva [36]. In this context the theranostics (simultaneous therapy and diagnosis) approach to cure neonatal jaundice could be very much helpful. In one of our optical fiber based projects, the concept of theranostics has been established.

On the other hand, recent world health organization (WHO) fact sheets (updated in June 2014) on global statistics of hepatitis (A, B, C & E) show that out of more than 400 million detected cases of potentially life-threatening liver infection, more than 1.3 million people die every year due to acute or chronic consequences of advanced liver damage. The global statistics of child mortality due to liver malfunction is also very alarming. It is stated in UNICEF report (2012) that twenty one children per minute die, mostly from preventive causes including neonatal jaundice, in most underdeveloped/developing countries. Jaundice is yellowish pigmentation of the skin and conjunctiva caused by high blood bilirubin levels [37,

38] and is an indicator of liver disease such as hepatitis or liver cancer [39]. An early diagnosis of the neonatal and maternal (particularly due to hepatitis E) jaundice is a proven means of prevention and cure. The diagnostic aspect of hyperbilirubinemia has been addressed in couple of our projects and described accordingly. It is important to note that in adults the elevated level of bilirubin and its oxidative products causes various serious diseases including Gilbert Syndrome (> 6 mg/dL), Crigler-Najjar type I disease (> 30 mg/dL) [40] and bilirubin-induced neurologic dysfunction (BIND) [41]. Severe neurotoxicity in case of neonates (Kernicterus) and damage in white matter of adult brain are also the consequences of higher bilirubin level [42]. In case of Hepatitis E infection in pregnant women, associated hyperbilirubinemia itself is found to increase the risk of preterm delivery [43]. Treatment options for hyperbilirubinemia include phototherapy [44], haemoperfusion, haemodialysis and exchange blood transfusion. Apart from the mentioned therapeutic procedures various organic, inorganic and phytochemicals have been used for reduction of elevated bilirubin level in blood [45-48]. All these therapeutic drugs function in hepatoprotective way and lack the ability to degrade bilirubin directly [49]. So, none of those became very fruitful in effective and quick reduction of serum bilirubin level. In the above context a safe, symptomatic and effective therapeutic strategy is extremely needed, and has been addressed in projects based on the surface functionalized Mn_3O_4 nanoparticles.

Evanescent field based sensing is well known technique for the sensing different physical parameters like concentration [50], pH level [50], water level, minor displacements etc. , which was first proposed by Paul et al. in 1987 [51]. Nonetheless, the details study of the detection process is still not fully explored. The potential use of such detection mechanism has an impact in medical diagnostics as well as environmental monitoring. In one of our evanescent field based projects, we have utilised light as tool for simultaneous diagnosis and therapy. In another fiber optic based projects we have validated the Förster resonance energy transfer (FRET) strategy in the tip of an optical fiber and utilised the fiber tip as sensor in different biomedically relevant applications. On the other hand, DNA biomaterial based fiber optic sensing project was designed with a goal to monitor the mercury contamination in biomedically relevant samples.

1.4. Summary of the Work Done

1.4.1. Optical Spectroscopy for Clinical Diagnostics of Hyperbilirubinemia

1.4.1.1. ***Development and optimization of a non-contact optical device for online monitoring of jaundice in human subjects*** **[52]:** In this study, we have described a method for measuring optical spectrum of our conjunctiva and derived pigment concentration by using diffused reflection measurement. The method uses no prior model and is expected to work across the races (skin color) encompassing a wide range of age groups. An optical fiber-based setup capable of measuring the conjunctival absorption spectrum from 400 to 800 nm is used to monitor the level of bilirubin and is calibrated with the value measured from blood serum of the same human subject. We have also developed software in the LabVIEW platform for use in online monitoring of bilirubin levels in human subjects by non-experts. The results demonstrate that relative absorption at 460 nm and 600 nm has a distinct correlation with that of the bilirubin concentration measured from blood serum. Statistical analysis revealed that our proposed method is in agreement with the conventional biochemical method. The innovative non-contact, low-cost technique is expected to have importance in monitoring jaundice in developing/undeveloped countries, where inexpensive diagnosis of jaundice with minimally trained manpower is obligatory.

1.4.2. Development of Nanoparticle-based Therapeutic Strategy for Hyperbilirubinemia Control

1.4.2.1. ***Unprecedented catalytic activity of Mn_3O_4 nanoparticles: potential lead of a sustainable therapeutic agent for hyperbilirubinemia*** **[53]:** In this study, we have studied an unprecedented catalytic decomposition of bilirubin, in absence of any photo-activation, by citrate functionalized Mn_3O_4 nanoparticles. Mechanistic studies on the catalytic process have resulted in greater understanding of the catalysts recyclability and additional insight into the active sites of the nanoparticles involved. Considering the critical need for improved techniques to remove bilirubin from blood plasma of patients suffering from hyperbilirubinemia, we have tested the *in vitro* reactivity of the catalyst on the whole blood specimen drawn from hyperbilirubinemia patients. It is revealed that the catalyst can significantly suppress the bilirubin level (both conjugated and unconjugated) in the whole blood specimens *in vitro*, without much affecting other important haematological constituents.

Given the outstanding catalytic activity, colloidal stability and biocompatibility of citrate-Mn_3O_4 NPs, we anticipate that the observations may open up a new avenue of nanotherapy in the fight against hyperbilirubinemia.

1.4.2.2. ***Safe & symptomatic medicinal use of surface functionalized Mn_3O_4 nanoparticles for hyperbilirubinemia treatment in mice*** **[54]:** In this study, we have extended our earlier work from ex-*in vivo* to *in vivo* in mice model. We have synthesized citrate capped Mn_3O_4 NPs and characterized their interaction with biological macromolecules *in vitro* for the potential use in mice model of hyperbilirubinemia (higher bilirubin level in blood). We have demonstrated ultrahigh efficacy of the Mn-based NPs in symptomatic treatment of hyperbilirubinemia for rapid reduction of blood bilirubin in mice compared to existing approved medicine silymarin without any toxicological implications in the experimental animals. These findings may pave the way for practical clinical use of the NPs as safe medication of hyperbilirubinemia in human subjects.

1.4.3. Development of an Online, Simultaneous Diagnosis and Therapeutic Strategy of Hyperbilirubinemia for Potential Application in Neonatal Subjects

1.4.3.1. ***Evanescent field: A potential light-tool for theranostics application*** **[55]:** In this study, we have demonstrated a minimally invasive optical approach for theranostics, which would reinforce diagnosis, treatment, and preferably guidance simultaneously, is considered to be a major challenge in biomedical instrument design. We have developed an evanescent field-based fiber optic strategy for the potential theranostics application in hyperbilirubinemia, an increased concentration of bilirubin in the blood and are a potential cause of permanent brain damage or even death in newborn babies. Potential problem of bilirubin deposition on the hydroxylated fiber surface at physiological pH (7.4), that masks the sensing efficacy and extraction of information of the pigment level, has also been addressed. Removal of bilirubin in a blood-phantom (hemoglobin and human serum albumin) solution from an enhanced level of 77 μM/L (human jaundice >50 μM/L) to ~30μM/L (normal level ~25 μM/L in human) using our strategy has been successfully demonstrated. In a model experiment using chromatography paper as a mimic of biological membrane, we have shown efficient degradation of the bilirubin under continuous monitoring for guidance of immediate/future course of action.

1.4.4. Detection of a Picosecond-resolved Dipole-dipole Interaction on Optical Fiber Surface for Potential Application in Sensing at Molecular Level

1.4.4.1. ***Ultrafast FRET at fiber tips: Potential applications in sensitive remote sensing of molecular interaction*** **[56]:** Förster resonance energy transfer (FRET) strategy is well adopted in fiber-optics for efficient sensor design. However, resonance type energy transfer from one molecule (donor) to other (acceptor) should meet few key properties including donor to acceptor energy migration in non-radiative way, which is hard to conclude from simply emission quenching of the donor, rather needs careful investigation of excited state lifetime of the donor molecule. In the present study, we have shown that the evanescent field of an optical fiber can be coupled to covalently attached donor (dansyl) molecule at the fiber tip. By using picosecond resolved time correlated single photon counting (TCSPC) we have demonstrated that dansyl at the fiber tip transfers energy to a well known DNA-intercalating dye ethidium upon surface adsorption of DNA at the fiber tip. Our ultrafast detection scheme selectively distinguishes the probe (dansyl) emission from the intrinsic emission of the fiber. The validation of the energy transfer mechanism to be of resonance type (FRET), allows us to estimate the distance between the probe dansyl and the surface adsorbed DNA. We have also used the setup for the remote sensing of the dielectric constant (polarity) of an environment as the excited sate lifetime of the probe dansyl heavily depends on the polarity of the immediate host environment. FRET signal from a used fiber tip immediately after adsorption of DNA reveals stepwise surface desorption of the biomolecule in saline solution. The reusability of the fiber tip for sensing has also been demonstrated.

1.4.4.2. ***Medical diagnosis and remote sensing at fiber-tip: Picosecond resolved FRET sensor*** **[57]:** In this study, we have extended our earlier work towards more practical and workable model upon simplifying the experimental setup. After successful validation of the FRET scheme at the fiber tip, we have utilised the setup for remote sensing applications. We have finally implemented the detection mechanism to detect an industrial synthetic dye methylene blue (MB) in water.

1.4.5. Development of a DNA-based Material for Potential Fiber Optic Sensing of Heavy Metals in Biomedically Relevant Environments

1.4.5.1. ***DNA biomaterial based fiber optic sensor: Characterization and application for monitoring in situ mercury pollution*** **[58]:** In the present work we have developed a novel silver-nanoparticle (Ag-NPs) impregnated genomic DNA-lipid (CTAB) complex, which is completely insoluble in water and forms excellent thin film on optical fiber tips. The intact structural as well as functional integrity of the genomic DNA (from a marine waste product of salmon fish processing) in the thin film is found to be a key factor for its specific affinity to mercury ions in aqueous environments. We have demonstrated that a dip-coated optical fiber tip can work as a fluorescence sensor in addition to a surface plasmon resonance (SPR) type absorption sensor due to nano surface energy transfer (NSET) between the DNA minor-groove binding dye 4', 6-diamidino-2-phenylindole (DAPI) and Ag-NPs. Nanomolar, specific detection of mercury ions with few seconds reaction time is found in this versatile and economic way revealing clearly the advantageous aspects of our work.

1.5. Plan of theThesis

The plan of the thesis is as follows:

Chapter 1: This chapter gives a brief introduction to the different types of spectroscopic methods used in various kinds of diagnostic and therapeutic applications. The scope and brief summary of the work done has also been included in this chapter.

Chapter 2: This chapter provides an overview of spectroscopic strategies, both the dynamical and steady-state, the structural aspects of biologically important systems (proteins, DNAs) and probes used in the research.

Chapter 3: Details of instrumentation, data analysis and experimental procedures have been discussed in this chapter.

Chapter 4: This chapter demonstrates the development and optimization of a non-contact optical device for online monitoring of jaundice in human subjects.

Chapter 5: Novel catalytic property of transition metal oxide nanoparticles towards bilirubin, upon surface modification has been discussed in this chapter. The application of the nanoparticles as safe and symptomatic medicine for hyperbilirubinemia in mice model has also been elaborated.

Chapter 6: This chapter deals with application of light as tool for simultaneous therapy and diagnosis for potential application in neonatal subjects with hyperbilirubinemia.

Chapter 7: The conventional FRET based fiber optic sensor relies on the steady state experimental observation. In this chapter we have demonstrated FRET in optical fiber tip through time resolved studies and also explored the possible application of this sensor in monitoring environmental polarity (dielectric constant of a medium) and water contaminant methylene blue.

Chapter 8: This chapter offers the synthesis and characterisation procedures of a DNA based biomaterial and also its application towards efficient mercury sensing in biomedically relevant environments.

References

1. Berger, D., A brief history of medical diagnosis and the birth of the clinical laboratory. Part 1-Ancient times through the 19th century*, MLO Med. Lab. Obs.* 31 (1999) 28-30.
2. Richards-Kortum, R. and E. Sevick-Muraca, Quantitative optical spectroscopy for tissue diagnosis*, Annu. Rev. Phys. Chem.* 47 (1996) 555-606.
3. Khandpur, R.S., *Handbook of biomedical instrumentation*. 1989: Tata McGraw-Hill Education.
4. Mallya, M., R. Shenoy, G. Kodyalamoole, M. Biswas, J. Karumathil, and S. Kamath, Absorption spectroscopy for the estimation of glycated hemoglobin (HbA1c) for the diagnosis and management of diabetes mellitus: a pilot study*, Photomed. Laser Surg.* 31 (2013) 219-224.
5. Sinex, J.E., Pulse oximetry: Principles and limitations*, Am. J. Emerg. Med.* 17 (1999) 59-66.
6. Papazoglou, T.G., Malignancies and atherosclerotic plaque diagnosis—is laser induced fluorescence spectroscopy the ultimate solution?*, J. Photochem. Photobiol.* 28 (1995) 3-11.
7. Shahzad, A., M. Knapp, M. Edetsberger, M. Puchinger, E. Gaubitzer, and G. Köhler, Diagnostic application of fluorescence spectroscopy in oncology field: Hopes and challenges*, Appl. Spectrosc. Rev.* 45 (2010) 92-99.
8. Alfano, R.R., Advances in ultrafast time resolved fluorescence physics for cancer detection in optical biopsy*, AIP Adv.* 2 (2012) 011103.
9. Mitchell, M.F., S.B. Cantor, N. Ramanujam, G. Tortolero-Luna, and R. Richards-Kortum, Fluorescence spectroscopy for diagnosis of squamous intraepithelial lesions of the cervix*, Obstet. Gynecol.* 93 (1999) 462-470.
10. Yahav, G., A. Hirshberg, O. Salomon, N. Amariglio, L. Trakhtenbrot, and D. Fixler, Fluorescence lifetime imaging of DAPI-stained nuclei as a novel diagnostic tool for the detection and classification of B-cell chronic lymphocytic leukemia*, Cytometry Part A* 89 (2016) 644-652.
11. Ye, B.H., S.J. Lee, Y.W. Choi, S.Y. Park, and C.D. Kim, Preventive effect of gomisin J from Schisandra chinensis on angiotensin II-induced hypertension via an increased nitric oxide bioavailability*, Hypertens. Res.* 38 (2015) 169-177.

12. Kong, K., C. Kendall, N. Stone, and I. Notingher, Raman spectroscopy for medical diagnostics — From in-vitro biofluid assays to in-vivo cancer detection, *Adv. Drug Deliv. Rev.* 89 (2015) 121-134.
13. Weltmann, K.D., E. Kindel, R. Brandenburg, C. Meyer, R. Bussiahn, C. Wilke, and T. von Woedtke, Atmospheric pressure plasma jet for medical therapy: Plasma parameters and risk estimation, *Contrib. Plasma Phys.* 49 (2009) 631-640.
14. Di Marzo, L., A. Miccheli, P. Sapienza, M. Tedesco, A. Mingoli, G. Capuani, T. Aureli, A. Giuliani, F. Conti, et al., 31Phosphorus magnetic resonance spectroscopy to evaluate medical therapy efficacy in peripheral arterial disease. A pilot study, *Panminerva Med.* 41 (1999) 283-290.
15. Bulte, J.W. and D.L. Kraitchman, Iron oxide MR contrast agents for molecular and cellular imaging, *NMR Biomed.* 17 (2004) 484-499.
16. Kim, J., J.E. Lee, S.H. Lee, J.H. Yu, J.H. Lee, T.G. Park, and T. Hyeon, Designed fabrication of a multifunctional polymer nanomedical platform for simultaneous cancer-targeted imaging and magnetically guided drug delivery, *Adv. Mater.* 20 (2008) 478-483.
17. Shin, J., R.M. Anisur, M.K. Ko, G.H. Im, J.H. Lee, and I.S. Lee, Hollow manganese oxide nanoparticles as multifunctional agents for magnetic resonance imaging and drug delivery, *Angew. Chem.* 121 (2009) 327-330.
18. Einaga, H. and S. Futamura, Catalytic oxidation of benzene with ozone over alumina-supported manganese oxides, *J. Catal.* 227 (2004) 304-312.
19. Shen, Y.F., R.P. Zerger, R.N. DeGuzman, S.L. Suib, L. McCurdy, D.I. Potter, and C.L. O'Young, Manganese oxide octahedral molecular sieves: Preparation, characterization, and applications, *Science* 260 (1993) 511-515.
20. Lvov, Y., B. Munge, O. Giraldo, I. Ichinose, S.L. Suib, and J.F. Rusling, Films of manganese oxide nanoparticles with polycations or myoglobin from alternate-layer adsorption, *Langmuir* 16 (2000) 8850-8857.
21. Giraldo, O., S.L. Brock, W.S. Willis, M. Marquez, S.L. Suib, and S. Ching, Manganese oxide thin films with fast ion-exchange properties, *J. Am. Chem. Soc.* 122 (2000) 9330-9331.

22. Toupin, M., T. Brousse, and D. Bélanger, Charge storage mechanism of MnO_2 electrode used in aqueous electrochemical capacitor*, Chem. Mater.* 16 (2004) 3184-3190.
23. Armstrong, A.R. and P.G. Bruce, Synthesis of layered $LiMnO_2$ as an electrode for rechargeable lithium batteries*, Nature* 381 (1996) 499-500.
24. Stobbe, E.R., B.A. de Boer, and J.W. Geus, The reduction and oxidation behaviour of manganese oxides*, Catal. Today* 47 (1999) 161-167.
25. Grootendorst, E.J., Y. Verbeek, and V. Ponec, The role of the mars and van krevelen mechanism in the selective oxidation of nitrosobenzene and the deoxygenation of nitrobenzene on oxidic catalysts*, J. Catal.* 157 (1995) 706-712.
26. Shin, J., R.M. Anisur, M.K. Ko, G.H. Im, J.H. Lee, and I.S. Lee, Hollow manganese oxide nanoparticles as multifunctional agents for magnetic resonance imaging and drug delivery*, Angew. Chem. Int. Ed.* 48 (2009) 321-324.
27. Ha, T.-L., H.J. Kim, J. Shin, G.H. Im, J.W. Lee, H. Heo, J. Yang, C.M. Kang, Y.S. Choe, et al., Development of target-specific multimodality imaging agent by using hollow manganese oxide nanoparticles as a platform*, Chem. Commun.* 47 (2011) 9176-9178.
28. Zener, C., Interaction between the d-shells in the transition metals. II. ferromagnetic compounds of manganese with perovskite structure*, Phys. Rev.* 82 (1951) 403-405.
29. Goodenough, J.B., Theory of the role of covalence in the perovskite-Type manganites [La,M(II)]MnO_3*, Phys. Rev.* 100 (1955) 564-573.
30. Anderson, P.W., New approach to the theory of superexchange interactions*, Phys. Rev.* 115 (1959) 2-13.
31. Urushibara, A., Y. Moritomo, T. Arima, A. Asamitsu, G. Kido, and Y. Tokura, Insulator-metal transition and giant magnetoresistance in $La_{\{1-x\}}Sr_{\{x\}}MnO_3$*, Phys. Rev. B* 51 (1995) 14103-14109.
32. Mortz, M.S., *System for pulse oximetry SpO_2 determination*. 1999, Google Patents.
33. Yamanouchi, I., Y. Yamauchi, and I. Igarashi, Transcutaneous bilirubinometry: preliminary studies of noninvasive transcutaneous bilirubin meter in the Okayama National Hospital*, Pediatrics* 65 (1980) 195-202.

34. Huang, Z., A. McWilliams, H. Lui, D.I. McLean, S. Lam, and H. Zeng, Near-infrared Raman spectroscopy for optical diagnosis of lung cancer, *Int. J. Cancer* 107 (2003) 1047-1052.

35. Bosschaart, N., J.H. Kok, A.M. Newsum, D.M. Ouweneel, R. Mentink, T.G. van Leeuwen, and M.C. Aalders, Limitations and opportunities of transcutaneous bilirubin measurements, *Pediatrics* 129 (2012) 689-694.

36. Ditzel, J. and R.W.S. Clair, Clinical method of photographing the smaller blood vessels and the circulating blood in the bulbar conjunctiva of human subjects, *Circulation* 10 (1954) 277-281.

37. Click, R., J. Dahl-Smith, L. Fowler, J. DuBose, M. Deneau-Saxton, and J. Herbert, An osteopathic approach to reduction of readmissions for neonatal jaundice, *Osteopath. Fam. Physician.* 5 (2013) 17-23.

38. Lister, T., P.A. Wright, and P.H. Chappell, Optical properties of human skin, *J. Biomed. Opt.* 17 (2012) 0909011-09090115.

39. Parkin, D.M., P. Srivatanakul, M. Khlat, D. Chenvidhya, P. Chotiwan, S. Insiripong, K.A. L'Abbé, and C.P. Wild, Liver cancer in Thailand. I. A case-control study of cholangiocarcinoma, *Int. J. Cancer.* 48 (1991) 323-328.

40. Mahtab, M.-A., *Liver: A Complete Book on Hepato-Pancreato-Biliary Diseases*. 2012: Elsevier Health Sciences.

41. Shapiro, S.M. *Chronic bilirubin encephalopathy: diagnosis and outcome*. in *Semin. Fetal. Neonatal. Med.* 2010. Elsevier.

42. Lakovic, K., J. Ai, J. D'Abbondanza, A. Tariq, M. Sabri, A.K. Alarfaj, P. Vasdev, and R.L. Macdonald, Bilirubin and its oxidation products damage brain white matter, *J. Cereb. Blood. Flow. Metab.* 34 (2014) 1837-1847.

43. Schramm, C., J. Herkel, U. Beuers, S. Kanzler, P.R. Galle, and A.W. Lohse, Pregnancy in autoimmune hepatitis: outcome and risk factors, *Am. J. Gastroenterol.* 101 (2006) 556-560.

44. Van Der Veere, C.N., M. Sinaasappel, A.F. McDonagh, P. Rosenthal, P. Labrune, M. Odiévre, J. Fevery, J. Otte, P. McClean, et al., Current therapy for Crigler-Najjar syndrome type 1: Report of a world registry, *Hepatology* 24 (1996) 311-315.

45. Kus, I., N. Colakoglu, H. Pekmez, D. Seckin, M. Ogeturk, and M. Sarsilmaz, Protective effects of caffeic acid phenethyl ester (CAPE) on carbon tetrachloride-induced hepatotoxicity in rats, *Acta Histochem.* 106 (2004) 289-297.

46. Kus, I., M. Ogeturk, H. Oner, S. Sahin, H. Yekeler, and M. Sarsilmaz, Protective effects of melatonin against carbon tetrachloride-induced hepatotoxicity in rats: a light microscopic and biochemical study, *Cell Biochem. Funct.* 23 (2005) 169-174.

47. Mansour, M.A., Protective effects of thymoquinone and desferrioxamine against hepatotoxicity of carbon tetrachloride in mice, *Life Sci.* 66 (2000) 2583-2591.

48. Babalola, O.O., J.I. Anetor, and F.A. Adeniyi, Amelioration of carbon tetrachloride-induced hepatotoxicity by terpenoid extract from leaves of Vernonia amydgalina, *Afr. J. Med. Sci.* 30 (2001) 91-93.

49. Dennery, P.A., D.S. Seidman, and D.K. Stevenson, Neonatal hyperbilirubinemia, *N. Engl. J. Med.* 344 (2001) 581-590.

50. Armin, A., M. Soltanolkotabi, and P. Feizollah, On the pH and concentration response of an evanescent field absorption sensor using a coiled-shape plastic optical fiber, *Sens. Actuator A-Phys.* 165 (2011) 181-184.

51. Paul, P.H. and G. Kychakoff, Fiber-optic evanescent field absorption sensor, *Appl. Phys. Lett.* 51 (1987) 12-14.

52. Polley, N., S. Saha, S. Singh, A. Adhikari, S. Das, B.R. Choudhury, and S.K. Pal, Development and optimization of a noncontact optical device for online monitoring of jaundice in human subjects, *J. Biomed. Opt.* 20 (2015) 067001.

53. Giri, A., N. Goswami, C. Sasmal, N. Polley, D. Majumdar, S. Sarkar, S.N. Bandyopadhyay, A. Singha, and S.K. Pal, Unprecedented catalytic activity of Mn_3O_4 nanoparticles: potential lead of a sustainable therapeutic agent for hyperbilirubinemia, *R. Soc. Chem. Adv.* 4 (2014) 5075-5079.

54. Polley, N., S. Saha, A. Adhikari, S. Banerjee, S. Darbar, S. Das, and S.K. Pal, Safe and symptomatic medicinal use of surface-functionalized Mn_3O_4 nanoparticles for hyperbilirubinemia treatment in mice, *Nanomedicine* 10 (2015) 2349-2363.

55. Polley, N., S. Singh, A. Giri, and S.K. Pal, Evanescent field: A potential light-tool for theranostics application, *Rev. Sci. Instrum.* 85 (2014) 033108.

56. Polley, N., S. Singh, A. Giri, P.K. Mondal, P. Lemmens, and S.K. Pal, Ultrafast FRET at fiber tips: Potential applications in sensitive remote sensing of molecular interaction, *Sens. Actuator B-Chem.* 210 (2015) 381-388.

57. Polley, N. and S.K. Pal. *Medical diagnosis and remote sensing at fiber-tip: picosecond resolved FRET sensor.* in *Proc. of SPIE*. 2016. SPIE.

58. Polley, N., P.K. Sarkar, S. Chakrabarti, P. Lemmens, and S.K. Pal, DNA biomaterial based fiber optic sensor: Characterization and application for monitoring *in situ* mercury pollution, *ChemistrySelect* 1 (2016) 2916-2922.

Chapter 2

Overview of Spectroscopic Tools and Systems

In order to investigate the various processes involved in course of study on ultrafast spectroscopy, synthesis, functionalization and potential application of the biomedically relevant sensors, different steady-state and dynamical tools have been used. In this chapter, a brief discussion about these tools has been provided. A brief overview of the various systems used has also been discussed.

2.1. Steady-state and Dynamical Tools

2.1.1. Diffuse Reflectance Spectroscopy: Reflectance spectroscopy is very closely related to UV/Vis spectroscopy, as both of these techniques use visible light to excite valence electrons to empty orbitals. The difference in these techniques is that in UV/Vis spectroscopy one measures the relative change of transmittance of light as it passes through a solution, whereas in diffuse reflectance, one measures the relative change in the amount of reflected light off of a surface. A solution that is completely clear and colorless has essentially 100% transmission of all visible wavelengths of light, which means that it does not contain any dissolved components that have (allowed) electronic transitions over that energy range. By the same line of reasoning, a white powder effectively reflects 100% of all visible wavelengths of light that interacts with it. However, if the material has electronic energy levels that are separated by energy in the visible region, then it may absorb some of light energy to move electrons from the filled energy level (valence band) into this empty level (conduction band). This causes an relative decrease in the amount of light at that particular energy, relative to a reference source. In other words, the % transmission/reflectance will decrease.

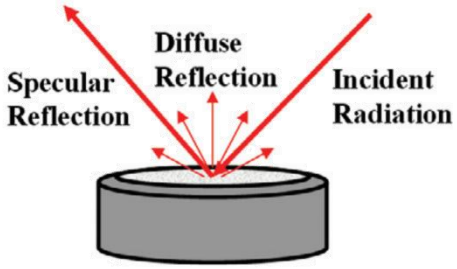

Figure 2.1. *Schematic representation of the diffuse reflection from a solid sample. The diffuse light can be collected for spectroscopic studies.*

2.1.2. Förster Resonance Energy Transfer (FRET): Förster Resonance Energy Transfer [1] is an electrodynamic phenomenon involving the non-radiative transfer of the excited state energy from the donor dipole (D) to an acceptor dipole (A) (Figure 2.2a). FRET has got wide uses in all fluorescence applications including medical diagnostics, DNA analysis and optical imaging. Since FRET can measure the size of a protein molecule or the thickness of a membrane, it is also known as "spectroscopic ruler" [2]. FRET is very often used to measure the distance between two sites on a macromolecule. Basically, FRET is of two types: (a) Homo-molecular FRET and (b) Hetero-molecular FRET. In the former case same fluorophore acts both as energy donor and acceptor, while in the latter case two different molecules act as donor and acceptor.

Each donor-acceptor (D-A) pair participating in FRET is characterized by a distance known as Förster distance (R_0) i.e., the D-A separation at which energy transfer is 50% efficient. The R_0 value ranges from 20 to 60 Å. The rate of resonance energy transfer (k_T) from donor to an acceptor is given by [3],

$$k_T = \frac{1}{\tau_D}\left(\frac{R_0}{r}\right)^6 \tag{2.1}$$

where, τ_D is the lifetime of the donor in the absence of acceptor, R_0 is the Förster distance and r is the donor to acceptor (D-A) distance. The rate of transfer of donor energy depends upon the extent of overlap of the emission spectrum of the donor with the absorption spectrum of the acceptor ($J(\lambda)$), the quantum yield of the donor (Q_D), the relative orientation of the donor and acceptor transition dipoles (κ^2) and the distance between the donor and acceptor molecules (r) (Figure 2.2b). In order to estimate FRET efficiency of the donor and hence to determine distances of donor-acceptor pairs, the methodology described below is followed [3]. The Förster distance (R_0) is given by,

$$R_0 = 0.211\left[\kappa^2 n^{-4} Q_D J(\lambda)\right]^{1/6} \text{ (in Å)} \tag{2.2}$$

where, n is the refractive index of the medium, Q_D is the quantum yield of the donor and $J(\lambda)$ is the overlap integral. κ^2 is defined as,

$$\kappa^2 = \left(\cos\theta_T - 3\cos\theta_D \cos\theta_A\right)^2 = \left(\sin\theta_D \sin\theta_A \cos\varphi - 2\cos\theta_D \cos\theta_A\right)^2 \tag{2.3}$$

where, θ_T is the angle between the emission transition dipole of the donor and the absorption transition dipole of the acceptor, θ_D and θ_A are the angles between these dipoles and the

vector joining the donor and acceptor and φ is angle between the planes of the donor and acceptor (Figure 2.2b). κ^2 value can vary from 0 to 4. For collinear and parallel transition dipoles, $\kappa^2 = 4$; for parallel dipoles, $\kappa^2 = 1$; and for perpendicularly oriented dipoles, $\kappa^2 = 0$. For donor and acceptors that randomize by rotational diffusion prior to energy transfer, the magnitude of κ^2 is assumed to be 2/3. J(λ), the overlap integral, which expresses the degree of spectral overlap between the donor emission and the acceptor absorption, is given by,

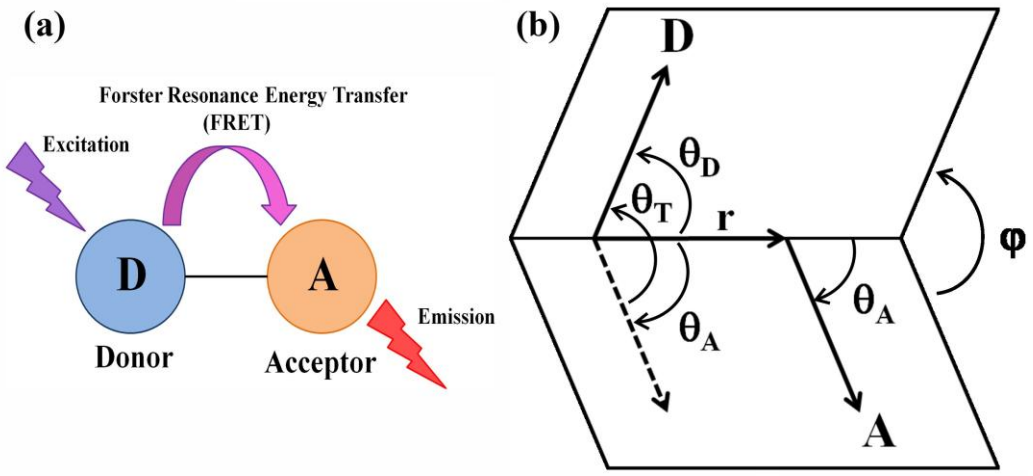

Figure 2.2. *(a) Schematic illustration of the Förster Resonance Energy Transfer (FRET) process. (b) Dependence of the orientation factor* κ^2 *on the directions of the emission and absorption dipoles of the donor and acceptor, respectively.*

$$J(\lambda) = \frac{\int_0^\infty F_D(\lambda)\varepsilon_A(\lambda)\lambda^4 d\lambda}{\int_0^\infty F_D(\lambda)d\lambda} \qquad (2.4)$$

where, $F_D(\lambda)$ is the fluorescence intensity of the donor in the wavelength range of λ to λ +dλ and is dimensionless. $\varepsilon_A(\lambda)$ is the extinction coefficient (in $M^{-1}cm^{-1}$) of the acceptor at λ. If λ is in nm, then J(λ) is in units of M^{-1} cm^{-1} nm^4.

Once the value of R_0 is known, the efficiency of energy transfer can be calculated. The efficiency of energy transfer (E) is the fraction of photons absorbed by the donor which are transferred to the acceptor and is defined as,

$$E = \frac{k_T(r)}{\tau_D^{-1} + k_T(r)} \qquad (2.5)$$

or $$E = \frac{R_0^6}{r^6 + R_0^6} \quad (2.6).$$

The transfer efficiency is measured using the relative fluorescence intensity of the donor, in absence (F_D) and presence (F_{DA}) of the acceptor as,

$$E = 1 - \frac{F_{DA}}{F_D} \quad (2.7a).$$

For D-A systems decaying with multiexponential lifetimes, E is calculated from the amplitude weighted lifetimes $\langle \tau \rangle = \sum_i \alpha_i \tau_i$ [3] of the donor in absence (τ_D) and presence (τ_{DA}) of the acceptor as,

$$E = 1 - \frac{\tau_{DA}}{\tau_D}. \quad (2.7b).$$

The D-A distances can be measured using equations (2.6), (2.7a) and (2.7b). The distances measured using Eq. 2.7a and 2.7b are revealed as R^S (steady state measurement) and R^{TR} (time-resolved measurement), respectively. In one of recent studies from our group [4], we have reported the potential danger of using Eq. 2.7a to conclude the nature of energy transfer as Förster type. The study shows that the energy transfer efficiency E, calculated from steady state experiment (Eq. 2.7a) might be due to re-absorption of donor emission, but not due to dipole-dipole interaction (FRET).

2.1.3. Nanosurface Energy Transfer (NSET): The D−A separations can also be calculated using another prevailing technique, NSET [5, 6], in which the energy transfer efficiency depends on the inverse of the fourth power of the D−A separation [7]. The NSET technique is based on the model of Persson and Lang [6], which is concerned with the momentum and energy conservation in the dipole-induced formation of electron−hole pairs. Here the rate of energy transfer is calculated by performing a Fermi golden rule calculation for an excited-state material depopulating with the simultaneous scattering of an electron in the nearby metal to above the Fermi level. The Persson model states that the damping rate to a surface of a noble metal may be calculated by,

$$k_{NSET} = 0.3 \times \left(\frac{\mu^2 \omega}{\hbar \omega_F k_F d^4} \right) \quad (2.8)$$

which can be expressed in more measurable parameters through the use of the Einstein A_{21} coefficient [8],

$$A_{21} = \frac{\omega^3}{3\varepsilon_0 \hbar \pi c^3} |\mu|^2 \quad (2.9).$$

To give the following rate of energy transfer in accordance with Coulomb's law ($1/4\pi\varepsilon_0$):

$$k_{NSET} = 0.225 \frac{c^3 \Phi_D}{\omega^2 \omega_F k_F d^4 \tau_D} \quad (2.10)$$

where, c is the speed of light, Φ_D is the quantum yield of the donor, ω is the angular frequency for the donor, ω_F is the angular frequency for acceptor, d is the D−A separation, μ is the dipole moment, τ_D is the average lifetime of the donor, and k_F is the Fermi wave-vector [9, 10]. In our studies, we used k_{NSET} as,

$$k_{NSET} = \frac{1}{\tau_{donor-acceptor}} - \frac{1}{\tau_{donor}} \quad (2.11)$$

where, $\tau_{donor-acceptor}$ is the average lifetime of the D−A system [11].

2.1.3. Data Analysis of Time-resolved Fluorescence Transients: Curve fitting of the time-resolved fluorescence transients was carried out using a nonlinear least square fitting procedure to a function (2.12) comprised of convolution of the IRF,

$$(X(t) = \int_0^t E(t')R(t-t')dt') \quad (2.12)$$

(E(t)) with a sum of exponentials (2.13) with pre-exponential factors (B_i),

$$(R(t) = A + \sum_{i=1}^{N} B_i e^{-t/\tau_i}) \quad (2.13)$$

characteristic lifetimes (τ_i) and a background (A). Relative concentration in a multiexponential decay is expressed as (2.14),

$$c_n = \frac{B_n}{\sum_{i=1}^{N} B_i} \times 100 \quad (2.14).$$

The average lifetime (amplitude-weighted) of a multiexponential decay is expressed as,

$$\tau_{av} = \sum_{i=1}^{N} c_i \tau_i \quad (2.15).$$

2.1.4. Transmission of Light through Optical Fiber: An optical fiber is a cylindrical dielectric waveguide (nonconducting waveguide) that transmits light along its axis, by the process of total internal reflection. The fiber consists of a core surrounded by a cladding layer, both of which are made of dielectric materials [48]. To confine the optical signal in the core, the refractive index of the core must be greater than that of the cladding. The boundary between the core and cladding may either be abrupt, in step-index fiber, or gradual, in graded-index fiber. When the light (electromagnetic wave) travels to the boundary between the core and the clad (with an angle greater than the critical angle) a localized attenuating electromagnetic field is generated which is called the evanescent field.

Evanescent wave is a near-field wave with an intensity that exhibits exponential decay without absorption as a function of the distance from the core-clad boundary of the optical fiber as shown in Figure 2.3. The standard practice for the estimation of penetration depth (d_p) of the evanescent field in a "non-absorbing" medium can be illustrated in the following way [12]. In a fiber optic cable the optical signal is transmitted by total internal reflection of the light. The light from the silica core with refractive index n_1 is incident on the clad with refractive index n_2, where $n_1 > n_2$. As a result the light is internally reflected totally, depending upon the incident angle θi, where $\theta i > \theta_c$ (θ_c is the critical angle). In practice the light does not reflect back from the exact plane of separation between core and clad, rather it has certain penetration depth in the clad region. The penetration depth or depth of penetration (d_p) is defined as [12],

$$d_p = \frac{\lambda}{2\pi\sqrt{(n_1{}^2 \sin^2\theta - n_2{}^2)}} \qquad (2.16).$$

The estimated penetration depth for our case is in the range of few hundreds of nm. However, if any portion of clad is removed or etched (as in our case) the depth of penetration would change. It is also worth mentioning that evanescent field strongly interacts with the environment outside the fiber and carry spectroscopic information, and is the key of all the waveguide-based sensors [12]. The scenario would change in the case of an environment, which offers strong optical absorption to the light responsible for the evanescent field.[13, 14] This can be conveniently taken into account by defining a complex refractive index [13],

$$\tilde{n} = n + i\varkappa \qquad (2.17)$$

where, the real part of the refractive index n indicates the phase speed, while imaginary part $\varkappa$ indicates the amount of absorption loss when electromagnetic wave propagates through the medium. Both the real and imaginary parts of the refractive index are the functions of wavelength of the light propagating through the optical fiber. One way to incorporate attenuation of the evanescent field in the absorbing medium is via an absorption coefficient (α_{abs}) [13, 14] in the following way,

$$I(z) = I_0 e^{-\alpha_{abs} z} \tag{2.18}$$

where, I(z) is the intensity of the evanescent field at a distance of z from the interface having field intensity of I_0. α_{abs} denotes absorption coefficient of the medium and equal to twice the magnitude of the imaginary component of the refractive index ($2x\varkappa$) [13]. In this formulation the penetration depth, d_p would be just inverse of the absorption coefficient ($1/\alpha_{abs}$) [13]. From the above formulation it is clear that the penetration depth of the evanescent field in an absorbing medium very much depends on the concentration of the analyte in the medium.

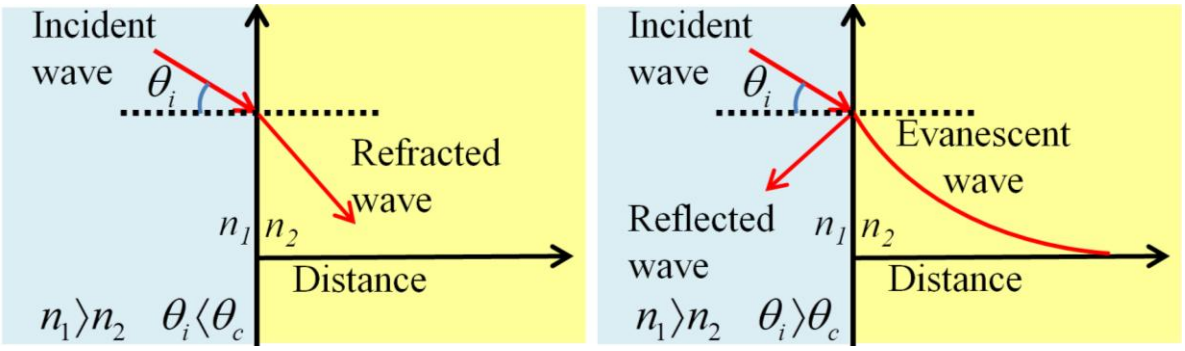

Figure 2.3. *Schematic representation of light refraction from medium with higher to lower refractive index and the evanescent wave in the medium with lower refractive index when* $\theta i > \theta_c$ *(right).*

2.1.5. Statistical Analysis: Comparison of different parameters between the groups in animal studies was performed using one-way analysis of variance (ANOVA) followed by Tukey's multiple comparison test using a computer program GraphPad Prism (version 5.00 for Windows), GraphPad Software, La Jolla California USA, www.graphpad.com. P values <0.05 were considered significant.

2.2. Systems:

2.2.1. Molecular Probes: In this section, we have discussed about the different probe molecules that have been used in the course of study.

2.2.1.1. ***Dansyl chloride [5-(Dimethylamino)naphthalene-1-sulfonyl chloride]:*** Dansyl chloride (Figure 2.4a) is one of the widely used extrinsic fluorescent probes in biological labeling [15, 16]. The reactive free amino groups of amino acids (lysine and arginine) react with dansyl chloride in their deprotonated form as a nucleophile and fluoresce at green region of the visible spectrum. Protein-dansyl conjugates are sensitive to their immediate environment. This, in combination with their ability to accept energy (by FRET) from the amino acid tryptophan, allows this labeling technique to be used in investigating protein folding and dynamics [17].

2.2.1.2. ***4', 6-diamidino-2-phenylindole (DAPI):*** The dye DAPI (Figure 2.4b) is another commercially available fluorescent cytological stain for DNA. Studies on the DAPI-DNA complexes show that the probe exhibits a wide variety of interactions of different strength and specificity with DNA [18]. The dye exhibits intramolecular proton transfer as an important mode of excited state relaxation at physiological pH, which takes place from the amidino to the indole moiety. Supression of this excited state pathway leads to enhancement of fluorescence quantum yield and hence the fluorescence intensity in hydrophobic restricted environments.

2.2.1.3. ***Bilirubin (BR):*** BR, the yellow-orange breakdown product of normal heme catabolism in mammalian systems, introduces great biological and diagnostic values [19]. Both antioxidant and toxic properties have been attributed to BR [20], which is normally conjugated with glucuronic acid and then excreted in the bile. However, when its conjugation with glucuronic acid is inhibited, as in neonatal jaundice and in hereditary forms of congenital jaundice, excess BR deposit to various tissues, giving rise to severe hyperbilirubinemia and neurotoxicity. Phototherapy, the most effective treatment for jaundice to date, decreases the BR levels in the blood by changing the *ZZ*-BR isomer into water-soluble *ZE*-BR [21-23]. Because this reaction is readily reversible, equilibrium is established between native BR and the *ZE* isomer when BR is photoirradiated in a closed system. The second fastest reaction that occurs when BR is exposed to light is the production of lumirubin, a structural isomer of BR.

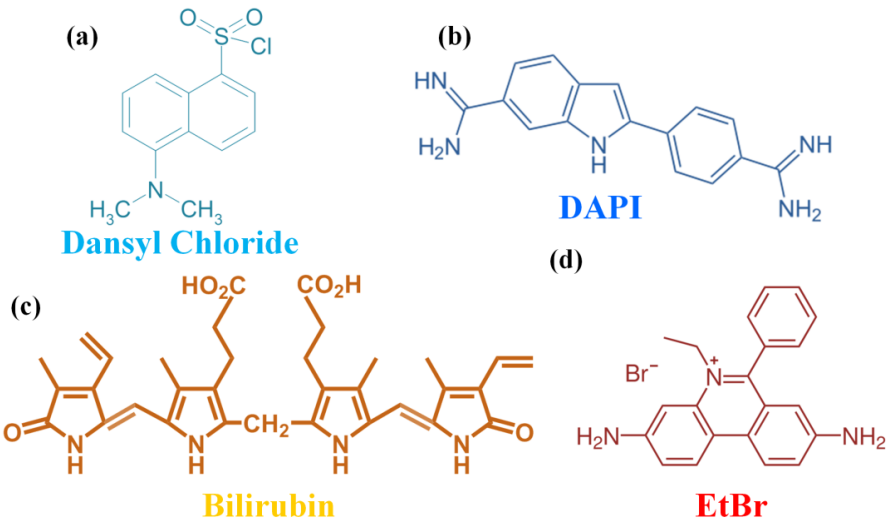

Figure 2.4. *Molecular structures of the molecular probes: (a) Dansyl chloride, (b) DAPI, (c) Bilirubin, (d) EtBr.*

2.2.1.4. ***Ethidium bromide (EtBr), [3,8-diamino-5-ethyl-6-phenylphenanthridinium bromide]*** **:** EtBr is a well known fluorescent probe for DNA, which readily intercalates into the DNA double helix [24]. Its structure is given in Figure 2.4d. Compared to the case of bulk water, the emission intensity and lifetime of EtBr increase nearly 11 times when EtBr intercalates into the double helix of DNA. This remarkable fluorescence enhancement of EtBr is utilized to study the motion of DNA segments, quenching of DNA bound EtBr by various agents, and the interaction of DNA with surfactants and drugs [25]. The photophysical processes of the fluorescence enhancement have recently been explored. The emission intensity of EtBr is low in highly polar, protic solvents, such as alcohol and water, compared to polar, aprotic solvents, e.g., acetone or pyridine. EtBr is insoluble in nonpolar, aprotic solvents like alkanes or dioxane. Compared to the case of water, the emission intensity and lifetime of EtBr increase nearly 5 times in acetone. Addition of water to acetone is found to quench fluorescence of EtBr, while deuterated solvents enhance emission of EtBr.

2.2.2. Biological Macromolecules:

2.2.2.1. ***Human serum albumin (HSA):*** Serum albumins are multi-domain proteins forming the major soluble protein constituent (60% of the blood serum) of the circulatory system [26]. Human Serum Albumin (HSA) (molecular weight 66,479 Da) is a heart-shaped tridomain protein (Figure 2.5) with each domain comprising of two identical subdomains A and B with each domain depicting specific structural and functional characteristics [27]. HSA having 585

amino acid residues assumes solid equilateral triangular shape with sides ~80 Å and depth ~30 Å [28]. Its amino acid sequence comprises of 17 disulfide bridges distributed over all domains, one free thiol (Cys34) in domain-I and a tryptophan residue (Trp214) in domain-IIA. About 67% of HSA is α-helical while the rest of the structure being turns and extended polypeptides [28]. Each domain contains 10 principle helices (h1-h10). Subdomains A and B share a common motif that includes h1, h2, h3 and h4 for subdomain-A, and h7, h8, h9, h10 for subdomain-B. The non-existence of disulfide linkage connecting h1 and h3 in subdomain-IA is an exception. HSA is engaged with various physiological functions involving maintenance of osmotic blood pressure, transportation of a wide variety of ligands in and out of the physiological system. The protein binds various kinds of ligands [29] including photosensitizing drugs [30]. The principal binding regions are located in subdomains IIA and IIIA of which IIIA binding cavity is the most active one [28] and binds digitoxin, ibuprofen and tryptophan. Warfarin, however, occupies a single site in domain-IIA. It is known that HSA undergoes reversible conformational transformation with change in pH of the protein solution [26, 31], which is very essential for picking up and releasing the drugs at sites of differing pH inside the physiological system.

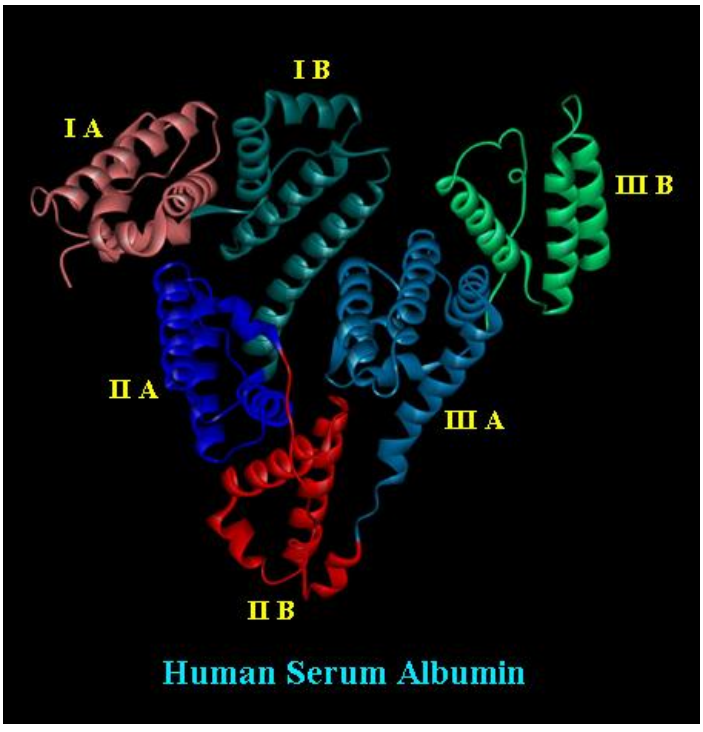

Figure 2.5. *X-ray crystallographic structure (PDB code: 1N5U) of human serum albumin depicting the different domains.*

At normal pH (pH = 7), HSA assumes the normal form (N) which abruptly changes to fast migrating form (F) at pH values less than 4.3, as this form moves "fast" upon gel electrophoresis [31]. Upon further reduction in pH to less than 2.7 the F-form changes to the fully extended form (E). On the basic side of the normal pH (above pH = 8), the N-form changes to basic form (B) and above pH = 10, the structure changes to the aged form (A). Serum albumin undergoes an ageing process when stored at low ionic strength and alkaline pH. The ageing process is catalyzed by the free sulfhydryl group and involves sulfhydryl-disulfide interchange that results in the conservation of the sulfhydryl at its original position.

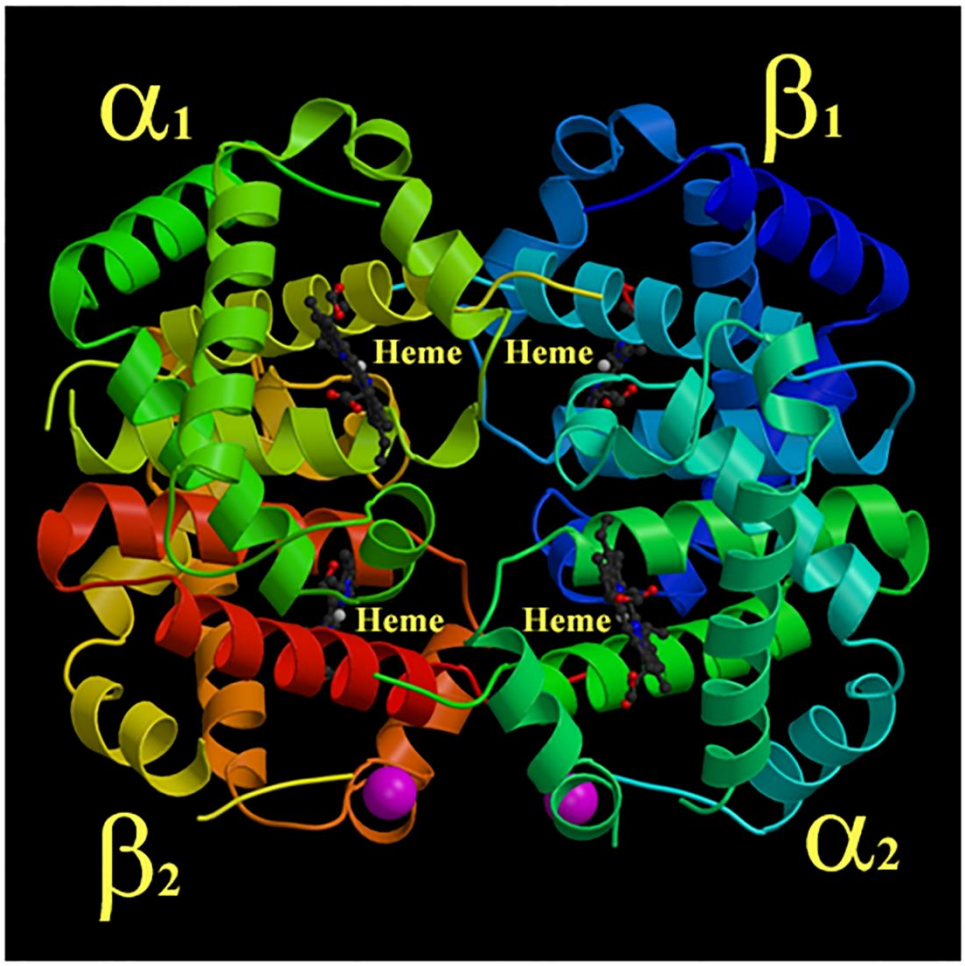

Figure 2.6. *Structure of hemoglobin. There are four subunits as shown by the various colors. The heme groups are shown in predominantly gray. Protein Data Bank ID-4hhb.*

2.2.2.2. *Hemoglobin:* Found in red blood cells, hemoglobin (Figure 2.6) is globular protein that ferry oxygen (O_2) molecules and carbon dioxide (CO_2) molecules throughout the body. Each hemoglobin protein structure consists of four polypeptide subunits, which are held

together by ionic bonds, hydrogen bonds, hydrophobic interactions, and van der Waals forces, as well as four heme pigments, one in each of the subunits [32, 33]. These heme groups contain positively-charged iron (Fe^{2+}) molecules which can reversibly bind to oxygen molecules and transport them to various areas of the body [32, 33]. As the heme groups bind or release their oxygen loads, the overall hemoglobin undergoes conformational changes which alters their affinity for oxygen. Hemoglobin tetramers are comprised of the four subunits, two α-globin chains and two β-globin chains all of which take the form of alpha helices [32]. Found in each chain is a non-protein heme group, which is an assembly of cyclic ring structures surrounding an iron ion that is tethered by nitrogen atoms. The heme group, which is typically hidden within the various subunits, is covalently bound to yet a different nitrogen atom that belongs to a nearby histidine group. This histidine chain, combined with other hydrophobic interactions, stabilize the heme group within each subunit. Oxygen molecules bind to the side of the iron ion that is opposite of the proximal histidine. Located near this opposite side is a different histidine chain, which serves two important function even though it is not directly bound to the heme group [34].

2.2.2.3. ***Deoxyribonucleic acid (DNA):*** Nucleic acids form the central molecules in transmission, expression and conservation of genetic information. DNA serves as carrier of genetic information [35]. The classic example of how biological function follows from biomolecular structure comes from the elucidation of double helical structure of DNA by Watson and Crick [36]. DNAs are polynucleotides with each nucleotide comprising of deoxyribose sugar, purine and pyrimidine bases and phosphate groups. The main bases whose

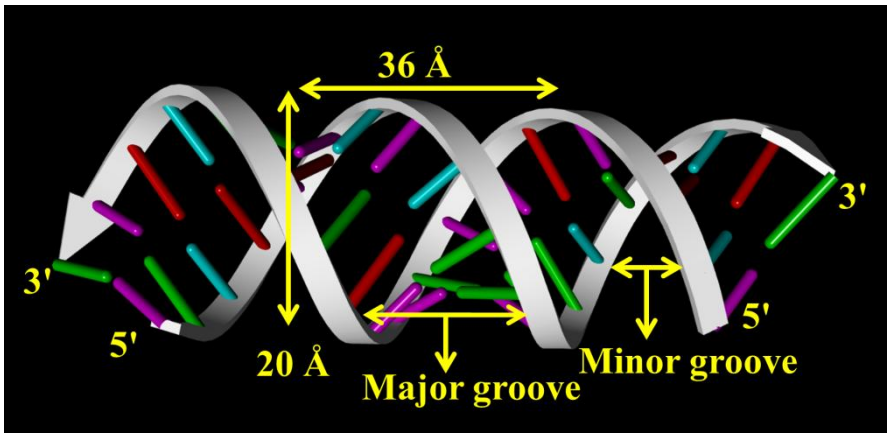

Figure 2.7. *Schematic representation of deoxyribonucleic acid (DNA).*

intermolecular hydrogen bonding holds the DNA strands together are adenine, guanine, thymine and cytosine. There are generally three forms of DNA: the A, B and Z-form. Native DNA, however, exists in B-form. Native DNA is about a metre long and comprises of hundreds of base pairs. The distance between two base pairs in B-DNA is 3.4 Å [37]. In about 4 M NaCl, B-form is converted into Z-form. DNA structures consist of major and minor grooves and intercalation spaces through which DNA interacts with ligands. There are two modes of interaction of DNA with ligands: (i) intercalation, where the planar polycyclic heteroaromatic ligands occupy the space in between the base pairs of DNA (Figure 2.5) and interact through π-π interaction [38, 39], and (ii) groove binding where the ligands bind in the major and minor grooves of DNA [40]. The water molecules at the surface of DNA are critical to the structure and to the recognition by other molecules, proteins and drugs. In one of our study, a synthetic DNA oligomer having sequence CTTTTGCAAAAG was used.

References

1. Förster, T., Intramolecular energy migration and fluorescence*, Ann. Phys.* 2 (1948) 55-75.
2. Stryer, L., Fluorescence energy transfer as a spectroscopic ruler*, Annu. Rev. Biochem.* 47 (1978) 819-846.
3. Lakowicz, J.R., *Principles of Fluorescence Spectroscopy*. 3rd ed. 2006, New York: Springer.
4. Majumder, P., R. Sarkar, A.K. Shaw, A. Chakraborty, and S.K. Pal, Ultrafast dynamics in a nanocage of enzymes: Solvation and fluorescence resonance energy transfer in reverse micelles*, J. Colloid Interface Sci.* 290 (2005) 462-474.
5. Montalti, M., N. Zaccheroni, L. Prodi, N. O'Reilly, and S.L. James, Enhanced sensitized nir luminescence from gold nanoparticles via energy transfer from surface-bound fluorophores*, J. Am. Chem. Soc.* 129 (2007) 2418-2419.
6. Persson, B.N.J. and N.D. Lang, Electron-hole pair quenching of excited states near a metal*, Phys. Rev. B* 26 (1982) 5409-5415.
7. Gersten, J. and A. Nitzan, Spectroscopic properties of molecules interacting with small dielectric particles *J. Chem. Phys.* 75 (1981) 1139-1152.
8. Craig, D. and T. Thirunamachandran, *Molecular Quantum Electrodynamics*. 1984, London: Academic Press.
9. Jennings, T.L., M.P. Singh, and G.F. Strouse, Fluorescent lifetime quenching near d = 1.5 nm gold nanoparticles: probing NSET validity*, J. Am. Chem. Soc.* 128 (2006) 5462-5467.
10. Muhammed, M.A.H., A.K. Shaw, S.K. Pal, and T. Pradeep, Quantum clusters of gold exhibiting FRET*, J. Phys. Chem. C* 112 (2008) 14324-14330.
11. Makhal, A., S. Sarkar, S.K. Pal, H. Yan, D. Wulferding, F. Cetin, and P. Lemmens, Ultrafast excited state deactivation of doped porous anodic alumina membranes*, Nanotechnology* 23 (2012) 305705.
12. Leung, A., P.M. Shankar, and R. Mutharasan, A review of fiber-optic biosensors*, Sens. Actuator B-Chem.* 125 (2007) 688-703.
13. Griffiths, D.J., *Introduction to electrodynamics*. 1999: Prentice Hall.
14. Jackson, J.D., *Classical electrodynamics*. 1975: Wiley.
15. Zhong, D., S.K. Pal, and A.H. Zewail, Femtosecond studies of protein-DNA binding and dynamics: Histone I*, ChemPhysChem* 2 (2001) 219-227.

16. Pal, S.K., J. Peon, and A.H. Zewail, Biological water at the protein surface: Dynamical solvation probed directly with femtosecond resolution, *Proc. Natl. Acad. Sci. U.S.A.* 99 (2002) 1763-1768.

17. Mondol, T., S. Batabyal, A. Mazumder, S. Roy, and S.K. Pal, Recognition of different DNA sequences by a DNA-binding protein alters protein dynamics differentially, *FEBS Lett.* 586 (2012) 258-262.

18. Wilson, W.D., F.A. Tanious, H.J. Barton, R.L. Jones, K. Fox, R.L. Wydra, and L. Strekowski, DNA sequence dependent binding modes of 4',6-diamidino-2-phenylindole (DAPI), *Biochemistry* 29 (1990) 8452-8461.

19. Ostrow, J.D., *Bile Pigments and Jaundice: Molecular, Metabolic and Medical Aspects*. 1986, New York: Marcel Dekker.

20. Stocker, R., A.N. Glazer, and B.N. Ames, Antioxidant activity of albumin-bound bilirubin, *Proc. Natl. Acad. Sci. U.S.A.* 84 (1987) 5918-5922.

21. Lightner, D.A. and A.F. McDonagh, Molecular mechanisms of phototherapy for neonatal jaundice, *Acc. Chem. Res.* 17 (1984) 417-424.

22. Lamola, A.A., W.E. Blumberg, R. McClead, and A. Fanaroff, Photoisomerized bilirubin in blood from infants receiving phototherapy, *Proc. Natl. Acad. Sci. U.S.A.* 78 (1981) 1882-1886.

23. Braslavsky, S.E., A.R. Holzwarth, and K. Schaffner, Solution conformations, photophysics, and photochemistry of bile pigments; bilirubin and biliverdin, dimethyl esters and related linear tetrapyrroles, *Angew. Chem. Int. Ed.* 22 (1983) 656-674.

24. Millar, D.P., R.J. Robbins, and A.H. Zewail, Torsion and bending of nucleic acids studied by subnanosecond time-resolved fluorescence depolarization of intercalated dyes, *J. Chem. Phys.* 76 (1982) 2080-2094.

25. Pal, S.K., D. Mandal, and K. Bhattacharyya, Photophysical processes of ethidium bromide in micelles and reverse micelles, *J. Phys. Chem. B* 102 (1998) 11017-11023.

26. J.F.Foster, *Some aspects of the structure and conformational properties of serum albumin*. 1977, Pergamon: Oxford.

27. Dockal, M., D.C. Carter, and F. Rüker, The three recombinant domains of human serum albumin: Structural characterization and ligand binding properties, *J. Biol. Chem.* 274 (1999) 29303-29310.

28. He, X.M. and D.C. Carter, Atomic structure and chemistry of human serum albumin, *Nature* 358 (1992) 209-215.
29. Ghuman, J., P.A. Zunszain, I. Petitpas, A.A. Bhattacharya, M. Otagiri, and S. Curry, Structural basis of the drug-binding specificity of human serum albumin, *J. Mol. Biol.* 353 (2005) 38-52.
30. Wardell, M., Z. Wang, J.X. Ho, J. Robert, F. Ruker, J. Ruble, and D.C. Carter, The atomic structure of human methemalbumin at 1.9 Å, *Biochem. Biophys. Res. Commun.* 291 (2002) 813-819.
31. Foster, J.F., *The plasma proteins*. 1st ed. 1960, New York: Academic Press.
32. Sadava, D.E., H. Craig Heller, D.M. Hillis, and M. Berenbaum, *Life: The science of biology*. 8th ed. 2008, Massachusetts and Virginia: Sinauer Associates Inc. and W.H. Freeman and Company.
33. Neer, E.J., W. Konigsberg, and G. Guidotti, The interactions between α and β chains of human hemoglobin, *J. Biol. Chem.* 243 (1968) 1971-1978.
34. Perutz, M.F., Mechanisms regulating the reactions of human hemoglobin with oxygen and carbon monoxide, *Annu. Rev. Physiol.* 52 (1990) 1-26.
35. Hershey, A.D. and M. Chase, Independent functionas of viral protein and nucleic acid in growth of bacteriophage, *J. Gen. Physiol.* 36 (1952) 39-56.
36. Watson, J.D. and F.H.C. Crick, Molecular structure of nucleic ccids: A structure for deoxyribose nucleic acid, *Nature* 171 (1953) 737-738.
37. Nelson, D.L. and M.M. Cox, *Lehninger principles of biochemistry*. 3rd ed. 2000, New York: Worth.
38. Lerman, L.S., The structure of the DNA-acridine complex, *Proc. Natl. Acad. Sci.* 49 (1963) 94-102.
39. Lyles, M.B. and I.L. Cameron, Interactions of the DNA intercalator acridine orange, with itself, with caffeine, and with double stranded DNA, *Biophys. Chem.* 96 (2002) 53-76.
40. Dervan, P.B., Molecular recognition of DNA by small molecules, *Bioorg. Med. Chem.* 9 (2001) 2215-2235.

Chapter 3

Instrumentation and Sample Preparation

In this chapter we will describe the details of instrumental setup for the spectroscopic investigation of biomedically relevant samples and corresponding preparation techniques used in our studies.

3.1. Instrumental Setup

3.1.1. Steady-state Absorption and Fluorescence Spectroscopy: Steady-state UV-vis absorption and emission spectra of the probe molecules were measured with Shimadzu UV-2450 spectrophotometer and Jobin Yvon Fluoromax-3 fluorimeter, respectively. Schematic ray diagrams of these two instruments are shown in Figures 3.1 and 3.2.

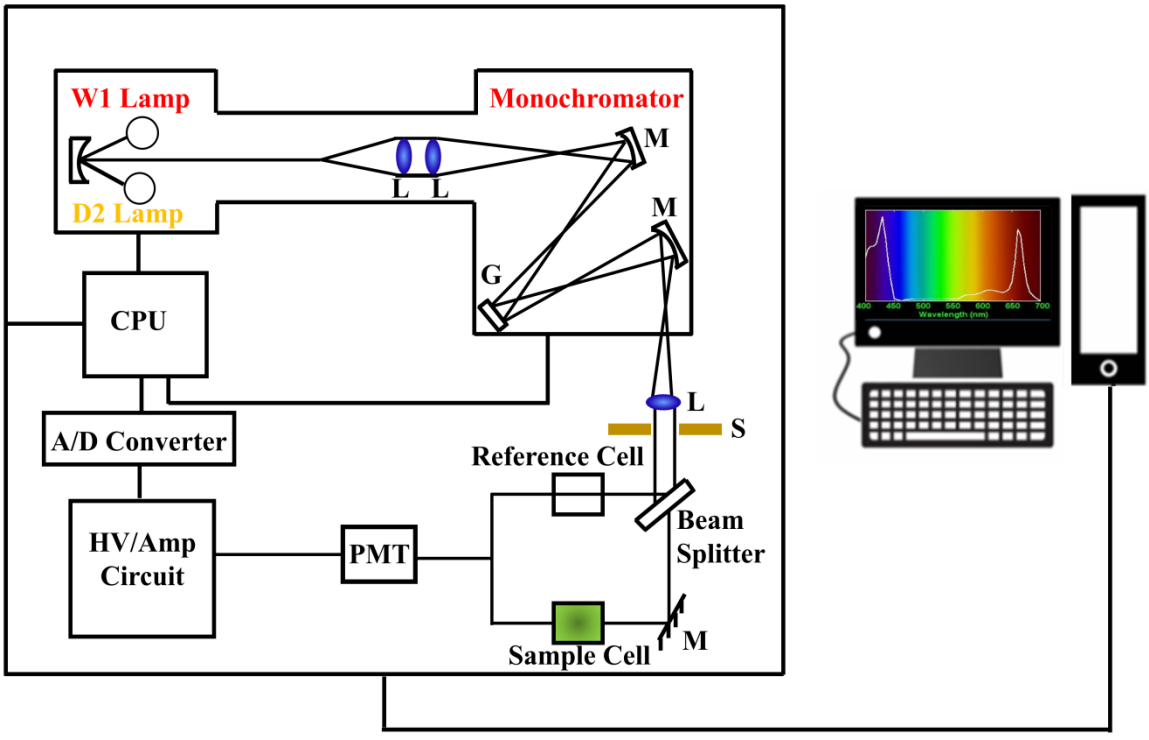

Figure 3.1. *Schematic ray diagram of an absorption spectrophotometer. Tungsten halogen (W1) and deuterium lamps (D2) are used as light sources in the visible and UV regions, respectively. M, G, L, S, PMT designate mirror, grating, lens, shutter and photomultiplier tube, respectively. CPU, A/D converter and HV/amp indicate central processing unit, analog to digital converter and high-voltage/amplifier circuit, respectively.*

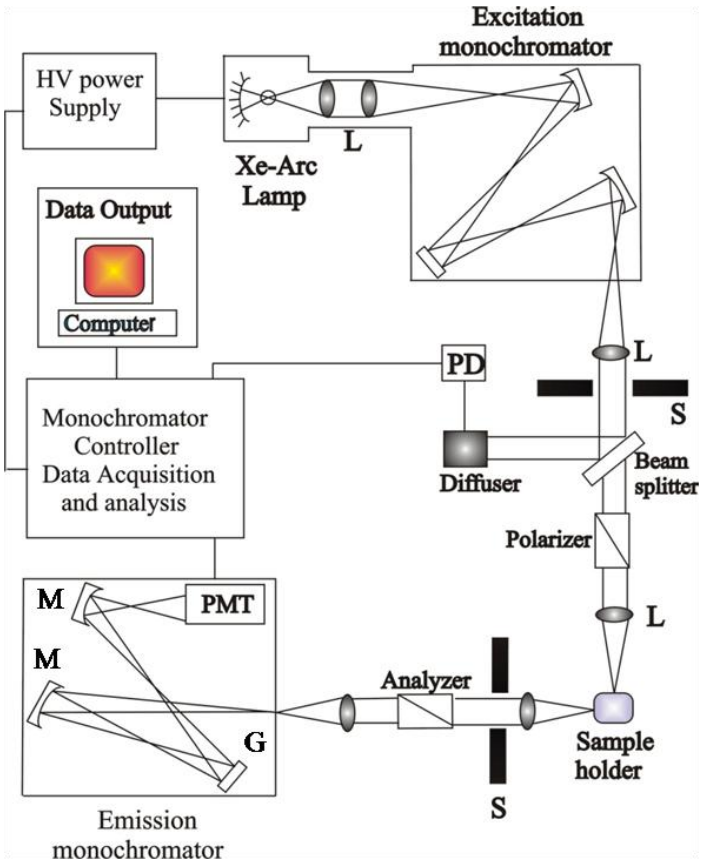

Figure 3.2. *Schematic ray diagram of an emission spectrofluorimeter. M, G, L, S, PMT and PD represent mirror, grating lens, shutter, photomultiplier tube and reference photodiode, respectively.*

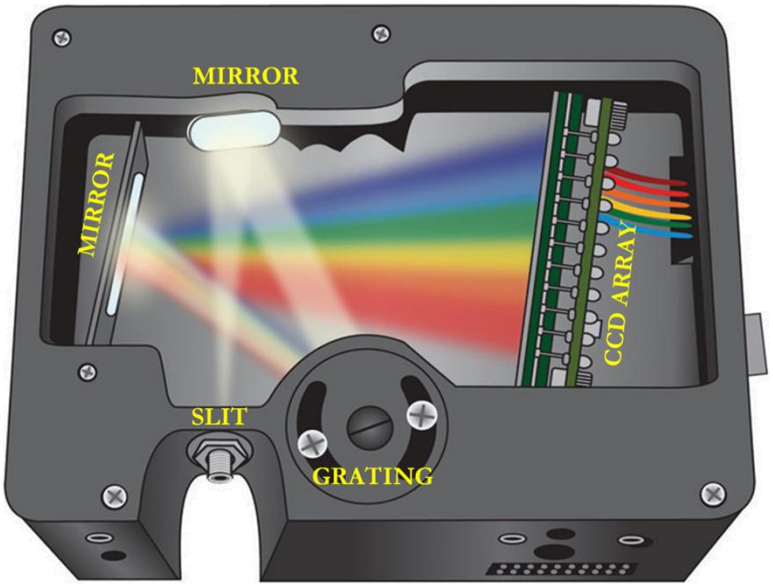

Figure 3.3. *Basic internal ray diagram of CCD array detector based STS-VIS and HR4000 spectrographs.*

For the studies on development of a noncontact device for monitoring bilirubin level in human subjects [1] we have used STS-VIS spectrograph from ocean optics. While, for the development of evanescent filed based theranostics tool [2] HR4000 spectrograph from ocean optics was used. The basic ray diagram of the devices is represented in the Figure 3.3.

3.1.2. Circular Dichroism (CD) Spectroscopy: Circular Dichroism (CD) is a form of spectroscopy based on the differential absorption of left and right-handed circularly polarized light. It can be used to determine the structure of macromolecules (including the secondary structure of proteins and the handedness of DNA). The CD measurements were done in a JASCO spectropolarimeter with a temperature controller attachment (Peltier) (Figure 3.4). The CD spectra were acquired using a quartz cell of 1 cm path length. For proteins, the typical concentration used for CD measurements were within 10 μM while that for DNA were about 20 μM.

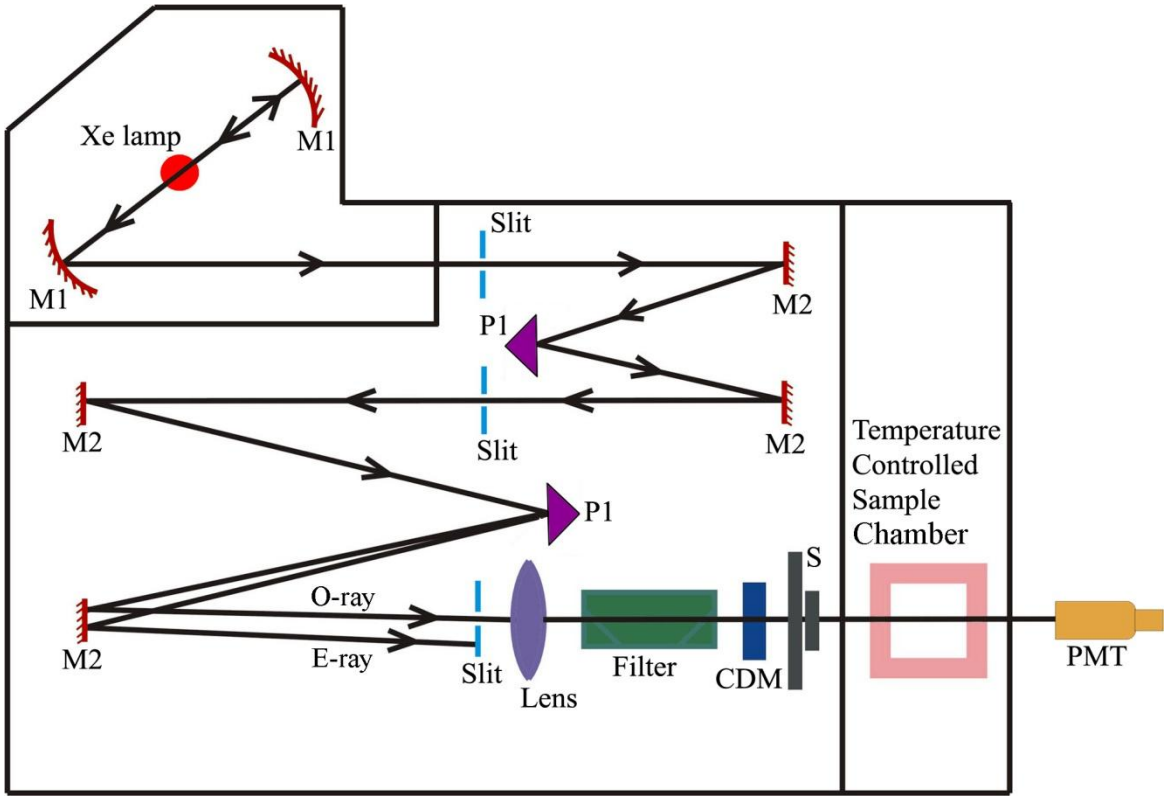

Figure 3.4. *Schematic ray diagram of a circular dichroism (CD) spectropolarimeter. M1, M2, P1, S, PMT, CDM, O-ray and E-ray represent concave mirror, plain mirror, reflecting prism, shutter, photomultiplier tube, CD-modulator, ordinary ray and extraordinary ray, respectively.*

3.1.3. Time Correlated Single Photon Counting (TCSPC): All the picosecond-resolved fluorescence transients were recorded using TCSPC technique. The schematic block diagram of a TCSPC system is shown in Figure 3.5. Primarily, TCSPC setup from Edinburgh instruments, U.K., was used during fluorescence decay acquisitions. The instrument response functions (IRFs) of the laser sources at different excitation wavelengths varied between 70 ps to 80 ps. The fluorescence from the sample was detected by a photomultiplier after dispersion through a grating monochromator. For all transients, the polarizer in the emission side was adjusted to be at 54.70 (magic angle) with respect to the polarization axis of excitation beam.

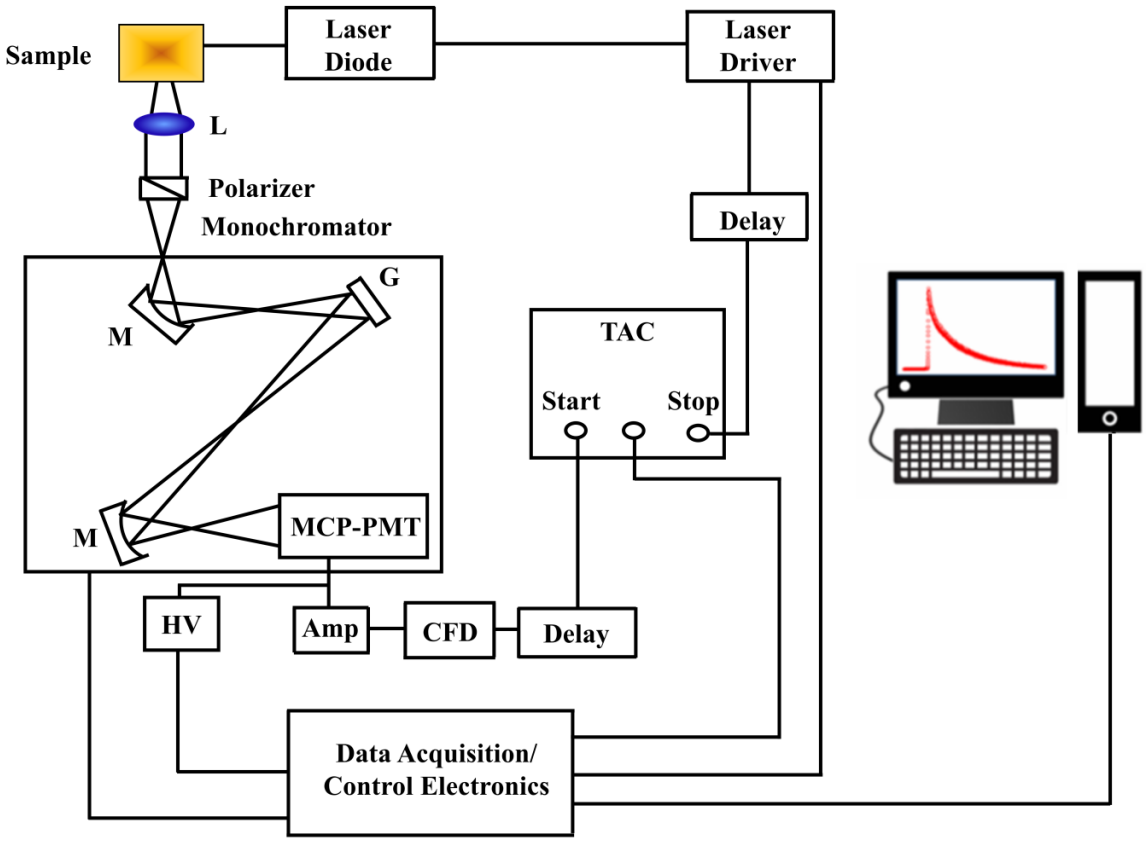

Figure 3.5. *Schematic ray diagram of a time correlated single photon counting (TCSPC) spectrophotometer. A signal from 16 channel photomultiplier tube (PMT) is amplified (Amp) and connected to start channel of time to amplitude converter (TAC) via constant fraction discriminator (CFD) and delay. The stop channel of the TAC is connected to the laser driver via a delay line. L, M, G and HV represent lens, mirror, grating and high voltage source, respectively.*

For tryptophan excitation of protein, femtosecond-coupled TCSPC setup were employed in which the sample was excited by the third harmonic laser beam (300 nm) of the 900 nm (0.5 nJ per pulse) using a mode-locked Ti-sapphire laser with an 80 MHz repetition rate (Tsunami, spectra physics), pumped by a 10 W Millennia (Spectra physics) followed by a

third harmonic generator (Spectra-physics, model 3980). The third harmonic beam was used for excitation of the sample inside the TCSPC instrument and the second harmonic beam was collected as for the start pulse.

3.1.4. Transmission Electron Microscope (TEM): An FEI Tecnai TF20 field-emission high-resolution transmission electron microscope (HRTEM) (Figure 3.6) equipped with an Energy Dispersive X-ray (EDAX) spectrometer was used to characterize the microscopic structures of samples and to analyze their elemental composition. The size of the nanoparticles was determined from the TEM images obtained at 200 kV. Samples for TEM were prepared by placing a drop of the colloidal solution on a carbon-coated copper grid and allowing the film to evaporate overnight at room temperature.

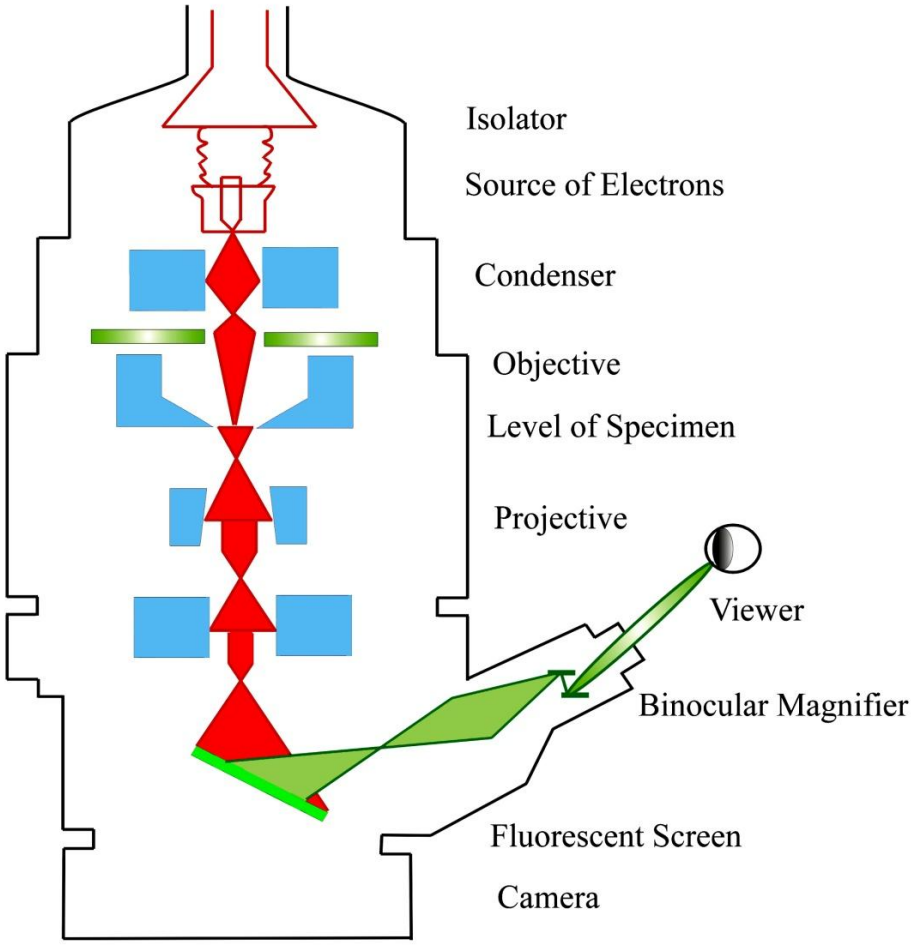

Figure 3.6. *Schematic diagram of a typical transmission electron microscope (TEM). After the transmission of electron beam through a specimen, the magnified image is formed either in the fluorescent screen or can be detected by a CCD camera.*

3.1.5. Scanning Electron Microscope (SEM): Surface characteristics of Porous silicon samples were done by scanning electron microscope FE-SEM; JEOL. Ltd., JSM-6500F. A electron-gun is attached to SEM and the electrons from filament triggered by 0 KV to 30 KV. These electrons go first through a condenser lens and then through an objective lens, then through a aperture and finally reach to the specimen. The high energy electrons go a bit in the sample and back again give secondary electrons. The signal from secondary electrons are detected by detector and amplified. The ray diagram of the SEM setup is shown in Figure 3.7.

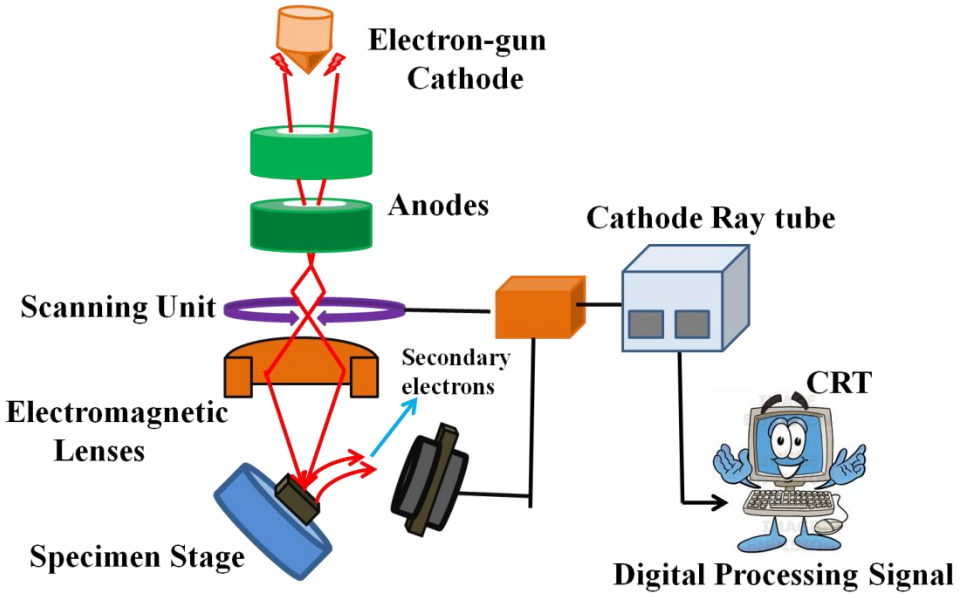

Figure 3.7. *Schematic diagram of typical scanning electron microscope (SEM).*

3.1.6. Fluorescence Microscope: A fluorescence microscope is much the same as a conventional light microscope with added features to enhance its capabilities. The conventional microscope uses visible light (400-700 nanometers) to illuminate and produce a magnified image of a sample. A fluorescence microscope, on the other hand, uses a much higher intensity light source which excites a fluorescent species in a sample of interest. This fluorescent species in turn emits a lower energy light of a longer wavelength that produces the magnified image instead of the original light source. In most cases the sample of interest is labelled with a fluorescent substance known as a fluorophore and then illuminated through the lens with the higher energy source. The illuminating light is absorbed by the fluorophores (now attached to the sample specimen) and causes them to emit a longer lower energy wavelength light. This fluorescent light can be separated from the surrounding radiation with filters designed for that specific wavelength allowing the viewer to see only the fluorescence.

The basic task of the fluorescence microscope is to let excitation light radiate the specimen and then sort out the much weaker emitted light from the image. First, the microscope has a filter that only lets through radiation with the specific wavelength that matches your fluorescing material. The radiation collides with the atoms of the sample specimen and electrons are excited to a higher energy level. When they relax to a lower level,

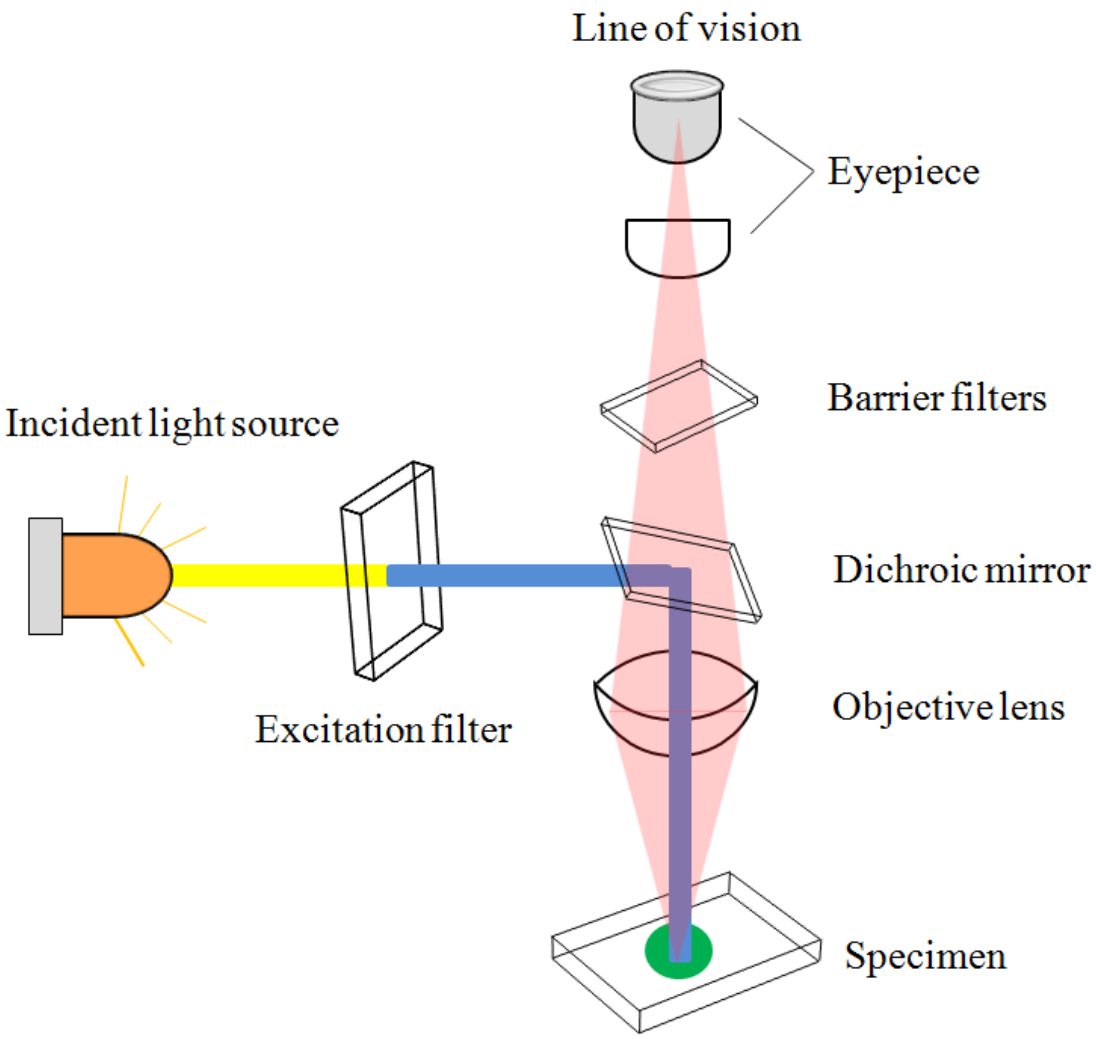

Figure 3.8. *Optical system of a fluorescence microscope.*

they emit light. Fluorescence from the sample is separated from the excitation light by a second filter (Figure 3.8) to make it detectable (visible to the human eye). Most of the fluorescence microscopes used in biology today are epi-fluorescence microscopes, meaning that both the excitation and the observation of the fluorescence occur above the sample. Most use a Xenon or Mercury arc-discharge lamp for more intense light.

3.1.7. **Laser Raman Spectroscopy:** Raman spectroscopy is a useful technique for the identification of a wide range of substances: solids, liquids, and gases. It is a straightforward, non-destructive technique requiring no sample preparation. Raman spectroscopy involves illuminating a sample with monochromatic light and using a spectrometer to examine light scattered by the sample. At the molecular level photons can interact with matter by absorption or scattering processes. Scattering may occur either elastically, or inelastically. The elastic process is termed Rayleigh scattering, whilst the inelastic process is termed Raman scattering. The electric field component of the scattering photon perturbs the electron cloud of the molecule and may be regarded as exciting the system to a 'virtual' state. Raman scattering occurs when the system exchanges energy with the photon, and the system subsequently decays to vibrational energy levels above or below that of the initial state. The frequency shift corresponding to the energy difference between the incident and scattered photon is termed the Raman shift. Depending on whether the system has lost or gained vibrational energy, the Raman shift occurs either as an up or down-shift of the scattered photon frequency relative to that of the incident photon. The down-shifted and up-shifted components are called, respectively, the Stokes and anti-Stokes lines. A plot of detected number of photons versus Raman shift from the incident laser energy gives a Raman spectrum. Different materials have different vibrational modes, and therefore characteristic Raman spectra. This makes Raman spectroscopy a useful technique for material identification. There is one important distinction to make between the Raman spectra of gases and liquids, and those taken from solids-in particular, crystals. For gases and liquids it is meaningful to speak of the vibrational energy levels of the individual molecules which make up the material. Crystals do not behave as if composed of molecules with specific vibrational energy levels, instead the crystal lattice undergoes vibration. These macroscopic vibrational modes are called phonons.

In modern Raman spectrometers (LabRAM HR, Jobin Yvon), lasers are used as a photon source due to their highly monochromatic nature, and high beam fluxes (Figure 3.9). This is necessary as the Raman effect is weak, typically the Stokes lines are $\sim 10^5$ times weaker than the Rayleigh scattered component. In the visible spectral range, Raman spectrometers use notch filters to cut out the signal from a very narrow range centred on the frequency corresponding to the laser radiation. Most Raman spectrometers for material characterization use a microscope to focus the laser beam to a small spot ($<1-100$ μm diameter). Light from the sample passes back through the microscope optics into the spectrometer. Raman shifted

radiation is detected with a charge-coupled device (CCD) detector, and a computer is used for data acquisition and curve fitting. These factors have helped Raman spectroscopy to become a very sensitive and accurate technique.

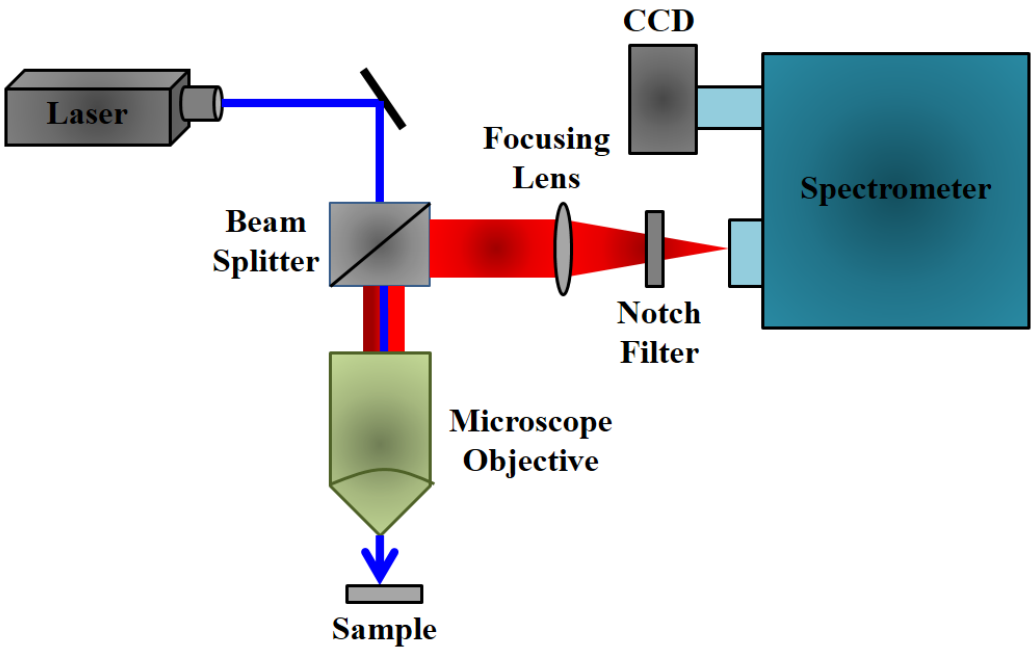

Figure 3.9. *Schematic diagram of a Raman spectrometer is shown.*

3.1.8. Native Gel Electrophoresis: Native gel (native polyacrylamide gel electrophoresis

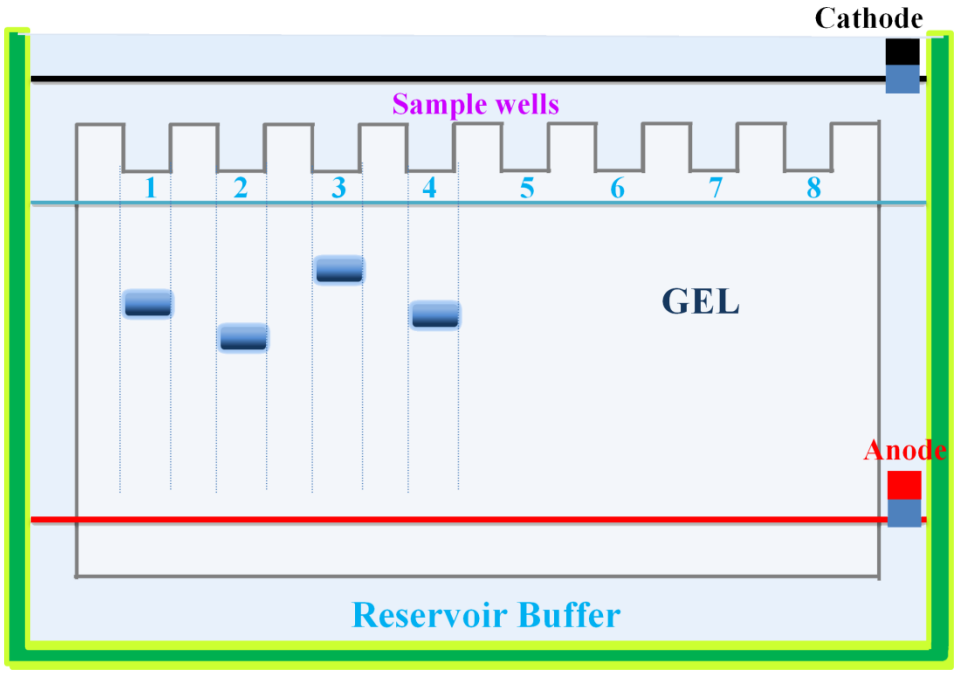

Figure 3.10. *Schematic representation of the native gel electrophoresis sample chamber.*

(PAGE)) electrophoresis studies was performed to discriminate between HSA and HSA-NP [3] (after 12 and 24 hours of incubation). The gel was prepared according to standard procedures [4], without the addition of SDS or β-mercaptoethanol. Gradient in the gels was non-linear. Electrophoresis was conducted in denaturing condition for about three hours in a vertical apparatus (Aplex 305II) at room temperature, at 120V. After completion protein bands were stained using coomassie blue.

3.1.9. Light Sources and Optical Components: Light emitting diode (LED) light sources ware used in fiber optic based detection systems. For the studies on development of a noncontact device for monitoring bilirubin level in human subjects [1] we have used a LS 450 white light source from ocean optics. Whereas, for the project on development of evanescent filed based theranostics tool [2] in addition to the previous light source an additional 450 nm 1W LED was used. All the optical parts used in our studies including optical fiber, collimator, fiber couplers etc. are from Ocean Optics. Whereas, the basic components like front surface reflecting mirrors, dichroic mirrors, parabolic mirrors and optical stands are from Thorlabs.

3.1.10. Experimental Setup for Sensing Studies: In the following section we have elaborated the experimental setup used in optical fiber based spectroscopic detection techniques. The basic experimental setup is represented in the Figure 3.11. A light source and a detector are connected to the end of a bifurcated optical fiber. On the other end of the bifurcated fiber the sensitized fiber tip is connected through a SMA connector. For absorbance based sensing xenon light source and HR4000 spectrograph were used. For fluorescence based sensing 'F-3000 Fiber Optic Mount' was used as an external attachment of the FluoroLog to transmit the excitation and emission light to and from the sensitized fiber tip, respectively. For the time resolve measurement the detector is replaced by a TCSPC setup to monitor the change in the excited state lifetime of the probe attached to the fiber tip. The light source is being replaced by 375nm UV picosecond pulsed laser (LDH-P-C-375) driven by PDL-80-D PicoQuant laser driver with a repetition frequency of about 62.5 KHz. The pulsed laser beam passes through a dichroic mirror (which reflects <400 nm and passes wavelengths in the visible range) and a off-axis parabolic mirror (focal length 25 mm), and eventually enters into the proximal end of the bifurcated optical fiber. Finally the fluorescence

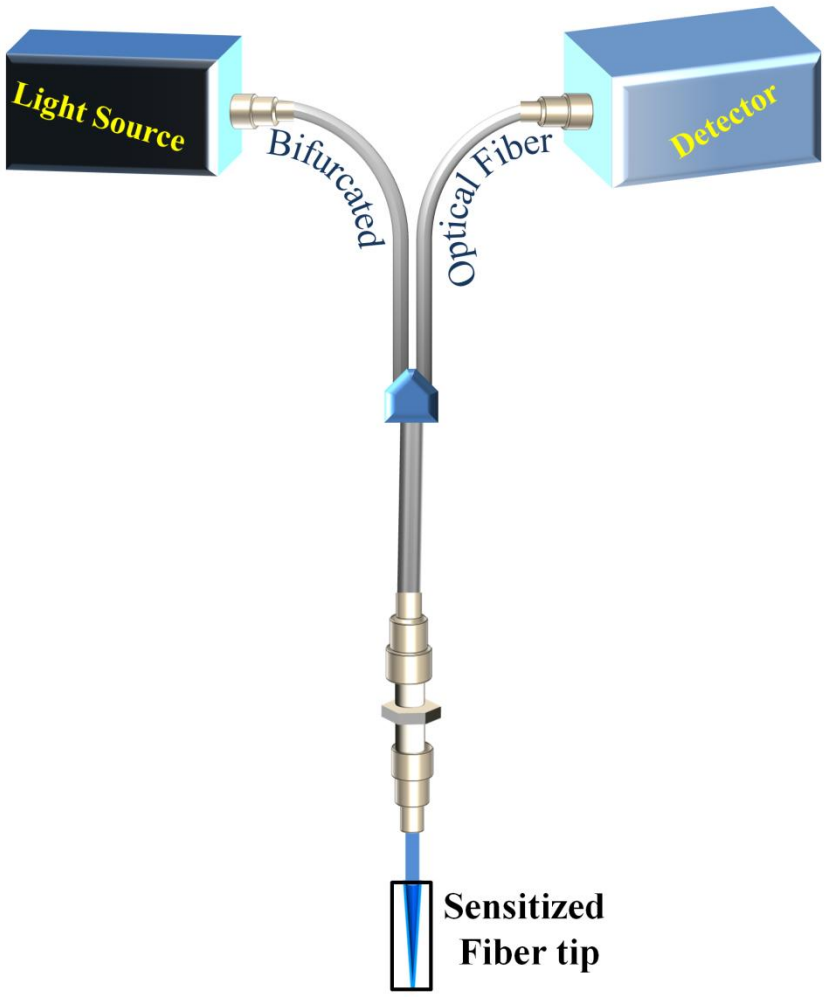

Figure 3.11. *Schematic representation of the experimental setup for different optical fiber based sensing studies. For steady sate studies Xenon or LED has been used as light sources and a spectrograph as detector. For the time resolved studies the light source is being replaced by a pulsed laser and the detector by a TCSPC system.*

signal was collected by the fiber bundle (F-100), placed at the focal point of a condenser lens. Upon collection of the fluorescence signal by the 16 channel PMT (PML-16-1-C), 16 decays corresponding to 16 different wavelengths ware generated by using the Simple Tau-130EM module consisting of two special purpose data processing cards SPC-130EM and DCC-100. The processed electronic signal is fed to the Lenovo ThinkPad laptop-PC with pre installed SPCM64 software through Express Card 54. The steady state emission spectrum has been generated using the histogram plot, corresponding to maximum intensity of each channel (wavelength). All the experiments are performed in dark room to avoid any ambient light exposure.

3.2. Sample Preparation

In this section the different sample preparation methods have been discussed.

3.2.1. Chemicals Used: The chemicals and spectroscopic probes were procured from the following sources. Analytical-grade chemicals were used for synthesis without further purification. All the aqueous solutions were prepared using deionized water from Millipore system. Human serum albumin (HSA), trisodium citrate, sodium hydroxide, manganese chloride, phosphate buffer, silymarin, heparin, acrylamide, bis-acrylamide, ammonium persulfate, isobutanol, tris base, bromophenol blue, dithiothreitol, tetramethylethylenediamine, calf thymus DNA, (3-aminopropyl) triethoxysilane, ethidium bromide, CTAB (cetyltrimethyl ammonium bromide; lipid), sodium borohydride, trisodium citrate , Hydro Fluoric acid as well as the nitrates and chlorides of various metal ions were purchased from Sigma-Aldrich. 2', 7'-Dichlorofluorescin diacetate, ethanol amine, hydrogen chloride, glycerol were received from Merck. Dansyl chloride, precursor of the probe dansyl and DAPI was received from Molecular Probes. All the kits for measurement of serum biochemical parameters were purchased from Autospan Liquid Gold, Span Diagnostics Ltd. (IND). All hematological tests were performed spectro-photometrically following the protocols described by the corresponding manufacturers.

3.2.2. Synthesis of Citrate Functionalized-Mn_3O_4 Nanoparticles (NPs): Synthesis of bulk Mn_3O_4 nanoparticles was done following a reported ultrasonic-assisted approach for preparation of colloidal Mn_3O_4 nanoparticles at normal temperature and pressure without any additional surfactants or templates [5]. For functionalizing the as-prepared Mn_3O_4 NPs by Citrate ligand first, 0.5 M citrate (ligand) solution was prepared in Milli-Q (from Millipore) water. Then, the pH of the solutions at ~7 was adjusted by drop wise addition of 1 (M) sodium hydroxide (NaOH) solution. In the ligand solution of pH~7, as-prepared Mn_3O_4 NPs (approximately 100 mg powder Mn_3O_4 NPs in 5 mL ligand solution) were added and extensively mixed for 12 hrs in a cyclo-mixer. Finally, using a syringe filter of 0.22 μm diameter the non-functionalized bigger sized NPs were filtered out. The resulting filtrated solutions were used for our experiments, both *in vivo* and *in vitro* studies without further dilution [6].

3.2.3. Donor Blood Study: Blood specimens were drawn under the ethical guidelines of Research Oversight Committee, IPGME&R, Kolkata (Memo No. Inst/IEC/333), from patients suffering from hyperbilirubinemia, those were not under any medications. 4 mL of blood specimen was drawn from each individual, 2 mL of which was collected in 2 plain VACUETTE vacutainer tubes (1 mL in each tube, for bilirubin and other liver function test parameters) and another 2 mL was collected in tubes containing K_3EDTA (1 mL in each tube, for hemocompatibility test) as anticoagulant. 50 μL aqueous citrate-Mn_3O_4 NPs solution in phosphate buffered saline (PBS) was added into one portion (~1 mL) of the freshly drawn blood specimen in a vacutainer tube (at a final concentration of 50 μM), another portion of the blood specimen was treated with citrate solution only (as reference), followed by 3 hrs of dark incubation at 2-8 °C. After incubation, to measure the total and conjugated BR content of both the blood specimens (NPs treated and reference), diazotised dichloroaniline has been used for diazo reaction photometry employing a pathological ABL 800 BASIC automated analyser (Radiometer).

3.2.4. Preparation of Dichlorofluorescein and ROS Measurements: DCFH was prepared [7, 8] from DCFH-DA (dichlorofluorescin diacetate obtained from Calbiochem) by mixing 0.5 mL of 1.0 mM DCFH-DA in methanol with 2.0 mL of 0.01 N NaOH. This deesterification of DCFH-DA proceeded at room temperature for 30 min and the mixture was then neutralized with 10 mL of 25 mM NaH_2PO_4, pH 7.4. This solution was kept on ice in the dark until use.

3.2.5. Preparation of Aqueous Bilirubin Solution: Bilirubin was dissolved in water (from Millipore) at pH~ 10 to prepare the stock solution. To prepare our test solution we diluted a small portion of this stock solution by water and the final pH of the test solution was adjusted around 7.5 (close to physiological pH). We have used freshly prepared aqueous solution of the test pigment for our experiments.

3.2.6. Sensitization of Fiber Tip with Dansyl Chloride: For the sensitization, we have etched the clad (1 cm) manually at the distal end of a 1 m long silicon fiber following the methodology reported in the literature [9, 10]. The SEM images of the fiber tips before and after the etching are represented in the Figure 3.12a and Figure 3.12b, respectively (Figure 3.12). The fiber diameters (core and clad) are found to be consistent with the supplier's

specification (Thorlabs, Inc., Newton, New Jersey, USA). After etching, the fiber tips were cleaned carefully. For cleaning, first the fiber tips were cleaned by bath sonication in acetone for 30 min to remove any residual clad material from the fiber core. Then another

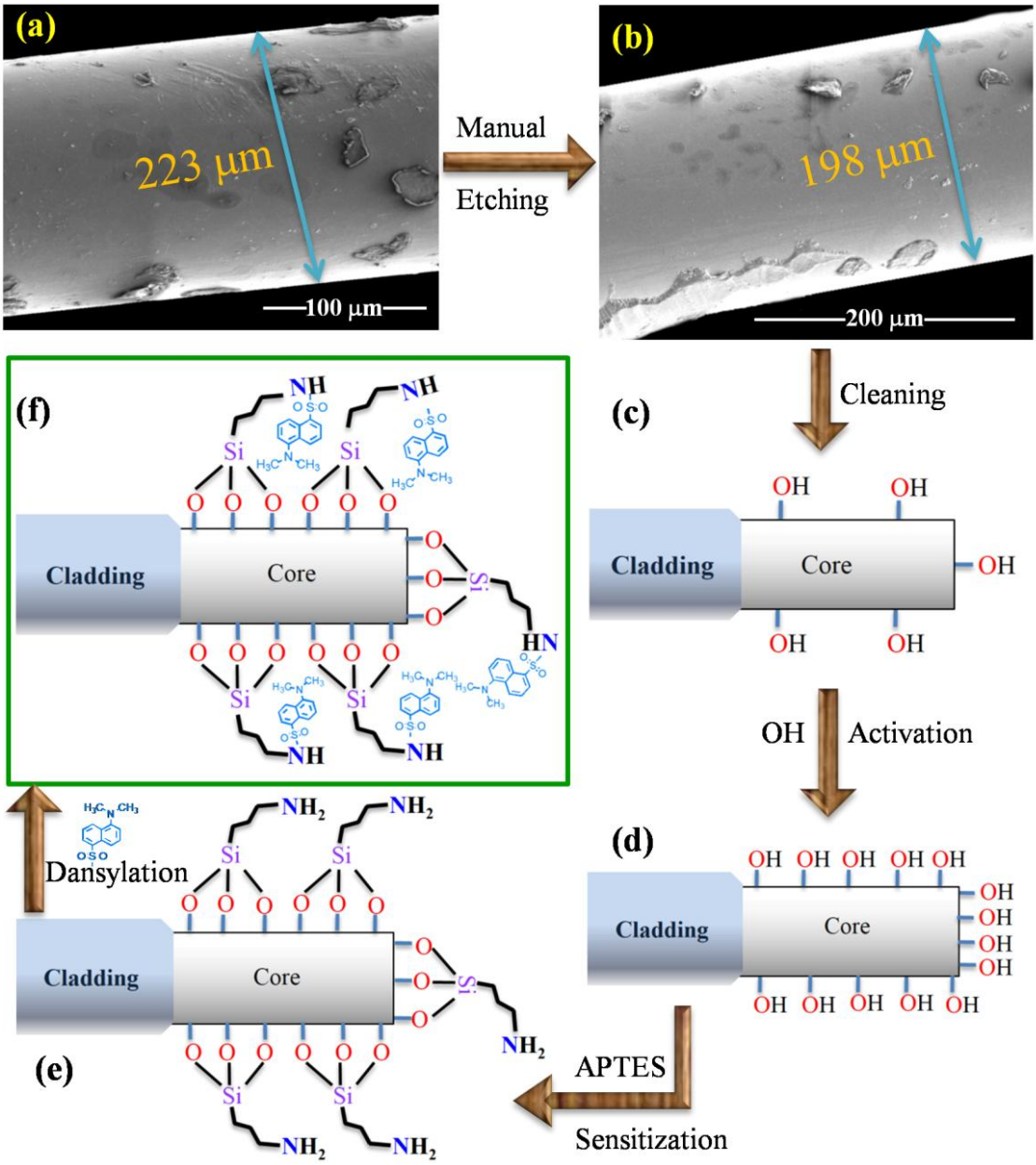

Figure 3.12. *Sensitization of the fiber tip: (a-b) Scanning electron micrographs (SEM) image of the fiber before and after etching respectively. (c) Schematic of a cleaned fiber tip. (d) Hydroxylated fiber tip. (e) APTES sensitized tip (d) Dansylated fiber for the final use.*

cleaning cycle with water-ethanol mixture in bath sonicator was run for the next 30 minutes. A typical fiber surface after the cleaning process is represented in Figure 3.12c. In order to start the sensitization process, as reported in the literature [10-12], the fiber tips were then immersed into H_2SO_4 solution maintaining a constant temperature at 80^0C using a hot plate. After H_2O_2 was added into the H_2SO_4 solution with a concentration ratio of H_2SO_4:H_2O_2=3:1 (also known as the piranha solution) the fiber tip was kept for another 20 min. This solution is a strong oxidizing agent that can remove the residual clad and organic constituents from the fiber tip surface. At the same time, the solution also serves as hydroxylating agent revealing the surface extremely hydrophilic as shown in Figure 3.12d. After thoroughly rinsing with millipore water several times, the fiber tips were immersed in APTES solution for 40 minutes at 45 ^{0}C to conjugate the APTES molecules with the surface hydroxyl groups of the fiber through dehydroxylation reaction (Figure 3.12e). Next, we have covalently functionalized the terminal amine functional groups of the conjugated APTES molecules with a fluorescent dye (dansyl chloride) by exploiting the nucleophilic reactivity of the amine groups. After thoroughly rinsing the fiber tips with water (to remove any free APTES molecule from the surface), for the attachment of dansyl group (dansylation), the tips were immersed in an aqueous solution of pH~10. Then, dansyl chloride solution in acetonitrile was added drop wise into the aqueous solution under continuous stirring. This dansylation process was performed in dark, at low temperature (4 ^{0}C), and after complete addition of dansyl chloride the system was kept overnight for proper dansylation. The fiber tips were finally taken out from the aqueous solution and properly rinsed with acetonitrile to remove the excess and unreacted dansyl chloride from the fiber surface. In this study, we have used these dansylated fiber tips (Figure 3.12f) as an efficient FRET based sensor and tool for monitoring the polarity (dielectric constant) of a test environment.

3.2.7. Preparation of the Silver Nanoparticles Impregnated DNA-lipid Films: The bio-films (DNA-DAPI-CTAB-Ag-NPs) were produced with minute modification of the procedure reported in earlier literature [13]. Ag-NPs were synthesized by reduction of $AgNO_3$ with $NaBH_4$ and stabilized using trisodium citrate [14]. For the preparation of the DNA-DAPI solution, first the DNA stock was prepared by dissolving the fiber-like NaDNA in 50 mM phosphate buffer (6.5 gm/L), followed by shaking incubation overnight at room temperature. Then, DAPI solution (in water) was added into the DNA with concentration

ratio 1:100 to ensure absence of free DAPI in the solution [15]. The DNA, DAPI mixture is left overnight in dark under stirring condition at room temperature for complete complexation. For the preparation of the DNA-DAPI-CTAB-Ag-NPs complex, the DNA-DAPI was added to a 5 mL volumetric flask containing as-prepared Ag-NPs with a volume ratio 1:3. Under stirring condition 500 μl of 40 mM CTAB solution (in water) was added. The DNA-DAPI-CTAB complex starts to form spontaneously and accumulate around the stirring bid. Simultaneously the complex starts to entrap the Ag-NPs in the solution and becomes pale yellow. The precipitate was collected by filtration, washed with distilled water and then lyophilized overnight. The resultant material is dissolved in ethanol upon vortexing for 8-10 hrs. The straw colored mixture is stored at 4 ^{0}C and used without further modifications. The DNA-CTAB, DNA-DAPI-CTAB, DNA-CTAB-Ag-NPs film materials were prepared using the same procedure described above with required modifications.

3.2.8. Preparation of the DNA-lipid Film on Fiber Tip: The optical fibers were taken with a length of 10 cm. Upon removal of jacket and clad (manual etching [2, 16]) from the tip (~1 cm) the fibers were dipped into HF (the tip portion) and kept overnight. The chemical etching [17] of the fibers leads to a sharp needle like fiber tips. The bio-film was coated on the etched fiber tip by dipping the tip into the bio-film material and by environmental drying for few minutes (dip-coating).

3.2.9. Human Studies for Noninvasive Bilirubin Measurement: A total of 90 patients arrived at the pathology section for Liver Function Test (LFT) in the Calcutta Medical Research Institute (CMRI) hospital, Kolkata were recruited in our study. Data were collected in two stages: first, for calibration of the device; second, for measuring the precision of the software driver device in contrast to the standard biochemical method. Soon after the blood sample collection, the volunteers were taken for the bilirubin assessment using our setup with a five minutes time window. Due to non-invasive and non contact nature of the test there is no need of disinfecting the measuring probe. Approval of the local medical ethical committee (Ref: IEC/07/2014/APRV/23) and informed consent from the patient's legally authorized representative ware obtained. Blood samples were taken only for clinical reasons and were obtained by professional technicians from CMRI hospital. A wide variety of age group of the recruited patients with mean age of 45 years (SD 14 years) with different skin toning is the subjects of the present study.

3.2.9.1. *Stage I: For calibration*: For the calibration purpose, 60 patients were incorporated in this set of study. After placing the probe close to the conjunctiva (~2 cm apart) of the patient's eye, the spectral response was generated and stored in the laptop computer for further processing. In order to avoid light interferences, minimum light was used to illuminate the place during collection of the data from the subjects.

3.2.9.2. *Stage II: Assessment of the device*: We studied statistically significant number of patients (n=30) for the assessment of the calibrated device. After placing the probe close to the conjunctiva (~ 2 cm apart) of the eye, the device acquires data and displays bilirubin value. The information is stored and a comprehensive medical report is generated for further study. In order to establish the potential of the device in terms of reproducibility, 20 patients from the total 30 patients in this stage were repetitively examined by our device by two independent examiners.

3.2.10. Animals Studies: Swiss albino mice of either sex (5-8 weeks old, weighing 28±4 gm) were procured from a CPCSEA approved animal house (Registration. No.-50/PO/99/CPCSEA) and housed in standard, clean polypropylene cages in a temperature controlled animal room (temperature 22±3 °C; relative humidity 45-60±1%; 12 hrs light/dark cycle). Water and standard laboratory pellet diet for mice (Hindustan Lever, Kolkata) were available *ad libitum*. All mice were allowed to acclimatize for one week prior to experimentation. The animals were maintained according to the guidelines recommended by Committee for the Purpose of Control and Supervision of Experiments on Animals (CPCSEA), New Delhi, India and approved by the Institutional Animal Ethics Committee (IAEC) (Approval No. JU-Dey's/IAEC/09/14, dated 31.01.2014).

3.2.10.1. *Acute toxicity study*: Single-dose intraperitoneal toxicity study was conducted to determine the possible acute toxicity of surface modified Mn_3O_4 NPs following the general principles of the organisation for economic co-operation and development (OECD) guideline 423 with some adjustments [18]. Twelve female mice were divided in four groups: 1 control group (received 0.2 mL Milli-Q water) and 3 experimental groups (received either 600, 2000 or 5000 mg/kg body weight of NP dissolved in 0.2 mL Milli-Q water). All the animals were kept in fasting condition overnight prior to the injection. Behavior, mortality and body weight (BW) were monitored daily for a period of 14 days.

3.2.10.2. *Treatment protocol; phase I*: Forty eight mice of either sex were randomly divided into six groups of eight mice each. Group I served as the vehicle control and was given olive oil daily (0.5 mL/kg body weight) for a period of two weeks. Group III served as NP control and left untreated for first two weeks, then received citrate capped Mn_3O_4 NPs (500 mg/kg BW dissolved in 0.2mL Milli-Q water) daily for last 7 days. For inducing hyperbilirubinemia and hepatotoxicity (*in vivo*), animals of Groups II, IV, V and VI were administered with carbon tetrachloride solution (50% CCl_4 in olive oil) 1 mL/kg BW daily for a period of two weeks. CCl_4 is a well-known hepatotoxic agent frequently used to study hepatoprotective activity of new drugs in *in vivo* experimental model. CCl_4 administration induces critical liver damage in mice which in turn simulates a condition of acute hepatitis showing similar symptoms as humans [19-21]. CCl_4 activated by liver enzyme cytochrome P450 forms the trichloromethyl free radical ($CCl_3^{\bullet}$) that damages hepatic cells [22]. These radicals binds covalently to sulfhydryl groups of glutathione and protein thiols in cells to initiate a chain of events leading to membrane lipid peroxidation and cell necrosis [23-25]. After CCl_4 intoxication, Group III served as the CCl_4 control and was left untreated. Group IV was administered with citrate capped Mn_3O_4 NP (500 mg/kg BW dissolved in 0.2mL Milli-Q water) for seven days. Group V served as citrate control and was treated with citrate (100 μL/mice; 1:1 solution in water). Group VI served as the positive control and was administered silymarin (100 mg/kg BW) [26, 27] daily for a period of one week. All the treatments were executed by intraperitoneal injection. At the end of the experiment, the animals were kept in fasting condition overnight and sacrificed by cervical dislocation.

3.2.10.3. *Treatment protocol; phase II*: For studying the efficiency of bilirubin degradation by citrate capped Mn_3O_4 NPs over standard drug silymarin forty eight mice were divided into four groups (n=12 per group). Group I served as vehicle control and received olive oil daily (0.5 mL/kg body weight) for a period of three weeks. Other four groups were administered with CCl_4 solution (50% CCl_4 in olive oil) 1mL/kg BW daily for a period of three weeks to induce hyperbilirubinemia. After induction Group II left untreated, Group III was administered with citrate capped Mn_3O_4 NPs (500 mg/kg BW dissolved in 0.2mL Milli-Q water) twice daily and Group IV received silymarin (100 mg/kg BW) twice daily. Serum biochemical tests were performed from blood collected at 2, 6, 12 and 24 hrs.

3.2.10.4. *Sample preparation for the measurement of serum biochemical parameters*: For biochemical studies blood samples were collected just before sacrifice in sterile tubes (non-heparinized) from retro-orbital plexus and allowed to clot for 45 min. Serum was separated by centrifugation at 3000 rpm for 15 min. All serum samples were sterile, hemolysis-free, and were kept at 4 ºC before determination of the biochemical parameters. Serum bilirubin concentration (Total and Direct) was measured using commercially available test kits and results were expressed as mg/dL. Liver damage was assessed by the estimation of serum activities of alanine aminotransferase (ALT, EC 2.6.1.2), aspartate aminotransferase (AST, EC 2.6.1.1), and alkaline phosphatase (ALP, EC 3.1.3.1), ɣ-glutamyltranferase (GGT, 2.3.2.2) using commercially available test kits. The results were expressed as units/liter (IU/L). Total protein concentration (TP) was estimated and expressed as gm/dL.

3.2.10.5. *Hematological study*: For hematological studies the blood was collected in heparinized tubes. Blood cell count was done using blood smears in Sysmax-K1000 Cell Counter. Parameters studied were Hemoglobin (Hb), Total Red Blood Corpuscles (RBC), Reticulocyte (Rt), Hematocrit (HCT), Mean Corpuscular Volume (MCV), Mean Corpuscular Hemoglobin (MCH), Mean Corpuscular Hemoglobin Concentration (MCHC), Platelets, Total White Blood Corpuscles (WHC), Neutrophils (N), Lymphocytes (L), Eosinophils (E) and Monocytes (M).

3.2.10.6. *Histopathological examination*: The liver was excised immediately after collection of blood, washed with ice-cold phosphate buffer and dried with tissue paper. It was weighed and fixed in neutral formalin solution (10%), dehydrated in graduated ethanol (50–100%), cleared in xylene, and embedded in paraffin. Sections 4–5 μm thick were prepared using microtome and then stained with hematoxylin and eosin (H–E) dye and examined for histopathological changes under the microscope.

References

1. Polley, N., S. Saha, S. Singh, A. Adhikari, S. Das, B.R. Choudhury, and S.K. Pal, Development and optimization of a noncontact optical device for online monitoring of jaundice in human subjects*, J. Biomed. Opt.* 20 (2015) 067001.
2. Polley, N., S. Singh, A. Giri, and S.K. Pal, Evanescent field: A potential light-tool for theranostics application*, Rev. Sci. Instrum.* 85 (2014) 033108.
3. Polley, N., S. Saha, A. Adhikari, S. Banerjee, S. Darbar, S. Das, and S.K. Pal, Safe and symptomatic medicinal use of surface-functionalized Mn_3O_4 nanoparticles for hyperbilirubinemia treatment in mice*, Nanomedicine* 10 (2015) 2349-2363.
4. Shalan, M.G., M.S. Mostafa, M.M. Hassouna, S.E.H. El-Nabi, and A. El-Refaie, Amelioration of lead toxicity on rat liver with Vitamin C and silymarin supplements*, Toxicology* 206 (2005) 1-15.
5. Lei, S., K. Tang, Z. Fang, and H. Zheng, Ultrasonic-assisted synthesis of colloidal Mn_3O_4 nanoparticles at normal temperature and pressure*, Cryst. Growth Des.* 6 (2006) 1757-1760.
6. Giri, A., N. Goswami, C. Sasmal, N. Polley, D. Majumdar, S. Sarkar, S.N. Bandyopadhyay, A. Singha, and S.K. Pal, Unprecedented catalytic activity of Mn_3O_4 nanoparticles: potential lead of a sustainable therapeutic agent for hyperbilirubinemia*, R. Soc. Chem. Adv.* 4 (2014) 5075-5079.
7. Cathcart, R., E. Schwiers, and B.N. Ames, Detection of picomole levels of hydroperoxides using a fluorescent dichlorofluorescein assay*, Anal. Biochem.* 134 (1983) 111-116.
8. LeBel, C.P., H. Ischiropoulos, and S.C. Bondy, Evaluation of the probe 2',7'-dichlorofluorescin as an indicator of reactive oxygen species formation and oxidative stress*, Chem. Res. Toxicol.* 5 (1992) 227-231.
9. Leung, A., P.M. Shankar, and R. Mutharasan, A review of fiber-optic biosensors*, Sens. Actuator B-Chem.* 125 (2007) 688-703.
10. Luo, J., J. Yao, Y. Lu, W. Ma, and X. Zhuang, A silver nanoparticle-modified evanescent field optical fiber sensor for methylene blue detection*, Sensors* 13 (2013) 3986-3997.
11. Arslan, G., M. Özmen, B. Gündüz, X. Zhang, and M. Ersöz, Surface modification of glass beads with an aminosilane monolayer*, Turk. J. Chem.* 30 (2006) 203-210.

12. Tauhardt, L., K. Kempe, M. Gottschaldt, and U.S. Schubert, Poly(2-oxazoline) functionalized surfaces: from modification to application, *Chem. Soc. Rev.* 42 (2013) 7998-8011.
13. Wang, L., J. Yoshida, N. Ogata, S. Sasaki, and T. Kajiyama, Self-assembled supramolecular films derived from marine deoxyribonucleic acid (DNA)−cationic surfactant complexes: Large-scale preparation and optical and thermal properties, *Chem. Mater.* 13 (2001) 1273-1281.
14. Flores, C.Y., C. Diaz, A. Rubert, G.A. Benítez, M.S. Moreno, M.A. Fernández Lorenzo de Mele, R.C. Salvarezza, P.L. Schilardi, and C. Vericat, Spontaneous adsorption of silver nanoparticles on Ti/TiO_2 surfaces. Antibacterial effect on Pseudomonas aeruginosa, *J. Colloid Interface Sci.* 350 (2010) 402-408.
15. Banerjee, D. and S.K. Pal, Dynamics in the DNA recognition by DAPI: Exploration of the various binding modes, *J. Phys. Chem. B* 112 (2008) 1016-1021.
16. Polley, N., S. Singh, A. Giri, P.K. Mondal, P. Lemmens, and S.K. Pal, Ultrafast FRET at fiber tips: Potential applications in sensitive remote sensing of molecular interaction, *Sensor. Actuat. B-Chem.* 210 (2015) 381-388.
17. Puygranier, B.A.F. and P. Dawson, Chemical etching of optical fibre tips — experiment and model, *Ultramicroscopy* 85 (2000) 235-248.
18. OECD, *Test No. 423: Acute Oral toxicity - Acute Toxic Class Method*. OECD Publishing.
19. Basu, S., Carbon tetrachloride-induced lipid peroxidation: eicosanoid formation and their regulation by antioxidant nutrients, *Toxicology* 189 (2003) 113-127.
20. Kabir, N., H. Ali, M. Ateeq, M.F. Bertino, M.R. Shah, and L. Franzel, Silymarin coated gold nanoparticles ameliorates CCl4-induced hepatic injury and cirrhosis through down regulation of hepatic stellate cells and attenuation of Kupffer cells, *R. Soc. Chem. Adv.* 4 (2014) 9012-9020.
21. Weber, L.W.D., M. Boll, and A. Stampfl, Hepatotoxicity and mechanism of action of haloalkanes: Carbon tetrachloride as a toxicological model, *Crit. Rev. Toxicol.* 33 (2003) 105-136.
22. Johnston, D.E. and C. Kroening, Mechanism of early carbon tetrachloride toxicity in cultured rat hepatocytes, *Pharmacol. Toxicol.* 83 (1998) 231-239.
23. Rechnagel, R.O. and E.A. Glende, Jr., Carbon tetrachloride hepatotoxicity: an example of lethal cleavage, *CRC Crit. Rev. Toxicol.* 2 (1973) 263-297.

24. Muriel, P., Regulation of nitric oxide synthesis in the liver*, J. Appl. Toxicol.* 20 (2000) 189-195.

25. Jaeschke, H., G.J. Gores, A.I. Cederbaum, J.A. Hinson, D. Pessayre, and J.J. Lemasters, Mechanisms of hepatotoxicity*, Toxicol. Sci.* 65 (2002) 166-176.

26. Hurkadale, P.J., P.A. Shelar, S.G. Palled, Y.D. Mandavkar, and A.S. Khedkar, Hepatoprotective activity of Amorphophallus paeoniifolius tubers against paracetamol-induced liver damage in rats*, Asian. Pac. J. Trop. Biomed.* 2 (2012) S238-S242.

27. Vuda, M., R. D'Souza, S. Upadhya, V. Kumar, N. Rao, V. Kumar, C. Boillat, and P. Mungli, Hepatoprotective and antioxidant activity of aqueous extract of Hybanthus enneaspermus against CCl_4-induced liver injury in rats*, Exp. Toxicol. Pathol.* 64 (2012) 855-859.

Chapter 4

Optical Spectroscopy for Clinical Diagnostics of Hyperbilirubinemia

4.1. Introduction

Recent world health organization (WHO) fact sheets (updated in June 2014) on global statistics of hepatitis (A, B ,C & E) show that out of more than 400 million detected cases of potentially life-threatening liver infection, more than 1.3 million people die every year due to acute or chronic consequences of advanced liver damage. The global statistics of child mortality due to liver malfunction are also very alarming. It is stated in United Nations Children's Fund report (2012) that twenty one children die per minute, mostly from preventive causes including neonatal jaundice, in most underdeveloped/developing countries. Jaundice is a yellowish pigmentation of the skin and conjunctiva caused by high blood bilirubin levels [1, 2] and is an indicator of liver disease such as hepatitis or liver cancer [3]. An early diagnosis of the neonatal and maternal (particularly due to hepatitis E) jaundice is a proven means of prevention and cure.

The current gold standard to measure the total serum bilirubin (TSB) is determined from a blood sample obtained in an invasive way. Although the method is approved for monitoring jaundice [4, 5], it has several drawbacks. Invasive blood sampling is painful and stressful for the neonates, resulting in blood loss and an increased risk of osteomyelitis [5-7] and infection at the site of sampling. In addition, a factor which is of particular concern is that in the developing world, the conventional method is expensive, laborious, time consuming and dilatory which prevents the possibility of immediate diagnosis [5]. In the case of neonates, the possible alternative for invasive blood sampling is a transcutaneous bilirubinometer (BiliChek and JM-103 are the commercial version of the device) that provides instantaneous cutaneous bilirubin concentration (TcB). The method is based on optical spectroscopy that relates the amount of light absorption by bilirubin (yellow skin) to the concentration of bilirubin in the skin. Since the discovery of the method in 1980 [8], several more devices have been developed in order to improve the accuracy of the device. However, even after 30 years

of development [5], no subcutaneous bilirubinometer can replace blood sampling for the following reasons. The first is the variation of accuracy in different skin color. Most importantly, the bilirubin measured by transcutaneous bilirubinometry (TcB) is a completely different physiological parameter from TSB in blood because TcB consists for over 99% of the concentration of extravascular bilirubin. Due to largely unpredictable processes that regulate the supply and clearance of bilirubin in the extravascular space, one-to-one comparison of the TcB with TSB is impossible. Therefore, an uncertainty in the replacement of blood sampling by TcB still exists. To date there are few other techniques described in the literature for non invasive assessment of bilirubin level in adults *i.e.*, assessment of the jaundice by image acquisition of both the eyes of the patients [9-11]. The system is not capable of making quantitative estimation of bilirubin and is not portable either. It is important to note that in adults, the elevated level of bilirubin and its oxidative products cause various serious diseases including Gilbert syndrome (> 6 mg/dL), Crigler-Najjar type I disease (> 30 mg/dL) [12] and bilirubin-induced neurologic dysfunction (BIND) [13]. Severe neurotoxicity in case of neonates (Kernicterus) and damage in white matter of adult brain are also the consequences of higher bilirubin levels [14]. In case of Hepatitis E infection in pregnant women, associated hyperbilirubinemia itself is found to increase the risk of preterm delivery [15].

In order to surmount the above mentioned limitations of a noninvasive bilirubin monitoring device, the following two strategies are viable alternatives: (1) a medical approach, requiring extensive risk analysis for the predictive value of TcB for mortality/morbidity. (2) A technological approach, where measurement volume of the device is essentially confined to intra vascular space, enabling a one-to-one comparison of TcB and TSB. Our present work basically adopts the latter strategy where the spectroscopic signal essentially comes from the vascular bed of bulbar conjunctiva [16]. As the sclera, duly covered by transparent conjunctiva is white in all human subjects across variety of races, the accuracy of the proposed device is independent of skin color. The light power in the visible region (400-700 nm) which is required (~20 microwatts) for such investigation is much lower than that used in commercially available ophthalmoscope (~100 microwatts) for regular eye check-up, given the sensitivity of the state of the art spectrograph used in the proposed device. Thus the features of the setup which make the device distinct from the existing non-invasive devices for jaundice detection are as follows: (1) directly monitors amount of bilirubin in blood (intensity

of the absorption peak at 460 nm) with extremely high precision without any interference from other pathological condition. (2) Non-contact device does not need any mechanical attachment to the subject, which is very important for the friendly use of the device in neonates/young infants and also virus infected maternal subjects. (3) Signal from conjunctiva, which is white in all human subjects independent of skin color offers uniform sensitivity across different communities in a country. (4) Very limited or almost no training would be required for the healthcare provider. Moreover, the ease of operation with precision in the detection strategy offers future development of the device for low-cost diagnosis of jaundice with minimal manual intervention.

4.2. Result and Discussion

4.2.1. Development and Optimization of a Non-contact Optical Device for Online Monitoring of Jaundice in Human Subjects [17]: The diffused reflectance spectroscopy based absorbance setup (Patented, Patent No. 467/KOL/2009) for monitoring the spectral response of the conjunctiva is represented in Figure 4.1a. A white light source (Model No. LS-450) and a spectrograph (Model No. STS-VIS) with wavelength resolution of 0.47 nm (both are from Ocean Optics, Florida) were used in our study. Lab-grade optical fibers from Ocean Optics were used for the transmission and collection of light to and from the sample (Conjunctiva) respectively. The light from the source is transmitted through the 6 surrounding fibers (Figure 4.1a, excitation fiber) and is incident on the conjunctiva while the single fiber, in the middle of the probe (Figure 4.1a, detection fiber) collects the diffused light and sends it back to the spectrograph. The corresponding spectral response as generated in the spectrograph is then transferred to a laptop computer through USB interface where it is processed in our developed software. The wavelength calibration of our setup has been established with a He-Ne Laser (632.8 nm), fluorescent lamp and emission/absorption of a number of dyes including aqueous bilirubin solution as shown in Figure 4.1b [18, 19]. The comparative spectral response of a normal volunteer and a jaundice patient is represented in the Figure 4.1b. A distinct difference in their spectral appearance is visible; the contribution of yellow pigment deposited in the conjunctiva of the jaundice patients is higher compared to the normal volunteer.

A total of 90 patients arrived at the pathology section for Liver Function Test (LFT) in the Calcutta Medical Research Institute (CMRI) hospital, Kolkata were recruited in our study. Data were collected in two stages: first, for calibration of the device; second, for measuring the precision of the software driver device in contrast to the standard biochemical method. Soon after the blood sample collection, the volunteers were taken for the bilirubin assessment

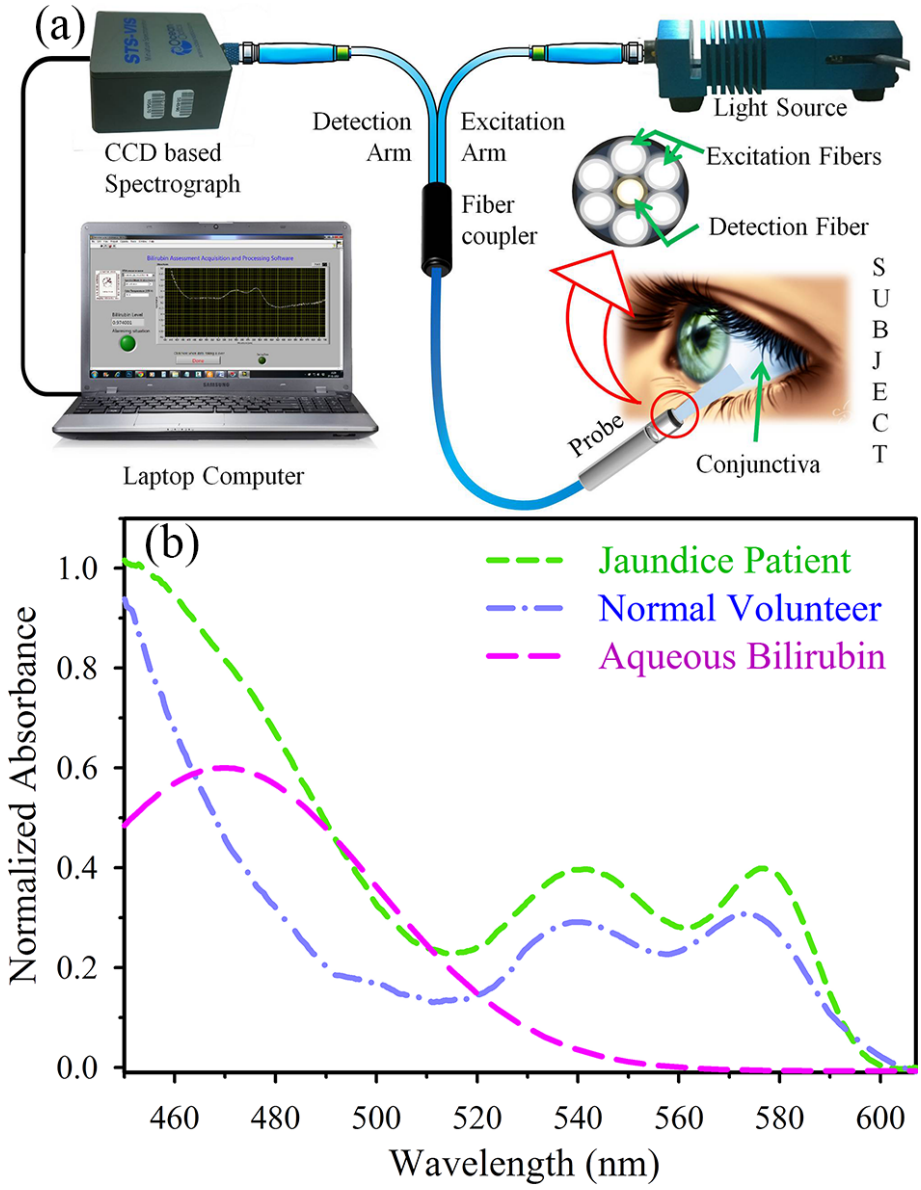

Figure 4.1. *(a) Schematic representation of our working device. The light from the source is transmitted through the six excitation fibers of the excitation arm and incident on the subject (conjunctiva). The diffused light is collected by the detection fiber and transmitted through detection arm to the spectrograph. The spectral response corresponding to the conjunctiva is processed and generated in the laptop computer. (b) The comparative spectral response of conjunctiva of a normal volunteer and jaundice patient has been represented. An absorption spectrum of aqueous bilirubin solution is also included as reference.*

using our setup with a 5 min time window. Due to the noninvasive and non contact nature of the test there is no need of disinfecting the measuring probe. Approval of the local medical ethical committee (Ref: IEC/07/2014/APRV/23) and informed consent from the patient's legally authorized representative were obtained. Blood samples were taken only for clinical reasons and were obtained by professional technicians from CMRI hospital. A wide variety of age group of the recruited patients with mean age of 45 years (SD 14 years) with different skin tones were the subjects of the present study.

For the calibration purpose, 60 patients were incorporated in this set of study. We studied statistically significant number of patients (n=30) for the assessment of the calibrated device. After placing the probe close to the conjunctiva (~2 cm apart) of the eye, the device acquires data and displays bilirubin value. The information is stored and a comprehensive medical report is generated for further study. In order to establish the potential of the device in terms of reproducibility, 20 patients from the total 30 patients in this stage were repetitively examined by our device by two independent examiners.

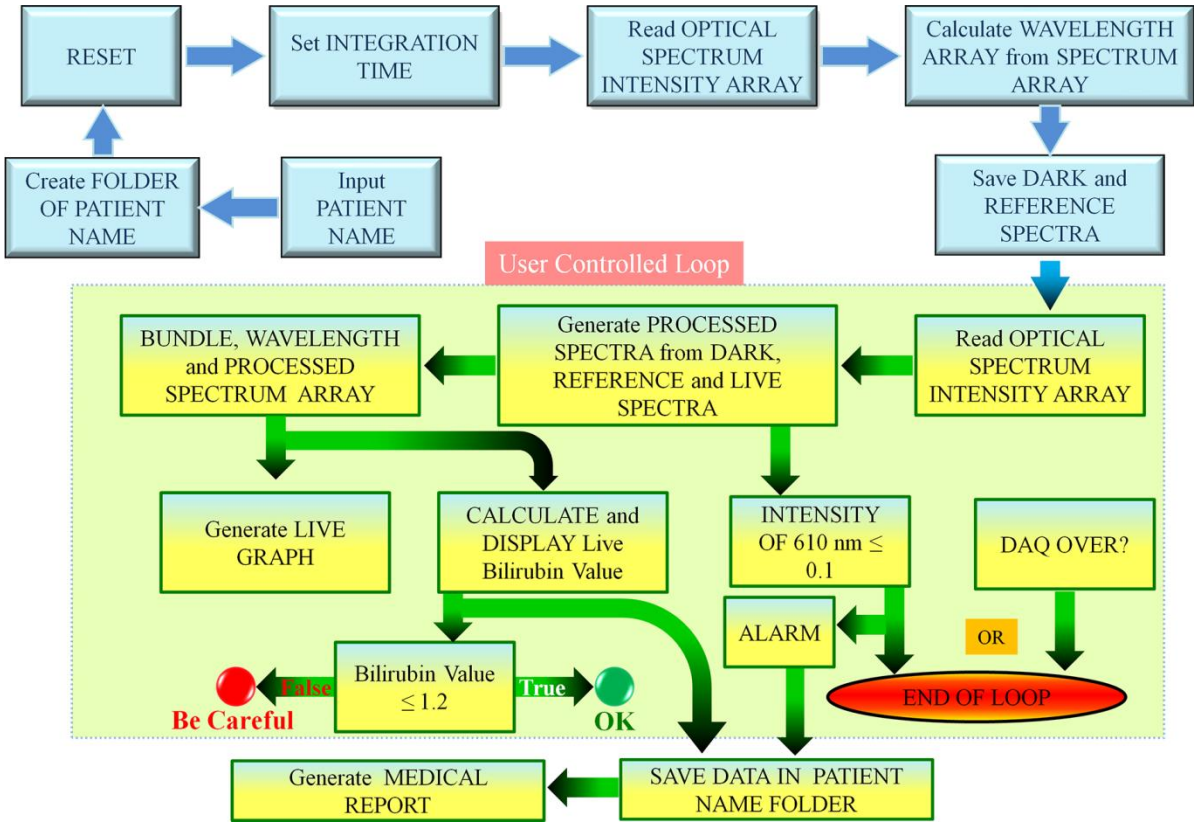

Figure 4.2. *Flow chart of the software designed in LABVIEW platform for non-contact online monitoring of bilirubin level in humans (see text for details).*

The optomechanical components have been connected to a laptop computer using a USB interface. The spectrometer (STS-VIS), which is the active detector in this set-up, has been programmed on LabVIEW platform and can be modified for user defined data acquisition. The online display of the acquired data has been used to analyze the data quality and asses the medical condition of the patients. Finally, the bilirubin level of the patient is displayed with a suggested medical attention on the monitor of DAQ laptop computer. The software for automatic data acquisition has been designed in LabVIEW platform. Figure 4.2 shows the sequential program flow or the algorithm of the developed software. The instrument is first re-initialized to its power on status programmatically to remove any previous custom settings. The software then sets the proper integration time for data acquisition to build up the right S/N ratio of the acquired data. This can either be set manually or automatically as decided by the software using an iterative algorithm. For a particular distance between the probe and the reference surface the software adjusts the integration time using the mentioned iterative algorithm until the peak count reaches the maximum allowed value (here 14000). The information is acquired through the raw socket of the USB port and the size of the array is determined, thus the wavelength array is calculated on the basis of instrument specifications. The "dark spectrum" and "reference spectrum" which can either be pre-acquired or can be determined in-situ are then loaded for spectrum processing. The software now acquires data, produces the processed spectrum, generates an online graph and displays the appropriate bilirubin value. The bilirubin value is calculated using the calibration equation. The data safety level of the patient is determined by the differential absorption values of wavelength 460 nm and 600 nm. The online display also suggests the condition of the patient being within or above the safety limits. The information is stored and a comprehensive medical report is generated for offline use for medical practitioners and patients. Complete care has been taken for the software to be simple on the front panel for the ease of operation even with non scientific personnel having no or minimal medical or instrumentation knowledge.

The stored data (stage I, n = 60) ware then processed to find the correlation between the TSB level of the volunteer with the spectral information obtained from the conjunctiva of the eye. It has already been reported that the spectral contribution near 460 nm wavelength is due to bilirubin, the yellow pigment [19-21]. Different characteristic wavelengths over the

conjunctival spectrum were selected for assessment but it was found that the differential absorbance of 460 nm (a_1) to 600 nm (a_4) and ratiometric values of 470 nm (a_2) to 576 nm (a_3) were found to be more consistent with the TSB level. The differential absorbance of 460 nm to 600 nm (a_1-a_4) was chosen as the index value (x_i) to calibrate the setup with the TSB level. The dependency of the of index value (x_i) with TSB level is represented in the Figure 4.3a. The correlation coefficient (r) is found to be 0.84; P<0.0001, which shows a significant relationship between the two methods (TSB and x_i). Further calibration was done in order to

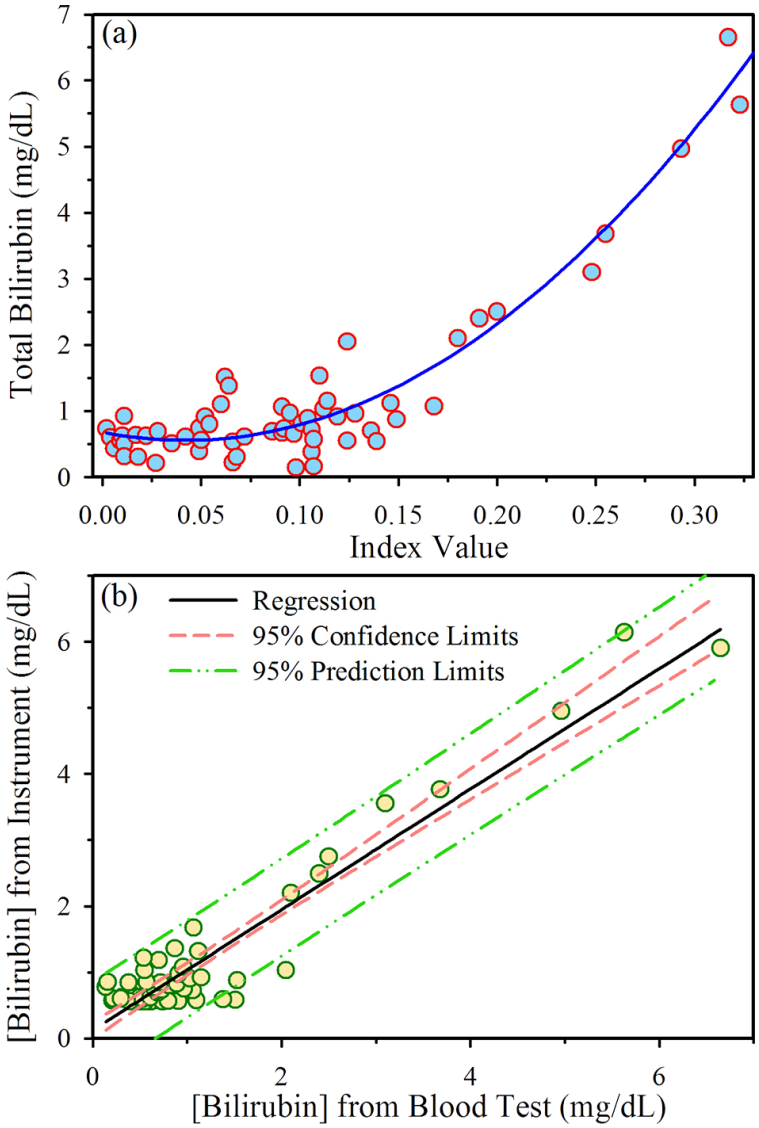

Figure 4.3. *Calibration: (a) The dependency of the total serum bilirubin (TSB) value from blood test with the index value from our instrument (n=60) has been represented graphically. The correlation between them is found to follow a second order polynomial equation with R^2 value of 0.89. (b) Correlation between the TSB value from blood test and from our instrument (correlation factor (r) = 0.96) with the 95% confidence limits and the 95% prediction interval have been represented.*

achieve a nearly perfect relationship. The x_i value is found to follow second order polynomial equation $y_i = 74.67x_i^2 - 7.686x_i + 0.748$ (calibration equation), where y_i is the individual TSB level. We used this calibration equation to calculate bilirubin level from the spectral information (x_i) obtained by our device. This modification greatly improved the correlation to almost perfect (correlation coefficient, r=0.96; P<0.0001). Corresponding linear regression curve is represented in the Figure 4.3b with Pearson correlation coefficient, r=0.96; P<0.0001 and F=627.1; slope 0.932; y intercept 0.118.

In order to find the statistical significance of the non contact optical device for online assessment of the bilirubin level correlation and regression analyses were used [22-24]. We have also used the Bland-Altman method for assessing agreement between the conventional biochemical technique and our non contact optical device [25]. Two crucial factors decide whether a new method can be used interchangeably with an already established method: the amount of agreement between the methods and its clinical evaluation. We compared our proposed non-invasive bilirubin detection method to an established biochemical method using the approach described by Bland and Altman [25, 26] in order to assess the statistical agreement. 30 patients (stage II, n=30) of all age groups were included in our study. Linear regression analysis and Bland-Altman plots are shown in Figure 4.4. Data obtained from the linear regression analysis (Figure 4.4a) show that the two methods show strong correlation as the Pearson correlation coefficient, r=0.99; P<0.0001 and F=1588; slope 1.026; y intercept 0.018.

For adequate comparison of the two methods the difference in measurement of the two methods are plotted against their average (Figure 4.4b). The mean difference between the two methods is depicted as a horizontal line and is rated as bias. The other two horizontal lines represent limits of agreement which explains that 95% of the differences were assumed to lie within these limits. The results exhibit reasonable agreement between our proposed method and the conventional pathological method of bilirubin detection. The difference in two methods (conventional-proposed) has mean value of -0.06 mg/dL and SD value of 0.182. The limits of agreement are from -0.42 to 0.30 mg/dL. Hence, it can be inferred that for 95% of individuals, a measurement by our method would be between 0.42 units less and 0.30 units greater than a measurement by the conventional method. This small difference has no serious clinical significance in the diagnosis of jaundice. The mean value of the differences indicates a

small bias of approximately -0.06 mg/dL. The 95% confidence interval (CI) for the bias represented in Figure 4.4b is -0.12 to 0.00. As the CI includes 0.00, the bias is statistically

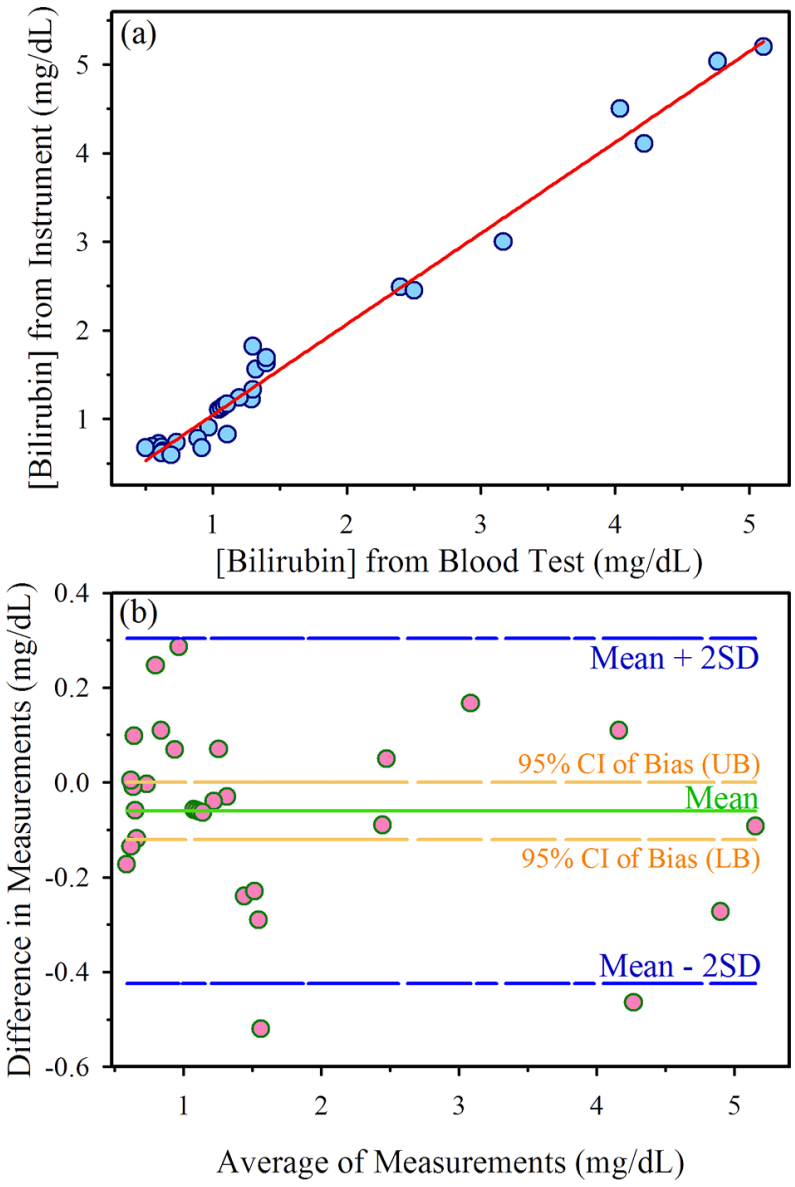

Figure 4.4. *Statistical significance: (a) The linear regression plot of the total serum bilirubin (TSB) level measured in both the ways. (b) Bland-Altman analysis: Difference against mean for the TSB data (see text).*

insignificant [27]. The negative bias along with CI indicates that the predominant tendency of our instrument is to overestimate the bilirubin levels, so dangerous clinical errors are unlikely to occur. In addition, the coefficient of variation (CV) between our method and conventional biochemical method found to be 1.81% which is comparable to the CV range of 0.35-1.96 %

for laboratory chemical analyzers in repeatability studies [28]. This clearly states the bias to be non-significant in clinical diagnosis.

In order to establish the potential of the device in terms of reproducibility, 20 patients were repetitively examined by our device. We found excellent precision between the bilirubin

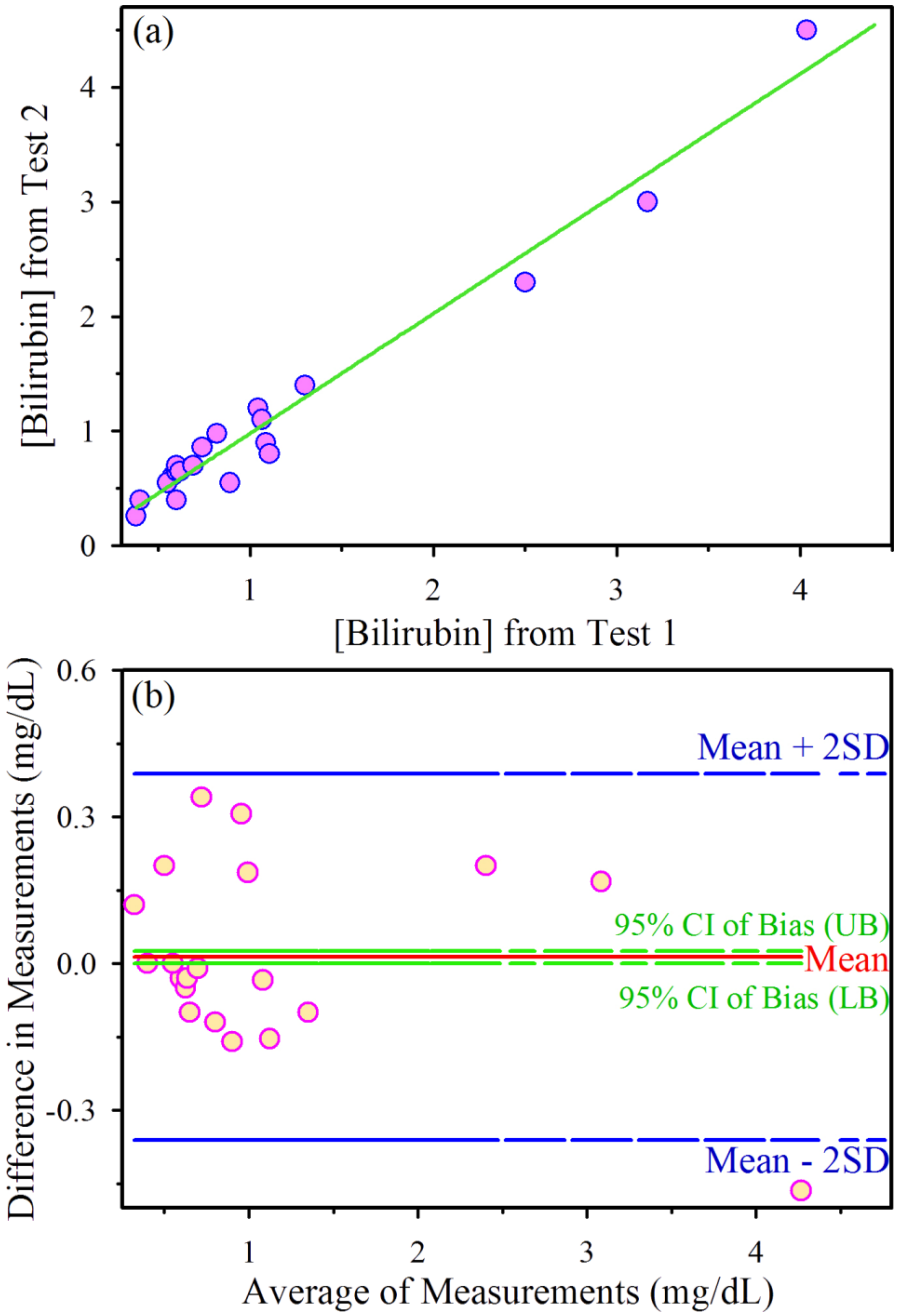

Figure 4.5. *Reproducibility: (a) The linear regression plot of the total serum bilirubin (TSB) level measured successively by two different observers (b) Bland-Altman analysis: Reproducibility in measuring the TSB level by the device (see text).*

levels detected from the same subject by two independent observers. Mean and SD were almost the same in both observations and the intra-class correlation values were highly significant (r=0.98; P<0.0001). Linear regression analysis also illustrates the accuracy of the two measurements (F=557.8; slope 1.04; y intercept -0.06) (Figure 4.5a). Furthermore, the Bland-Altman plot of the two successive measurements by two different observers is represented in Figure 4.5b (mean 0.01 mg/dL and SD 0.18). The bias should be zero for an ideal instrument [25]. However, in our case the bias is 0.01 mg/dL and CV in between repetitive measurements is 0.79%, which have insignificant contributions in clinical diagnosis.

4.3. Conclusion

In conclusion, we have demonstrated that the conjunctiva could be a targeted organ to diagnose jaundice independent of race, age and sex by using a simple diffused reflection measurement technique. Based on the aforementioned principle, we have also developed a non-invasive, easy, expeditious, reliable and practical device for routine measurement of bilirubin level. Although serum bilirubin measurements are still required for precise diagnosis, the proposed device has the potential to reduce frequent blood sampling. The setup would be particularly useful for the initial screening of the patients for the blood test and routine examination of the prognosis of some therapeutic strategies including phototherapy in neonates. It has to be noted that evaluation of the instrument with a much larger data set with a wide range of serum bilirubin concentration, various degrees of medical severity, and a variety of age groups including neonates are our immediate future plan. We have also realized that there is an enormous scope for the development of the setup including the use of two-color LED (460 nm and 600 nm) instead of spectrograph in a very low-cost version. Different calibration equation for different age group of subjects would also increase the sensitivity in measurement. In the future, our study is expected to find relevance in quick, non contact diagnosis of jaundice in rural areas as well as in urban clinics.

References

1. Click, R., J. Dahl-Smith, L. Fowler, J. DuBose, M. Deneau-Saxton, and J. Herbert, An osteopathic approach to reduction of readmissions for neonatal jaundice*, Osteopath. Fam. Physician.* 5 (2013) 17-23.
2. Lister, T., P.A. Wright, and P.H. Chappell, Optical properties of human skin*, J. Biomed. Opt.* 17 (2012) 0909011-09090115.
3. Parkin, D.M., P. Srivatanakul, M. Khlat, D. Chenvidhya, P. Chotiwan, S. Insiripong, K.A. L'Abbé, and C.P. Wild, Liver cancer in Thailand. I. A case-control study of cholangiocarcinoma*, Int. J. Cancer.* 48 (1991) 323-328.
4. Kirk, J.M., Neonatal jaundice: a critical review of the role and practice of bilirubin analysis*, Ann. Clin. Biochem.* 45 (2008) 452-462.
5. Bosschaart, N., J.H. Kok, A.M. Newsum, D.M. Ouweneel, R. Mentink, T.G. van Leeuwen, and M.C. Aalders, Limitations and opportunities of transcutaneous bilirubin measurements*, Pediatrics* 129 (2012) 689-694.
6. Dai, J., D.M. Parry, and J. Krahn, Transcutaneous bilirubinometry: its role in the assessment of neonatal jaundice*, Clin. Biochem.* 30 (1997) 1-9.
7. Lilien, L.D., V.J. Harris, R.S. Ramamurthy, and R.S. Pildes, Neonatal osteomyelitis of the calcaneus: complication of heel puncture*, J. Pediatr.* 88 (1976) 478-480.
8. Yamanouchi, I., Y. Yamauchi, and I. Igarashi, Transcutaneous bilirubinometry: preliminary studies of noninvasive transcutaneous bilirubin meter in the Okayama National Hospital*, Pediatrics* 65 (1980) 195-202.
9. Nash, K. and I.N. Guha, *Hepatology: Clinical cases uncovered*. Vol. 27. 2011: John Wiley & Sons.
10. Issac, B. and N. Israr, *Case studies in intelligent computing: Achievements and trends*. 2014: CRC Press.
11. Castro-Ramos, J., C. Toxqui-Quitl, F. Villa Manriquez, E. Orozco-Guillen, A. Padilla-Vivanco, and J.J. Sánchez-Escobar. *Detecting jaundice by using digital image processing*. in *Proc. SPIE*. 2014. SPIE.
12. Mahtab, M.-A., *Liver: A complete book on hepato-pancreato-biliary diseases*. 2012: Elsevier Health Sciences.

13. Shapiro, S.M. *Chronic bilirubin encephalopathy: diagnosis and outcome*. in *Semin. Fetal. Neonatal. Med.* 2010. Elsevier.
14. Lakovic, K., J. Ai, J. D'Abbondanza, A. Tariq, M. Sabri, A.K. Alarfaj, P. Vasdev, and R.L. Macdonald, Bilirubin and its oxidation products damage brain white matter*, J. Cereb. Blood. Flow. Metab.* 34 (2014) 1837-1847.
15. Schramm, C., J. Herkel, U. Beuers, S. Kanzler, P.R. Galle, and A.W. Lohse, Pregnancy in autoimmune hepatitis: outcome and risk factors*, Am. J. Gastroenterol.* 101 (2006) 556-560.
16. Ditzel, J. and R.W.S. Clair, Clinical method of photographing the smaller blood vessels and the circulating blood in the bulbar conjunctiva of human subjects*, Circulation* 10 (1954) 277-281.
17. Polley, N., S. Saha, S. Singh, A. Adhikari, S. Das, B.R. Choudhury, and S.K. Pal, Development and optimization of a noncontact optical device for online monitoring of jaundice in human subjects*, J. Biomed. Opt.* 20 (2015) 067001.
18. Polley, N., S. Singh, A. Giri, and S.K. Pal, Evanescent field: A potential light-tool for theranostics application*, Rev. Sci. Instrum.* 85 (2014) 033108.
19. Bosschaart, N., R. Mentink, J.H. Kok, T.G. Van Leeuwen, and M.C. Aalders, Optical properties of neonatal skin measured in vivo as a function of age and skin pigmentation*, J. Biomed. Opt.* 16 (2011) 097003.
20. Doi, M. and S. Tominaga. *Spectral estimation of human skin color using the Kubelka-Munk theory*. in *Electronic Imaging*. 2003. SPIE.
21. Tenhunen, R., H.S. Marver, and R. Schmid, The enzymatic conversion of heme to bilirubin by microsomal heme oxygenase*, Proc. Natl. Acad. Sci. U. S. A.* 61 (1968) 748-755.
22. Bland, J.M. and D.G. Altman, Statistics notes: Correlation, regression, and repeated data*, BMJ* 308 (1994) 896.
23. Bland, J.M. and D.G. Altman, Statistics notes: Calculating correlation coefficients with repeated observations: Part 1—correlation within subjects*, BMJ* 310 (1995) 446.
24. Bland, J.M. and D.G. Altman, Calculating correlation coefficients with repeated observations: Part 2—correlation between subjects*, BMJ* 310 (1995) 633.
25. Bland, J.M. and D. Altman, Statistical methods for assessing agreement between two methods of clinical measurement*, Lancet* 327 (1986) 307-310.

26. Bland, J.M. and D.G. Altman, Applying the right statistics: analyses of measurement studies*, Ultrasound. Obstet. Gynecol.* 22 (2003) 85-93.

27. Gardner, M.J. and D.G. Altman, Confidence intervals rather than P values: estimation rather than hypothesis testing*, BMJ* 292 (1986) 746-750.

28. Borgard, J.-P., A. Szymanowicz, I. Pellae, V. Szmidt-Adjidé, and M. Rota, Determination of total bilirubin in whole blood from neonates: results from a French multicenter study*, Clin. Chem. Lab. Med.* 44 (2006) 1103-1110.

Chapter 5

Development of Nanoparticle-based Therapeutic Strategy for Hyperbilirubinemia Control

5.1. Introduction

The term hyperbilirubinemia is defined as increased bilirubin (BR) level (>1.3 mg/dL in human) in blood. Hyperbilirubinemia is caused when there is an imbalance between production of BR (resulting from hemolysis, sepsis, blood extravasation or polycythemia) and decrease in BR excretion due to inadequate hepatic conjugation and increased enterohepatic reabsorption (resulting from pyloric stenosis, delayed bacterial gut colonization, gastrointestinal tract immobility or obstruction) [1-3]. Although at micromoler concentrations BR acts as an antioxidant for scavenging peroxyl radicals in blood [4], yet it can be toxic and harmful to cells at higher concentration [5, 6]. Elevated level of BR and its oxidative products in human blood causes various diseases including neonatal jaundice (>10 mg/dL), Gilbert Syndrome (with bilirubin level reaching > 6 mg/dL), Crigler-Najjar type I disease (> 30 mg/dL) [7] and BR-induced neurologic dysfunction (BIND) [8]. Severe neurotoxicity in case of neonates (Kernicterus) and damage in white matter of adult brain are also the consequences of higher bilirubin level [9]. In case of Hepatitis E infection in pregnant women, associated hyperbilirubinemia itself is found to increase the risk of pre-term delivery [10]. Treatment options for hyperbilirubinemia include phototherapy [11], haemoperfusion, haemodialysis and exchange blood transfusion [12]. Although phototherapy is widely used and one of the best choice for the treatment of hyperbilirubinemia in neonates, its efficacy is noted to diminish as children with Crigler-Najjar syndrome advance in age and in particular during adolescence [11, 13, 14]. Hemoperfusion and exchange blood transfusion have significant morbidity and even mortality [1]. Apart from the mentioned therapeutic procedures various organic, inorganic and phytochemicals have been used for reduction of elevated BR level in blood [15-18]. All these therapeutic drugs function in hepatoprotective way and lack the ability to degrade BR directly [2]. So, none of those became very fruitful in effective and quick reduction of serum BR level.

In the above context a safe, symptomatic and effective therapeutic strategy is extremely needed, and is the principal motive of the present work.

Manganese (Mn), one of the safest materials is a natural constituent, and often a cofactor for enzymes and receptors [19]. Herein, we describe a convenient nanochemistry based approach for highly efficient catalytic decomposition of bilirubin by citrate functionalized Mn_3O_4 NPs (citrate-Mn_3O_4 NPs), in absence of any photo-activation. It is revealed that the mixed valence state of Mn (+2, +3 and +4) along with the functional groups on the surface coordinating ligands of Mn_3O_4 NPs lead to the exceptional catalytic activity. The *in vitro* studies of citrate-Mn_3O_4 NPs on the whole blood specimens of hyperbilirubimia patients as well as the in vivo study in mice model show that, the NPs can selectively reduce the bilirubin level (both conjugated and unconjugated) in the blood specimens very fast and without any significant alteration of other essential blood parameters. Given the remarkable efficiency of the NPs towards the suppression of the blood bilirubin level combined with their colloidal stability and biocompatibility indicates the promise of this NPs in direct therapeutic applications against hyperbilirubinemia.

In the present study we have synthesized citrate capped Mn_3O_4 NPs by ligand etching technique as described in earlier studies [20]. The structural characterization and the interaction of the NPs with a model blood protein have been performed using high resolution transmission electron microscopy (HRTEM), steady state and time resolved optical spectroscopy. Ultrahigh efficacy of generation of reactive oxygen species (ROS) and surface mediated catalysis of the synthesized NPs, have also been established. We have also performed systematic *in vitro* and *in vivo* preclinical studies on the toxicity of the functionalized NPs. All the measurements confirm that the Mn-based nanomedicine is safe and biocompatible due to lack of any potential toxicity. In order to assess the effectiveness of the NPs as symptomatic nanomedicine (NPs) in managing hyperbilirubinemia in mice, we have checked the BR concentration and found to become almost normal in 6 hours after intraperitoneal injection of the NPs. Therefore, these results demonstrate that the functionalized NPs are strong candidate as effective drug for hyperbilirubinemia treatment, and superior to the commercially available drug, silymarin in terms of efficacy with a satisfactory biocompatibility.

5.2. Result and Discussion

5.2.1. Unprecedented Catalytic Activity of Mn_3O_4 Nanoparticles: Potential Lead of a Sustainable Therapeutic Agent for Hyperbilirubinemia [21]: TEM study has been carried out in order to characterize the water soluble citrate-Mn_3O_4 NPs in details. As shown in

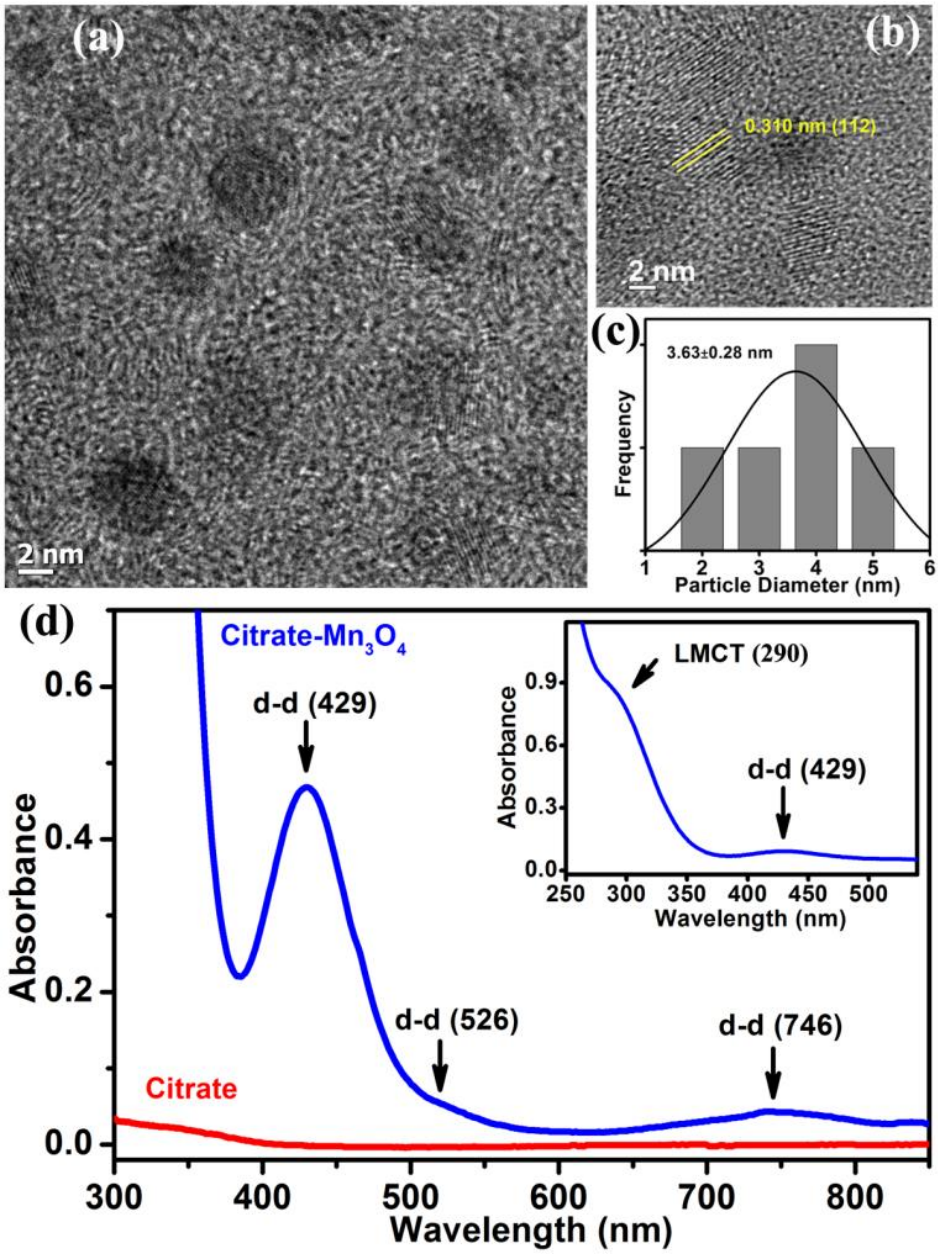

Figure 5.1. *(a) TEM image of citrate-Mn_3O_4 NPs. (b) Lattice fringes in the corresponding HRTEM image indicating high crystalline nature of the NPs. (c) Size distribution of citrate-Mn_3O_4 NPs. (d) UV-Vis absorption spectrum for citrate-Mn_3O_4 NPs and citrate at pH ~7. Inset shows higher energy strong absorption band due to LMCT for very dilute citrate-Mn_3O_4 NPs solution.*

Figure 5.1a, citrate-Mn_3O_4 NPs are nearly spherical in shape with an average diameter of 3.63±0.28 nm (Figure 5.1c). The HRTEM image (Figure 5.1b) confirms the crystalline nature of the citrate-Mn_3O_4 NPs having interplanar distance of 0.310 nm, corresponding to the (112) plane of the crystal lattice. Figure 5.1d illustrates the UV-Vis absorption spectrum of citrate-Mn_3O_4 NPs and citrate, at pH ~ 7. The observed peak at around 290 nm (in the inset) could be assigned to the possible high energy ligand-to-metal charge transfer transition (LMCT) involving citrate-Mn^{4+} interaction. The other bands at 430, 565 and 752 nm are attributed to the Jahn-Teller (J-T) distorted d-d transitions centered over Mn^{3+} ions in citrate-Mn_3O_4 NPs [22, 23].

To determine the catalytic performance of citrate-Mn_3O_4 NPs in BR decomposition at pH=7.4 and without any photo-activation, the characteristic absorbance of BR at 450 nm has been chosen for monitoring the kinetic study using UV-Vis spectroscopy. Figure 5.2a shows the relative concentration (C_t/C_0) of BR plotted against reaction time. As shown in the Figure, in absence of catalyst, only a slight decomposition (less than 3%) of BR can be observed after 50 min, whereas about 92% of BR is decomposed in the presence of citrate-Mn_3O_4 NPs and a concomitant colour change of BR from bright yellow to colourless was observed. Therefore, the observed colour change is attributed to catalytic decomposition of BR and the decomposition curve has been found to follow a first-order exponential equation with kinetic rate constant (k) of 6.62×10^{-2} min^{-1}. Time dependent Raman study of aqueous solution of BR (Figure 5.2b) also reveals significant perturbations of its main characteristic bands for lactam and pyrrole moities lie within 1100-1700 cm^{-1} [24], upon addition of catalyst into the solution. To ensure that the catalyst could be recycled without any significant loss of activity, we have tested the recyclability of the catalyst up to 20 cycles (inset of Figure 5.2a represents data up to 10 cycles and Figure 5.2c)). Through comparing the morphology of the fresh and used citrate-Mn_3O_4 NPs catalyst it is found that there is no obvious change in the morphology before and after the catalytic process, which is in line with its repeated catalytic activity.

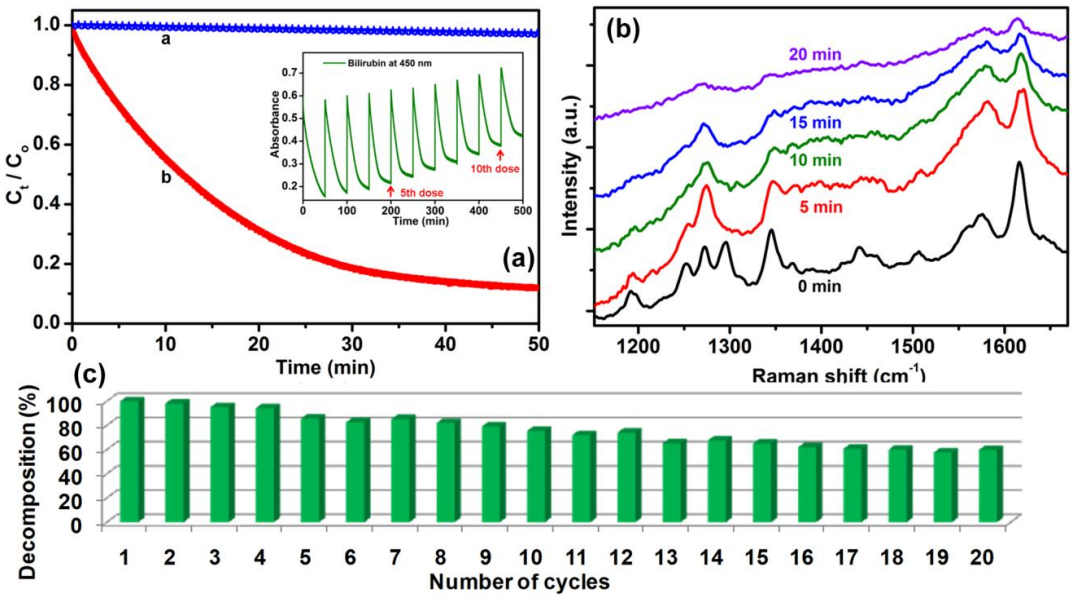

Figure 5.2. *(a) Catalytic decomposition of the aqueous solution of bilirubin in absence of any photo activation. Relative concentration (C_t/C_0) versus time plots for the catalytic decomposition of bilirubin (UV-Vis absorbance of bilirubin monitored at 450 nm) in the absence (a) and presence (b) of citrate-Mn_3O_4 NPs are shown. Inset shows the cycling curves of bilirubin decomposition kinetics upto 10 cycles. (b) Time dependent Raman study of the aqueous solution of bilirubin (0 min spectrum) in presence of citrate-Mn_3O_4 NPs (c) Percentage of catalytic decomposition up to 20 cycles. Where, decomposition of the first cycle has been normalized to 100%.*

To elucidate the nature of the catalytic decomposition products, we have phase transferred the products from aqueous to chloroform medium, in order to avoid possible interference of the catalyst in the characterization process and also considering solubility of previously reported BR degradation products in less polar solvents [25]. Figure 5.3a shows the UV-Vis absorption spectrum of the decomposition products in chloroform and the inset represents photoluminescence spectra (λ_{ex}=350 nm) of the same. UV-Vis absorption bands at 248 and 312 nm along with the ~450 nm photoluminescence peaks are closely resembled with previously reported photo-oxidation product of BR, methylvinylmaleimide (MVM) [25]. The identity of the 278 nm absorption band is not known at this time, which could possibly be due to the formation of other decomposition products. To investigate the mechanistic insight of the catalytic process and the active sites of the nanoparticles involved, we have monitored the changes in the characteristic ligand to metal charge transfer bands (LMCT, which are originated due to the interaction of $Mn^{3+/4+}$ centres in the NPs with the surface bound citrate ligands) of citrate-Mn_3O_4 NPs employing UV-Vis spectroscopy, upon stepwise addition of BR. Figure 5.3b illustrates the UV-Vis absorption spectra of 10 μM aqueous solution of citrate-Mn_3O_4 NPs (catalyst) after complete decomposition (takes 2 hrs) of each dose of BR

into the solution at pH=7.4. The characteristic absorption bands of the catalyst at 242 and 288 nm are attributed to the LMCT bands originated due to Mn^{3+}-citrate and Mn^{4+}-citrate interactions, respectively [23, 26]. The stepwise addition of BR to the aqueous solution of catalyst resulted in a monotonous decrease of absorption at 242 nm and subsequent increase in absorption at 288 and 368 nm, accompanied by the formation of an isosbestic point at 270 nm (Figure 5.3b). The decrease of absorption at 242 nm could be due to the possibility that, upon stepwise addition of BR, more and more Mn^{3+} ions at the NPs surface are converted to Mn^{4+} state and the growing amount of Mn^{4+}-citrate charge transfer states has been witnessed by the increase in absorption at 288 and 368 nm [23]. The appearance of an isosbestic point at 270 nm is evidence for two absorbing systems namely the Mn^{3+}-citrate LMCT band at 242 nm and Mn^{4+}-citrate LMCT bands at 288 and 368 nm.

The definite proof of the involvement of Mn^{3+} and its conversion into Mn^{4+} state during the catalytic process was obtained from pH dependent study. We have evaluated the catalytic efficiency of citrate-Mn_3O_4 NPs at pH-7 and pH-10. As shown in Figure 5.4, at pH-10, catalytic efficiency of the NPs reduced very significantly. This phenomenon is consistent with the fact that, in acidic/neutral pH, Mn^{3+} ions are unstable and tend to disproportionate into Mn^{2+} and Mn^{4+}, whereas it is stabilized by the comproportionation of Mn^{2+} and Mn^{4+} in alkaline conditions [27]. Thus, due to its stability, Mn^{3+} in the NPs surface dose not tends to

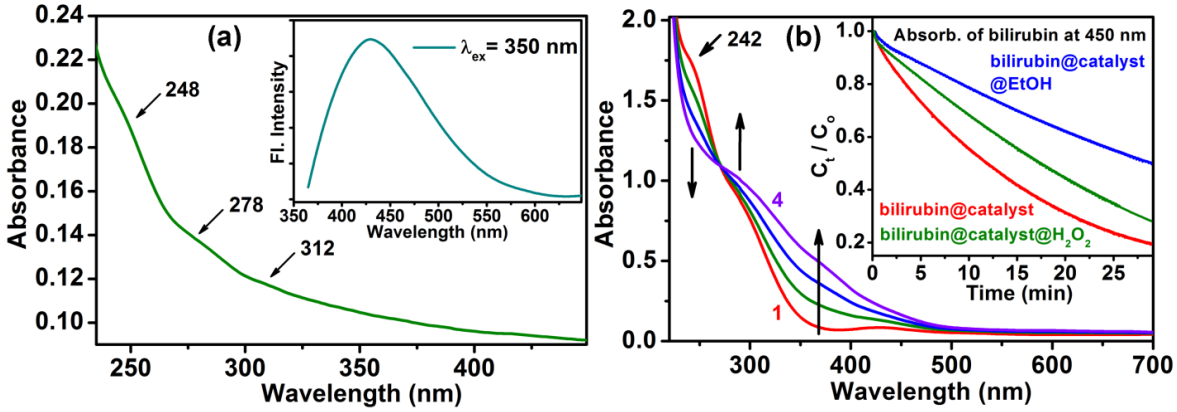

Figure 5.3. *(a) Shows the UV-Vis absorption spectrum of bilirubin decomposition products in chloroform. Inset represents the photoluminescence spectra (λ_{ex}=350 nm) of the products at room temperature. (b) Illustrates the UV-Vis absorption spectra of 10 μM aqueous solution of citrate-Mn_3O_4 NPs after complete decomposition (takes 2 hrs) of each dose of bilirubin into the solution at pH=7.4. Inset shows the plots of relative concentration (C_t/C_0) versus time for bilirubin decomposition (monitored at 450 nm) in presence of citrate-Mn_3O_4 NPs, citrate-Mn_3O_4@H_2O_2 and citrate-Mn_3O_4@EtOH.*

react with BR at higher pH. Given the valence state conversion of Mn from +3 to +4 states upon increasing dose of BR, we anticipated that the catalytic outcome would be the reductive decomposition products of BR.

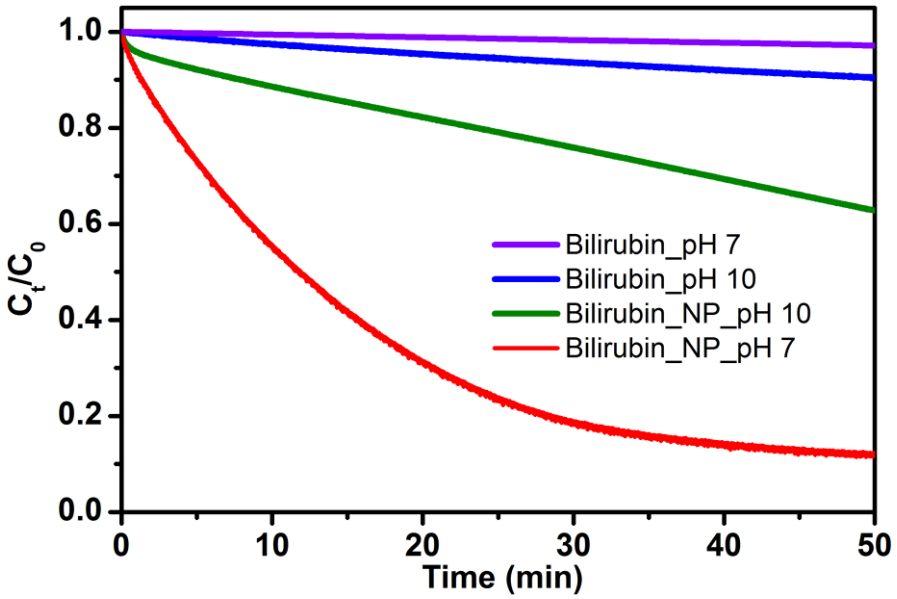

Figure 5.4. *pH dependent catalytic decomposition of the aqueous solution of bilirubin in presence of citrate-Mn_3O_4 NPs. Relative concentration (C_t/C_0) versus time plots for the catalytic decomposition of bilirubin (UV-Vis absorbance of bilirubin monitored at 450 nm) in the presence of citrate-Mn_3O_4 NPs are shown.*

However, as discussed earlier we have found that, spectroscopic signature of the resulting compound closely resemble with the oxidative decomposition product (MVM) of BR. Thus the catalytic process followed a different pathway other than a direct redox reaction involving $Mn^{3+/4+}$ metal ions at the NPs surface and BR molecules. To investigate whether the catalytic process is associated with any radical pathways, we have performed the BR decomposition study in presence of a radical initiator (H_2O_2, a source of $^{\bullet}OH$ radical) and a radical scavenger (ethanol) separately. As shown in the inset of Figure 5.3b, in both cases, a slower catalytic rates have been observed, which validates the role of $^{\bullet}OH$ radicals in the catalytic process. Although, slower rate in case of H_2O_2 seems unexpected, however, this result can be explained by the fact that, H_2O_2 itself can influence the conversion of Mn^{+3} to Mn^{+4} states to a great extent and consequently diminish the number of active catalytic sites on the NPs surface. Therefore, we hypothesized that, the origin of such unprecedented catalytic activity might be initiated by the conversion of Mn^{3+} to Mn^{+4} states at the NPs surface and subsequent formation of reactive oxygen species [28] (such as $^{\bullet}OH$ radicals), that ultimately leads to the decomposition of the analyte, BR.

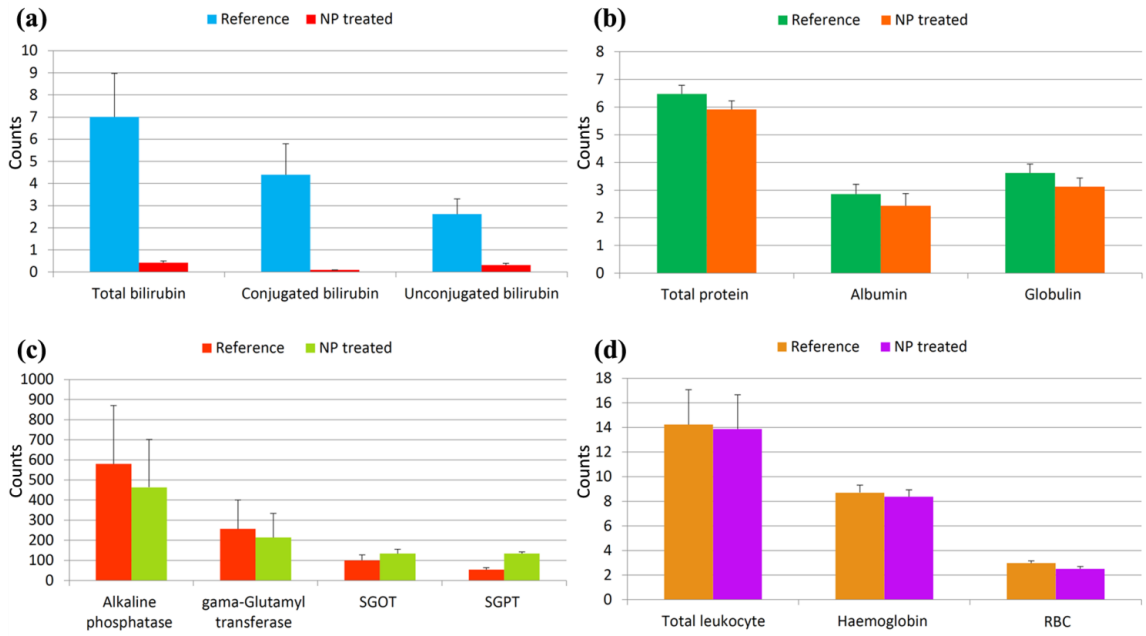

Figure 5.5. *Assay results of different parameters in the blood specimens, with and without treatment (reference) with citrate-Mn_3O_4 NPs. Data are plotted as mean + standard error of the mean (SEM) [n=12].*

Having developed the highly active citrate-Mn_3O_4 NPs for BR decomposition, we sought to test their *in vitro* effectiveness by adding the catalyst to human peripheral blood specimens collected from hyperbilirubinemia patients. Our primary objective was to evaluate the BR levels of the blood specimens with and without treatment by citrate-Mn_3O_4 NPs. Figure 5.5 represents the assay results, performed over blood specimens of hyperbilirubinemia patients. As shown in Figure 5.5a, average BR level (total, conjugated and unconjugated) in the blood specimens of 12 patients, treated with citrate-Mn_3O_4 NPs, reduced down remarkably with respect to the reference (Table 5.1). It has also been observed that conjugated portion of the total BR decreases more than its unconjugated counterpart, this is expected, as the water soluble glucuronic acid conjugated portion get higher chance to interact with NPs than the albumin bound unconjugated part. In the same blood specimens where we have evaluated BR level, simultaneously, we have also checked the effects of citrate-Mn_3O_4 NPs on other liver function parameters such as total protein, albumin, globulin, alkaline phosphatase, γ-glutamyl transferase, SGOT and SGPT. As shown in Figure 5.5b and 5.5c, the change in the parameters upon interaction with citrate-Mn_3O_4 NPs is statistically insignificant (Table 5.2, *P* value > 0.05), except in case of SGPT. Exact reason for the increase of SGPT upon interaction with the NPs is not known in the present time and needs further investigation. In case of different haematological parameters such as haemoglobin, red blood cell (RBC) count

and total leukocyte count (Figure 5.5d and Table 5.3), it has been found that there is also insignificant variation (*P* value > 0.05) upon treatment of the blood specimens with citrate-Mn_3O_4 NPs. Nominal variation in the count of RBC and total leukocyte cells in the NPs treated specimens, directly indicates the blood biocompatibility of citrate-Mn_3O_4 NPs.

Table 5.1. *In vitro effect of citrate-Mn_3O_4 NPs on the bilirubin level of blood specimen. Data are expressed as mean ± standard deviation [n=12]. P values indicating statistical significance, were determined by Student's unpaired t-test. P values less than 0.05 considered statistically significant.*

Parameters (mg/dL)	Reference specimen	NP treated specimen	*P* Value
Total bilirubin	7.01±6.80	0.42±0.29	<0.0001
Conjugated bilirubin	4.40±4.81	0.10±0	<0.0001
Unconjugated bilirubin	2.62±2.36	0.32±0.29	0.0001

Table 5.2. *In vitro effect of citrate-Mn_3O_4 NPs on other liver function parameters of blood specimen. Data are expressed as mean ± standard deviation [n=12]. P values were determined by Mann–Whitney test.*

Parameters	Reference specimen	NP treated specimen	*P* Value
Total protein (gm/dL)	6.47±0.90	5.91±0.87	0.22
Albumin (gm/dL)	2.85±1.02	2.43±1.27	0.48
Globulin (gm/dL)	3.62±0.91	3.12±0.89	0.28
SGOT (AST) (U/L)	100.25±76.06	134.12±60.85	0.27
SGPT (ALT) (U/L)	53.75±28.70	133.25±27.62	0.0003
Alkaline phosphatase (U/L)	579.37±823.58	463.37±672.70	0.57
γ-Glutamyl transferase (U/L)	256.62±407.92	213.50±340.16	0.50

Table 5.3. *In vitro effect of citrate-Mn_3O_4 NPs on haemoglobin and different blood cells. Data are expressed as mean ± standard deviation [n=12]. P values were determined by Student's unpaired t-test.*

Parameters	Reference specimen	NP treated specimen	*P* Value
Haemoglobin (gm/dL)	8.70±1.93	8.36±1.85	0.70
RBC count (x10^6/μL)	2.97±0.64	2.50±0.67	0.13
Total leukocyte count (x 10^9/L)	14.23±9.01	13.86±8.83	0.92

Moreover, we have also evaluated the effectiveness of citrate-Mn_3O_4 NPs against the conventional blue light used in phototherapy, towards BR decomposition. As shown in Figure 5.6, citrate-Mn_3O_4 NPs exhibit comparable efficiency against blue light along with an added advantage of dark reactivity.

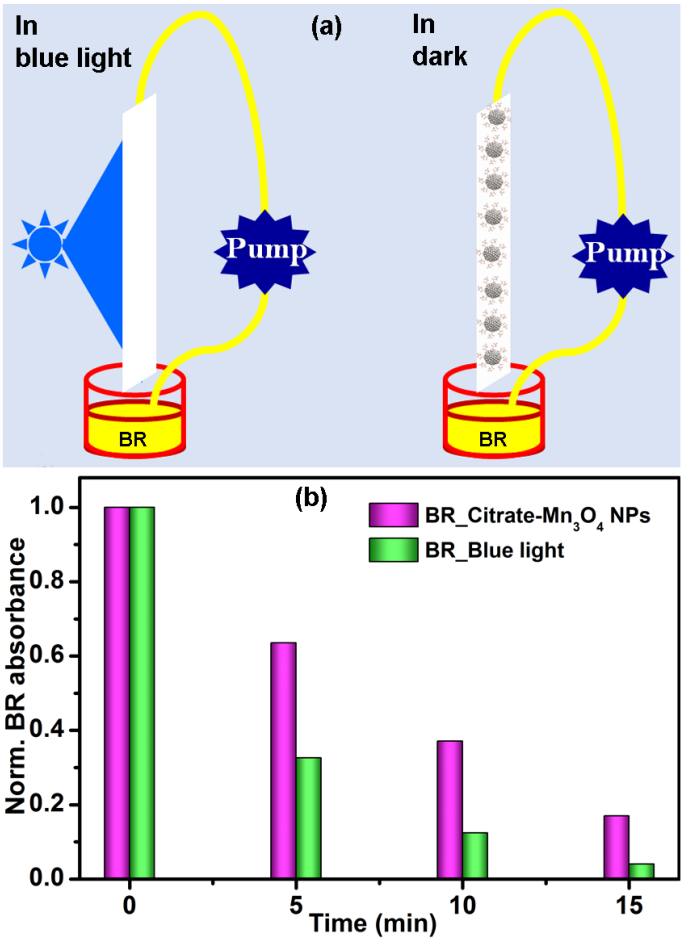

Figure 5.6. *(a) Schematic view of bilirubin decomposition study in presence of blue light (wavelength 460 nm) and citrate-Mn_3O_4 NPs, separately. We have used a strip of chromatography paper to maintain bilirubin flow in both cases. (b) Plots of time dependent UV-Vis absorbance of* BR *in presence of blue light and citrate-Mn_3O_4 NPs (in dark). Proposed potential future use of nanotherapy as an alternative to phototherapy is justified (see text).*

5.2.2. Safe & Symptomatic Medicinal Use of Surface Functionalized Mn_3O_4 Nanoparticles for Hyperbilirubinemia Treatment in Mice [29]: The spherical Mn_3O_4 NPs were imaged by transmission electron microscopy (Figure 5.7a) and statistical evaluation found a size distribution of about 3.69±0.12 nm (Figure 5.7b). Figure 5.7c is the HRTEM image of an isolated Mn_3O_4 NPs. The observed inter-fringe distance of 0.314 nm is consistent

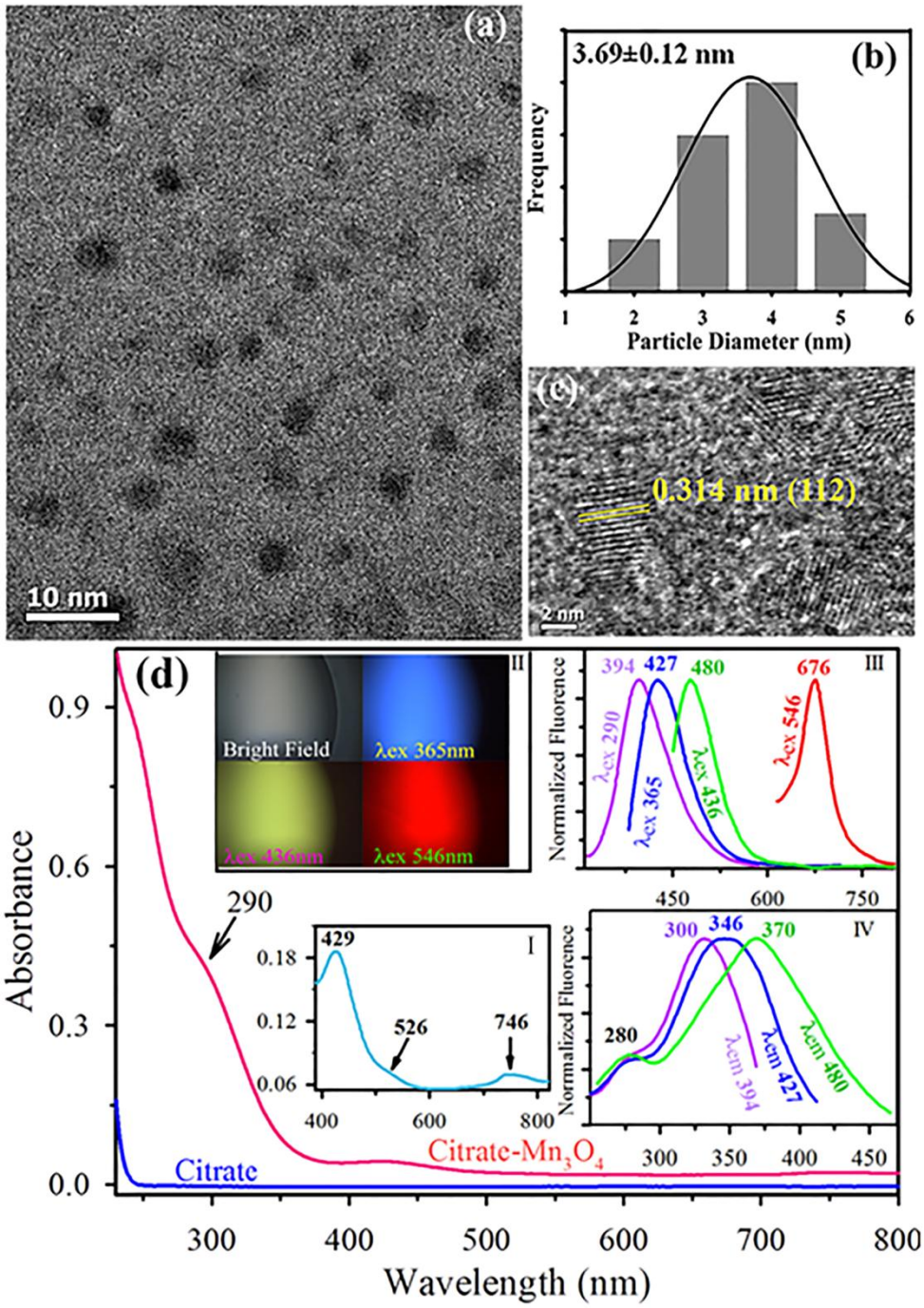

Figure 5.7. *(a) The particle distribution of the NPs recorded under TEM; (b) The particle size distribution is shown with average size of 3.69 ± 0.12 nm and (c) High resolution electron micrograph (HRTEM) of the NPs with a clear inter-planer distance of 0.314 nm for 112 planes in the Mn_3O_4 NPs is evident. (d) The absorption spectra of citrate capped NPs used as nano-medicine in the present study and the capping agent citrate are shown in panel. A magnified version of the absorption spectrum of the NPs in the rage of 400 to 800 nm is shown in the inset. Different absorption peaks due to d-d transitions (see text) are evident. Fluorescence microscopic view of the liquid solution of the NPs with different excitation is shown in the inset (II). The corresponding emission and excitation spectra of the solution are shown in the insets (III) and (IV) respectively.*

with Mn_3O_4 inter-planar distance of 112 plane revealing crystalline nature of the nanoparticle [21]. The absorbance spectra of the NPs and the capping ligand citrate are represented in Figure 5.7d. A magnified view of the absorption spectrum of the NPs in the range of 400-800 nm is shown in the inset 5.7d-I. The absorbance maxima at around 290 nm and 429 nm, 526 nm, 746 nm correspond to the high energy ligand-to-metal charge transfer transition (LMCT) involving citrate–Mn^{4+}interaction and Jahn–Teller (J–T) distorted d–d transitions centered over Mn^{3+}ions respectively [21]. The NPs are also found to be fluorescent under various excitation wavelengths as reported earlier [22]. A fluorescence microscopic image containing bright field and fluorescence from the NPs solution under UV (365 nm), blue (436 nm) and green (546 nm) excitation is shown in the inset 5.7d-II. The corresponding emission spectra of the NPs-solution are shown in Figure 5.7d-III revealing distinct emission peaks for different excitation wavelengths. Different peaks in the excitation spectra (Figure 5.7d-IV) form the solution for different detection wavelengths, confirm the multiple excited state in the emission from the NPs as detailed in earlier literature.

In order to investigate the efficacy of the NPs in bilirubin (BR) degradation *in vitro*, we have monitored BR decomposition at pH=7.4 in presence and absence of the serum protein HSA (Figure 5.8a). We have maintained the concentration of the NPs similar to that used in the *in vivo* experiment (from same stock solution). The characteristic absorbance of BR at 450 nm has been chosen for monitoring the kinetic study using UV-Vis spectroscopy. Figure 5.8a shows the relative concentration (C_t/C_0) of BR plotted against reaction time. In absence of HSA decomposition of BR after 60 minutes by the NPs can be observed to be around 80%, whereas in presence of HSA the decomposition reduced to 40%. In contrast to the catalytic decomposition of BR, only 2-5 % of BR degradation is observed without the NPs. These results are self-explanatory since, the water soluble bilirubin gets either higher chance to interact with NPs than the in the albumin protein or more accessible to the NPs-generated radical in the aqueous solution [21]. Here, we have found that the NPs are efficient generator of ROS in aqueous solution. Enhanced emission of a ROS indicator DCFH is used for the monitoring of oxidative stress in the solution. The emission maxima of DCFH (520 nm) upon excitation at λ_{ex}= 488 nm was plotted against time to generate the fluorescence kinetic plot (Figure 5.8b) for repetitive addition of DCFH in the solution. The NPs were capable of producing ROS for at least 8 cycles as highlighted in Figure 5.8b-I. The reduction in oxidative

stress generation has also been observed in presence of well known ROS quencher Ethanol (EtOH) [21] in the medium Figure 5.8b-II. Figure 5.8c clearly indicates that the generated ROS was inefficient to degrade the bilirubin with increased level of ethanol concentration.

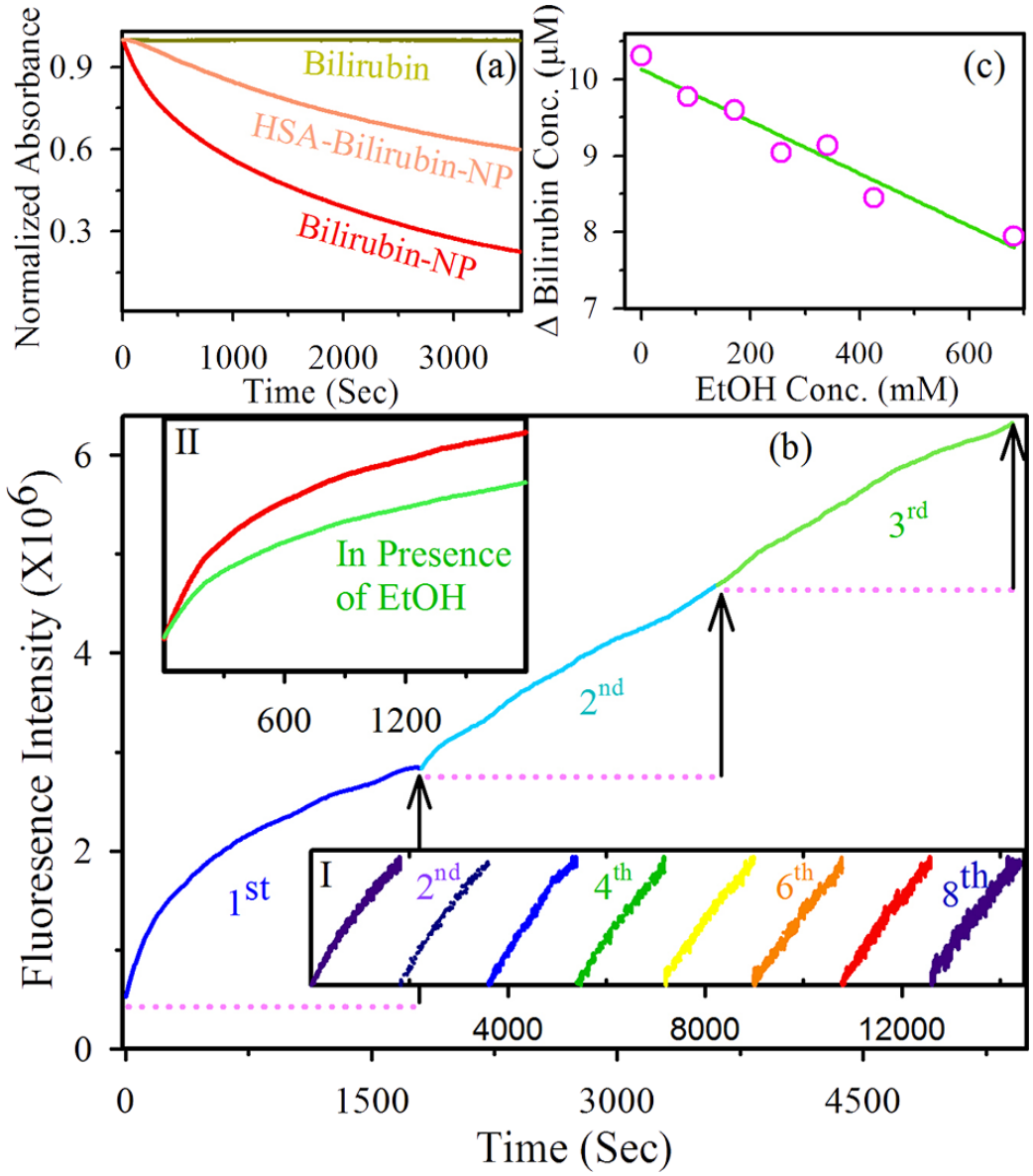

Figure 5.8. *Degradation kinetics of bilirubin in solution (in vitro) in presence of the NPs are shown in panel (a). Effect of encapsulation of bilirubin in HSA protein and the controlled kinetics of bilirubin in absence of NPs in our experimental condition are also shown in the panel. The efficacy of generation of reactive oxygen species (ROS), the key for the degradation of bilirubin for a number of cycles are shown in panel (b). Re-usability of the NPs (inset I) over 8 cycles and reduction of the efficacy in presence of ROS quencher ethanol (inset II) are also shown. A linear dependency concentration of bilirubin degradation in one hour on the concentration of ethanol is shown in panel (c).*

The observed reduction efficacy of the NPs in presence of HSA (Figure 5.8a) could be rationalized in the following two ways. Firstly, the BR may interact directly with the NPs and

undergoes surface mediated catalysis (Langmuir-Henselwood type) and encapsulation of the bilirubin in the presence of HSA hinders the interaction leading to less degradation of BR. Secondly, the NPs could be encapsulated by the protein, HSA for the less interaction with the BR in the aqueous solution. We have ruled out the first possibility by an attempt to study the rate of bilirubin degradation kinetics with the concentration of the NPs in the solution. The rate of the kinetics was found to be independent of the NPs concentration, which should not be the case of surface mediated catalysis. In order to address the second possibility, we have investigated the interaction of the NPs with the protein HSA as shown in Figure 5.9. The far-UV circular dichroism (CD)spectra of HSA, exhibited two negative bands in the UV region at 208 and 220 nm (Figure 5.9a), characteristic of an α-helical structure of protein [30]. The percentage of helix content of HSA both in presence and absence of NPs is found to be similar revealing insignificant conformational alteration in α-helical structure of HSA in presence of the NPs. The molecular mass of the protein HSA in presence of the NPs is also found to be intact as shown in native get electrophoresis study (Figure 5.9b). A direct evidence of the nature of interaction of the NPs with the protein is clear from picosecond resolved fluorescence transient of the single tryptophan Trp-214 (excitation 283 nm) in absence and presence of the NPs as shown in Figure 5.9c (average lifetime of 1.95 ns). In case of proximity of the NPs to Trp-214, a quenching of the fluorescence is unavoidable due to Förster resonance energy transfer (FRET) [31] as a result of strong spectral overlap of the Trp-214 emission with the absorption of the NPs (Figure 5.7d). Insignificant change in the Trp-214 emission transient in presence of the NPs, clearly rules out proximal interaction of the protein with the NPs.

For assessing the maximal-tolerated dose of surface functionalized Mn_3O_4 NPs we performed single dose acute toxicity study as per OECD guideline. Intraperitoneal injection of Mn_3O_4 NPs did not cause any mortality throughout the experimental period for all three dose groups. Behavioral and physical symptoms of acute toxicity such as decreased activity or decreased uptake of food and water were not also been observed during the study period. As no clinical signs of toxicity were observed upto 5000 mg/kg BW, hence 1/10th of the maximum dose administered (i.e., 500 mg/kg BW) was selected for the present study.

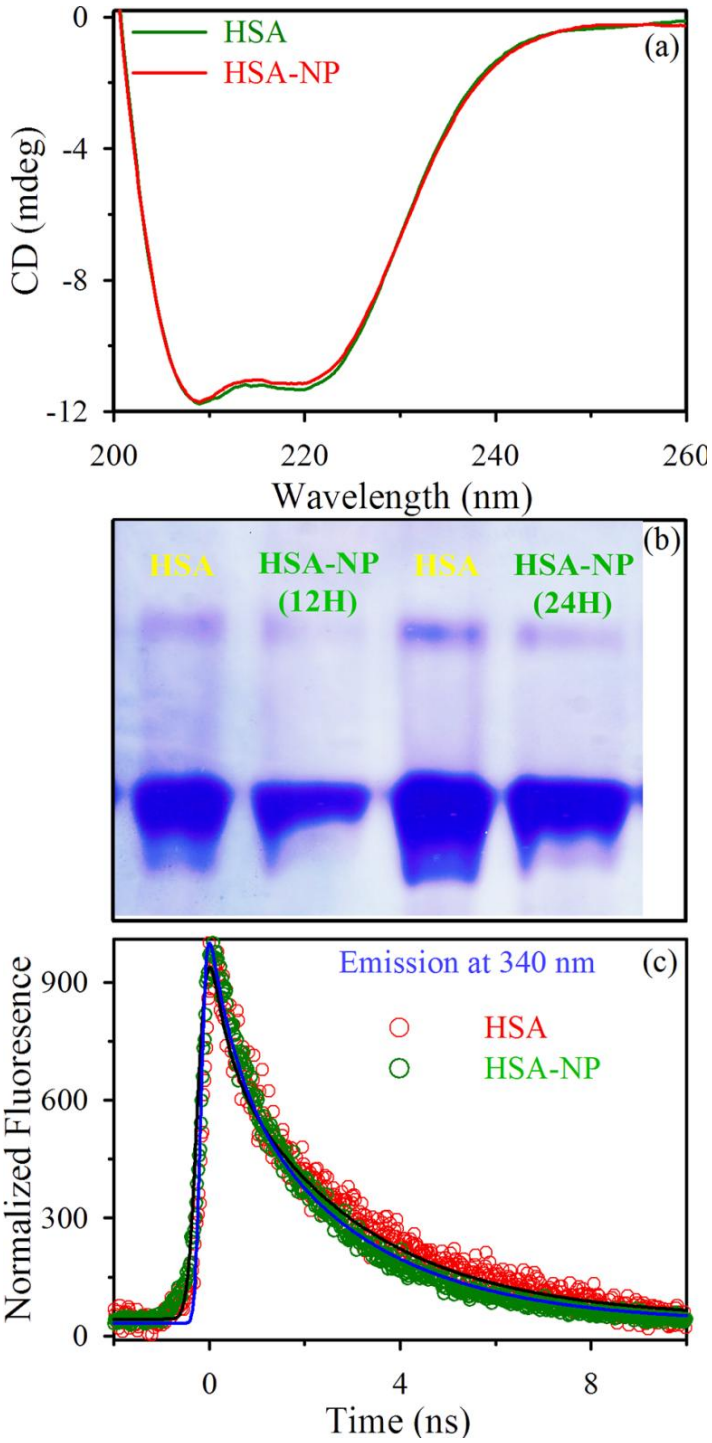

Figure 5.9. *(a) Circular dichroism (CD) spectra of HSA without and with the NPs (see text). An insignificant effect of the NPs in the secondary structure of the serum protein is evident. (b) The overall structural integrity of the protein upon interaction with the NPs with various incubation time is shown from the mobility of the protein in a native gel. (c) Picosecond resolved transient of the single tryptophan (Trp-214) of the serum protein without and with the NPs. In case of direct interaction of the NPs with the protein, quenching (due to FRET) of the transient in presence of the NPs is unavoidable because of the strong spectral overlap of the tryptophan emission and absorption of the NPs. However, insignificant quenching of Trp-214 in presence of NPs rules out the possibility of direct interaction (see text).*

In the phase I study the total serum BR (TSB) level of CCl_4 treated group (Group II) increased to 0.89±0.07 mg/dL which is far higher than the control group (Group I; 0.32±0.04 mg/dL), indicative of hyperbilirubinemia. This group (Group II) was left untreated for a week to see the auto recovery. The serum biochemical tests were done after treatment of seven days and represented in Table 5.4. The results show that treatment with the NPs significantly decreased BR level (total and direct) even lower than the sham control (Figure 5.10a and 5.10b). But for Group II, we have seen very mild decrease in serum BR concentration even after removal of the hepatoxin, indicating slow recovery process. However in case of direct BR level the reduction is not significantly different from the clinical standard silymarin (Table 5.4). The NPs directly interacts with the BR and degrade the same. In the case of direct BR (soluble in aqueous environments and complex with glucuronic acid), hindrance of the interaction with NPs could be possible reason of lower efficacy of the NP in reducing direct BR.

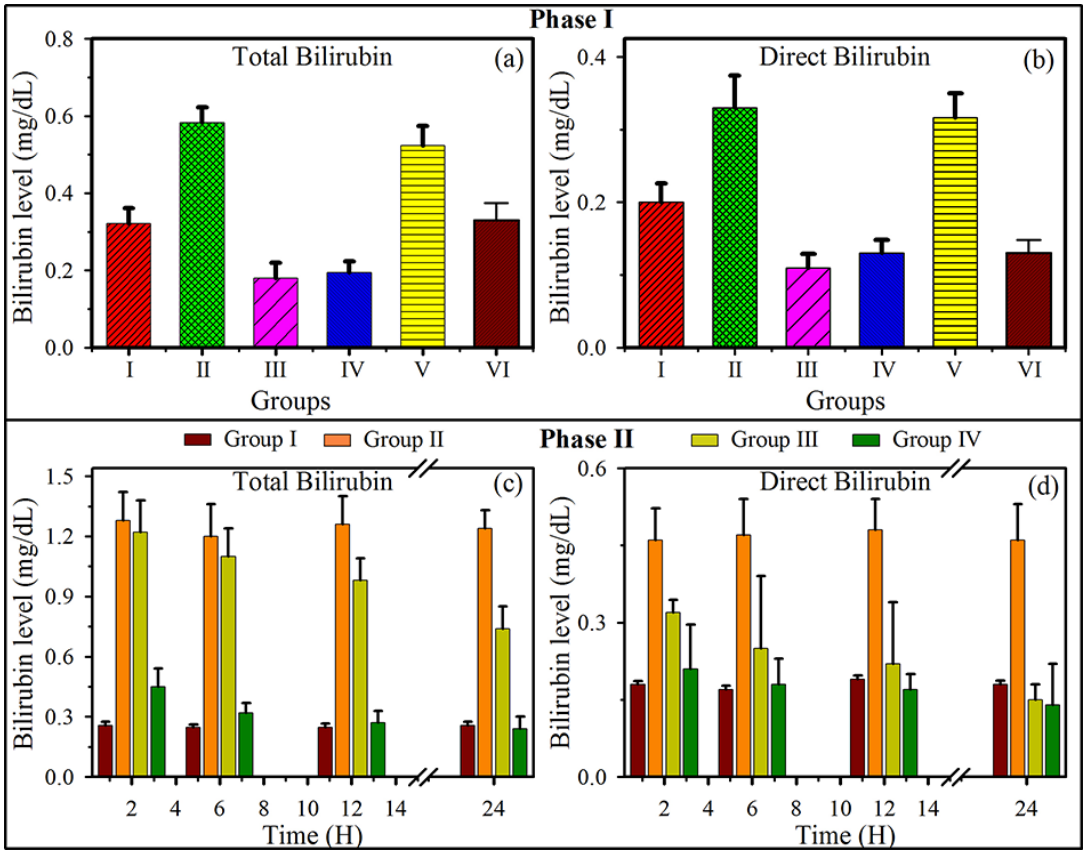

Figure 5.10. *Assay results of total and direct bilirubin concentration in the blood specimens of mice in Phase I (a and b) and Phase II (c and d). In Phase II study single dose of NPs was able to restore normal serum bilirubin level in less than 6 hours from hyperbilirubinemia condition. Data are plotted as mean ± standard error of the mean (SEM).*

For assessing the efficiency of BR degradation *in vivo* by NPs over standard drug silymarin we performed the second phase of experiment. Here, BR concentration was monitored for a period of 24 hrs after intoxication. Three weeks' CCl_4 intoxication increased the total serum BR level upto 1.28±0.14 mg/dL. Single dose of Mn_3O_4 NPs decreases TSB to 0.40±0.07 mg/dL within 2 hrs and back to normal level (0.32±0.05 mg/dL) within 6 hrs compared to the silymarin treated group 1.22±0.16 mg/dL (2 hrs) and 1.10±0.14 mg/dL (6 hrs), respectively. The results are represented in Figure 5.10c & 5.10d. Treatment with NPs decreased TSB level almost 70% compared to that of silymarin (8%) in 2 hrs and restored normal TSB concentration within six hrs. The results suggests the efficiency of citrate functionalized Mn_3O_4 NPs in targeted degradation of BR in a much faster rate compared to that of standard drug silymarin in *in vivo* experimental system.

For assessment of liver injury, serum activity of various hepatic lysosomal enzymes are used as diagnostic indicators [32]. Earlier studies have shown that CCl_4 administration increases serum levels of AST, ALT, ALP and GGT [15-18, 33-36]. Normal liver contains high concentrations of these enzymes. When there is hepatocyte necrosis or membrane damage, these enzymes are released into the circulation, as indicated by elevated serum enzyme levels [37]. The hepatotoxicity of CCl_4 was confirmed in our study by a significant elevation of serum ALT (197.86%), AST (157.63 %), ALP (106.77%) and GGT (105.36%) activities in the CCl_4-treated group as compared to the vehicle control which are summarized in Table 5.5. However, treatment with NPs at a dose of 500 mg/kg BW for seven days decreased the percentages of AST, ALP and GGT by 53.93%, 13.01%, and 10.82%, respectively, compared to the CCl_4-treated group. The liver function parameters for the NPs control group (Group III) remain almost same as the vehicle control group indicating no toxicity of the NPs on liver. Furthermore, no significant change in serum protein concentration indicates the non-toxic effect of NPs which is in agreement with the *in vitro* study involving HAS, described in the earlier section. The statistical analysis of the all liver biochemical-parameters (except BR) is represented in Table 5.5. The hematological status of animals of Group I, Group II Group III and Group IV has been assessed and are given in the Table 5.6. It is evident that there is insignificant change in the hematological parameters across the four groups. The result clearly shows that the presence of NPs does not affect hematological system.

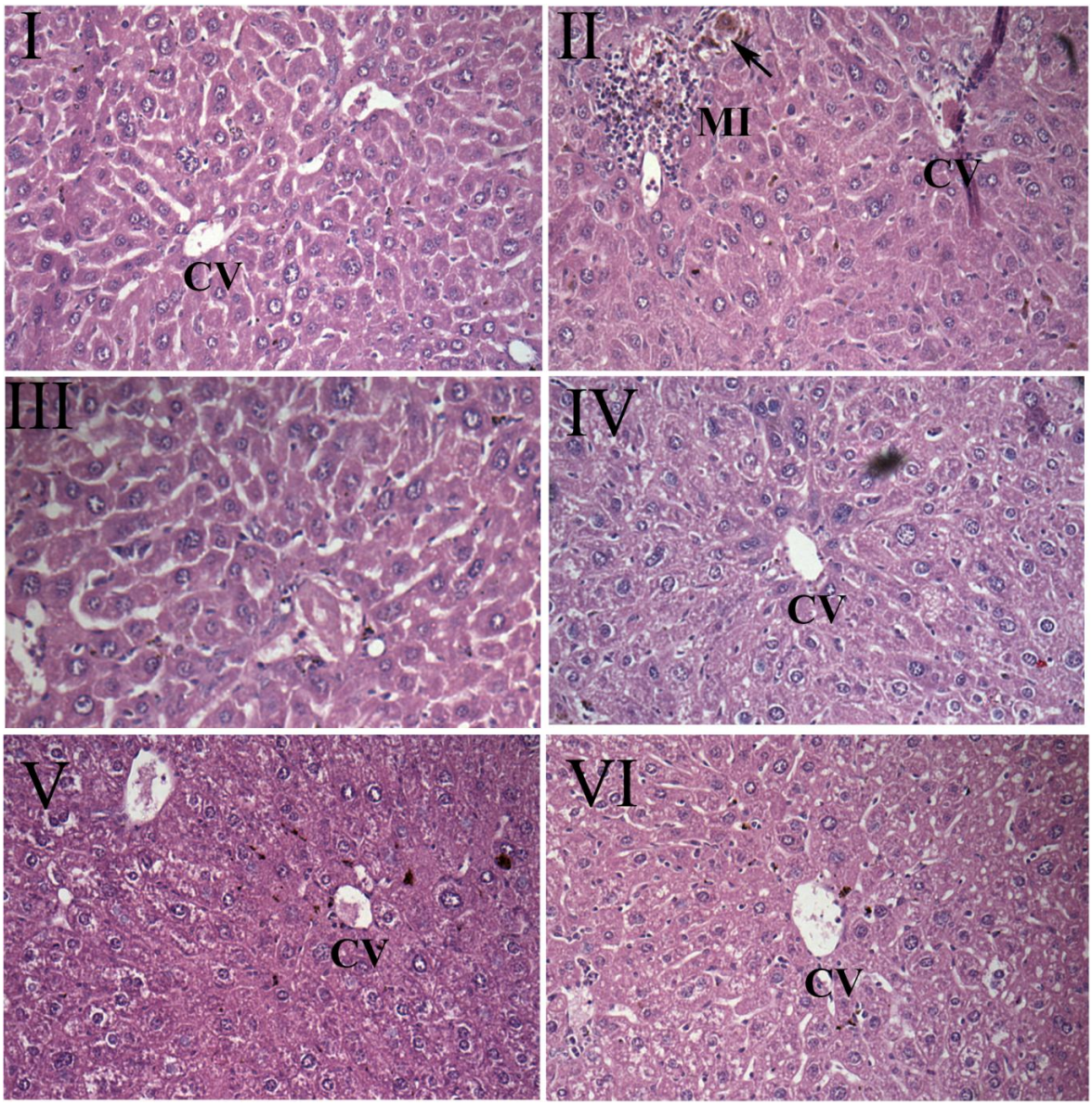

Figure 5.11. *(**CV**- Central Vein, **MI**- Mononuclear cell Infiltration, ↖- Hemorrhage)*
Effect of NPs on hepatic morphological analysis in CCl_4-intoxicated mice. Livers were sectioned and stained with hematoxylin eosin by standard techniques (taken under 100X magnification). (I) Sham control, (II) CCl_4 control, (III) NP control (IV) NP treated (V) Citrate Control (VI) Silymarin.

The histopathological observations also support the results obtained from serum biochemical assays (Figure 5.11).The liver lobules of the vehicle control animals (Group I) showed a classical structure with hepatocyte plates directed from the portal triads towards the central vein, where they freely anastomose. The liver sinusoids are normally irregularly dilated, and spaces of Disse can be seen. The liver sections of this group showed normal hepatic cells i.e., with well-preserved cytoplasm and prominent nucleus, nucleolus (Figure 5.11-I). The

livers of CCl_4-intoxicated mice(Group II, Figure 5.11-II) revealed moderate to severe hepatocellular vacuolization, hepatic necrosis and swelling, bile-duct hyperplasia, and increasing cellular mitosis as well as dilation of Disse spaces with focal disruption of the sinusoidal endothelium, inflammatory infiltrations of the portal triads (Figure 5.11-II), and distortion of the central venules. Mononuclear cell infiltration, hemorrhage, fatty degeneration and formation of regenerative nodules were also observed in CCl_4 treated group indicating that CCl_4-induced severe damage to the hepatic cells. The animals treated with NPs (Group IV) and silymarin (Group VI) (Figure 5.11-IV and Figure 5.11-VI, respectively) revealed slight to mild hepatocellular vacuolation and better preservation of the normal liver architecture, with moderate hepatocyte plate disorganizations and smaller dilations of Disse spaces. These treated animals displayed rare periportal inflammatory infiltrate in the liver lobules. The animals treated with only NPs (Group III) showed normal liver architecture comparable to the vehicle control group. This indicates the non-toxic effect of citrate capped Mn_3O_4 on hepatocytes which are in good correlation with the liver function tests. It has been reported that CCl_4 causes necrosis, [33, 38-41] fibrosis, [38, 42-44] mononuclear cell infiltration, [40, 44] steatosis and foamy degeneration of hepatocytes, increase in mitotic activity [45] and cirrhosis [33, 40] in liver. Therefore, our histopathological findings in the liver due to CCl_4 administration are in agreement with previous studies. However, treatment with NPs significantly decreased these hepatotoxicity characteristics in mouse liver, suggesting that NPs provided protection against CCl_4-induced liver injury. So, according to the microscopic examinations, severe liver damage induced by CCl_4 was remarkably reduced by the administration of the NPs, which was in good correlation with the results of the liver functional parameters of the serum.

Table 5.4. *Effect of NPs on serum Bilirubin level in CCl_4-intoxicated mice.*

Gr.	Design of treatment	Total Bilirubin (mg/dL)		Direct Bilirubin (mg/dL)	
		After induction	After treatment	After induction	After treatment
I	Sham Control	0.33 ± 0.05	0.32 ± 0.04[b]	0.19 ± 0.008	0.20 ± 0.009[b,c]
II	CCl_4 Control	0.89 ± 0.07	0.58 ± 0.04[a,c]	0.39 ± 0.054	0.33 ± 0.044[a,c]
III	NP Control	0.34 ± 0.04	0.18 ± 0.04[a,b,c]	0.21 ± 0.009	0.11 ± 0.019[a,b]
IV	CCl_4 + NPs	0.93 ± 0.06	0.19 ± 0.03[a,b,c]	0.42 ± 0.045	0.13 ± 0.019[a,b]
V	CCl_4 + Citrate	0.88 ± 0.06	0.52 ± 0.05[a,c]	0.38 ± 0.036	0.32 ± 0.034[a,c]
VI	CCl_4 + Silymarin	0.87 ± 0.07	0.33 ± 0.04[b]	0.38 ± 0.038	0.13 ± 0.019[a,b]

NPs: nanoparticle. Data are expressed as mean ± SD (n=8)
One-way ANOVA Tukey post hoc: [a] $p< 0.05$ compared with vehicle control. [b] $p< 0.05$ compared with CCl_4. [c] $p< 0.05$ compared with silymarin.
Dosage:- Olive Oil: 0.5 mL/kg body weight.CCl_4 + Olive Oil Sol.: 1ml/kg body weight. NPs: 500 mg/kg BW. Silymarin: 100 mg/kg body weight. Citrate (1:1 sol. in water): 100 µL/mice.

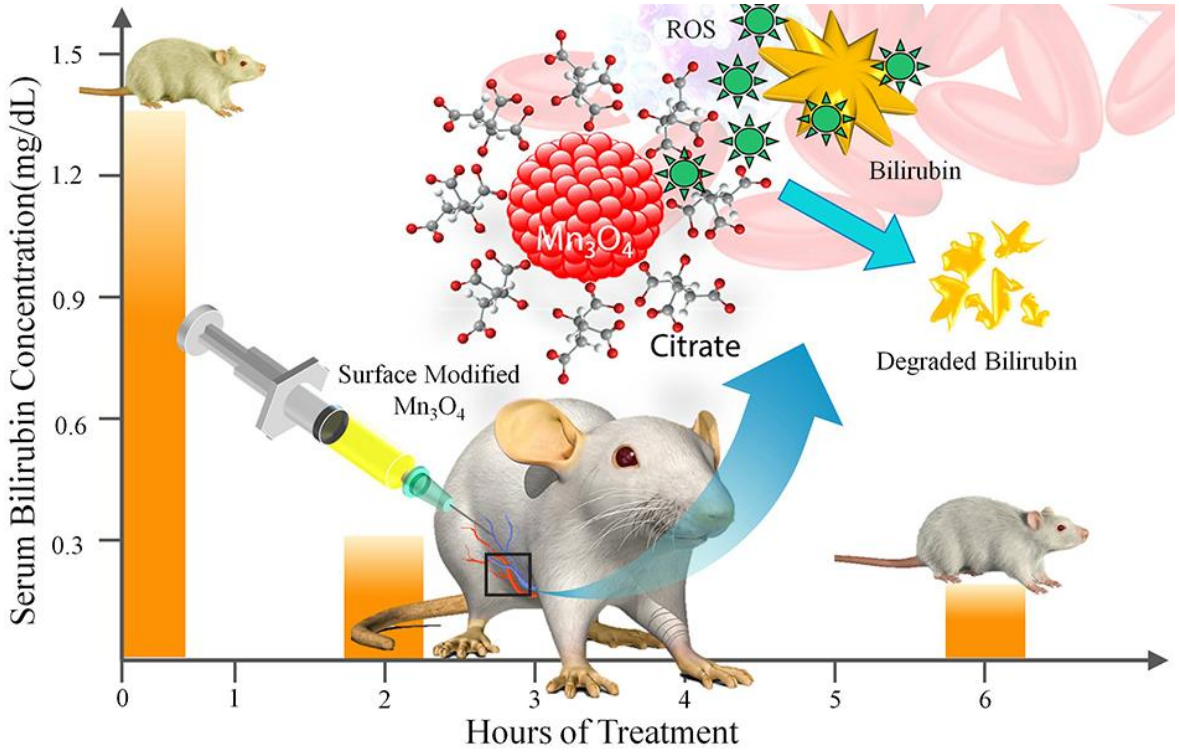

Scheme 5.1. *Schematic representation of the nano-therapy using surface modified Mn_3O_4 nanoparticles (NPs). The efficacy of the NPs in reducing serum bilirubin in mice in hours without any side effect is also represented (see text).*

Table 5.5. *Effect of NPs on ALT, AST, ALP, GGT, and Total Protein in CCl_4 intoxicated mice.*

Gr.	Design of treatment	AST (IU/L)	ALT (IU/L)	ALP (IU/L)	GGT (IU/L)	Total Protein (gm/dL)
I	Sham Control	81.43 ± 7.31[b]	19.67 ± 1.67[b,c]	26.30 ± 2.63[b]	2.61 ± 0.30[b,c]	6.28 ± 0.54
II	CCl_4 Control	209.78 ± 22.77[a,c]	58.58 ± 3.28[a,c]	54.38 ± 5.48[a,c]	5.36 ± 0.66[a]	5.78 ± 0.40
III	NP Control	79.45 ± 8.32[b]	17.95 ± 1.92[b,c]	24.58 ± 3.14[b]	2.60 ± 0.42[b,c]	6.12 ± 0.64
IV	CCl_4 + NPs	96.65 ± 7.72[b]	59.58 ± 3.81[a,c]	47.30 ± 5.88[a,b]	4.78 ± 0.53[a]	5.88 ± 0.44
V	CCl_4 + Citrate	66.98 ± 10.19[b]	42.72 ± 3.28[a,b,c]	40.23 ± 4.41[a,b]	4.78 ± 0.48[a]	5.78 ± 0.44
VI	CCl_4 + Silymarin	86.43 ± 9.44[b]	26.79 ± 2.89[a,b]	45.98 ± 4.69[a,b]	4.61 ± 0.47[a,b]	5.78 ± 0.42

Data are expressed as mean ± SD (n=8)
One-way ANOVA Tukey post hoc:
[a] $p < 0.05$ compared with vehicle control.
[b] $p < 0.05$ compared with CCl_4.
[c] $p < 0.05$ compared with silymarin.
Dosage:- Olive Oil: 0.5 ml/kg body weight.CCl_4 + Olive Oil Sol.: 1 mL/kg body weight. NPs: 200 µL/mice. Silymarin: 100 mg/kg body weight. Citrate (1:1 sol. in water): 100 µL/mice.
ALP: Alkaline phosphatase; ALT: Alanine aminotransferase; AST: Aspartate aminotransferase; GGT: γ-glutamyltranferase; NPs: Nanoparticle.

Table 5.6. *Hematological parameters as studied across the Group I (Sham control), Group II (CCl_4 control), Group III (NP control), Group IV (CCl_4+NP). Data are expressed as mean ± SD (n=8).*

Hematological Parameters	Groups			
	I	**II**	**III**	**IV**
Hb (gm/dL)	13.57 ±1.04	13.95±0.89	13.84±0.92	13.90±0.85
RBC ($x10^6$/μL)	6.48±0.56	6.40±0.52	6.45±0.48	6.50±0.58
Rt (%)	1.25±0.19	1.18±0.21	1.22±0.32	1.22±0.23
HCT (%)	40.50±3.42	41.12±3.09	39.85±3.16	40.63±2.13
MCV (fl)	62.72±6.06	64.67±7.81	62.42±5.54	63.02±7.32
MCH (pg)	21.02±2.05	21.94±2.46	21.36±2.48	21.52±2.21
MCHC (gm/dL)	40.50±0.61	33.96±0.85	38.54±3.12	34.23±1.68
Platelets ($x10^3$/μL)	6.53±0.56	6.50±0.55	6.55±0.61	6.42±0.58
WBC ($x10^5$/μl)	6.38±0.58	6.65±1.05	6.36±0.95	6.78±0.85

5.3. Conclusion

We have for the first time demonstrated that highly water-soluble citrate-Mn_3O_4 NPs can catalytically decompose yellow aqueous solution of bilirubin to its colourless oxidative break down products in a very quick time and most importantly, without any photo-activation. Mechanistic studies on the catalytic process have resulted in greater understanding of the catalytic cycle and additional insight into the active sites of the nanoparticles involved. Furthermore, the remarkable *in vitro* reactivity of the catalyst towards the suppression of bilirubin level in the whole blood specimens of hyperbilirubinemia patients, without much affecting other important blood constituents, represents a great promise of citrate-Mn_3O_4 NPs in direct therapeutic applications against hyperbilirubinemia. We further demonstrated that these Mn-based NPs are safe, biocompatible and effective targeted probes for hyperbilirubinemia in mice model based on the *in vitro* and *in vivo* assessments, especially without any toxicological implications. The study to compare the efficacy of the NPs with that of a commercially available drug silymarin shows that in hyperbilirubinemia mice, administration of the NPs brings the bilirubin level to normal limits in 6 hours whereas silymarin needs several days to control hyperbilirubinemia in mice. The overall therapeutic procedure is pictorially presented in scheme 5.1. These findings break through the bottleneck in therapeutic procedures for the treatment of hyperbilirubinemia by fast and direct degradation of bilirubin and pave the way for the practical clinical therapy of Mn-based NPs as safe nano-medicines.

References

1. Burgos, A.E., V.J. Flaherman, and T.B. Newman, Screening and follow-up for neonatal hyperbilirubinemia a review*, Clin. Pediatr.* 51 (2012) 7-16.
2. Dennery, P.A., D.S. Seidman, and D.K. Stevenson, Neonatal hyperbilirubinemia*, N. Engl. J. Med.* 344 (2001) 581-590.
3. Alkhotani, A., E.E.M.N. Eldin, A. Zaghloul, and S. Mujahid, Evaluation of neonatal jaundice in the Makkah region*, Sci. Rep.* 4 (2014) 4802.
4. Maghzal, G.J., M.-C. Leck, E. Collinson, C. Li, and R. Stocker, Limited role for the bilirubin-biliverdin redox amplification cycle in the cellular antioxidant protection by biliverdin reductase*, J. Biol. Chem.* 284 (2009) 29251-29259.
5. Mireles, L.C., M.A. Lum, and P.A. Dennery, Antioxidant and cytotoxic effects of bilirubin on neonatal erythrocytes*, Pediatr. Res.* 45 (1999) 355-362.
6. Kapitulnik, J., Bilirubin: An endogenous product of heme degradation with both cytotoxic and cytoprotective properties*, Mol. Pharmacol.* 66 (2004) 773-779.
7. Mahtab, M.A., *Liver: A complete book on hepato-pancreato-biliary diseases*. 2012: Elsevier Health Sciences APAC.
8. Shapiro, S.M., Chronic bilirubin encephalopathy: diagnosis and outcome*, Semin. Fetal. Neonatal. Med.* 15 (2010) 157-163.
9. Lakovic, K., J. Ai, J. D'Abbondanza, A. Tariq, M. Sabri, A.K. Alarfaj, P. Vasdev, and R.L. Macdonald, Bilirubin and its oxidation products damage brain white matter*, J. Cereb. Blood. Flow. Metab.* 34 (2014) 1837-1847.
10. Shalan, M.G., M.S. Mostafa, M.M. Hassouna, S.E.H. El-Nabi, and A. El-Refaie, Amelioration of lead toxicity on rat liver with Vitamin C and silymarin supplements*, Toxicology* 206 (2005) 1-15.
11. Van Der Veere, C.N., M. Sinaasappel, A.F. McDonagh, P. Rosenthal, P. Labrune, M. Odiévre, J. Fevery, J. Otte, P. McClean, et al., Current therapy for Crigler-Najjar syndrome type 1: Report of a world registry*, Hepatology* 24 (1996) 311-315.
12. Xia, B., G. Zhang, and F. Zhang, Bilirubin removal by cibacron blue F3GA attached nylon-based hydrophilic affinity membrane*, J. Membr. Sci.* 226 (2003) 9-20.
13. Toietta, G., V.P. Mane, W.S. Norona, M.J. Finegold, P. Ng, A.F. McDonagh, A.L. Beaudet, and B. Lee, Lifelong elimination of hyperbilirubinemia in the Gunn rat with a

single injection of helper-dependent adenoviral vector, *Proc. Natl. Acad. Sci. U. S. A.* 102 (2005) 3930-3935.

14. Strauss, K., D. Robinson, H. Vreman, E. Puffenberger, G. Hart, and D.H. Morton, Management of hyperbilirubinemia and prevention of kernicterus in 20 patients with Crigler-Najjar disease, *Eur. J. Pediatr.* 165 (2006) 306-319.
15. Kus, I., N. Colakoglu, H. Pekmez, D. Seckin, M. Ogeturk, and M. Sarsilmaz, Protective effects of caffeic acid phenethyl ester (CAPE) on carbon tetrachloride-induced hepatotoxicity in rats, *Acta Histochem.* 106 (2004) 289-297.
16. Kus, I., M. Ogeturk, H. Oner, S. Sahin, H. Yekeler, and M. Sarsilmaz, Protective effects of melatonin against carbon tetrachloride-induced hepatotoxicity in rats: a light microscopic and biochemical study, *Cell Biochem. Funct.* 23 (2005) 169-174.
17. Mansour, M.A., Protective effects of thymoquinone and desferrioxamine against hepatotoxicity of carbon tetrachloride in mice, *Life Sci.* 66 (2000) 2583-2591.
18. Babalola, O.O., J.I. Anetor, and F.A. Adeniyi, Amelioration of carbon tetrachloride-induced hepatotoxicity by terpenoid extract from leaves of Vernonia amydgalina, *Afr. J. Med. Sci.* 30 (2001) 91-93.
19. Pan, D., S.D. Caruthers, G. Hu, A. Senpan, M.J. Scott, P.J. Gaffney, S.A. Wickline, and G.M. Lanza, Ligand-directed nanobialys as theranostic agent for drug delivery and manganese-based magnetic resonance imaging of vascular targets, *J. Am. Chem. Soc.* 130 (2008) 9186-9187.
20. Lei, S., K. Tang, Z. Fang, and H. Zheng, Ultrasonic-assisted synthesis of colloidal Mn_3O_4 nanoparticles at normal temperature and pressure, *Cryst. Growth Des.* 6 (2006) 1757-1760.
21. Giri, A., N. Goswami, C. Sasmal, N. Polley, D. Majumdar, S. Sarkar, S.N. Bandyopadhyay, A. Singha, and S.K. Pal, Unprecedented catalytic activity of Mn_3O_4 nanoparticles: potential lead of a sustainable therapeutic agent for hyperbilirubinemia, *R. Soc. Chem. Adv.* 4 (2014) 5075-5079.
22. Giri, A., N. Goswami, M. Pal, M.T. Zar Myint, S. Al-Harthi, A. Singha, B. Ghosh, J. Dutta, and S.K. Pal, Rational surface modification of Mn_3O_4 nanoparticles to induce multiple photoluminescence and room temperature ferromagnetism, *J. Mater. Chem. C* 1 (2013) 1885-1895.

23. Bodini, M.E., L.A. Willis, T.L. Riechel, and D.T. Sawyer, Electrochemical and spectroscopic studies of manganese(II), -(III), and -(IV) gluconate complexes. 1. Formulas and oxidation-reduction stoichiometry, *Inor. Chem.* 15 (1976) 1538-1543.

24. Yang, B., M.D. Morris, M. Xie, and D.A. Lightner, Resonance raman spectroscopy of bilirubins: Band assignments and application to bilirubin/lipid complexation, *Biochemistry* 30 (1991) 688-694.

25. Kurtin, W.E., Spectroscopy and photochemistry of bilirubin photoproducts. I. Methyvinylmaleimide, *Photochem. Photobiol.* 27 (1978) 503-509.

26. Giri, A., N. Goswami, M.S. Bootharaju, P.L. Xavier, R. John, N.T.K. Thanh, T. Pradeep, B. Ghosh, A.K. Raychaudhuri, et al., Emergence of multicolor photoluminescence in $La_{0.67}Sr_{0.33}MnO_3$ nanoparticles, *J. Phys. Chem. C* 116 (2012) 25623-25629.

27. Takashima, T., K. Hashimoto, and R. Nakamura, Mechanisms of pH-dependent activity for water oxidation to molecular oxygen by MnO_2 electrocatalysts, *J. Am. Chem. Soc.* 134 (2011) 1519-1527.

28. Purdey, M., Ecosystems supporting clusters of sporadic TSEs demonstrate excesses of the radical-generating divalent cation manganese and deficiencies of antioxidant co factors Cu, Se, Fe, Zn, *Med. Hypotheses* 54 (2000) 278-306.

29. Polley, N., S. Saha, A. Adhikari, S. Banerjee, S. Darbar, S. Das, and S.K. Pal, Safe and symptomatic medicinal use of surface-functionalized Mn_3O_4 nanoparticles for hyperbilirubinemia treatment in mice, *Nanomedicine* 10 (2015) 2349-2363.

30. Khan, S.N., B. Islam, R. Yennamalli, A. Sultan, N. Subbarao, and A.U. Khan, Interaction of mitoxantrone with human serum albumin: Spectroscopic and molecular modeling studies, *Eur. J. Pharm. Sci.* 35 (2008) 371-382.

31. Mitra, R.K., P.K. Verma, D. Wulferding, D. Menzel, T. Mitra, A.M. Todea, P. Lemmens, A. Müller, and S.K. Pal, A molecular magnet confined in the nanocage of a globular protein, *ChemPhysChem* 11 (2010) 389-393.

32. Wolf, P., Biochemical diagnosis of liver disease, *Ind. J. Clin. Biochem.* 14 (1999) 59-90.

33. Wang, M.-Y., G. Anderson, D. Nowicki, and J. Jensen, Hepatic protection by noni fruit juice against ccl_4-induced chronic liver damage in female sd rats, *Plant Food Hum. Nutr.* 63 (2008) 141-145.

34. Janbaz, K.H., S.A. Saeed, and A.H. Gilani, Protective effect of rutin on paracetamol- and CCl_4-induced hepatotoxicity in rodents, *Fitoterapia* 73 (2002) 557-563.

35. Paquet, K.J. and U. Kamphausen, The carbon-tetrachloride-hepatotoxicity as a model of liver damage. First report: Long-time biochemical changes, *Acta Hepato. Gastroenterol.* 22 (1975) 84-88.

36. Rajkapoor, B., B. Jayakar, S. Kavimani, and N. Murugesh, Effect of dried fruits of *carica papaya* LINN on hepatotoxicity, *Biol. Pharm. Bull.* 25 (2002) 1645-1646.

37. Drotman, R.B. and G.T. Lawhorn, Serum enzymes as indicators of chemically induced liver damage, *Drug Chem. Toxicol.* 1 (1978) 163-171.

38. Zalatnai, A., I. Sarosi, A. Rot, and K. Lapis, Inhibitory and promoting effects of carbon tetrachloride-induced liver cirrhosis on the diethylnitrosamine hepatocarcinogenesis in rats, *Cancer Lett.* 57 (1991) 67-73.

39. Burr, A.W., M.R. Carpenter, J.E. Hines, W.J. Gullick, and A.D. Burt, Intrahepatic distribution of transforming growth factor-alpha (TGF alpha) during liver regeneration following carbon tetrachloride-induced necrosis, *J. Pathol.* 170 (1993) 95-100.

40. Naziroglu, M., M. Cay, B. Ustundag, M. Aksakal, and H. Yekeler, Protective effects of vitamin E on carbon tetrachloride-induced liver damage in rats, *Cell Biochem. Funct.* 17 (1999) 253-259.

41. Al-Shabanah, O.A., K. Alam, M.N. Nagi, A.C. Al-Rikabi, and A.M. Al-Bekairi, Protective effect of aminoguanidine, a nitric oxide synthase inhibitor, against carbon tetrachloride induced hepatotoxicity in mice, *Life Sci.* 66 (2000) 265-270.

42. Ogata, I., A.S. Auster, A. Matsui, P. Greenwel, A. Geerts, T. D'Amico, K. Fujiwara, E. Kessler, and M. Rojkind, Up-regulation of type I procollagen C-proteinase enhancer protein messenger RNA in rats with CCl_4-induced liver fibrosis, *Hepatology* 26 (1997) 611-617.

43. Mackinnon, M., C. Clayton, J. Plummer, M. Ahern, P. Cmielewski, A. Ilsley, and P. Hall, Iron overload facilitates hepatic fibrosis in the rat alcohol/low-dose carbon tetrachloride model, *Hepatology* 21 (1995) 1083-1088.

44. Natsume, M., H. Tsuji, A. Harada, M. Akiyama, T. Yano, H. Ishikura, I. Nakanishi, K. Matsushima, S. Kaneko, et al., Attenuated liver fibrosis and depressed serum albumin

levels in carbon tetrachloride-treated IL-6-deficient mice, *J. Leukoc. Biol.* 66 (1999) 601-608.

45. Theocharis, S.E., A.P. Margeli, S.D. Skaltsas, C.A. Spiliopoulou, and A.S. Koutselinis, Induction of metallothionein in the liver of carbon tetrachloride intoxicated rats: an immunohistochemical study, *Toxicology* 161 (2001) 129-138.

Chapter 6

Development of an Online, Simultaneous Diagnosis and Therapeutic Strategy of Hyperbilirubinemia for Potential Application in Neonatal Subjects

6.1. Introduction

Importance of light in the medical diagnosis and therapy is unanimous. Starting from invention of light microscope in sixteenth century for the pathological use till "bloodless" laser surgery in the twentieth century are the few exemplary evidences [1-5]. Advent of nanotechnology further opens up the scope of light for the diagnosis and therapy. For example, use of quantum dots (QDs) for the early diagnosis and photodynamic therapy of cancer are reported in the literature [6-8]. Potentiality in the use of zinc oxide nanoparticle in the light-assisted treatment of hyperbilirubinemia is also reported from this group [9]. Light as universal excitation source of spectroscopy in optical biopsy is evident in the literature [10, 11]. Use of optical fiber in the biomedical instrumentation for guiding light is also found to be another important way for the medical use of light in endoscopy [12-14]. A significant portion of fiber optic-based biosensors relies on the efficient interaction of evanescent field with the environments under investigation [15-19]. Several good reviews on the use and control of evanescent field are reported in the present literature [17, 20, 21]. The studies are mainly focused on the sensing of biomedically important analytes, aiming to develop novel diagnostic protocol. However, use of evanescent field for a potential therapeutic use is sparse in the literature [15-23]. In one of the application based works, a pad of woven fibers used to transport light from a light source to the neonatal skin through leaky modes for the treatment of neonatal jaundice [24]. Other products for the sensing of variety of physical parameters including oxygen level, pH of a solution, temperature based on fiber optic absorption and fluorescence techniques are also reported in the literature [25-28]. Nonetheless, to the best of our knowledge, use of evanescent field for the simultaneous diagnosis and therapy is absent in the literature and is the motive of present work.

In the present study, we have used evanescent field of a silica fiber for probing a bile pigment bilirubin in aqueous solution. Bilirubin is a metabolic waste product that generally excreted through bile and urine, but for some disease conditions in liver and biliary tract, bilirubin starts to accumulate in tissues and blood, leading to jaundice [29]. Accumulation of bilirubin is very much common in neonates, causing neonatal jaundice. During the first week of life, around half of the all neonates are affected by jaundice [30]. Till date phototherapy is the most effective treatment for neonatal jaundice [30, 31]. In phototherapy the neonates are placed under blue light, since, bilirubin absorbs light in the blue region of the optical spectrum [32-35]. In conventional phototherapy, bilirubin level of the patients is recommended to be monitored time to time through blood test, in order to determine the required dosage and future course of action. In this context, a noninvasive/minimally invasive procedure for the phototherapy can be very helpful. In the present study, we have shown that the evanescent field coupled to the aqueous environment can efficiently be used for degradation of bilirubin. Our method offers a strategy for continuous monitoring the level of bilirubin during the degradation process, which is extremely important for the immediate course of action. We have found that deposition of our test pigment bilirubin on the surface of the sensor silica core fiber due to the presence of unavoidable hydroxyl functional groups [26] at physiological pH (~7.4). Apparent masking of the sensitivity of fiber optic biosensors due to deposition and extraction of relevant information, have also been addressed in our studies. We have successfully demonstrated our strategy in the removal of clinically significant amount of bilirubin in blood-phantom solution (hemoglobin and human serum albumin (HSA)). In a model study using chromatography paper as biological membrane mimic, we have established the efficacy of the developed technique, *in vitro*. Briefly, the developed evanescent optical approaches are expected to unite diagnosis, treatment and potential treatment-guidance in one procedure for the management of hyperbilirubinemia.

6.2. Result and Discussion

6.2.1. Evanescent Field: A Potential Light-tool for Theranostics Application [36]: In the present work, we have used evanescent field of the optical fibers for the potential theranostics application in hyperbilirubinemia. It has to be noted that the evanescent wave is a near-field wave with an intensity that exhibits exponential decay without absorption as a function of the distance from the core-clad boundary of the optical fiber as shown in Figure 6.1. The standard

practice for the estimation of penetration depth (d_p) of the evanescent field in a "non-absorbing" medium has been illustrated in the section 2.1.4.

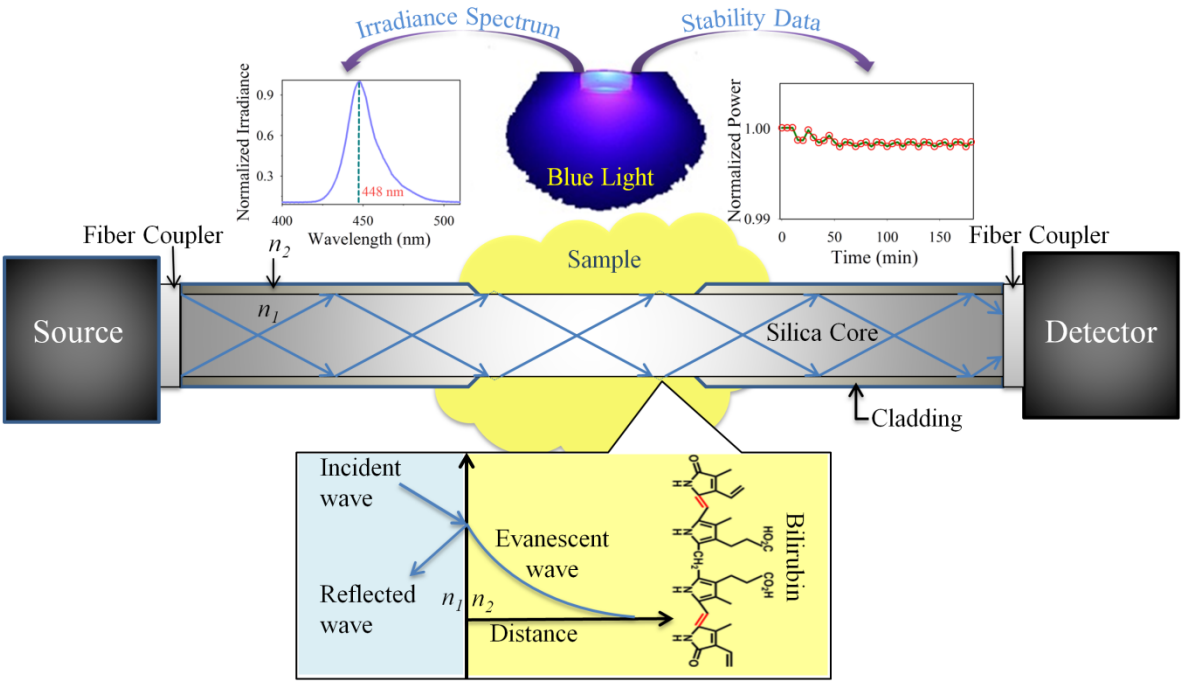

Figure 6.1. *Schematic representation of our experimental setup. For the spectroscopic monitoring of photodegradation by an external blue LED (of 450 nm wavelength) a white light as "Source" and a spectrograph as "Detector" was used for bilirubin sensing. Potential use of the setup in theranostics application has been demonstrated by replacing the white light with blue LED (source) and optical power meter (detector) at the other end of the fiber, without employing any external light source for photodegradation of bilirubin. The upper insets in left and right represent the irradiation spectra of the LED and its stability respectively. The lower inset shows mechanistic details of evanescent field for the detection of bilirubin.*

In order to investigate the quality of the surface of optical fibers and their modification after the treatment of physical etching (silica) and heating (plastic), we have observed the fibers under scanning electron microscope (SEM). Figure 6.2 depicts the SEM images of the optical fibers before and after etching. From the Figure, the surface of the base fibers (6.2a and 6.2c) and the modifications (6.2b and 6.2d) due to physical etching/heating are evident. It is also clear that the measured diameters of the silica and plastic fibers (223 μm and 997μm respectively) are consistent with the literature values provided by the manufacturer (225 μm and 1000 μm respectively). The thickness of the clad (12 μm, Figure 6.2b) in the case of silica fiber is also similar to that of the literature value of 12.5 μm. Figure 6.3a shows

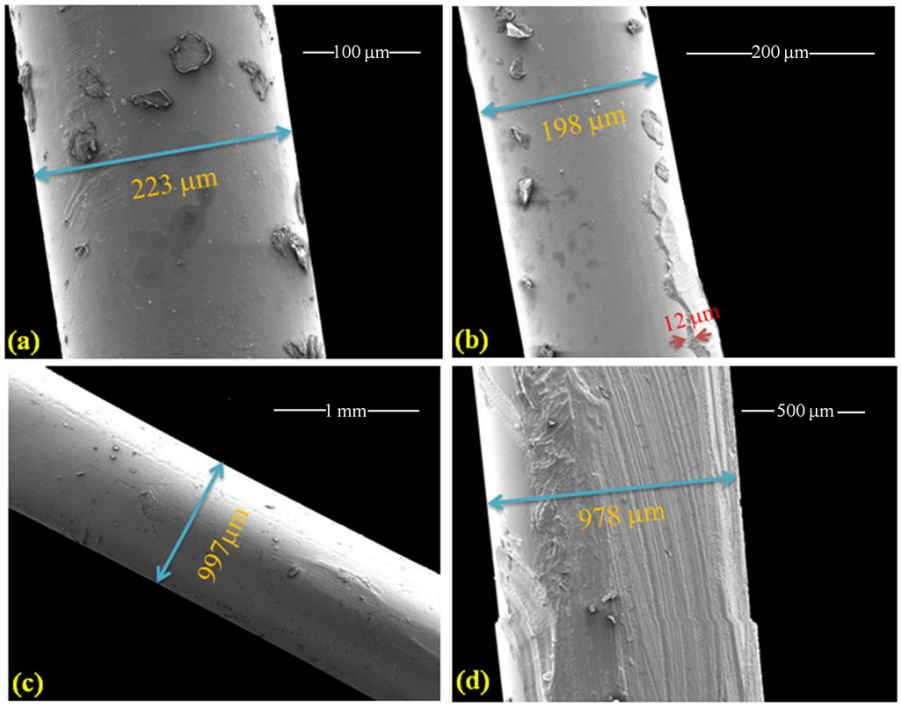

Figure 6.2. *Scanning electron microscopic image of bare silica (a), plastic (c) fibers. The modified surface of the silica (b) and plastic (d) fibers after manual etching/ heating are also shown.*

absorption spectrum of aqueous bilirubin solution (9.2 µM at pH~7.5) measured in Shimadzu spectrophotometer having a peak around 450 nm and consistent with reported literature [37]. In order to study the spectral response of bilirubin white light was introduced into the fiber, the absorption spectrum of aqueous bilirubin solution (concentration 10 µM, pH 7.5) using the spectrograph at the end of the fiber is shown in Figure 6.3b. The spectra of 6.3a and 6.3b are apparently looking different and the spectrum in Figure 6.3b is similar to that of the solid bilirubin as shown in the inset of Figure 6.3a. The observation is consistent with the fact that the evanescent field essentially monitors solid form of bilirubin deposited at the surface of the fiber. The deposition can be rationalized from the fact that the surface of the fiber is heavily hydroxylated at pH 7.4 [26] and deposition of bilirubin on the hydroxylated surface is unavoidable [18]. In order to further investigate the possibility of deposition of bilirubin, we have checked the precipitation of bilirubin on a hydroxylated glass slide at different pH values. As shown in the inset of Figure 6.3b, a significant amount of bilirubin can be deposited on the plate at physiological pH (7.4). It is to be noted that the deposition of bilirubin on the fiber surface may augment the evanescent field to the environments as indicated in Equation 2.18, reducing the penetration depth of the probe field. In earlier studies the deposition issue of the

test analytes in fiber optic sensors is concluded to be a limiting factor for the overall sensitivity of detection [18, 22, 23]. However, detail investigation of the deposition of the test analytes in the optical fiber sensors was beyond the scope of the earlier studies.

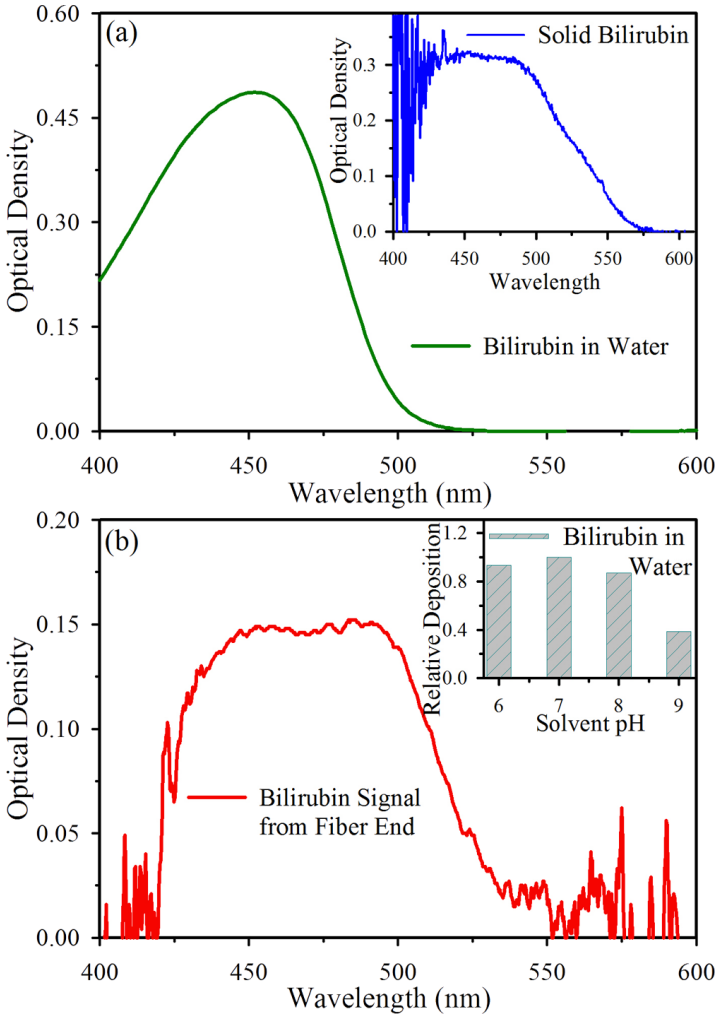

Figure 6.3. *(a) Absorption spectrum of bilirubin in aqueous solution (pH~7.5). (b) Absorption spectrum of bilirubin solution (pH~7.5) detected at the end of etched silica fiber. Similarity of the spectra with that of the solid bilirubin (inset of (a)) is clearly evident. Deposition effect of bilirubin at different pH values is shown in the inset of (b).*

For the potential application of optical fiber as a theranostics tool, the deposition may work in a positive manner. The proximity of bilirubin to the evanescent field significantly increases the possibility of photodegradation of bilirubin. In our studies we have found that the spectroscopic signature of the photodegradation product is closely resemble with previously reported photo-oxidation product of bilirubin, methylvinylmaleimide (MVM) [38]. After the photodegradation of bilirubin at the fiber surface, the evanescent field may "search" for new bilirubin molecule in the solution by increasing the depth of penetration (Equation

2.16). Deposition and degradation of bilirubin in aqueous solution under an external blue light (Figure 6.1) is shown in Figure 6.4. The efficacy of the optical fiber sensor to monitor the

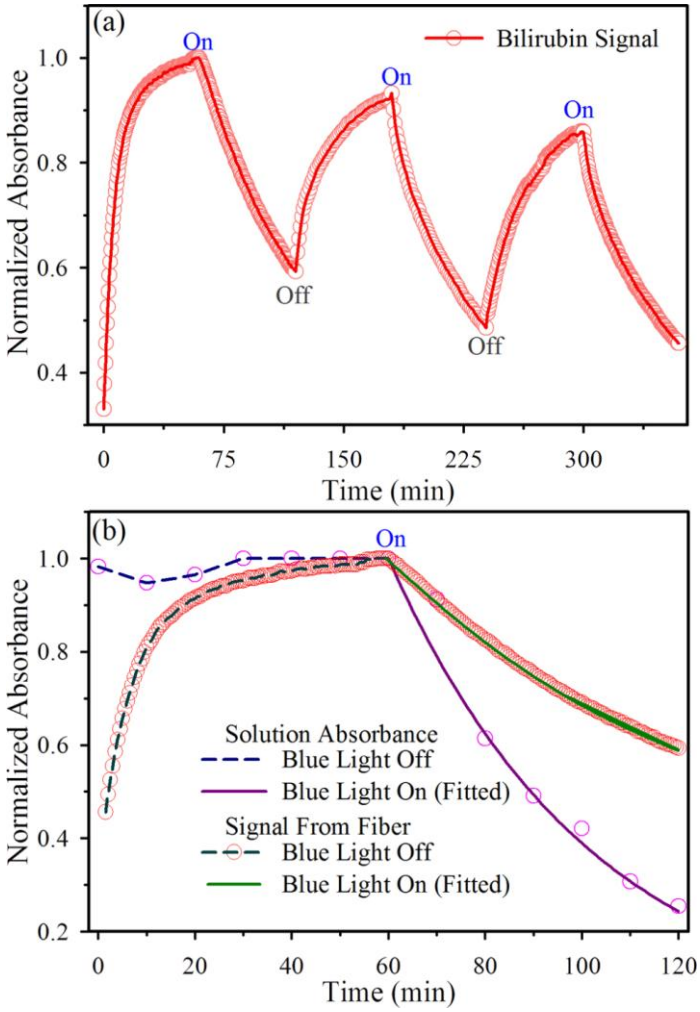

Figure 6.4. *(a) Time dependent absorption kinetics of aqueous bilirubin solution (12 μM, pH 7.5) as detected at the end of the silica fiber. The growth in the absence of external blue light (Off) and subsequent decay in presence of blue light (On) over three cycles is evident from the figure. (b) A comparison of the kinetics detected at the end of the silica fiber (as shown in panel (a)) by the spectrograph with that of the time dependent concentration of the same solution measured with Shimadzu-2600 spectrophotometer, is demonstrated.*

concentration of bilirubin in the solution for several cycles is demonstrated in Figure 6.4a. Figure 6.4b shows a comparative study of monitoring the bilirubin concentrations in solution by spectrograph in the fiber sensor, with that of the readings obtained from Shimadzu spectrophotometer. From Figure 6.4b it is evident that the spectrophotometer unable to monitor the deposition of the bilirubin, which is very local effect at the surface of the fiber only, however, very important for the sensing efficiency. Numerical fitting of the deposition

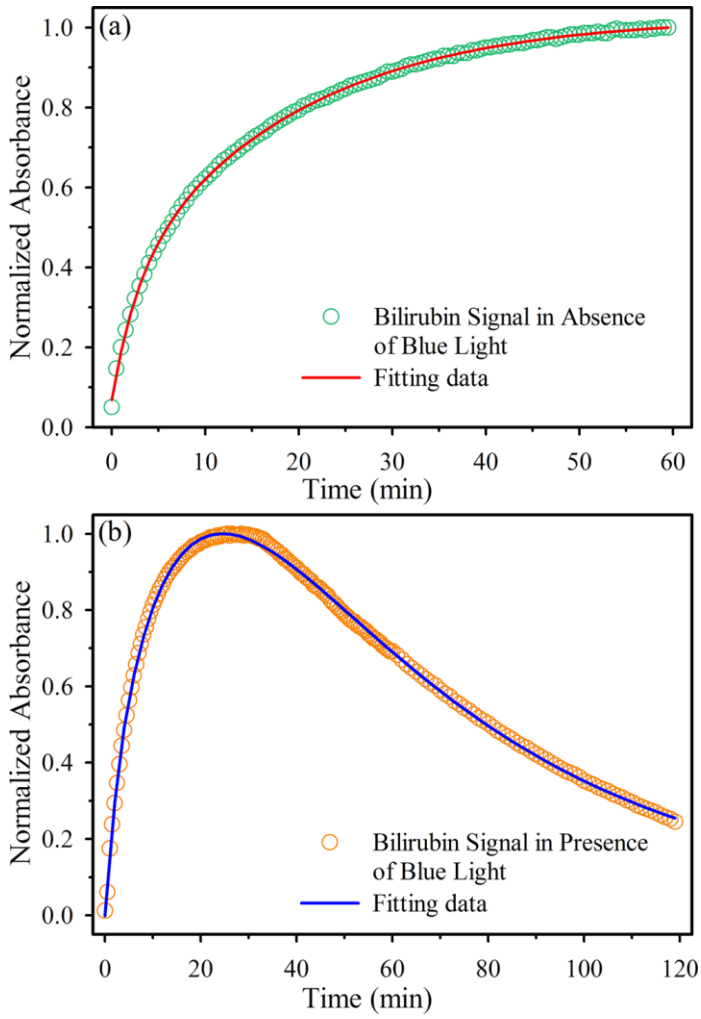

Figure 6.5. *Deposition of bilirubin in aqueous solution (pH 7.5, 12μM), detected at the end of the fiber in (a) absence and (b) presence of an external blue light (1W, 460nm).*

(Figure 6.4b) in absence of light reveal exponential rise of time constant 21.00 min. In presence of blue light the decay kinetics can be fitted with bi-exponential function with a rise component of 21.00 min followed by a decay of time constant 42.05 min with residual component (y_0) of 0.46. It has to be noted that the kinetics measured with the spectrophotometer can be fitted with a single exponential decay with time constant of 42.44 min, which is consistent with the decay component measured with spectrograph (τ_2=42.00 min). The observation reveals that fiber sensor attached with the spectrograph measures similar decay kinetics, convoluted with a rise component due to the deposition of bilirubin at the surface and invites care for the interpretation of kinetics data from a fiber sensor used to measure concentration of an analyte in solution phase.

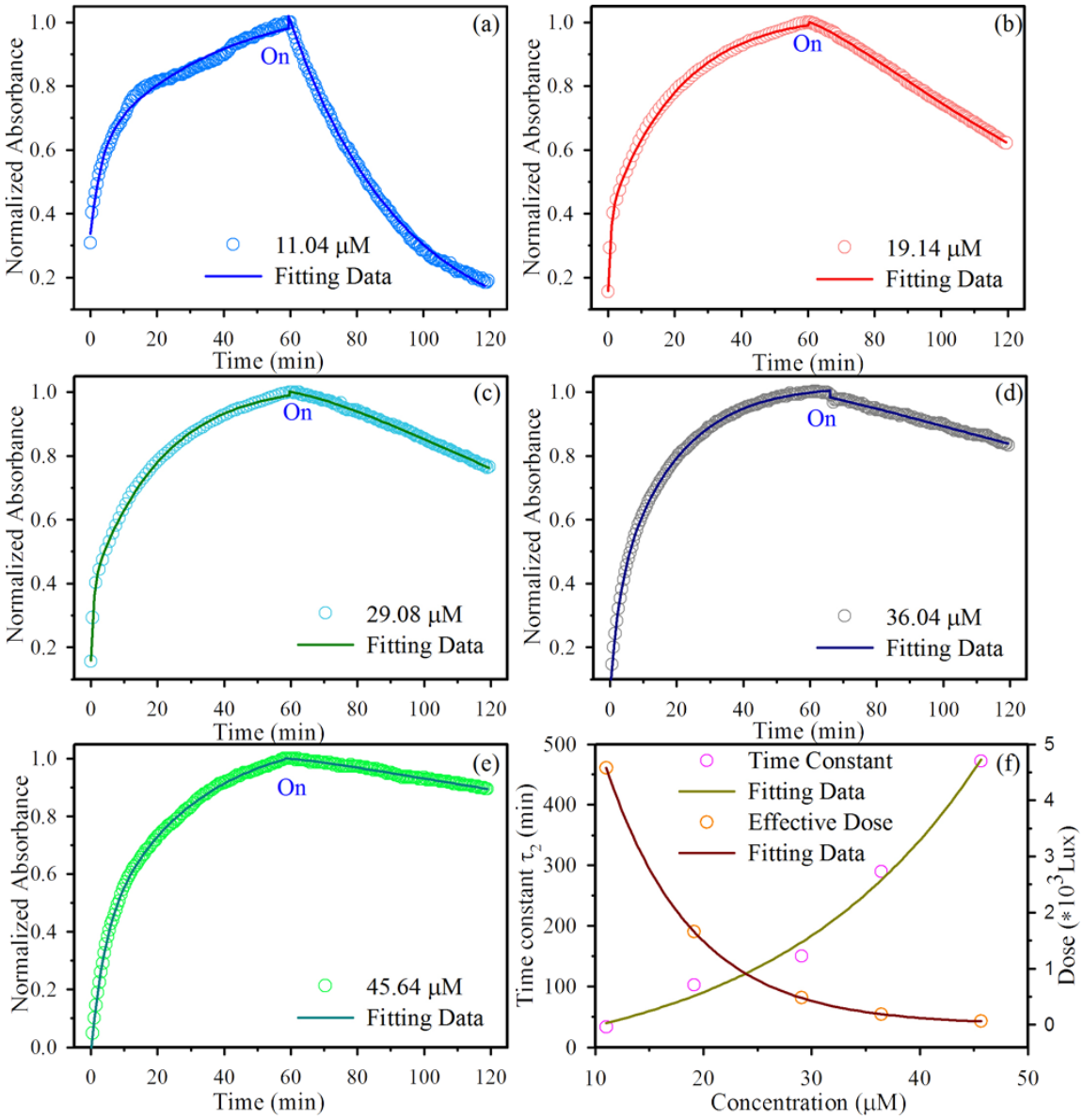

Figure 6.6. *Concentration dependent deposition and degradation (in absence and presence of blue light) of bilirubin as detected by fiber (panel (a)-(e)). Dominance of degradation kinetics in presence of blue light is evident. Panel (f) shows slower degradation with high bilirubin concentration. The effective dose of light at the fiber surface with bilirubin concentration is also shown.*

In order to investigate the deposition effect on the surface of the fiber, we have studied the signal from the fiber sensor in absence and presence of external blue light source, as shown in Figure 6.5a and 5b. Table 6.1 represents the fitting kinetics data. It is clear that the deposition is also an integral part of the decay kinetics and needs numerical fitting for the

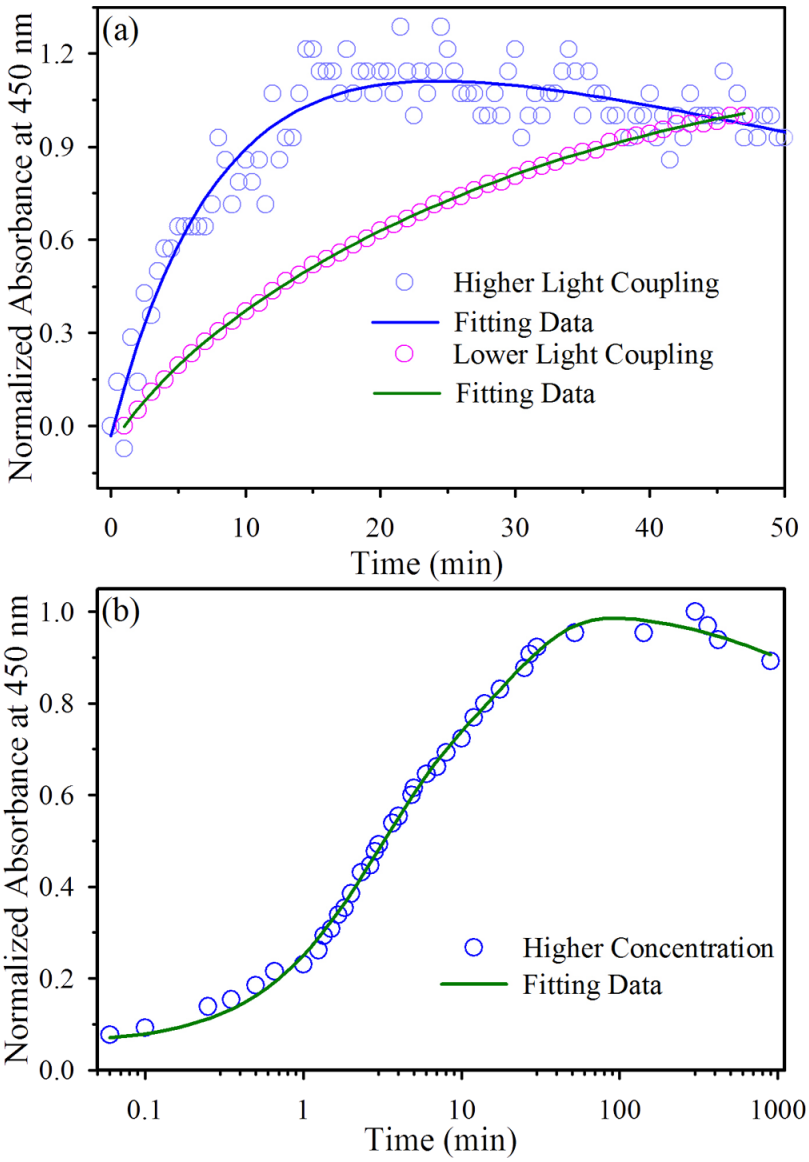

Figure 6.7. *Efficacy of the setup in potential theranostics application is demonstrated in a prototype experiment. It is clear from both the figures that, degradation of bilirubin depends on the amount of light coupled to the silica fiber.*

interpretation of the kinetics. The deposition and the degradation (in absence and presence of blue light) of bilirubin at various concentrations are shown in Figure 6.6. Corresponding kinetics data are tabulated in Table 6.1. As evident from Table 6.1 and Figure 6.6f, with increasing the concentration of bilirubin, the decay kinetics gradually becomes slower. This observation can be rationalized in term of our experimental set up (Figure 6.1), revealing lowers effective dose of light at the fiber surface with the increase in solution concentration (inner filter effect). From Figure 6.6 and corresponding fitting data in Table 6.1, it is also clear that the rise time constants almost remain unperturbed in the range of solution concentrations

in our study. While the faster rise time constants 2-4 min may be consistent with homogenization of the solution, long time constants in the range of 20-40 min account for deposition of bilirubin at the fiber surface.

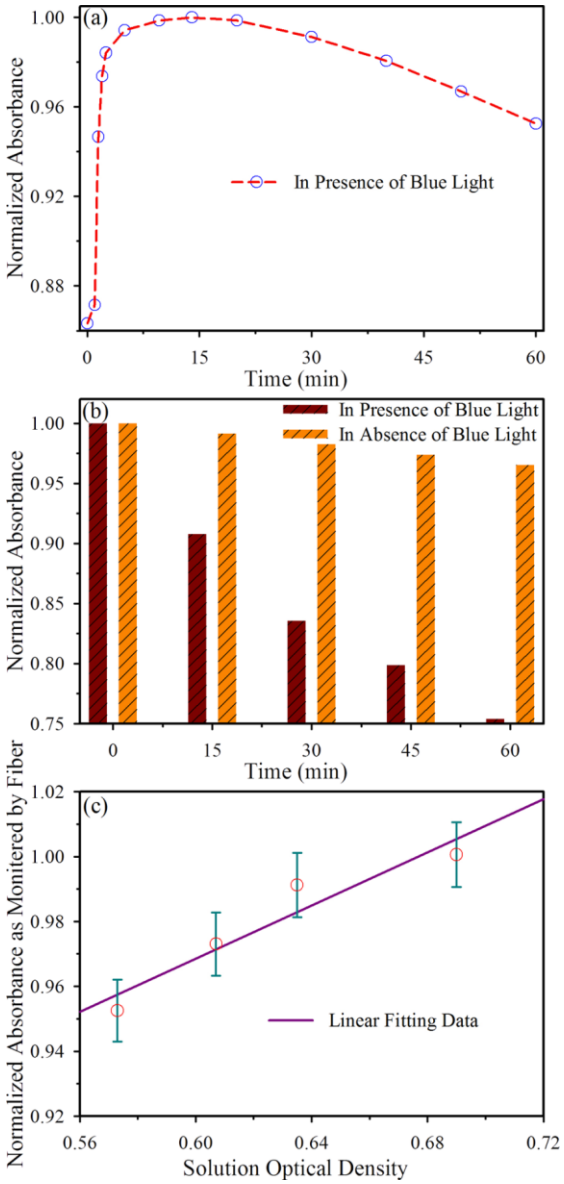

Figure 6.8. *The theranostics applicability of the prototype is represented using 1mm fiber as sensor and Coherent FieldMate with OP-2 VIS sensor as detector. (a) The detected signal from the fiber end. (b) Comparative solution concentration measured in Shimadzu spectrophotometer in presence and absence of blue light. (c) The linear dependency between the signals detected at the fiber end and the solution concentration.*

In real theranostics application there is very little scope to use external light source rather use of the light through the fiber for both sensing and phototherapy. Figure 6.7 shows the efficacy of the setup, in which a blue LED is coupled to the etched silica fiber and the

transmitted optical power is detected by a spectrograph (Figure 6.7a) and a power meter (Figure 6.7b). It is evident from Figure 6.7a, the degradation depends on the amount of power coupled to the fiber which can be differentiated in terms of light intensity at the detector end of the fiber. Although, sensing of bilirubin is irrespective of the coupling efficiency, bilirubin degradation very much depends on the coupled light to the fiber.

In our experimental condition (e.g. fiber end polishing, surface etching) the coupling efficiency varies revealing output power of the blue LED light at the fiber end in the range of 22-25 μW (higher coupling) to 4-5 μW (lower coupling). Figure 6.7b clearly indicates that for moderately coupled systems someone has to wait significant amount of time in order to get reasonable degradation effect. These observations clearly justify the increased amount of modes coupled to the optical fiber for potential application in theranostics. Figure 6.8 shows the data obtained using plastic fiber of diameter 1 mm. As shown in Figures 6.8a and 6.8b, a significant amount of photodegradation can be achieved in 60 minutes. It has to be noted that we have calibrated the concentration of bilirubin measured by the fiber sensor with that measured using spectrophotometer. In 60 minutes of experimental time span we have found reasonable linearity (Figure 6.8c), revealing the reliability of the data reported by the fiber sensor. In order to address the specific question, whether the sensor able to degrade bilirubin up to clinically meaningful amount in a physiologically relevant environment so that it can be actually used for therapy. We also have studied the photodegradation of bilirubin in a mixture of human serum albumin (HSA) and Hemoglobin (100 μM/L of each protein), two major ingredients of human blood. As shown in Figure 6.9 (a), the removal of bilirubin from the "blood-phantom" solution is significant revealing bilirubin degradation from 77 μM/L to 30μM/L. It has to be noted that the level of bilirubin in the human blood in normal and jaundice conditions are ~20 μM/L and >50 μM/L respectively. The spectral deconvolution of the absorption spectra (solid lines) in the range from 390 nm to 550 nm shows the presence of hemoglobin (soret band peak at 404 nm) and bilirubin (peak at 450 nm). The peak of HSA is supposed to be at 350 nm and beyond the spectral range. The deposition followed by the degradation measured from the optical power meter is clear from the inset of Figure 6.9a. The deconvoluted spectra peaking at 404 nm (hemoglobin) and 450 nm (bilirubin) at different time of irradiation are shown in Figure 6.9b. A clear decrease of the spectrum peaking at 450 nm with time, as a consequence of photodegradation of bilirubin is evident from the inset Figure

6.9b without affecting the hemoglobin count in the blood-phantom. Our observation further justifies the potentiality of our strategy for novel theranostics tool in future applications.

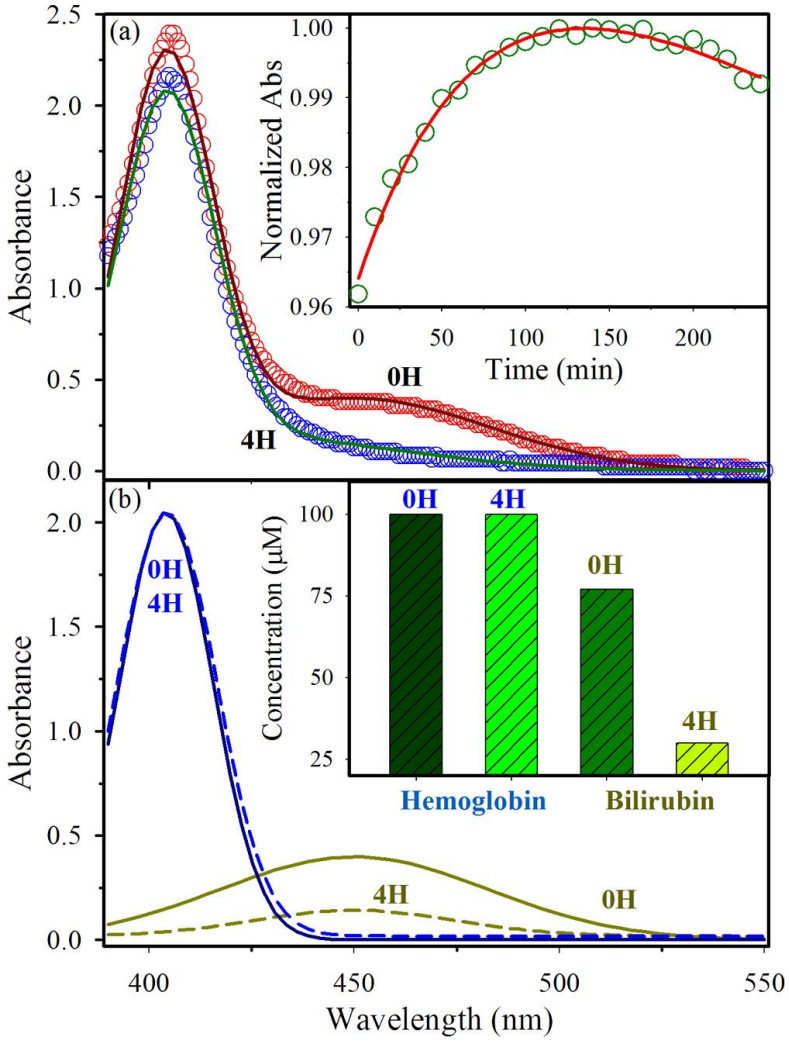

Figure 6.9. *(a) Absorption spectra of bilirubin (77 μM/L) in blood-phantom (HSA and hemoglobin mixture) solution before (0H) and after 4 hours of photodegradation (4H) by blue LED evanescent field. Solid lines indicate the goodness of spectral deconvolution the experimental data with two peaks at 404 nm (soret band of hemoglobin) and 450 nm (bilirubin). The inset represents time dependence of detected absorbance signal at the fiber end. Initial rise in the signal depicts the dominance of deposition of bilirubin and following photodegradationt leads the consequent decrease. (b) The deconvoluted spectra peaking at 404 nm (soret band of hemoglobin) and 450 nm (bilirubin) before and after the photo (450 nm) irradiation of the blood phantom are shown. Inset shows a clear decrease in the bilirubin (estimated value from 77 μM/L to 30 μM/L) and intactness of hemoglobin concentration.*

The promising experimental observation as shown in Figures 6.8 and 6.9, directed us for an *in vitro* theranostics application on a wet-chromatography paper as membrane mimic. Cellulose or polysaccharides are the primary constituent of chromatography paper, which are also the major components of fibrous extracellular matrix of skin dermis of green plants,

many forms of algae and eukaryotic microorganisms. Thus in order to effectively simulate the structure and composition of native skin, we have used wet-chromatography paper. Since, cellulose is significantly amphiphilic in nature, incorporation of bilirubin (which is generally considered as a lipophilic substance) in to the chromatography paper is primarily governed by the lipophilic or hydrophobic interactions [39-41].

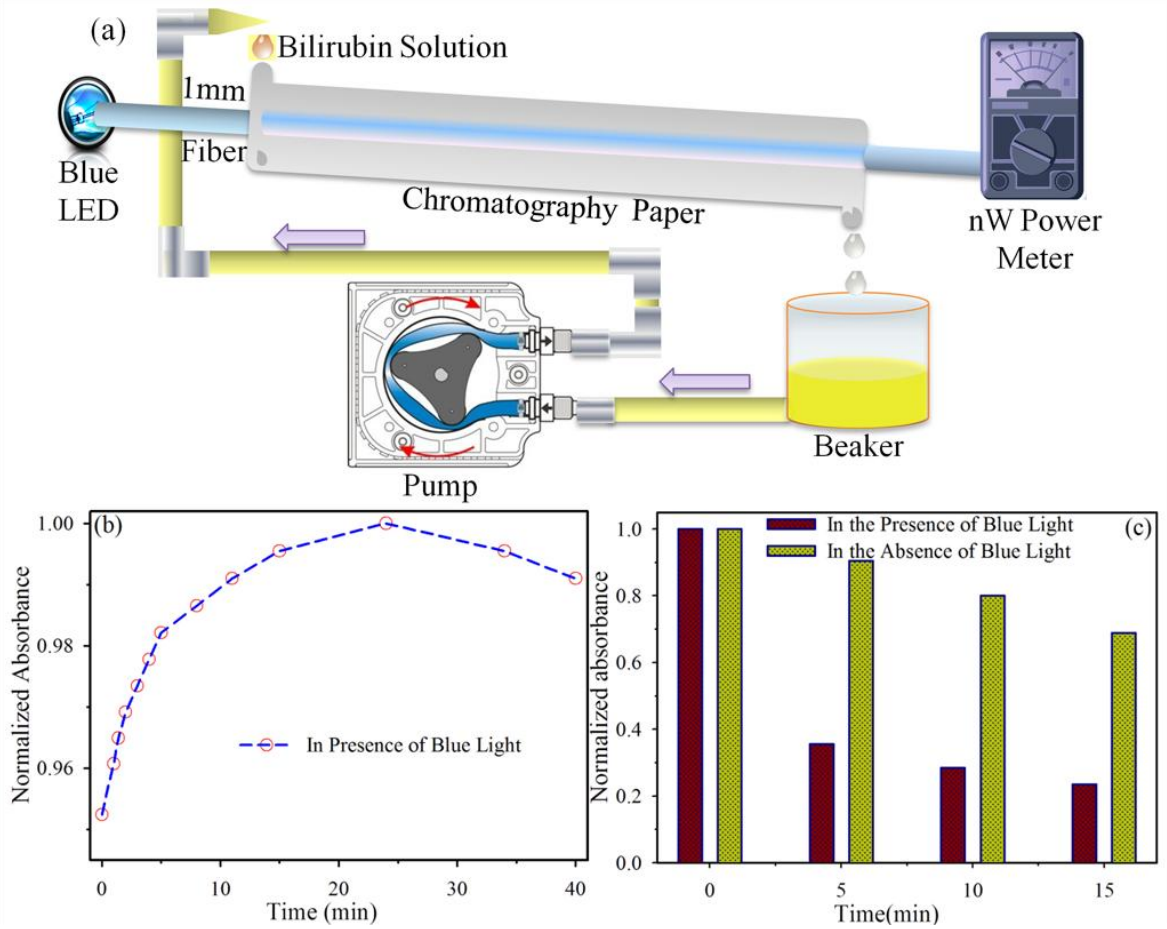

Figure 6.10. *The in vitro theranostics application for hyperbilirubinemia is represented using 1mm fiber as sensor and Coherent FieldMate with OP-2 VIS sensor as detector. (a) The schematic presentation of the experimental setup. (b) The signal detected at the Fiber end by the power meter. (c) The comparative solution concentration measured in Shimadzu spectrophotometer in presence and absence of blue light.*

The experimental set up for the *in vitro* studies is shown in Figure 6.10a. The experimental data on the bilirubin degradation measured with power meter (Figure 6.10b) and spectrophotometer (Figure 6.10c) are shown. From both the model experiments, it is clear that the degradation monitored by the power meter is apparent after sufficient photodegradation of the test pigment in the solution as monitored by the spectrophotometer.

Continuous deposition of the bilirubin on the plastic fiber surface is concluded to be reason for such observation. In a separate experiment on the deposition of bilirubin on the plastic fiber (data not shown), a time constant of 46.00 min is evident. It has to be noted that the degradation time constant is also in the similar order as monitored from spectrophotometer (Figures 6.8b and 6.10c). The model experiments also suggest that concentration monitored by the power-meter at the end of the fiber starts showing the decrease of bilirubin level in test medium, when the concentration of the pigment is significantly lower than the starting value. The observation clearly reveals the efficacy of continuous monitoring the level of bilirubin in the test environments during phototherapy.

Table 6.1: *Numerical fitting parameter of the bilirubin deposition (No Blue light) and Photo-degradation (in presence Blue light) kinetics as shown in Figure 6.5 and Figure 6.6.*

Sample		Con. (μM)	y_0	A_1	τ_1 (min)	A_2	τ_2 (min)	A_3	τ_3 (min)
Silica Fiber in Aqueous Solution (Figure 6.5)	Absence of blue light	10.00	0.97	-0.28	2.74	-0.70	19.71	0.08	170.57
	Presence of blue light	10.00	0.029	-0.27	2.66	-2.01	16.00	2.26	51.66
Bilirubin Deposition/ Degradation on Silica Fiber (No Blue Light)	Figure 6.6a	11.04	1.02	-0.27	3.22	-0.51	40.00	0.10	200.00
	Figure 6.6b	19.14	0.96	-0.23	0.78	-0.67	22.40	0.10	200.00
	Figure 6.6c	29.08	0.96	-0.23	0.77	-0.66	22.26	0.10	200.00
	Figure 6.6d	36.04	0.95	-0.27	2.63	-0.71	19.32	0.10	196.43
	Figure 6.6e	35.64	1.03	-0.39	3.92	-0.76	30.28	0.10	186.61
Bilirubin Deposition/ Degradation on Silica Fiber (In Blue Light)	Figure 6.6a	11.04	0.00	-0.20	3.2	-0.1	40.00	6.15	33.51
	Figure 6.6b	19.14	0.00	-1.55	1.34	-3.23	17.98	2.00	103.03
	Figure 6.6c	29.08	0.00	-0.03	2.95	-1.32	30.79	1.81	150.00
	Figure 6.6d	36.04	0.00	-0.20	2.30	-0.34	27.33	1.27	289.70
	Figure 6.6e	35.64	0.00	-0.79	4.79	-1.07	14.06	1.15	472.00

6.4. Conclusion

In the present study, we have developed a fiber optic evanescent field-based sensor for the detection of bilirubin in an aqueous medium. Our pH dependent studies show the efficacy of our developed fiber sensor depends on the deposition of bilirubin on the fiber surface due to the presence of unavoidable hydroxyl moieties on the silica surface. Our studies clearly reveal the importance of numerical fitting considering the deposition effect on the kinetics data obtained from the fiber sensor. We have demonstrated the efficacy of our strategy in the

maintenance of controlled bilirubin level in a blood-phantom solution (mixture of hemoglobin and HSA). We have also shown that bilirubin deposited at the fiber surface can be removed using the evanescent field. In a prototype experiment we have designed a way to detect the level of bilirubin (diagnosis) and its photodegradation (therapy) simultaneously, using a single fiber. The method could be useful for both noninvasive (on skin, like phototherapy) and invasive (in contact with blood); however, actual therapeutic strategy may be determined after a rigorous clinical trial. Apart from its fundamental importance, we believe that this work represents a step forward in the use of evanescent field (light) for potential theranostics application in hyperbilirubinemia.

References

1. Lapotko, D.O., Nanophotonics and theranostics: will light do the magic?, *Theranostics* 3 (2013) 138-140.
2. Sliney, D.H. and S.L. Trokel, *Medical lasers and their safe use*. 1993: Springer-Verlag New York.
3. Houston, S.K., C.C. Wykoff, A.M. Berrocal, D.J. Hess, and T.G. Murray, Laser treatment for retinopathy of prematurity, *Laser Med. Sci.* 28 (2013) 1-10.
4. Chmait, R.H., L.M. Korst, A. Llanes, P. Mullin, R.H. Lee, and J.G. Ouzounian, Perioperative characteristics associated with preterm birth in twin-twin transfusion syndrome treated by laser surgery, *Am. J. Obstet. Gynecol.* 209 (2013) 264-264.
5. Kong, K., C.J. Rowlands, S. Varma, W. Perkins, I.H. Leach, A.A. Koloydenko, H.C. Williams, and I. Notingher, Diagnosis of tumors during tissue-conserving surgery with integrated autofluorescence and Raman scattering microscopy, *Proc. Natl. Acad. Sci.* 110 (2013) 15189-15194.
6. Wu, X., Liu, Hongjian, Liu, Jianqua, Haley, Kari N., Treadway, Joseph A., Larson, J Peter, Ge, Nianfeng, Peale, Frank, Bruchez, Marcel P., Immunofluorescent labeling of cancer marker Her2 and other cellular targets with semiconductor quantum dots, *Nat. Biotech.* 21 (2003) 41-46.
7. Zhang, H., D. Yee, and C. Wang, Quantum dots for cancer diagnosis and therapy: biological and clinical perspectives, *Nanomedicine* 3 (2008) 83-91.
8. Luo, G., J. Long, B. Zhang, C. Liu, S. Ji, J. Xu, X. Yu, and Q. Ni, Quantum dots in cancer therapy, *Expert Opin. Drug Deliv.* 9 (2012) 47-58.
9. Sarkar, S., A. Makhal, S. Baruah, M.A. Mahmood, J. Dutta, and S.K. Pal, Nanoparticle-Sensitized Photodegradation of Bilirubin and Potential Therapeutic Application, *J. Phys. Chem. C* 116 (2012) 9608-9615.
10. Tearney, G.J., M.E. Brezinski, B.E. Bouma, S.A. Boppart, C. Pitris, J.F. Southern, and J.G. Fujimoto, In vivo endoscopic optical biopsy with optical coherence tomography, *Science* 276 (1997) 2037-2039.
11. Alfano, R.R., Advances in ultrafast time resolved fluorescence physics for cancer detection in optical biopsy, *AIP Advances* 2 (2012) 011103-011110.

12. Edmonson, J.M., History of the instruments for gastrointestinal endoscopy, *Gastrointest. Endosc.* 37 (1991) S27–S56.
13. Abe, N., H. Takeuchi, A. Ooki, G. Nagao, T. Masaki, T. Mori, and M. Sugiyama, Recent developments in gastric endoscopic submucosal dissection: Towards the era of endoscopic resection of layers deeper than the submucosa, *Dig. Endosc.* 25 (2013) 64-70.
14. Yao, K., G. Anagnostopoulos, and K. Ragunath, Magnifying endoscopy for diagnosing and delineating early gastric cancer, *Endoscopy* 41 (2009) 462-467.
15. Paul, P.H. and G. Kychakoff, Fiber-optic evanescent field absorption sensor, *Appl. Phys. Lett.* 51 (1987) 12-14.
16. Ruddy, V., B.D. MacCraith, and J.A. Murphy, Evanescent wave absorption spectroscopy using multimode fibers, *J. Appl. Phys.* 67 (1990) 6070-6074.
17. Leung, A., P.M. Shankar, and R. Mutharasan, A review of fiber-optic biosensors, *Sens. Actuator B-Chem.* 125 (2007) 688-703.
18. Armin, A., M. Soltanolkotabi, and P. Feizollah, On the pH and concentration response of an evanescent field absorption sensor using a coiled-shape plastic optical fiber, *Sens. Actuator A-Phys.* 165 (2011) 181-184.
19. Beres, C., F.V.B. de Nazaré, N.C.C. de Souza, M.A.L. Miguel, and M.M. Werneck, Tapered plastic optical fiber-based biosensor – Tests and application, *Biosens. Bioelectron.* 30 (2011) 328-332.
20. Velasco-Garcia, M.N., Optical biosensors for probing at the cellular level: A review of recent progress and future prospects, *Sem. Cell Dev. Biol.* 20 (2009) 27-33.
21. Ciminelli, C., C.M. Campanella, F. Dell'Olio, C.E. Campanella, and M.N. Armenise, Label-free optical resonant sensors for biochemical applications, *Prog. Quant. Electron.* 37 (2013) 51-107.
22. Safaai-Jazi, A. and J.V. Petersen, Evanescent field fibre-optic chlorine sensor, *Opt. Laser Technol.* 26 (1994) 399-402.
23. Choudhury, P.K. and T. Yoshino, On the fiber-optic chlorine sensor with enhanced sensitivity based on the study of evanescent field absorption spectroscopy, *Optik* 115 (2004) 329-333.
24. Russell, T.A., *Flexible illuminators for phototherapy*. 2001: U.S.

25. Allen, C.B., B.K. Schneider, and C.W. White, Limitations to oxygen diffusion and equilibration in in vitro cell exposure systems in hyperoxia and hypoxia*, Am. J. Physiol. Lung Cell Mol. Physiol.* 281 (2001) L1021-L1027.

26. Deboux, B.-C., E. Lewis, P. Scully, and R. Edwards, A novel technique for optical fiber pH sensing based on methylene blue adsorption*, J. Lightwave Technol.* 13 (1995) 1407-1414.

27. Ganesh, A.B. and T. Radhakrishnan, Fiber-optic pH sensor*, Fiber Integrated. Opt.* 25 (2006) 403-409.

28. Li, E., X. Wang, and C. Zhang, Fiber-optic temperature sensor based on interference of selective higher-order modes*, Appl. Phys. Lett.* 89 (2006) 091119-091119-3.

29. Ostrow, J., *Bile Pigments and Jaundice: Molecular, Metabolic and Medical, MD Aspects*. 1986, Marcel Dekker Inc, New York.

30. Maisels, M.J. and A.F. McDonagh, Phototherapy for Neonatal Jaundice*, N. Engl. J. Med* 358 (2008) 920-928.

31. Cremer, R., P. Perryman, and D. Richards, Influence of light on the hyperbilirubinaemia of infants*, Lancet* 271 (1958) 1094-1097.

32. Lightner, D.A. and A.F. McDonagh, Molecular mechanisms of phototherapy for neonatal jaundice*, Acc. Chem. Res.* 17 (1984) 417-424.

33. Lamola, A.A., W.E. Blumberg, R. McClead, and A. Fanaroff, Photoisomerized bilirubin in blood from infants receiving phototherapy*, Proc. Natl. Acad. Sci.* 78 (1981) 1882-1886.

34. Braslavsky, S.E., A.R. Holzwarth, and K. Schaffner, Solution conformations, photophysics, and photochemistry of bile pigments; bilirubin and biliverdin, dimethyl esters and related linear tetrapyrroles*, Angew. Chem. Int. Ed.* 22 (1983) 656-674.

35. Sebbe, P.F., A.G.J.B. Villaverde, R.A. Nicolau, A.M. Barbosa, and N. Veissid, Characterization of an optical device with an array of blue light emitting diodes leds for treatment of neonatal jaundice*, AIP Conf. Proc.* 992 (2008) 606-610.

36. Polley, N., S. Singh, A. Giri, and S.K. Pal, Evanescent field: A potential light-tool for theranostics application*, Rev. Sci. Instrum.* 85 (2014) 033108.

37. Blauer, G. and T.E. King, Interactions of bilirubin with bovine serum albumin in aqueous solution*, J. Biol. Chem.* 245 (1970) 372-381.

38. Kurtin, W.E., Spectroscopy and photochemistry of bilirubin photoproducts. I. Methylvinylmaleimide*, Photochem. Photobiol.* 27 (1978) 503-509.

39. Sticklen, M.B., Plant genetic engineering for biofuel production: towards affordable cellulosic ethanol*, Nat. Rev. Genet.* 9 (2008) 433-443.

40. Medronho, B., A. Romano, M. Miguel, L. Stigsson, and B. Lindman, Rationalizing cellulose (in) solubility: Reviewing basic physicochemical aspects and role of hydrophobic interactions*, Cellulose* 19 (2012) 581-587.

41. Vatankhah, E., M.P. Prabhakaran, G. Jin, L.G. Mobarakeh, and S. Ramakrishna, Development of nanofibrous cellulose acetate/gelatin skin substitutes for variety wound treatment applications*, J. Biomater. Appl.* 28 (2014) 909-921.

Chapter 7

Detection of a Picosecond-resolved Dipole-dipole Interaction on Optical Fiber Surface for Potential Application in Sensing at Molecular Level

7.1. Introduction

Immediately after development of the quantitative theory for the resonance energy transfer by Theodor Förster in 1948, the state of Förster resonance energy transfer (FRET) became popular in biophysical research [1]. However, the use of FRET in fiber optics is evident in 1990s [2, 3], which is relatively late given the first development of the field in the mid-20th century [4]. FRET is a photophysical process where the excited state energy from a donor is transferred 'non-radiatively' to an acceptor molecule at close distance via dipole-dipole coupling. Till date the reports on the FRET based fiber sensors rely on the fluorescence quenching of the donor (probe) molecule in sensitized fiber [5-9]. However, fluorescence quenching of a donor molecule may result from the radiative energy transfer, which is just a re-absorption of the donor radiation by the acceptor in the medium due to spectral overlap between donor emission and acceptor absorption spectra. The potential danger of concluding resonance type energy transfer has been discussed in a recent literature [10]. The study shows [10] that faster excited state lifetime in the presence of an acceptor is the only way to conclude a resonance type energy transfer in a donor-acceptor system. This issue is addressed pictorially in Figure 7.1. Although from the definition of the resonance type energy transfer, the importance of excited state lifetime of donor molecule is clearly evident, no report on the use of lifetime in the FRET based fiber optic sensor is surprisingly evident in contemporary literature.

In a typical development of FRET based fiber optic biosensors for the biomedical diagnostics, a specific fluorophore (energy donor) conjugated antibody is immobilized to the distal end of an optical fiber. Another fluorophore (energy acceptor) in the antibody specific antigen in the medium under test quenches the emission of donor fluorophore. The proximal

end of the fiber is connected to a fluorometer in order to monitor the quenching as FRET signal concluding the presence of the specific antigen in the medium [6]. Such sensing scheme has been successfully used for the detection of pathogenic microbes [8] in ground pork samples. In all the sensors, evanescent field of the propagating light is used to deliver excitation energy to the donor molecules and eventually collect FRET signal from the distal sensitized end to the proximal end of the fiber. Sensible use of the evanescent field of an optical fiber for the simultaneous use of potential diagnostics and therapy (theranostics) of hyperbilirubinemia is recently reported from our group [11]. In the above mentioned applications, the time resolved fluorescence properties remain unexplored. However, validation of FRET and consequent use of the formulism for the estimation of the molecular distance between the donor and the acceptor demands a careful analysis of the excited state lifetime of the fluorophores with picosecond resolution [12]. In some of the recent studies, the usefulness of the picosecond resolved fluorescence measurement for the FRET based sensor (not using an optical fiber) has been recognized [13-15]. In a report using quantum

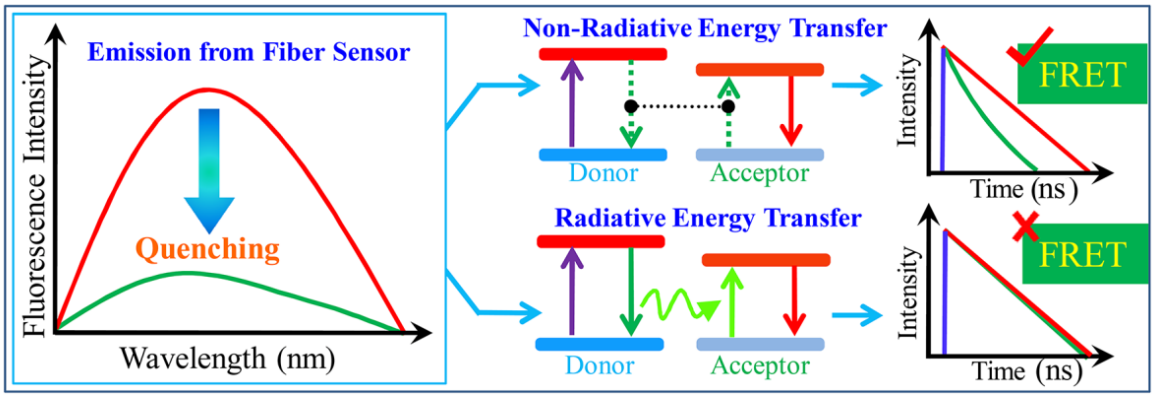

Figure 7.1. *Two mechanisms of fluorescence quenching namely non-radiative and radiative are shown. In the non-radiative-type (resonance) fluorescence quenching dipolar interaction between energy donor and acceptor is unavoidable due to their close proximity. Quenching of fluorescence transient of the donor in the presence of acceptor should be evident. On the other hand radiative type fluorescence quenching could be mere re-absorption of energy donor emission by the acceptor molecule due to significant donor-acceptor spectral overlap. Neither close-proximity of the donor-acceptor pair nor quenching of the fluorescence transient of the donor is required.*

dots linked to DNA have been used in an ultrasensitive nanosensor based on fluorescence resonance energy transfer (FRET) capable of detecting low concentrations of DNA in a separation-free format [13]. Another study demonstrated that fluorescence lifetime data accurately be recorded via miniature fiber endoscopes that can discriminate dichotomous

labeled structures and cells [14]. In a recent study, FRET between donor nanoparticle and acceptor quantum dots is utilized in protein quantification [15].

In the present study, we have sensitized the distal end of a silicon fiber tip by covalently tethering the well known biological probe dansyl [16]. A self developed optical setup containing two off-axis parabolic mirrors and a dichroic mirror has been used to launch light from a picosecond laser to the proximal end of the fiber tip and to collect fluorescence signal for a 16-channel PMT array connected to picosecond resolved time correlated single photon counting (TCSPC) modules. Ethidium labeled genomic DNA (from calf thymus) [17-19] is used as a model analyte for the sensing application. The absorption spectrum of the well known DNA-label ethidium has strong spectral overlap with the emission spectrum of the probe dansyl at the fiber tip, which is the prerequisite of efficient resonance energy transfer from dansyl (donor) to ethidium (acceptor) in the test DNA. We have observed that the fiber itself is having an intrinsic emission at the wavelength around 460 nm, which is close to the emission (505 nm) of the probe dansyl at the fiber tip. Our picosecond resolved measurement strategy allows us to distinguish the background emission from the fluorescence signal of the probe dansyl. A significant shortening of the donor fluorescence lifetime in presence of ethidium labeled DNA at the sensor tip not only validates the resonance type sensing mechanism (FRET), also estimates the distance between the donor at the fiber surface to the test DNA using dipole-dipole coupling formulism. The advantage of using dansyl as a probe is also evident in our use of the sensitized fiber tip as remote sensor of polarity (dielectric constant) of a liquid mixture of two miscible solvents (water and 1,4-dioxane). A molecular pathway in the surface desorption of DNA from the fiber tip in saline solution is evident during our studies on the reusability of the sensor tip for the repetitive measurement. On the other hand synthetic dyes like Methylene Blue (MB) are being extensively used in various industries such as textile, paper and plastics with harmful effect in the environment [20]. The released aromatic amines from MB (benzidine, methylene etc) are found to be potential carcinogen. Extensive research has been devoted to remove MB from waste water (adsorption, filtration or chemical reaction) before dumping. However, monitoring the concentration of MB present in the waste water before or after the treatment is relatively less emphasized. The advantageous aspect of our detection mechanism has been further proven by detecting methyl blue (MB) in water after attachment of the DNA-EtBr in the fiber tip.

7.2. Results and Discussion

7.2.1. Ultrafast FRET at Fiber Tips: Potential Applications in Sensitive Remote Sensing of Molecular Interaction [21]: The instrumentation with TCSPC is designed to monitor the change in the excited state lifetime of the dansyl probe due to Förster resonance energy transfer (FRET) from the sensitized fiber tip. The schematic representation of the setup is shown in Figure 7.2. A picosecond (pulse width of 70 ps) laser beam passes through L_1 (an aspheric condenser lens of 30 mm focal length), M_1 (a dichroic mirror, which reflects <400 nm and passes wavelengths in the visible light) and a pair of off-axis parabolic mirrors (M_2 and M_3 of focal lengths 132 mm and 25 mm, respectively), and eventually enters into the proximal end of the sensitized fiber. For the collection of the fluorescence signal from the sensitized fiber tip, the fiber bundle (F-100) is placed at the focal point of M_2, which carries the signal to the polychromator-PMT array and finally to the TCSPC module. The 16 channel PMT was used to measure simultaneous time resolved decays corresponding to 16 different wavelengths. From maximum counts of the channels, in a given acquisition time, the steady state emission spectrum of the probe dansyl (fluorescence intensity versus wavelength) can be generated. All the experiments were performed in dark condition to avoid any ambient light interference. The schematic of the sensitized fiber tip and the sensing strategy is shown in the inset of Figure 7.2.

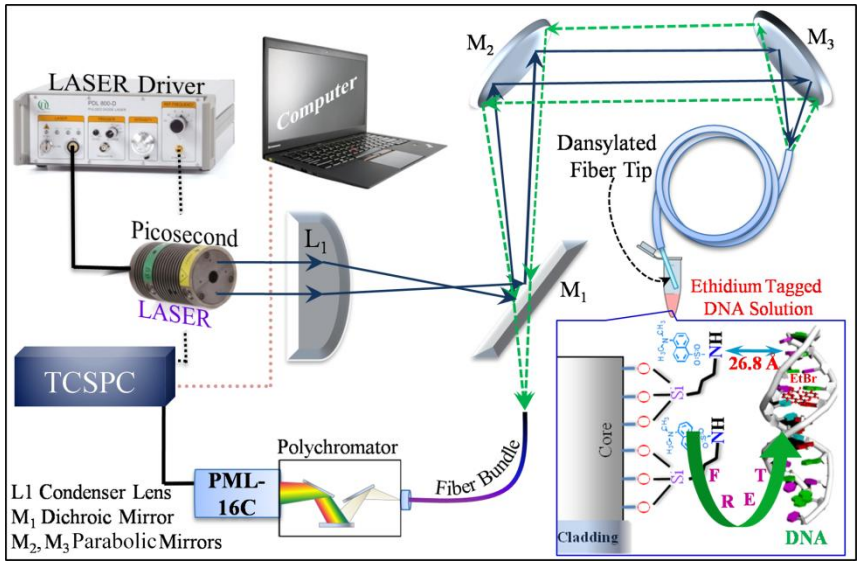

Figure 7.2. *Schematic ray diagram of the ultrafast FRET instrumentation used in the study. (Inset) The FRET mechanism between the sensitized fiber tip and ethidium (EtBr) labeled DNA is represented, where the Förster distance is found to be 26.8 Å.*

We have observed that bare fiber without sensitization shows a fluorescence signal (peak around 460 nm) under 375 nm excitation, which is close to the emission from the probe dansyl (peak at 505 nm) as shown in the inset of Figure 7.3a. Coupling of laser beam and eventually collecting signal from fiber without sensitization also reveal fluorescence transient. For the optimization of the fiber length in our application, first we have used a 30 cm long optical fiber with one end sensitized with dansyl. The sensitized fiber reveals two peaks in the

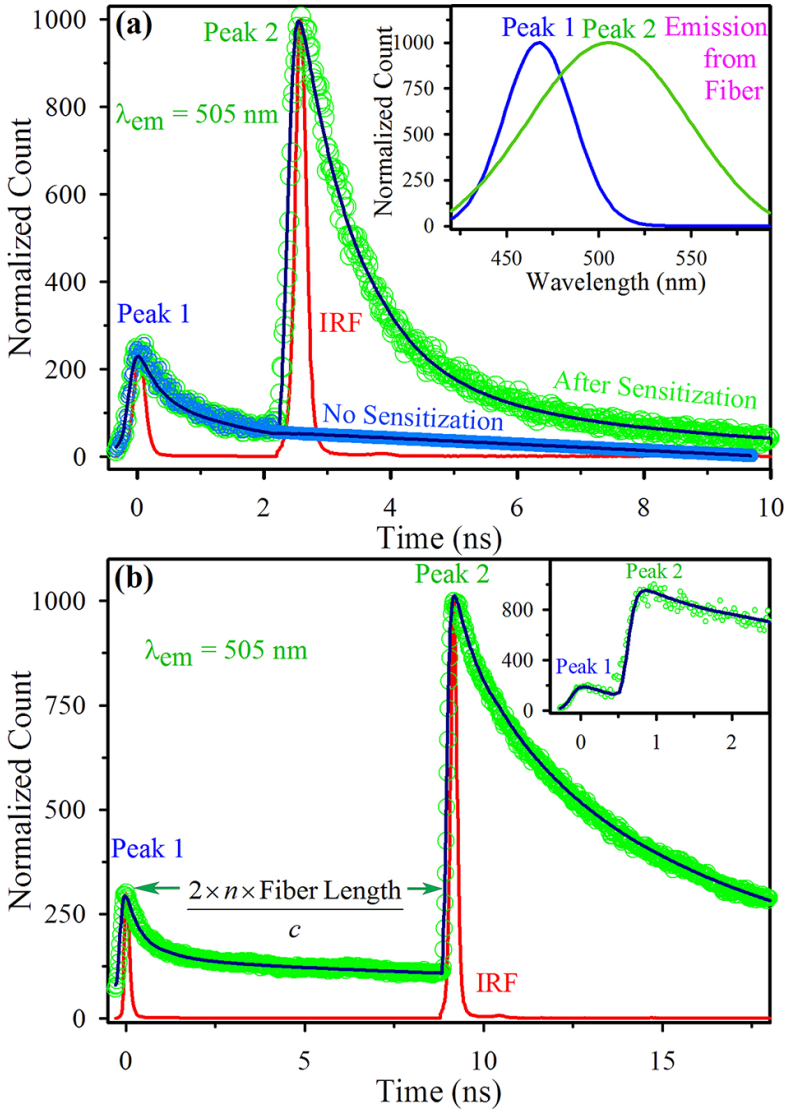

Figure 7.3. *Optimization of fiber length for sensor application: (a) The fluorescence decay from the fiber tip (fiber length 30 cm) before (blue line) and after dansylation (green line). For both the cases the first decay (peak 1) is present, however, the second decay (peak 2) is present only for the dansylated fiber. (Inset) Steady state fluorescence spectra of the fiber with (peak at 505 nm) and without (peak at 460 nm) dansylation are shown in the inset of the Figure. (b) The fluorescence transient of the 1 meter dansylated fiber, where the distance travelled by the light is approximately twice the length of the fiber. (Inset) fluorescence decay from the fiber tip (fiber length 11 cm). Inter-peak time interval decrease with the decrease in fiber length. Justification of using 1 meter long fiber for any practical sensing application is clearly evident (see text).*

fluorescence transient measurement (Figure 7.3a). Our control experiment with the fiber of similar length without sensitization shows only one peak (peak 1) with lifetime of 2.65 ns, revealing the contribution of the background emission from the bare fiber. 2.65 ns lifetime value is found to be consistent with that of the clad only, which is made of technology enhanced clad silica (TECS) polymer (details of the spectroscopic properties are not available from the vendor) upon UV excitation (data not shown). Upon sensitization of the fiber tip with dansyl, we have observed two peaks in the time resolved studies as shown in Figure 7.3a. While numerical fitting of peak 1 reveals time constant of 2.65 ns, peak 2 shows a lifetime of 3.83 ns (Table 7.1). The lifetime of peak 2 is also found to be consistent with that of the fully dansylated short fiber, essentially confirming the signal from the fiber tip. In order to further confirm the origin of the peak 2 to be from the fiber tip we have performed the time resolved studies with optical fiber of different lengths. For the fiber of 30 cm length the time interval between two peaks (peak1 and peak 2 in Figure 7.3a) is measured to be 2.58 ns, which is consistent with the estimated time interval ($t = \frac{2 \times n \times Fiber\ length}{c}$, where n and c are the refractive index of fiber core and the speed of light in vacuum, respectively) of 2.82 ns. For fibers of lengths 1 meter (Figure 7.3b) and 11 cm (Inset of Figure 7.3b) the measured time intervals of 9.17 ns and 0.82 ns respectively are in agreement with the estimated values of 9.74 ns and 0.97 ns. The observation clearly justifies the optimization of the length of the optical fiber for the sensing application and confirms peak 2 in the Figure 7.3 to be the signal from sensitized fiber tip in the distal end. For example, our studies on a fiber of length around 11 cm shows that background emission is very close to the signal from the sensitized fiber tip (Figure 7.3b inset). Here, we have used a fiber length of 1 m with one end sensitized with dansyl probe and transient signal obtained is shown in Figure 7.3b.

After the optimization of the required length of the fiber, we use the sensitized fiber tip as FRET based sensor for the detection of DNA. A strong spectral overlap between the donor emission with that of the absorption spectrum of the acceptor is the prerequisite of FRET [12] and is evident from Figure 7.4a. From Figure 7.4a, we have estimated the overlap integral of dansyl (donor) emission spectrum with that of the ethidium (acceptor) labeled DNA absorption (Equation 2.4) to be 1.36×10^{13} $M^{-1}cm^{-1}nm^4$. A significant steady state quenching of dansyl emission at the fiber tip is evident from Figure 7.4b, where the emission

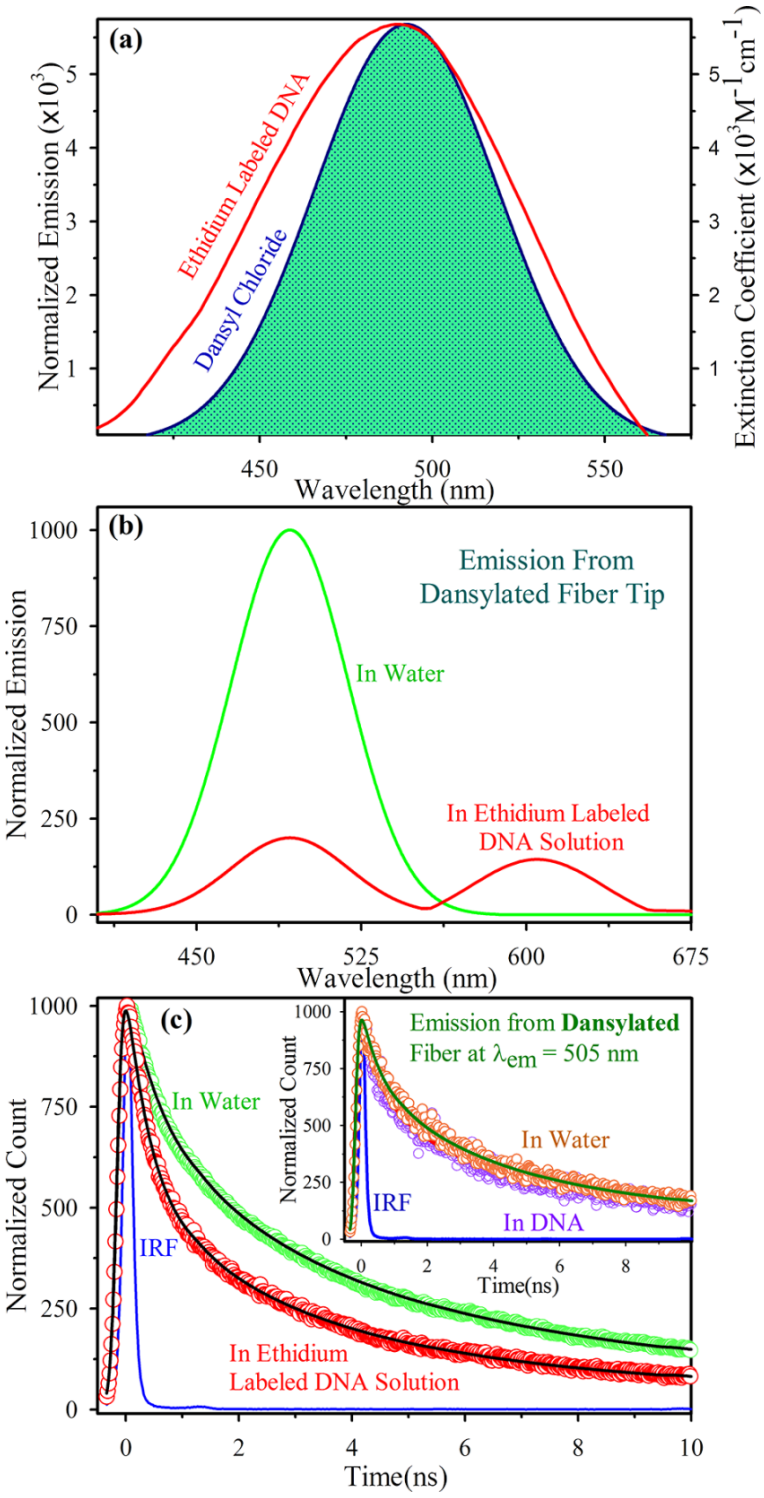

Figure 7.4. (a) *Spectral overlap between the emission spectrum of dansylated fiber tip and the absorption spectrum of ethidium tagged DNA. (b) Steady-state fluorescence quenching of dansylated fiber tip in presence of the acceptor ethidium labeled DNA. (c) Picosecond-resolved fluorescence transients of dansylated fiber tip in absence (green line) and presence (red line) of ethidium labeled DNA monitored at* λ_{em} *= 505 nm. (Inset) Picosecond-resolved fluorescence transients of dansylated fiber tip in absence (orange line) and presence (violet line) of unlabeled DNA, monitored at* λ_{em} *= 505 nm.*

peaking at 610 nm is the energy acceptor ethidium in the DNA. In a controlled experiment the magnitude of the steady state quenching of the dansyl emission upon surface adsorption of EtBr-labeled DNA the concentration of DNA in the solution could be measured. An earlier report from this group shows that the concentration of a model analyte bilirubin in an aqueous solution can be measured from the surface adsorption of the analyte on a sensing optical fiber dipped in the solution [11]. A direct evidence of the resonance type energy transfer is evident from both the steady state quenching (Figure 7.4b) and time resolved fluorescence transients of the donor dansyl at the fiber tip as shown in Figure 7.4c. The faster fluorescence decay of the dansyl in ethidium labeled DNA solution is evident from Figure 7.4c and Table 7.1, which confirms the proximity of the biomolecule to the fiber surface. Inset of Figure 7.4c shows similar fluorescence decay transients of dansylated fiber tip in absence and presence of unlabelled DNA in water, monitored at λ_{em} = 505 nm eliminating the possibility of the steady state and temporal quenching due to electron transfer [22]. On taking a quantum yield of dansylated fiber tips in absence of acceptor ethidium to be 0.7 [23], we have estimated a FRET efficiency of 49% using Equation 2.7b which is found to be reproducible within 5% error limit. The estimated Förster distance, R_0, for the FRET pair is found to be 26.4 Å. The donor–acceptor distance (r) using Equation 2.2 is calculated to be 26.8 Å, indicating a very close proximity of the DNA molecules to the fiber tip.

Monitoring the polarity in a hazardous environment including petroleum processing column is reported to be important for the quality control of the petroleum product [24]. However, the remote sensing of the polarity in the reaction chamber (column) is unavoidable for the very hazardous nature of the reaction chamber. The remote sensing ability of the sensitized fiber tip using the picosecond resolved TCSPC strategy is evident from Figure 7.5a and Table 7.1. Here, we have used a liquid mixture of two different miscible solvents 1,4-dioxane and water with different proportions. It has been reported earlier [25] that a solution of different dielectric constants can easily be prepared by mixing various proportions if 1,4-dioxane (dielectric constant = 4) and water (dielectric constant = 80). We have used the liquid mixture as model environment for the remote sensing studies. As shown in Figure 7.5a (numerical fitting is shown in Table 7.1), a distinct change in the lifetime of the probe dansyl at the fiber tip is evident with the change in dielectric constant of the liquid mixture. While

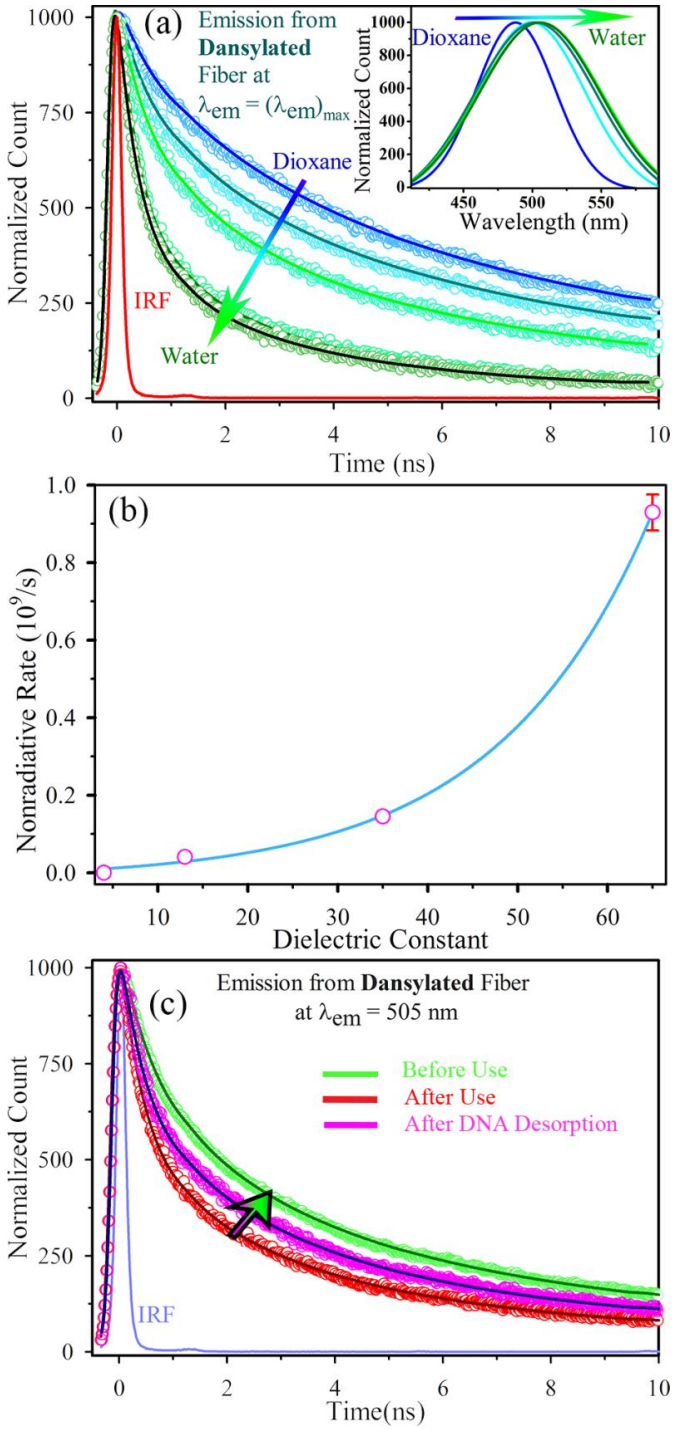

Figure 7.5. *(a) Fluorescence transients of the fiber tip in liquid mixture of water and dioxane revealing different dielectric constants of the medium. (Inset) Red shift of the steady state emission maxima of the sensitized fiber from 486 nm to 505 nm with increase in water content is represented. (b) Exponential increase of the measured non radiative rates of the dansyl probes at the fiber tip with increase in dielectric constant of the test medium. One may use the calibration (see text) for the remote sensing of an medium of unknown dielectric constant.(c) Fluorescence transients of the used (with ethidium labeled DNA) fiber tips in 1 M NaCl solution for 10 min. Surface desorption of DNA at molecular level is clear (see text).*

longer lifetime in environment with lower dielectric constant is evident from the Figure 7.5a, the inset of the Figure 7.5a shows gradual red-shifting of the steady state emission spectrum of the dansyl probe at the fiber tip with the increase in the water content of the medium (higher dielectric constant). The observation is consistent with the fact that the excited state of the probe is heavily dependent on the dielectric constant of the host medium (polarity) due to the nonradiative twisted intra-molecular charge transfer (TICT) events upon photo-excitation [16]. In Figure 7.5b we have plotted the dielectric constant of the medium with the nonradiative TICT rate (k_{nr}) estimated in the following way [22]: $k_{nr} = {}^{1}/_{\tau_s} - {}^{1}/_{\tau_{diox}}$, where τ_s is the average lifetime of the probe dansyl in any medium and τ_{diox} is that in pure dioxane. As evident in Figure 7.5b, the rate constants follow an exponential rise function with the increase in dielectric constant of the medium. The dielectric constant of the medium can be estimated by using the empirical formula: $k_{nr} = 0.016 \times e^{({}^{D}/_{15.94})}$, where D is the dielectric constant of the test medium.

In order to investigate the efficacy of the sensitized fiber tip for repetitive usage, we have investigated the surface desorption of ethidium labeled DNA from the fiber tip. The detachment of the DNA from the fiber tip is achieved by dipping the used dansylated fiber tip (sensor) in 1 M sodium chloride (NaCl) solution for 10 min [16]. DNA initially attached to the fiber tip by electrostatic interaction between the positively charged amine (NH_3^+) groups of APTES and negatively charged phosphate (PO_3^-) backbone of DNA itself. NaCl detaches the DNA molecules from the dansylated fiber surface and interestingly the average excited state lifetime of the sensor also recovered subsequently from 1.97 ns to 2.46 ns (tending towards its original value of 3.83 ns in absence of DNA), as shown in Figure 7.5c. Surface desorption of DNA from the sensor tip is evident from the observation. Involvement of multiple steps in the desorption revealing different DNA distances from the fiber surface in presence of NaCl is also clear from the studies. We have estimated that the intermediate distance of the test DNA from the surface (Equation 2.2) is 30 Å in 10 minutes, before the biomolecule goes 80-100 Å from the surface, which is beyond the scope of a FRET based sensor [12]. The exploration of such molecular details can only be achieved using picosecond resolved FRET sensors.

Table 7.1. *Numerical fitting of the fluorescence transients shown in Figures 7.3-7.6. Numbers in parenthesis indicate relative contributions of correnponding decay time constants.*

Figure	Description	τ_1 (%) (ns)	τ_2 (%) (ns)	τ_3 (%) (ns)	τ_{avg} (ns)
Figure 7.3(a)	1st Decay	0.27 (45%)	0.71 (33%)	10.42 (22%)	2.65
	2nd Decay	0.50 (36%)	2.46 (37%)	10.16 (27%)	3.83
Figure 7.4(c)	Sensitized fiber tip in water	0.50 (36%)	2.46 (37%)	10.16 (27%)	3.83
	Sensitized fiber tip in Ethidium labeled DNA	0.37 (57%)	2.10 (26%)	7.19 (17%)	1.98
	(Inset) Sensitized fiber tip in unlabeled DNA	0.50 (37%)	2.94 (38%)	13.10 (19%)	3.79
Figure 7.5(a), Sensitized fiber tip in	Dioxane	0.43 (19%)	2.55 (32%)	10.30 (49%)	5.94
	Dioxane: Water = 3:1	0.41 (30%)	2.22 (30%)	9.91 (40%)	4.75
	Dioxane: Water = 1:1	0.40 (38%)	1.91 (31%)	7.84 (31%)	3.17
	Dioxane: Water = 1:3	0.38 (73%)	2.00 (25%)	6.71 (2%)	0.91
	Water	0.32 (22%)	0.95 (6%)	3.34 (72%)	2.53
Figure 7.5(c), Sensitized fiber tip in	In 1M NaCl (saline) solution	0.38 (49%)	2.37 (31%)	7.69 (20%)	2.46
Figure 7.8(c)	Fiber tip with DNA-EtBr	1.34 (57%)	11.50 (43%)	-	5.68
	In MB solution	1.12 (50%)	5.14 (50%)	-	3.13

7.2.2. Medical Diagnosis and Remote Sensing at Fiber-Tip: Picosecond Resolved FRET Sensor [26]: Upon simplification of the earlier reported TCSPC setup [21] we were able to monitor the change in the excited state lifetime of the probe attached to the fiber tip. The schematic representation of the TCSPC setup is shown in the Figure 7.6. The PDL-80-D PicoQuant laser driver was used to drive the 375nm UV picosecond pulsed laser (LDH-P-C-375) with a repetition frequency of about 62.5 KHz. The pulsed laser beam passes through a dichroic mirror (which reflects <400 nm and passes wavelengths in the visible range) and a off-axis parabolic mirror (focal length 25 mm), and eventually enters into the proximal end of the sensitized fiber. Finally the fluorescence signal was collected by the fiber bundle (F-100),

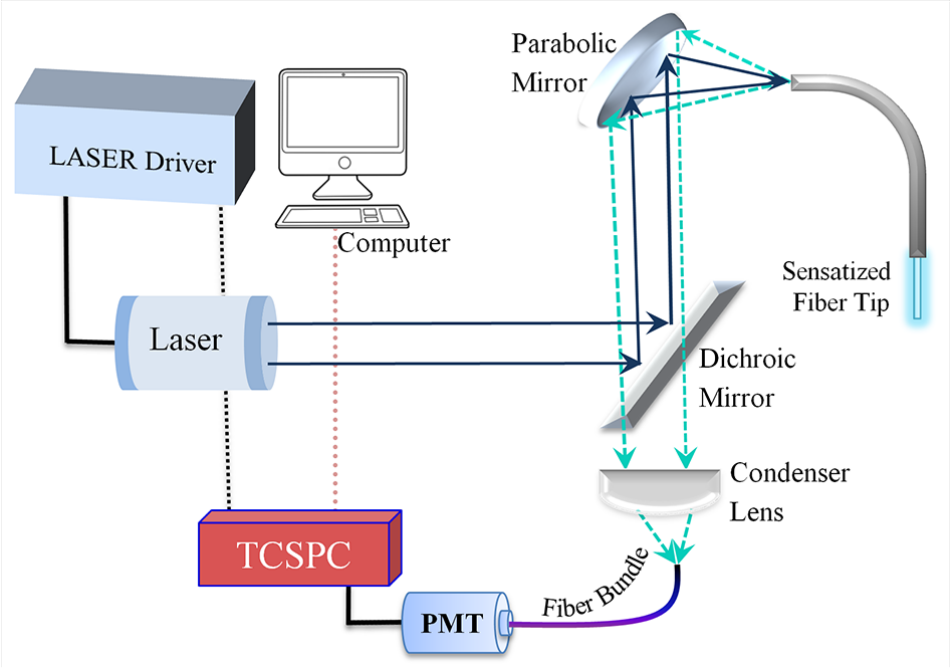

Figure 7.6. *Experimental setup: Schematic diagram of the instrumentation based on time resolved based Förster resonance energy transfer (FRET) sensor.*

placed at the focal point of a condenser lens. Upon collection of the fluorescence signal by the 16 channel PMT (PML-16-1-C), 16 decays corresponding to 16 different wavelengths ware generated by using the Simple Tau-130EM module consisting of two special purpose data processing cards SPC-130EM and DCC-100. The processed electronic signal is fed to the Lenovo ThinkPad laptop-PC with pre installed SPCM64 software through Express Card 54. The steady state emission spectrum has been generated using the histogram plot, corresponding to maximum intensity of each channel (wavelength) (inset Figure 7.7). All the experiments are performed in dark room to avoid any ambient light exposure.

The decay transients from the dansylated fiber (1 m) corresponding to 16 different wavelengths are represented in Figure 7.7. It is evident that the decay pattern consists of two decay peaks. The detail investigation of such observation is already reported [21]. The histogram plot of the intensity maximas (inset Figure 7.7) revealed two different emission peaks at 460 nm and 505 nm for peak 1 and peak 2 respectively. At λ_{em}= 505 nm the decay of peak 1 has an average lifetime of 2.68 ns, where as peak 2 was observed with an average excited state life time of 3.84 ns. Additionally, the path traveled (~ 2m) by light during the time difference (10 ns) between peak 1 and peak 2 is twice the length of the fiber (1 m), which confirms the origin of the second decay (peak 2) is from the sensitized tip.

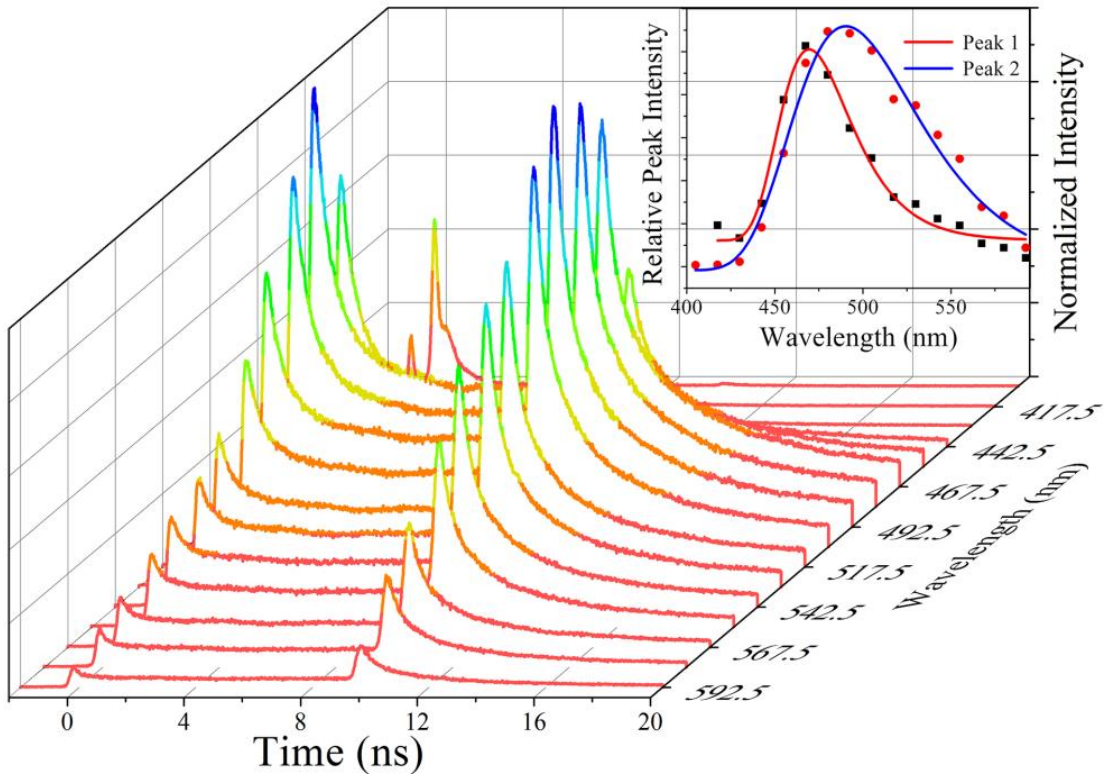

Figure 7.7. *Characterization of the fiber sensor: 16 channel decay (400nm -600 nm) from the sensor (Fiber length 1 m) with dansylated fiber tip. (Inset) The histogram plot of the 16 channel decay maxima from both the decays with emission peak at 460 nm and 505 nm respectively.*

After validating the FRET in optical fiber tip by following the previously mentioned instrumental and experimental techniques, the application of the sensor was extended to detection of methylene blue solution in aqueous environment. DNA-EtBr was attached to the fiber tip by dipping the APTES modified tip in the solution. A strong spectral overall between the emission of donor (DNA-EtBr) with that of the absorption spectrum of the acceptor (MB) is evident from Figure 7.8a. From the Figure 7.8a the overlap integral of DNA-EtBr (donor) emission spectrum with that of the MB (acceptor) absorption (Equation 2.4) was estimated to be 5.2×10^{15} $M^{-1}cm^{-1}nm^4$. A significant steady state quenching of DNA-EtBr emission at 600 nm at the fiber tip is evident from Figure 7.6b. A direct evidence of the resonance type energy transfer is obtained from both the steady state quenching (Figure 7.8b) and time resolved fluorescence transients of the donor DNA-EtBr at the fiber tip as shown in Figure 7.8c. The faster fluorescence decay of the DNA-EtBr in MB solution is evident from the Figure 7.8c and corresponding bi-exponential decay flitting has been represented in Table 7.1, which confirms proximity of the synthetic dye at the fiber surface. On taking quantum

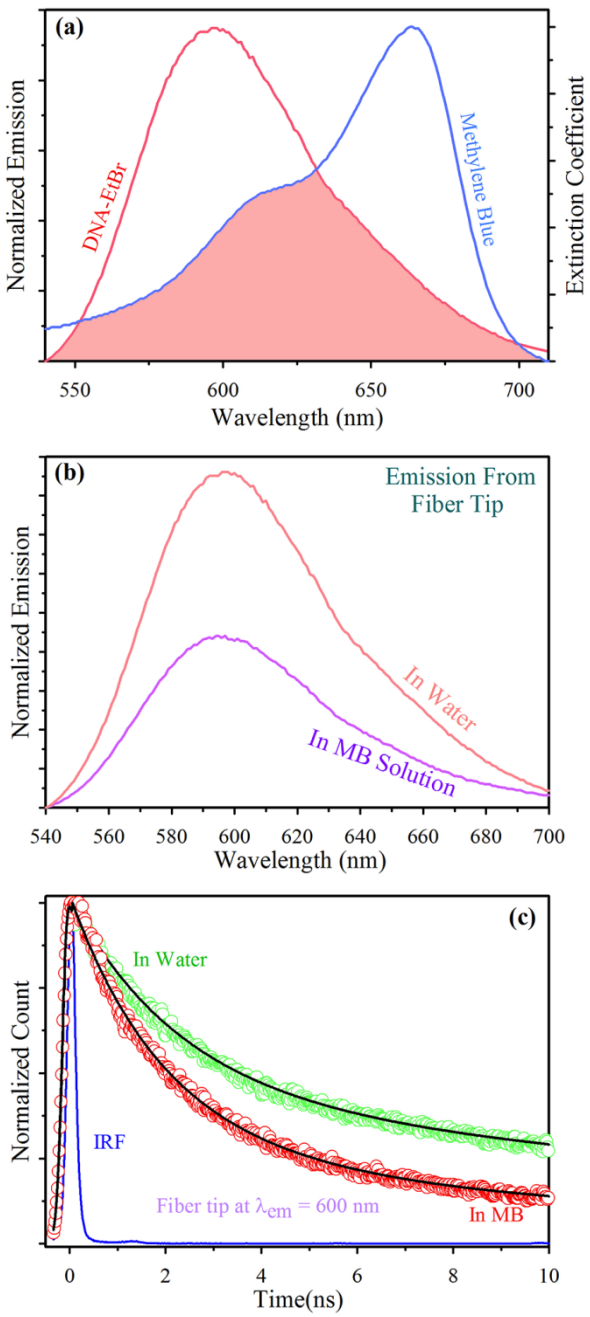

Figure 7.8. *Methylene blue (MB) sensing: (a) Spectral overlap between emission spectrum of EtBr-labeled DNA attached fiber tip and the absorption spectrum MB. (b) Steady-state fluorescence quenching of EtBr-labeled DNA attached fiber tip in presence of the acceptor MB (c) Picosecond-resolved PL transients of EtBr-labeled DNA attached fiber tip in presence and absence of MB monitored at* λ_{em} *= 600 nm.*

yield of DNA-EtBr in absence of acceptor MB to be 0.2, we have estimated a FRET efficiency of 44% using Equation 2.7b. The estimated Förster distance, R_0, for the FRET pair is found to be 49.16 Å. The donor–acceptor distance (r) using Equation 2.2 is calculated to be 51.14 Å.

7.3. Conclusion

In conclusion, we have validated resonance type energy transfer scheme in a model FRET based fiber optic sensor for the first time using picosecond resolved time correlated single photon counting (TCSPC) technique. The ultrafast time domain measurement strategy also avoids possible interference from the background emission of the bare fiber. Confirmation of the FRET mechanism allows us to use dipole-dipole coupling formulism for the estimation of proximity of ethidium labeled DNA with respect to the sensitized fiber tip in molecular resolution. The efficacy of the designed fiber sensor for the detection of various dielectric constants and the presence of MB, a model aqueous pollutant in water has also been established. The reusability of the sensor tip for repetitive application is confirmed. Stepwise surface desorption of DNA from the fiber tip is also evident from our studies. In future, our study is expected to find the relevance in the sensitive FRET based optical sensor development.

References

1. Förster, T., Zwischenmolekulare energiewanderung und fluoreszenz*, Ann. Phys. (Berlin)* 437 (1948) 55-75.
2. Meadows, D.L. and J.S. Schultz, Design, manufacture and characterization of an optical fiber glucose affinity sensor based on an homogeneous fluorescence energy transfer assay system*, Anal. Chim. Acta* 280 (1993) 21-30.
3. Ballerstadt, R. and J.S. Schultz, A fluorescence affinity hollow fiber sensor for continuous transdermal glucose monitoring*, Anal. Chem.* 72 (2000) 4185-4192.
4. Hecht, J., *City of light: the story of fiber optics*. 1999, Oxford, New York: Oxford University Press.
5. Lichlyter, D.J., S.A. Grant, and O. Soykan, Development of a novel FRET immunosensor technique*, Biosens. Bioelectron.* 19 (2003) 219-26.
6. Pierce, M. and S. Grant, Development of a FRET based fiber-optic biosensor for early detection of myocardial infarction*, Conf. Proc. IEEE Eng. Med. Biol. Soc.* 3 (2004) 2098-101.
7. Grant, S.A., M.E. Pierce, D.J. Lichlyter, and D.A. Grant, Effects of immobilization on a FRET immunosensor for the detection of myocardial infarction*, Anal. Bioanal. Chem.* 381 (2005) 1012-1018.
8. Ko, S.H. and S.A. Grant, A novel FRET-based optical fiber biosensor for rapid detection of Salmonella typhimurium*, Biosens. Bioelectron.* 21 (2006) 1283-1290.
9. Liao, K.-C., T. Hogen-Esch, F.J. Richmond, L. Marcu, W. Clifton, and G.E. Loeb, Percutaneous fiber-optic sensor for chronic glucose monitoring in vivo*, Biosens. Bioelectron.* 23 (2008) 1458-1465.
10. Majumder, P., R. Sarkar, A.K. Shaw, A. Chakraborty, and S.K. Pal, Ultrafast dynamics in a nanocage of enzymes: Solvation and fluorescence resonance energy transfer in reverse micelles*, J. Colloid Interface Sci.* 290 (2005) 462-474.
11. Polley, N., S. Singh, A. Giri, and S.K. Pal, Evanescent field: A potential light-tool for theranostics application*, Rev. Sci. Instrum.* 85 (2014) 033108.
12. Lakowicz, J.R., *Principles of fluorescence spectroscopy*. 3rd ed. 1999, New York: Kluwer Academic/Plenum.

13. Zhang, C.-Y., H.-C. Yeh, M.T. Kuroki, and T.-H. Wang, Single-quantum-dot-based DNA nanosensor, *Nat. Mater.* 4 (2005) 826-831.
14. Fruhwirth, G.O., S. Ameer-Beg, R. Cook, T. Watson, T. Ng, and F. Festy, Fluorescence lifetime endoscopy using TCSPC for the measurement of FRET in live cells, *Opt. Express* 18 (2010) 11148-11158.
15. Härmä, H., S. Pihlasalo, P.J. Cywinski, P. Mikkonen, T. Hammann, H.-G. Löhmannsröben, and P. Hänninen, Protein quantification using resonance energy transfer between donor nanoparticles and acceptor quantum dots, *Anal. Chem.* 85 (2013) 2921-2926.
16. Zhong, D., S.K. Pal, and A.H. Zewail, Femtosecond studies of protein–DNA binding and dynamics: Histone 1, *ChemPhysChem* 2 (2001) 219-227.
17. Banerjee, D. and S.K. Pal, Simultaneous binding of minor groove binder and intercalator to dodecamer DNA: Importance of relative orientation of donor and acceptor in fret, *J. Phys. Chem. B* 111 (2007) 5047-5052.
18. Sarkar, R. and S.K. Pal, Interaction of hoechst 33258 and ethidium with histone1−DNA condensates, *Biomacromolecules* 8 (2007) 3332-3339.
19. Choudhury, S., S. Batabyal, T. Mondol, D. Sao, P. Lemmens, and S.K. Pal, Ultrafast dynamics of solvation and charge transfer in a DNA-based biomaterial, *Chem. Asian J.* 9 (2014) 1395-1402.
20. Ghosh, D. and K.G. Bhattacharyya, Adsorption of methylene blue on kaolinite, *Appl. Clay Sci.* 20 (2002) 295-300.
21. Polley, N., S. Singh, A. Giri, P.K. Mondal, P. Lemmens, and S.K. Pal, Ultrafast FRET at fiber tips: Potential applications in sensitive remote sensing of molecular interaction, *Sens. Actuator B-Chem.* 210 (2015) 381-388.
22. Mondol, T., S. Batabyal, and S.K. Pal, Ultrafast electron transfer in the recognition of different DNA sequences by a DNA-binding protein with different dynamical conformations, *J. Biomol. Struct. Dyn.* 30 (2012) 362-370.
23. Stryer, L. and R.P. Haugland, Energy transfer: a spectroscopic ruler, *Proc. Natl. Acad. Sci. U.S.A.* 58 (1967) 719-725.
24. Bruning, I., Crude-oil polarity measures quality, predicts behavior, *Oil Gas J.* 89 (1991) 38-40.

25. Åkerlöf, G. and O.A. Short, The dielectric constant of dioxane—water mixtures between 0 and 80°*, J. Am. Chem. Soc.* 58 (1936) 1241-1243.
26. Polley, N. and S.K. Pal. *Medical diagnosis and remote sensing at fiber-tip: Picosecond resolved FRET sensor.* in *SPIE BiOS*. 2016. San Francisco, California, United States: SPIE.

Chapter 8

Development of a DNA-based Material for Potential Fiber Optic Sensing of Heavy Metals in Biomedically Relevant Environments

8.1. Introduction

DNA, 'the molecule of life' has been used extensively for the development of biomaterials in the last decade [1]. Applications of the biomaterial covers fully functional equivalents of the majority of electronic and photonics elements like light emitting diodes (LED), photovoltaic cells, transistors, memory chips, waveguides, laser, holographic gratings, elements of non-linear optics etc [2]. Among the different types of DNA based biomaterials the water insoluble DNA–lipid (surfactant) complex, produced upon reaction between DNA and a cationic surfactant [3] (such as, cetyltrimethyl ammonium chloride: CTMA or cetyltrimethyl ammonium bromide: CTAB) is most popular. The optical properties including high transmission (~100% at λ =300–1600 nm) [3], low optical loss (0.05 dB/cm at λ =800 nm) and favorable index of refraction (1.535 at λ = 350 nm) [4] of the thin film motivates many optoelectronic applications of this material [4, 5]. In recent years considerable efforts have been devoted to utilize the materials as a sensor. Such as, dual detection of ultraviolet and visible light [6], chemical sensing using thin films as wave guides [7], metal-biopolymer-metal photodiode for light sensing [8]. On the other hand, optical fiber sensors (OFS) are popular since 1987 [9]. In a few recent reviews, the development of Fiber-Optic Chemical Sensors (FOCS) and Biosensors (FOBS) has been summarized [10-13]. Sensing by FOCS and FOBS includes temperature, humidity, different gases (oxygen, hydrogen, nitrogen, ammonia, carbon dioxide etc.), glucose, salinity and others [14, 15]. However, reports on elemental analysis like heavy metal ions dissolved in water is limited in the contemporary literature. There are few reports on potential OFS tools for the detection of mercury [16-20], with limited portability, versatility and cost-effectiveness. Though there are several reports on the solution based efficient mercury sensors [21-24], we have restricted our study in the development of in situ optical fiber based detection strategies. In the present work, we have used a DNA based thin

film on the tips of optical fibers for specific sensing of mercury ions (Hg^{2+}) in dissolved water with 9 nM (~1.8 ppb) detection limit. The nano surface energy transfer (NSET) between 4', 6-diamidino-2-phenylindole (DAPI), an efficient DNA minor-groove binding luminescent dye and silver-nanoparticle (Ag-NPs) in the thin film plays the key role in the nanomolar specific detection of Hg^{2+} in aqueous environments. Since, no external processing (sample collection, preparation, handling and measurement) is required, OFS based mercury sensor is highly efficient for field measurements in natural waters in contrast to the kits based *ex situ* measurement with standard field portable equipment. Additionally, in the kits based system the presence of an expert is required due to its very precise sample preparation process (which is the main source of erroneous results). Whereas, OFS based system can be handled by any non expert with little or no knowledge of instrument handling.

DNA, the polymeric molecule with two intertwined spirals of sugar and phosphate molecules linked by hydrogen-bonded base pairs is shown to be useful in developing novel nanostructured materials [25]. Structural properties of biopolymers including DNA often have unusual properties that are not easily replicated using conventional organic or inorganic materials [1, 2]. Moreover, they are abundant in nature and can easily be degraded without

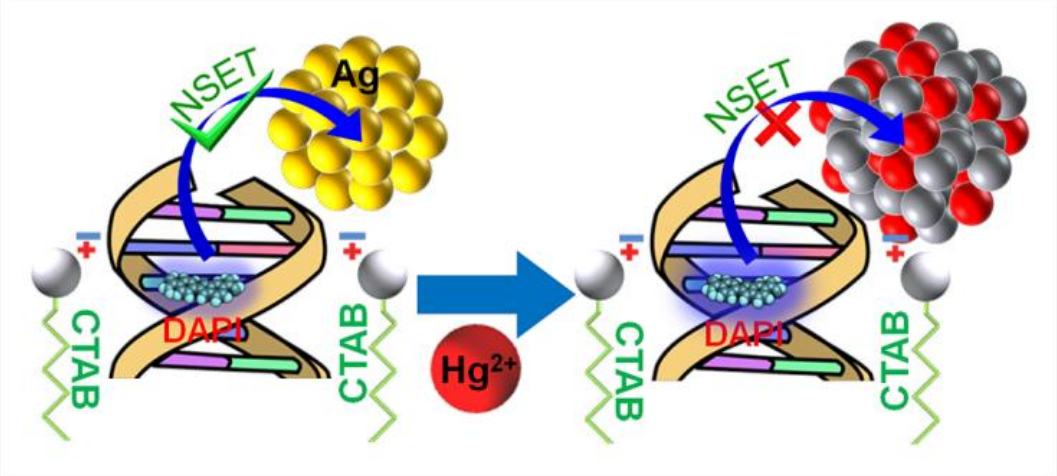

Scheme 8.1. *Schematic representation of the nano surface energy transfer (NSET) between DNA-DAPI and silver nanoparticles (Ag-NPs) and De-NSET upon interaction with mercury (Hg^{2+}) due to amalgamation of Ag-NPs with Hg^{2+}.*

causing any harm to the environment. In our study, we have used the salmon sperm DNA which is a waste product of fish-processing industry. The DNA is highly soluble in water but forms complex polymers upon interaction with cationic surfactants. The complex is insoluble

in water but soluble in alcohol [26], which is advantageous not only in terms of casting DNA thin-films over any surface but also ideal for sensing analytes in water. We have utilized the exceptional affinity of DNA towards different dyes to insert DAPI [27] into the DNA (DNA-DAPI). Furthermore using DNA for templating inorganic nanostructures has been frequently reported in recent years [28-30]. We have used DNA to impregnate silver nanoparticles (Ag-NPs) during the complexation reaction with surfactant CTAB. The lyophilized powder of DNA-DAPI-CTAB-Ag-NPs complex is dissolved in ethanol. Upon characterization of the thin film by optical spectroscopy and imaging, we have dip-coated a chemically etched fiber tip for sensing mercury (Hg^{2+}) in water. The regenerative use of the fiber tip can be achieved by removing the coating using ethanol followed by further dip-coating of the tip. The phenomenon of nano surface energy transfer (NSET) in the bio-material of DNA-DAPI with Ag-NPs reduces the emission of DAPI significantly (Scheme 8.1). Upon interaction of Ag-NPs in the fiber tip with the Hg^{2+} the Ag-NPs in the film undergoes an amalgamation reaction with Hg^{2+} and eventually lose the surface plasmon resonance (SPR) (Scheme 8.1). We have shown that the decrease in SPR, at the fiber tip has strong dependency on the Hg^{2+} concentration in the test water. On the other hand, due to the absence of the acceptor, SPR of the Ag-NPs, the emission of DAPI in the film is restored.

8.2. Results and Discussion

8.2.1. DNA Biomaterial Based Fiber Optic Sensor: Characterization and Application for Monitoring in situ Mercury Pollution [31]: Figure 8.1a presents a TEM image of Ag-NPs impregnated bio-films. It is found that Ag-NPs are spherical in shape with an average diameter of 19.45 nm, which is slightly lager compare to earlier results of the followed synthesis procedure [32]. A reason for that could be an interaction of the citrate capped Ag-NPs with CTAB during the preparation of the bio-films [33]. However, no change in the particle size distribution (lower inset of the Figure 8.1a) is observed even after few months from the synthesis of the bio-film material. The HRTEM image (Upper inset Figure 8.1a) has provided us further insight into the microstructure and crystallinity of the Ag-NPs in the bio-films. The high crystalline nature of the Ag-NPs with lattice spacing of 0.23 nm corresponds to (111) planes of silver, which further corroborates the (111) planes as dominant faces of the silver spheres. The SEM image of the bio-film upon casting on a silicon wafer is shown in Figure 8.1b. The spherical Ag-NPs with an average diameter of 17.45 nm are observed on the

surface of the film. The particle size distribution is represented in the inset of Figure 8.1b. The apparent decrease in diameter of Ag-NPs compare to the TEM measurement

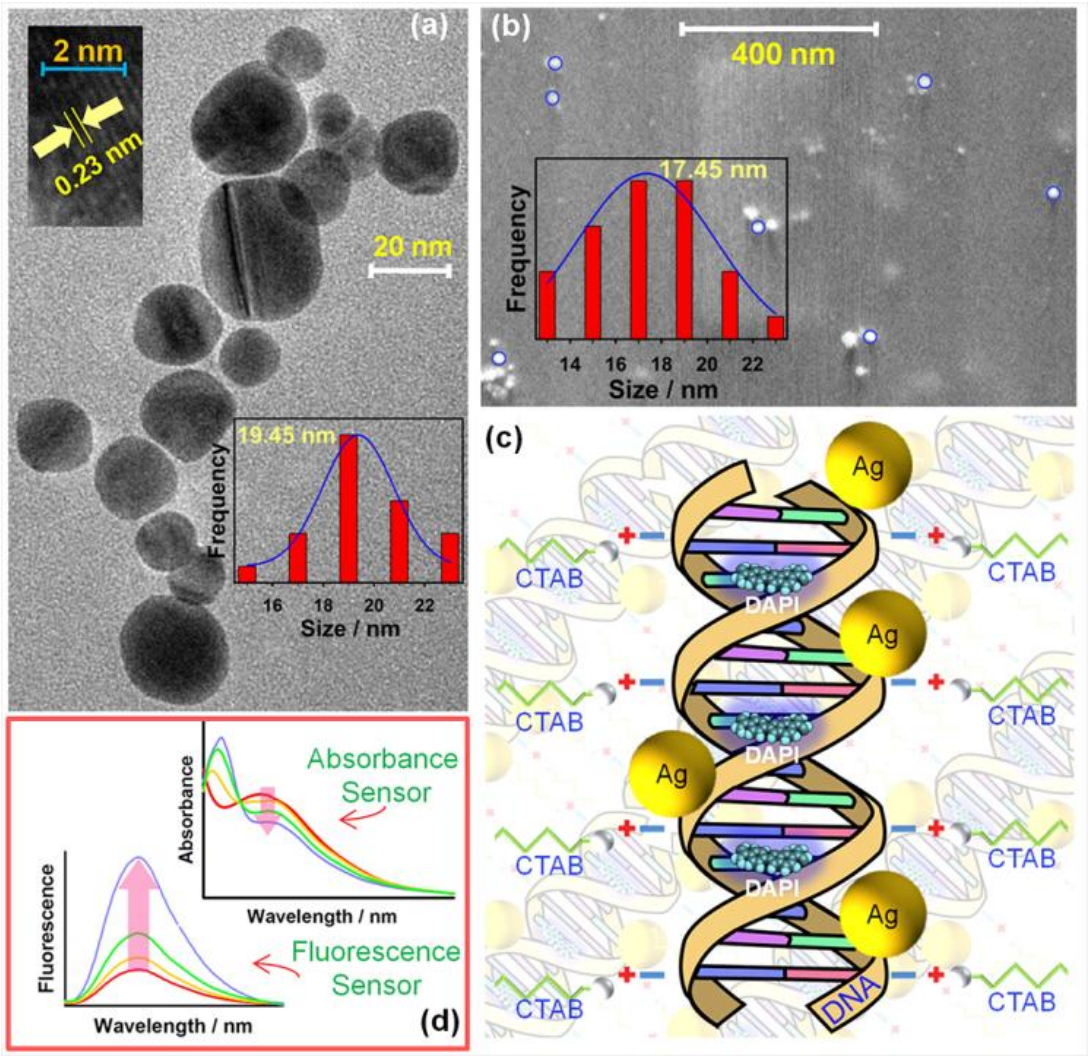

Figure 8.1. *(a) TEM image of Ag-NPs impregnated DNA-DAPI bio-film. (a-upper inset) Lattice fringes in the corresponding HRTEM image indicating high crystalline nature of the Ag-NPs. (a-lower inset) Size distribution of Ag-NPs in the bio-film. (b) SEM image of Ag-NPs impregnated DNA-DAPI bio-film. (b-inset) Size distribution of Ag-NPs in the bio-film. (c) Schematic representation of the bio-film based on spectroscopic and imaging studies. (d) Potential application of the bio-film has been schematically represented.*

is observed due to the fact that all the particles are submerged in the film and we are able to see only the rise part of the Ag-NPs. From both observations, in Figure 8.1a and 8.1b, the structure of the bio-films is represented schematically in Figure 8.1c. The water insoluble DNA-CTAB complex is formed due to the binding of CTAB cationic polar head to the negative phosphate sugar chain of the DNA strands. During the binding process of DNA with CTAB it impregnates Ag-NPs in the solution and precipitates. So the overall view of the

bio-material should be Ag-NPs are embedded in the water insoluble DNA-CTAB complex. We have highlighted only a section of the matrix in Figure 8.1c for clarity. Since the DNA is tagged with DAPI, the biomaterial fluoresce around 440 nm [27] under UV excitation. On the other hand the Ag-NPs have a SPR band around 400 nm [32]. Thus a strong overlap between the emission spectra of DNA-DAPI and SPR of Ag-NPs suggests the possibility of energy transfer (ET) upon close proximity, which could be utilized for sensing. Possible applications of the bio-films have been summarized pictorially in Figure 8.1d. Upon perturbation of the SPR band of Ag-NPs leads to change in color of the bio-films (absorbance) as well as fluorescence of the material, both can be utilized in sensing applications.

The comparative study of different bio-film coated fiber tips under bright field and UV excitation is represented in Figure 8.2 (Integration time (IT) for photogtaphic images; Bright Filed = 20 ms, UV Excitation = 100 ms). In this study the fiber tips were first dip-coated with the desired bio-film and placed under microscope. During imaging, the light

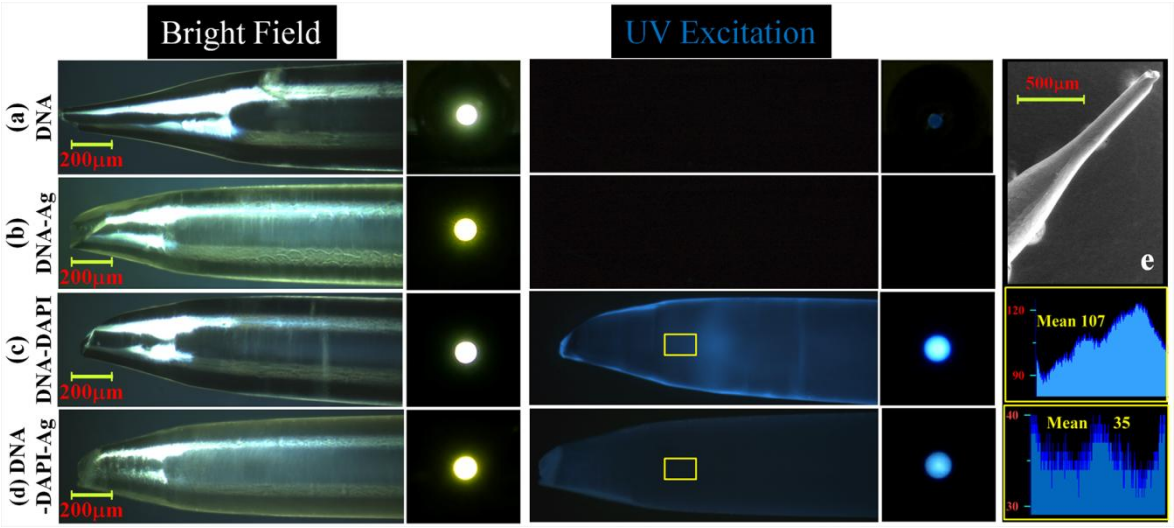

Figure 8.2. *The comparative study of different bio-film coated fiber tips under bright field (Integration time (t) = 20 ms) and UV excitation (t = 100 ms) (a) DNA, (b) DNA-Ag-NPs, (c) DNA-DAPI, (d) DNA-DAPI-Ag-NPs. The adjacent images represent the image of the other fiber end (Bright field t = 10 ms, UV excitation t = 40 ms). The rectangles on the right represent the blue channel area histogram data corresponding to the RGB analysis of the highlighted portions of (c) and (d). (e) SEM image of bio-film coated fiber optic sensor tip.*

coupled into the fiber through the tip and transmitted all the way to the other end of the fiber, image of this end (Bright field IT= 10 ms, UV excitation IT= 40 ms) of the fiber is represented in adjacent to each fiber tip images. We have considered four variants of bio-film

DNA (a), DNA-Ag-NPs (b), DNA-DAPI (c), DNA-DAPI-Ag-NPs (d) (CTAB is common for all). (a) And (b) both are invisible under UV excitation since there in no fluorescence but under bright field (b) is yellowish compare to (a) due to the presence of Ag-NPs in the tip. Since the Ag-NPs in the tip acts as a filter, for (b) the other end of the fiber is observed as bright yellow. In case of (c) and (d) the observation under bright field is the same as (a) and (b) respectively due to the same reason (presence of Ag-NPs in (d)) but they are both visible under UV excitation because of the DNA intercalating dye DAPI. Though the concentration of DAPI present in both the films are same but (d) fluoresce less due the presence of Ag-NPs in the film, which indicates the possibility of energy transfer between the DAPI and Ag-NPs in the film. The corresponding image of the fiber ends show that the intensity of (d) is much less compare to (c). This is also reflected in the RGB (red-green-blue) analysis of the selected area ((c) and (d) Yellow rectangle) of the fiber tip images under UV excitation. The blue channel data corresponding to the area histogram of the selected portions, represented in the Figure 8.2 (Left, yellow rectangle) reveals that the average blue channel intensity for (c) is 107 whereas for (d) it is 35 only. The SEM image of the bio-film coated fiber tip is represented in Figure 8.2e.

The experimantal set up (Figure 8.3) was used for the testing upon dip coating the optical fibers with the bio-material (details in the 3.1.10 section). The absorbance spectra of the DNA-DAPI-CTAB-Ag-NPs (DNA-D-Ag, Figure 8.4) film obtained in the experimental setup is represented in the Figure 8.4a. The SPR of the Ag-NPs is clearly observed, peaking at a wavelength of 400 nm. The spectra of the bio-film material (in ethanol) recorded in spectrophotometer is also provided in the inset of the Figure 8.4a. Along with the SPR of Ag-NPs, the huge absorbance peak of the DNA at 260 nm is evident. The emission and excitation spectra of the bio-film recorded under the experimental setup are represented in Figure 8.4b. A strong blue (440 nm) emission is observed with the excitation of 350 nm (λ_{ex} = 350 nm). The excitation spectra corresponding to 440 nm (λ_{em}= 440 nm) reveals the excitation wavelength at around 340 nm. The decrease in emission intensity with the presence of Ag-NPs (DNA-D-Ag) in the DNA-DAPI (DNA-D) bio-film is represented in the inset of of Figure 8.4b. Initially, time resolved Förster resonance energy transfer (FRET)

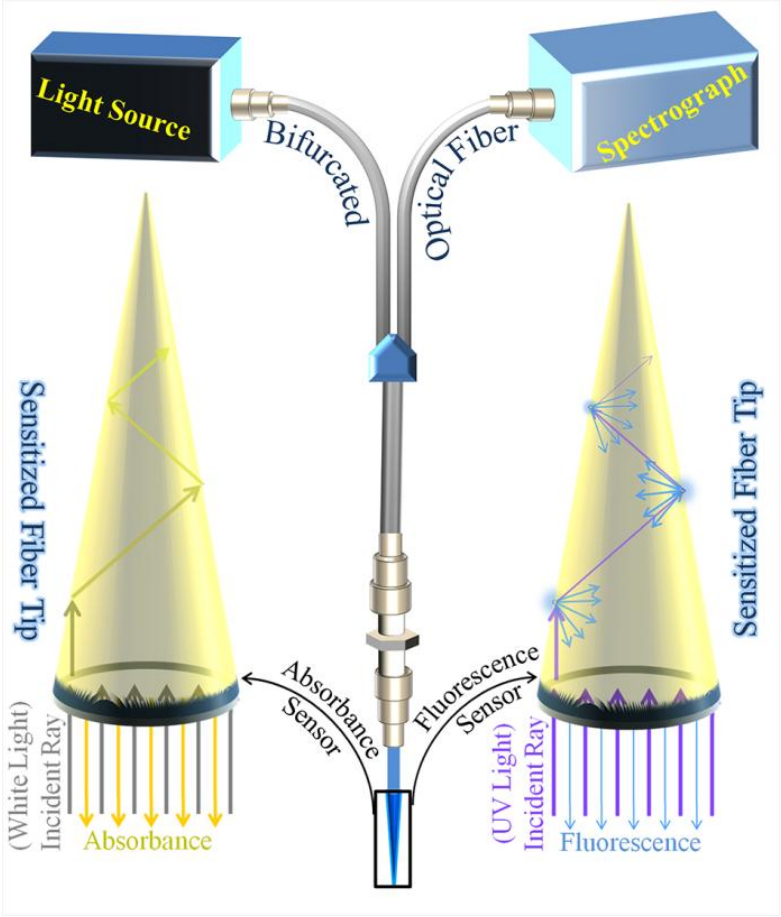

Figure 8.3. *Schematic representation of the experimental setup. With the introduction of the white light in the bio-film region it starts to lose its intensity as well as spectral property with each interaction. The Ag-NPs present in the bio-film absorbs the SPR band from white light, as a result the exited light from the fiber becomes yellow (left). Whereas with the introduction of the UV light in the bio-film region, the DPAI present in the film fluoresces as a result the fiber end become blue, which is the signal measured by the fluorometer (right).*

technique was employed to detect and study the interaction of DNA-DAPI (DNA-D) with the Ag-NPs. Inset of Figure 8.4c shows the strong spectral overlap between the emission spectrum of DNA-DAPI (donor) and the SPR band of Ag-NPs (acceptor). Picosecond resolved photo luminescent transients (Figure 8.4c) of both donor and donor–acceptor systems, monitored at 440 nm, shows significant shortening in the DNA-DAPI fluorescence lifetime upon introduction of Ag-NPs in the system. The picosecond resolved fluorescence decay of DNA-DAPI revealed multi-exponential time constants of 0.06 ns (29%), 0.742 ns (14%) and 2.61 ns (57%) giving an average time constant (τ_{avg}) of 1.61 ns. For the donor–acceptor system time constants are obtained as 0.03 ns (56%), 0.7 ns (11%) and 2.58 ns (33%)

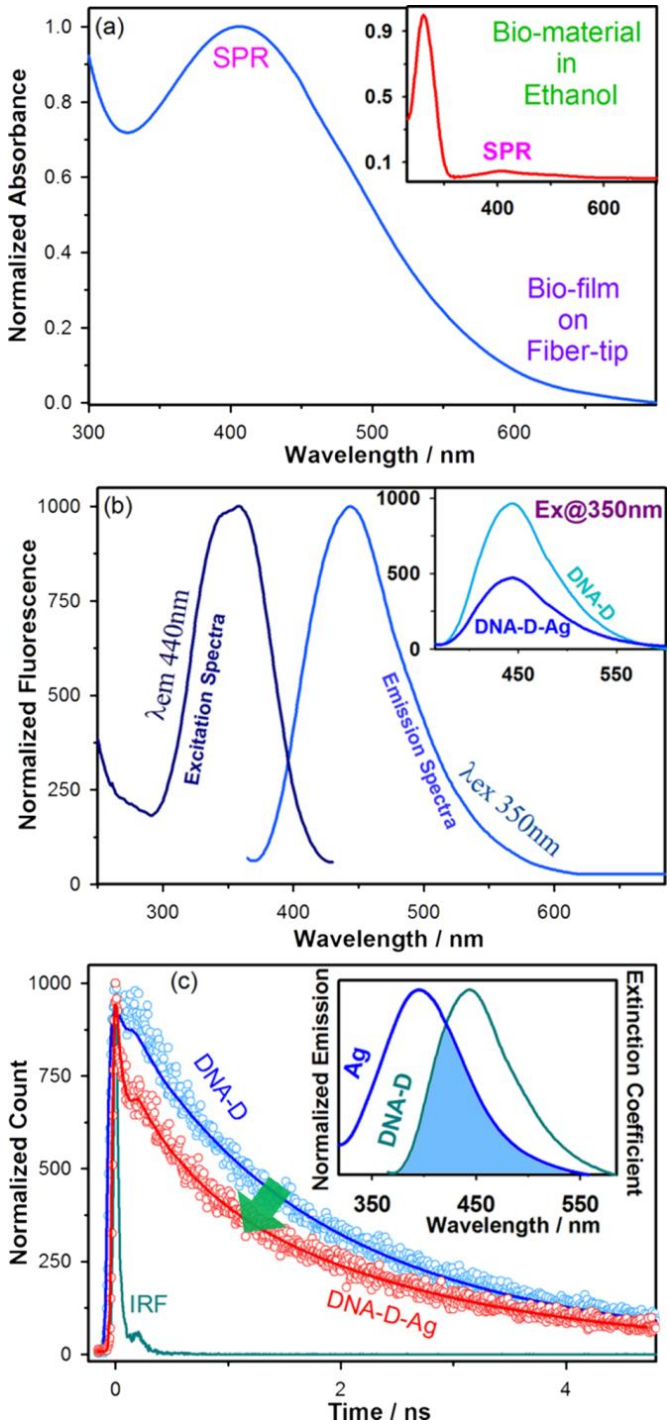

Figure 8.4. *(a) The absorbance spectra of the bio-film obtained from the proposed experimental setup. (inset) The absorbance spectra of the bio-material in ethanol with the DNA peak at 260 nm. (b) The emission upon excitation at 350 nm (λ_{ex} 350 nm) and excitation spectra corresponding to 440 nm (λ_{em}= 440 nm) of the bio-film obtained from the proposed experimental setup. (inset) The emission quenches due to presence of Ag-NPs in the DNA-DAPI bio-film. (c) Picosecond-resolved PL transients of DNA-DAPI (Blue), DNA-DAPI-Ag-NPs (Red) bio-material coated fiber tips and monitored at λ_{em} = 440 nm. (Inset) Spectral overlap between emission spectrum of DNA-DAPI and the surface plasmon resosnence (SPR) band of Ag-NPs.*

giving an average time constant (τ_{avg}) of 0.95 ns (Table 8.1). The substantial shortening in the excited state lifetime of DNA-DAPI upon conjugate formation indicates conclusively that efficient FRET could occur from the DNA-DAPI donor to the Ag-NPs acceptor. Considering the quantum yield of DNA-DAPI in absence of acceptor as 0.92 [34, 35] and based on the spectral overlap, we have estimated a FRET efficiency of 41% using Equation 2.7b. The measured donor–acceptor distance (r) calculated using Equation 2.6 is 21 nm, which is greater than 100 Å. The phenomenon of Ag-NPs based surface energy transfer (SET) process serves as a ruler to unravel the distance range well beyond 10 nm, which follows $1/d^4$ distance dependence [36-38]. In order to favor the NSET formulism, the distance between donor DAPI and acceptor Ag-NPs is calculated to be 8.05 nm (d_0=7.40 nm) from Equation 2.10 and 2.11, respectively. As the calculated donor-acceptor distance is in consonance with the size of the Ag-NPs (radius 10 nm), hence, it is worth emphasizing that the energy transfer from DAPI to Ag-NPs results in the reduced DAPI emission as observed in the figures(Figure 8.2 (variant d) and inset of Figure 8.4b).

Sensitivity of the fiber sensor towards Hg^{2+} in water was first assessed through the absorbance pathway. The comparative kinetics (at 400 nm) of the SPR band with different concentration (9 nM, 90 nM, 500 nM, 900 nM, 1.4 μM, 9 μM, 25 μM and 50 μM) of mercury in water is represented in Figure 8.5a. The reduction in the amplitude of SPR band with time upon interaction of the bio-film coated optical fiber sensor with Hg^{2+} with time is observed (Figure 8.5a inset I). It has been also found that the change in absorbance is linearly proportional with the concentration of the mercury in the range of 0 to 1500 nM ((Figure 8.5a inset II, r = 0.96, slope 9.06×10^{-5} and Y intercept 0.05). The Sensing ability of the bio-film coated tip sensor toward Hg^{2+} in water was also assessed through the fluorescence pathway. The emission kinetics (at 440 nm) of sensor with different concentration of mercury in the range mentioned above is represented in Figure 8.5b. The increment in the intensity is clearly evident from the emission spectra obtained from the sensor (Figure 8.5b inset I). The linear dependency between the concentration of the mercury and intensity change establishes the potential of this detection mechanism ((Figure 8.5b inset II, r = 0.99, slope 4.97 and y intercept 4345.62). In order to investigate the probable reaction pathway the decay transient

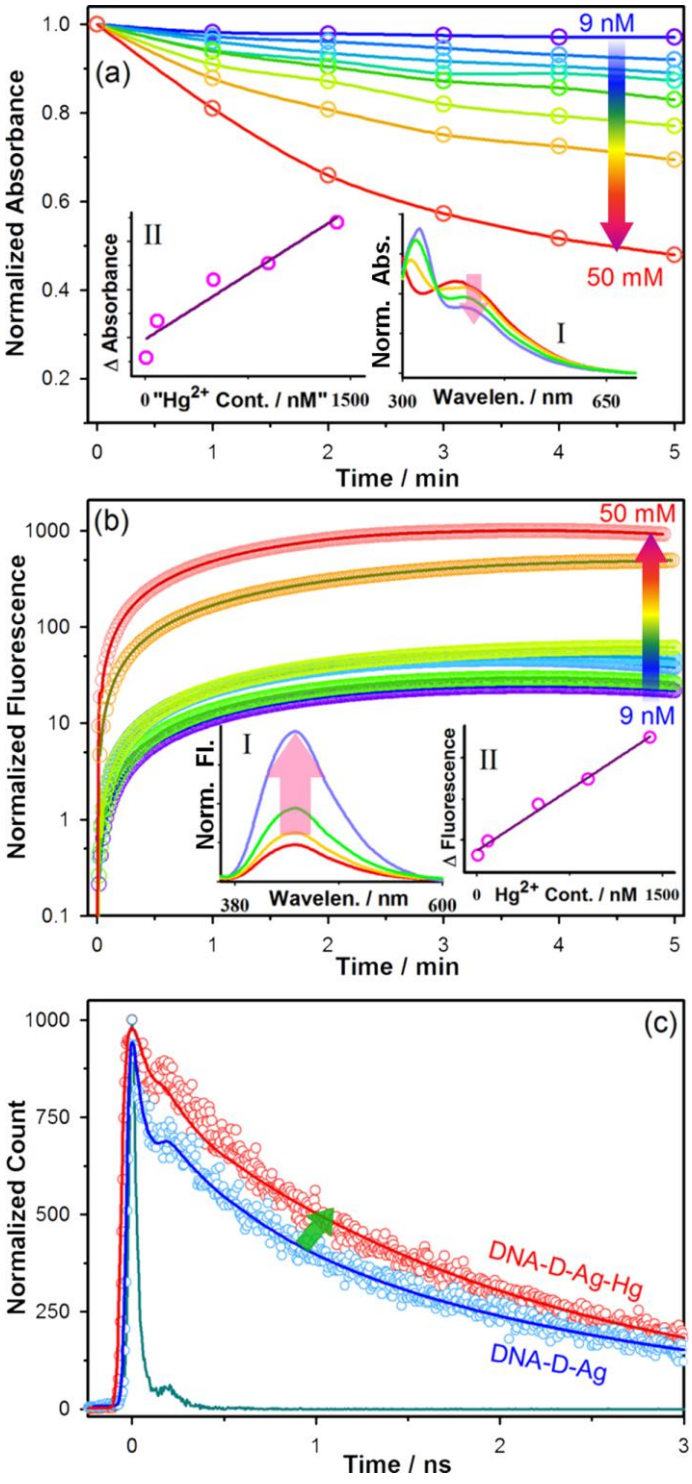

Figure 8.5. *(a) and (b) Absorbance and fluorescence kinetics of the bio-film coated fiber tip with different concentration of mercury from 9 nM to 50 μM respectively. (Inset aI) & (Inset bI) Reduction in amplitude of SPR band (absorbance) and increment in the emission of DAPI with time upon interaction of the sensor with mercury (Hg^{2+}) respectively. (Inset aII) & (Inset bII) Change in absorbance and fluorescence is linearly proportional with the Hg^{2+} concentration in the range 0- 1600 nM.(c) The De-NSET of the DNA-DAPI and Ag-NPs due the amalgamation of Ag-NPs with Hg^{2+}.*

of sensors after interaction with Hg^{2+} were recorded. The average excited state lifetime (Table 8.1) of the sensor recovered subsequently from 0.95 ns to 1.32 ns, (tending toward DNA-DAPI value of 1.61 ns without Ag-NPs) revealing the possibility of de-NSET mechanism in the fiber tip sensor (Figure 8.5c). Or in other words the state of the acceptor (Ag-NPs) is perturbed. The possible reasons could be that the Ag-NPs leave the film or it is present in the film but due to interaction with the Hg^{2+} it loses the SPR, the observed results are justified in both the cases. To have a better insight into the reaction mechanism, following electron microscopic studies has been performed.

In order to investigate the mechanism of action, we have performed the TEM, SEM as well as EDX study of the bio-film material before and after interaction with mercury (Hg^{2+}). The TEM image (Figure 8.6a before and 8.6b after) suggests that upon interaction with the Hg^{2+} the average particle size of Ag-NPs has drastically increased from 20 nm to more than 200 nm. Same characteristic change of Ag-NPs has been reflected from the SEM study of the bio-film material (Figure 8.6c before and 8.6d after). The EDX study of the bio-film (Figure 8.6e before and 8.6f after) reveals that though the amount of silver present in the film before and after the interaction remains almost same (4 wt%, Figure 8.6e and 6f inset) but the presence of Hg^{2+} increased from 0 wt% to 20 wt% (Figure 8.6f inset). The results clearly suggests that the Ag-NPs does not leave the film rather due to highly reactive nature of the Hg^{2+} it could be possible that they are undergoing for the amalgam formation. In earlier reports on silver nanoparticle based Hg^{2+} sensing, it has been concluded to form Ag-Hg amalgam [39-41]. The statement is also supported by the observation (Figure 8.5 a inset I) of simultaneous decrease in SPR peak due to larger NPs (~400 nm) followed by blue shift in the spectra due to the reduction of effective size of the NPs and formation of bimetallic NPs [39-41].

The optical responses of the biosensor towards metal ions such as Ag (II), Ca(II), Cd(II), Co(II), Cu(II), Fe(II), K(I), Mg(II), Na(I), Ni(II), Pb(II), Zn(II), Hg(II), have been investigated. Among these ions, only Hg(II)/Hg^{2+} has a significant effect on the absorbance (Figure 8.7a) as well as in emission (Figure 8.7b) spectra of the bio-material. The changes of absorbance and fluorescence after the interaction (5 min) with different ions have

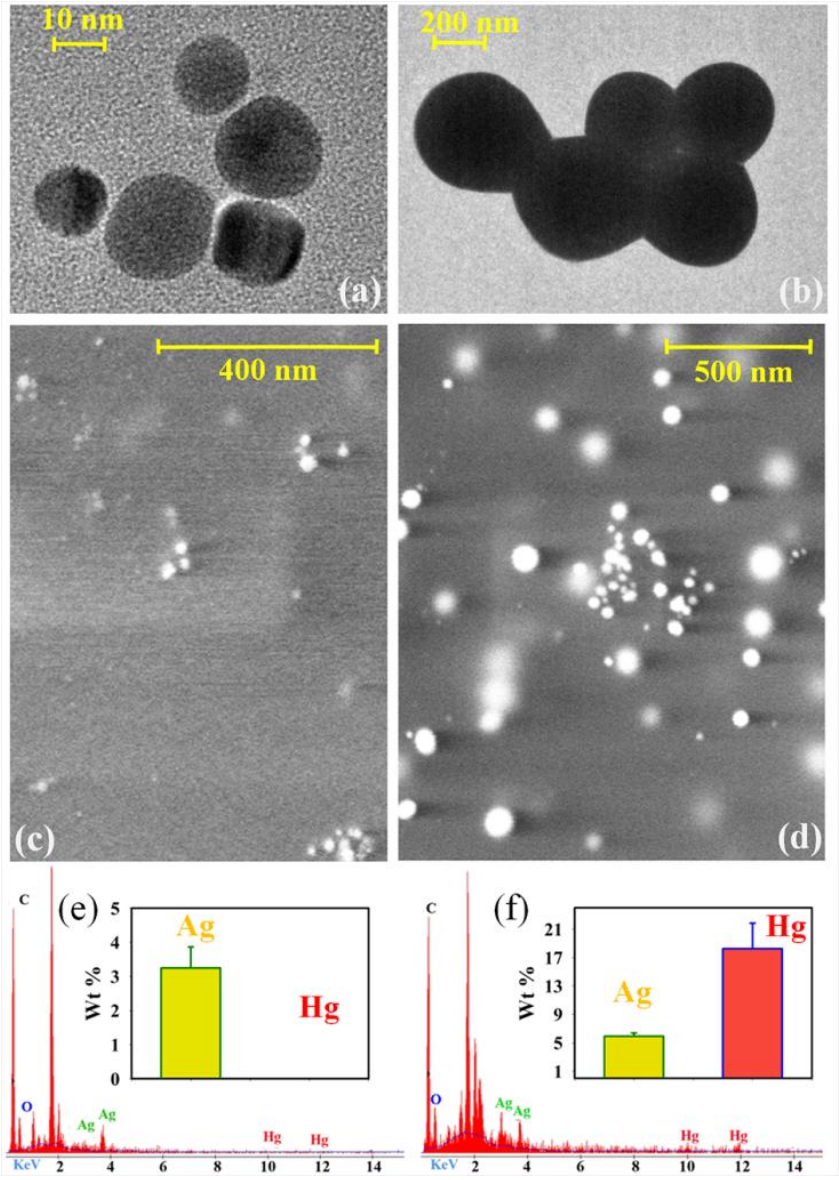

Figure 8.6. *The TEM image of the Ag-NPs impregnated bio-film before and after interaction with Hg^{2+} (a) and (b) respectively. The SEM image of the Ag-NPs impregnated bio-film before and after interaction with mercury ions (Hg^{2+}) (c) and (d) respectively. The EDX curve corresponding to the bio-films before and after interaction with Hg^{2+} with (inset) comparative presence (wt%) of silver (Ag) and mercury (Hg) in the bio-film.*

been represented in Figure 8.7 with a 5% error bar. The high selectivity of the biosensor towards Hg^{2+}over other biologically relevant metal ions can be seen with the naked eye also (Figure 8.7, insets). The disappearance (or reduction) of SPR band of Ag-NPs in the bio-film upon interaction with Hg^{2+} (Figure 8.7a, inset) and consequent increase in intensity (Figure 8.7b, inset) is evident from the images obtained from microscopic studies.

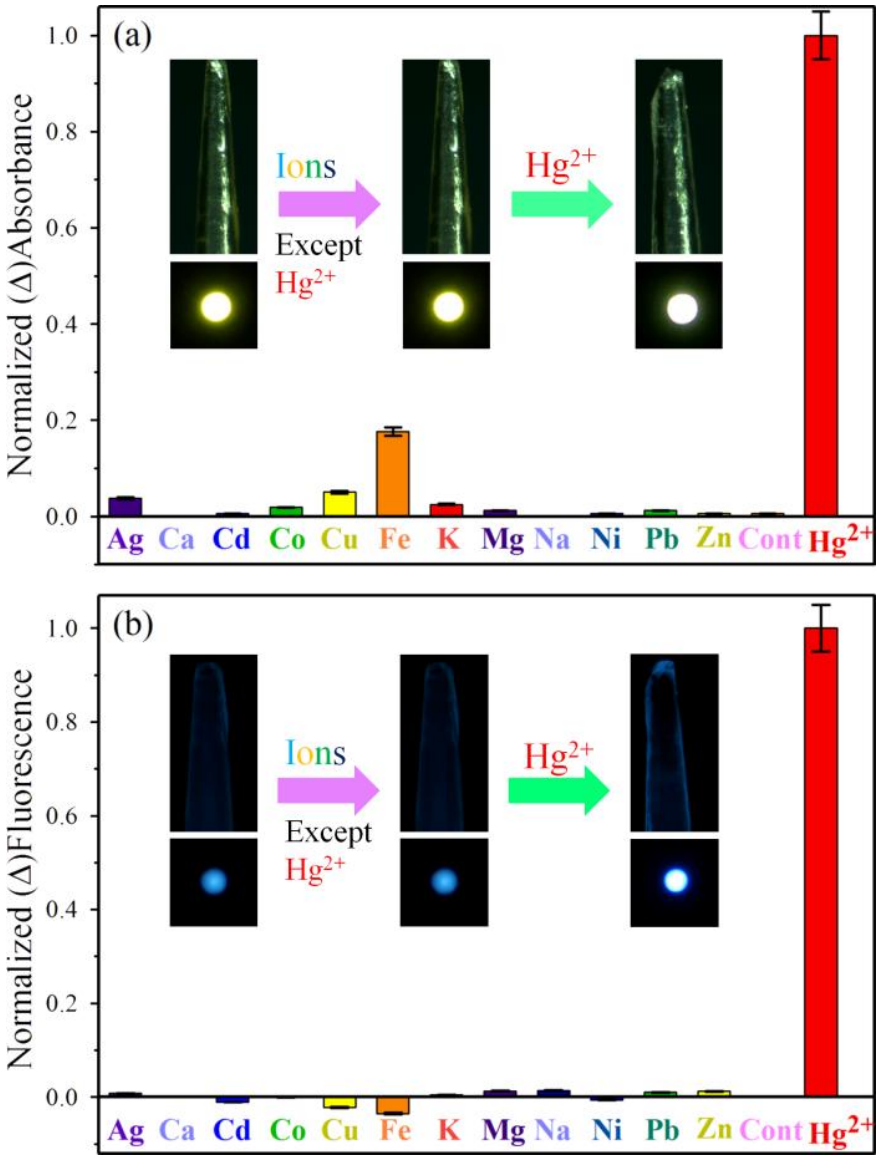

Figure 8.7. *Specificity test of the bio-film coated fiber sensor towards Hg^{2+} in contrast to the other metal ions in both the absorbance and the fluorescence way is represented in (a) and (b) respectively. (a- inset) The disappearance (reduction) of SPR band of Ag-NPs in the bio-film upon interaction with mercury ions (Hg^{2+}), (b-inset) the consequent increase in intensity of the bio-film is represented.*

Table 8.1. *Tri-exponential decay fitting of bio-film coated fiber tip sensor before and after the interaction with mercurry corroesponding to Figure 8.4(c) and Figure 8.5 (c) respectively.*

Figures	Description	τ_1 [ns]	τ_2 [ns]	τ_3 [ns]	τ_{avg} [ns]
Fig. 8.4c	DNA-DAPI	0.06 (29%)	0.74 (14%)	2.61 (57%)	1.61
	DNA-DAPI-Ag-NPs	0.03 (56%)	0.70 (11%)	2.58 (23%)	0.95
Fig. 8.5c	DNA-DAPI-Ag-NPs	0.03 (56%)	0.70 (11%)	2.58 (23%)	0.95
	DNA-DAPI-Ag-NPs-Hg	0.10 (29%)	0.71 (18%)	2.25 (53%)	1.32

8.3. Conclusions

In summary, we have developed a DNA-based optical fiber sensor for the *in situ* measurement of mercury pollution with nM detection efficiency. Impregnated citrate capped silver nanoparticles (Ag-NPs ~20 nm) in a water insoluble DNA-lipid complex at the tip of a multimodal optical fiber is shown to play crucial role in the ultra-sensitive sensing mechanism. While, loss of SPR of the Ag-NPs in the proximity of mercury ions due to amalgamation and size enhancement is shown to be a key factor for the absorption based-sensing. Simultaneous de-NSET from a minor groove binding dye (DAPI) to the impregnated Ag-NPs (due to amalgamation) revealing restoration of DAPI fluorescence in presence of Hg^{2+} ions is an important mechanism for fluorescence based sensing. Our study clearly shows that the sensor is extremely selective to mercury ions, even in presence of other interfering cations generally present in water of natural sources. We have also developed a prototype of the system for potential field trials.

References

1. Steckl, A.J., DNA - a new material for photonics?*, Nat. Photon.* 1 (2007) 3-5.
2. Nizioł, J. and M. Śniechowski. *DNA-CTMA complex for applications in organic electronics: Thermal annealing phenomena*. in *Transparent Optical Networks (ICTON), 2014 16th International Conference on*. 2014. IEEE.
3. Tanaka, K. and Y. Okahata, A DNA−lipid complex in organic media and formation of an aligned cast film*, J. Am. Chem. Soc.* 118 (1996) 10679-10683.
4. Hagen, J.A., *Enhanced luminous efficiency and brightness using DNA electron blocking layers in bio-organic light emitting diodes*. 2006, University of Cincinnati.
5. Shinar, J. and V. Savvateev, *Introduction to Organic Light-Emitting Devices*, in *Organic Light-Emitting Devices*, J. Shinar, Editor. 2004, Springer New York. p. 1-41.
6. Reddy, M.S.P., B.-J. Kim, and J.-S. Jang, Dual detection of ultraviolet and visible lights using a DNA-CTMA/GaN photodiode with electrically different polarity*, Opt. Express* 22 (2014) 908-915.
7. Yaney, P.P., E.M. Heckman, D.E. Diggs, F.K. Hopkins, and J.G. Grote. *Development of chemical sensors using polymer optical waveguides fabricated with DNA*. in *Proc. SPIE–Int. Soc. Opt. Eng.* 2005.
8. Zhou, B., S.J. Kim, C.M. Bartsch, E.M. Heckman, F. Ouchen, and A.N. Cartwright. *Optical properties of DNA-CTMA biopolymers and applications in metal-biopolymer-metal photodetectors*. in *SPIE NanoScience+ Engineering*. 2011. San Diego, California, USA: SPIE.
9. Villarruel, C.A., D.D. Dominguez, and A. Dandridge. *Evanescent Wave Fiber Optic Chemical Sensor*. 1987.
10. Wolfbeis, O.S., Fiber-optic chemical sensors and biosensors*, Anal. Chem.* 80 (2008) 4269-4283.
11. Wang, X.-D. and O.S. Wolfbeis, Fiber-optic chemical sensors and biosensors (2008–2012)*, Anal. Chem.* 85 (2013) 487-508.
12. Wang, X.-d. and O.S. Wolfbeis, Fiber-optic chemical sensors and biosensors (2013–2015)*, Anal. Chem.* 88 (2015) 203-227.
13. Pospíšilová, M., G. Kuncová, and J. Trögl, Fiber-optic chemical sensors and fiber-optic bio-sensors*, Sensors* 15 (2015) 25208-25259.

14. Verma, R. and B.D. Gupta, Optical fiber sensor for the detection of tetracycline using surface plasmon resonance and molecular imprinting, *Analyst* 138 (2013) 7254-7263.
15. Sergachev, I., A. Rusanov, E. Trushkin, D. Sakharov, U. Marx, and A. Tonevitsky, Fluorescent optical fiber sensors for cell viability monitoring, *Analyst* 138 (2013) 4066-4069.
16. Zhang, X.-B., C.-C. Guo, Z.-Z. Li, G.-L. Shen, and R.-Q. Yu, An optical fiber chemical sensor for mercury ions based on a porphyrin dimer, *Anal. Chem.* 74 (2002) 821-825.
17. Yin, M., B. Gu, J. Qian, A.P. Zhang, Q. An, and S. He, Highly sensitive and selective fiber-optic modal interferometric sensor for detecting trace mercury ion in aqueous solution, *Anal. Methods* 4 (2012) 1292-1297.
18. Crosby, J.S., D. Lucas, and C.P. Koshland, Fiber optic based evanescent wave sensor for the detection of elemental mercury utilizing gold nanorods, *Sens. Actuator B-Chem.* 181 (2013) 938-942.
19. Bhavsar, K., R. Prabhu, and P. Pollard, Development of dithizone based fibre optic evanescent wave sensor for heavy metal ion detection in aqueous environments, *P. J. Phys.: Conf. Ser.* 450 (2013) 012011.
20. Long, F., C. Gao, H.C. Shi, M. He, A.N. Zhu, A.M. Klibanov, and A.Z. Gu, Reusable evanescent wave DNA biosensor for rapid, highly sensitive, and selective detection of mercury ions, *Biosens. Bioelectron* 26 (2011) 4018-4023.
21. Ono, A. and H. Togashi, Highly selective oligonucleotide-based sensor for mercury(II) in aqueous solutions, *Angew. Chem. Int. Ed.* 43 (2004) 4300-4302.
22. Huang, C.-C., Z. Yang, K.-H. Lee, and H.-T. Chang, Synthesis of highly fluorescent gold nanoparticles for sensing mercury(II), *Angew. Chem.* 119 (2007) 6948-6952.
23. Dai, H., F. Liu, Q. Gao, T. Fu, and X. Kou, A highly selective fluorescent sensor for mercury ion (II) based on azathia-crown ether possessing a dansyl moiety, *Luminescence* 26 (2011) 523-530.
24. Goswami, N., A. Giri, S. Kar, M.S. Bootharaju, R. John, P.L. Xavier, T. Pradeep, and S.K. Pal, Protein-directed synthesis of nir-emitting, tunable hgs quantum dots and their applications in metal-ion sensing, *Small* 8 (2012) 3175-3184.
25. Seeman, N.C., DNA in a material world, *Nature* 421 (2003) 427-431.

26. Sergeyev, V.G., S.V. Mikhailenko, O.A. Pyshkina, I.V. Yaminsky, and K. Yoshikawa, How does alcohol dissolve the complex of dna with a cationic surfactant?*, J. Am. Chem. Soc.* 121 (1999) 1780-1785.

27. Banerjee, D. and S.K. Pal, Dynamics in the DNA recognition by dapi: Exploration of the various binding modes*, J. Phys. Chem. B* 112 (2008) 1016-1021.

28. Watson, S.M.D., A.R. Pike, J. Pate, A. Houlton, and B.R. Horrocks, DNA-templated nanowires: morphology and electrical conductivity*, Nanoscale* 6 (2014) 4027-4037.

29. Watson, S.M.D., H.D.A. Mohamed, B.R. Horrocks, and A. Houlton, Electrically conductive magnetic nanowires using an electrochemical DNA-templating route*, Nanoscale* 5 (2013) 5349-5359.

30. Shemer, G., O. Krichevski, G. Markovich, T. Molotsky, I. Lubitz, and A.B. Kotlyar, Chirality of silver nanoparticles synthesized on dna*, J. Am. Chem. Soc.* 128 (2006) 11006-11007.

31. Polley, N., P.K. Sarkar, S. Chakrabarti, P. Lemmens, and S.K. Pal, DNA biomaterial based fiber optic sensor: Characterization and application for monitoring *in situ* mercury pollution*, ChemistrySelect* 1 (2016) 2916-2922.

32. Flores, C.Y., C. Diaz, A. Rubert, G.A. Benítez, M.S. Moreno, M.A. Fernández Lorenzo de Mele, R.C. Salvarezza, P.L. Schilardi, and C. Vericat, Spontaneous adsorption of silver nanoparticles on Ti/TiO_2 surfaces. Antibacterial effect on Pseudomonas aeruginosa*, J. Colloid Interface Sci.* 350 (2010) 402-408.

33. Sui, Z.M., X. Chen, L.Y. Wang, L.M. Xu, W.C. Zhuang, Y.C. Chai, and C.J. Yang, Capping effect of CTAB on positively charged Ag nanoparticles*, Phys. E* 33 (2006) 308-314.

34. Kapuscinski, J., DAPI: a DNA-Specific Fluorescent Probe*, Biotech. Histochem.* 70 (1995) 220-233.

35. Polley, N., S. Singh, A. Giri, P.K. Mondal, P. Lemmens, and S.K. Pal, Ultrafast FRET at fiber tips: Potential applications in sensitive remote sensing of molecular interaction*, Sensor. Actuat. B-Chem.* 210 (2015) 381-388.

36. Muhammed, M.A.H., A.K. Shaw, S.K. Pal, and T. Pradeep, Quantum clusters of gold exhibiting FRET*, J. Phys. Chem. C* 112 (2008) 14324-14330.

37. Sarkar, P.K., N. Polley, S. Chakrabarti, P. Lemmens, and S.K. Pal, Nanosurface energy transfer based highly selective and ultrasensitive "turn on" fluorescence mercury sensor, *ACS Sens.* 1 (2016) 789-797.
38. Chaudhuri, S., S. Sardar, D. Bagchi, S.S. Singha, P. Lemmens, and S.K. Pal, Sensitization of an endogenous photosensitizer: electronic spectroscopy of riboflavin in the proximity of semiconductor, insulator, and metal nanoparticles, *J. Phys. Chem. A* 119 (2015) 4162-4169.
39. Deng, L., X. Ouyang, J. Jin, C. Ma, Y. Jiang, J. Zheng, J. Li, Y. Li, W. Tan, et al., Exploiting the higher specificity of silver amalgamation: selective detection of mercury(ii) by forming ag/hg amalgam, *Anal. Chem.* 85 (2013) 8594-8600.
40. Ramesh, G.V. and T.P. Radhakrishnan, A universal sensor for mercury (Hg, HgI, HgII) based on silver nanoparticle-embedded polymer thin film, *ACS Appl. Mater. Interfaces* 3 (2011) 988-994.
41. Chen, G., Z. Guo, G. Zeng, and L. Tang, Fluorescent and colorimetric sensors for environmental mercury detection, *Analyst* 140 (2015) 5400-5443.

List of Publication

1. **N. Polley**, S. Saha, S. Singh, A. Adhikari, S. Das, B. R. Choudhury and S. K. Pal "Development and optimization of a non-contact optical device for online monitoring of jaundice in human subjects", ***Journal of Biomedical Optics*** 20 (2015) 067001.

2. A. Giri, N. Goswami, C. Sasmal, **N. Polley**, D. Majumdar, S. Sarkar, S. N. Bandyopadhyay, A. Singha and S. K. Pal "Unprecedented catalytic activity of Mn_3O_4 nanoparticles: potential lead of a sustainable therapeutic agent for hyperbilirubinemia", ***RSC Advances*** 4 (2014) 5075.

3. **N. Polley**, S. Saha, A. Adhikari, S. Banerjee, S. Darbar, S. Das and S. K. Pal "Safe & symptomatic medicinal use of surface functionalized Mn_3O_4 nanoparticles for hyperbilirubinemia treatment in mice" , ***Nanomedicine*** 10 (2015) 2349.

4. **N. Polley**, S. Singh, A. Giri and S. K. Pal "Evanescent field: A potential light-tool for theranostics application", ***Review of Scientific Instruments*** 85 (2014) 033108.

5. **N. Polley**, S. Singh, A. Giri, P. K. Mondal, P. Lemmens and S. K. Pal "Ultrafast FRET at fiber tips: Potential applications in sensitive remote sensing of molecular interaction", ***Sensors and Actuators B: Chemical*** 210 (2015) 381.

6. **N. Polley**, P. K. Sarkar, S. Chakrabarti, P. Lemmens and S. K. Pal "DNA biomaterial based fiber optic sensor: Characterization and application for monitoring in situ mercury pollution", ***ChemistrySelect*** 1 (2016) 2916.

7. **N. Polley** and S. K. Pal "Medical diagnosis and remote sensing at fiber-tip: picosecond resolved FRET sensor", ***Proceeding of SPIE*** 9702 (2016) 970211-1.

8. *P. K. Sarkar, **N. Polley**, S. Chakrabarti, P. Lemmens and S. K. Pal "Nano-surface energy transfer based highly selective and ultrasensitive "turn on" fluorescence mercury sensor", ***ACS Sensors*** 1 (2016) 789.

9. *S. Singh, **N. Polley**, A. Mitra and S. K. Pal "Spark spectrometry of toxic smokes: Towards a portable, inexpensive, and high-resolution environment monitoring instrument", ***Clean Technologies and Environmental Policy*** 16 (2014) 1703.

10. *S. Chaudhuri, S. Batabyal, **N. Polley** and S. K. Pal "Vitamin B2 in nanoscopic environments under visible light: Photosensitized antioxidant or phototoxic drug?", ***Journal of Physical Chemistry*** **A** 118 (2014) 3934.

11. *D. Bagchi, S. Chaudhuri, S. Sardar, S. Choudhury, **N. Polley**, P. Lemmens and S. K. Pal "Modulation of stability and functionality of a phyto-antioxidant by weakly interacting metal ions: curcumin in aqueous solution", ***RSC Advances*** 5 (2015) 102516.

List of Patents

1. System and Method for Monitoring and Analyzing Trace Elements in Smoke/Air

Indian Pat. Appl. (2014), 327/KOL/2014 dated 17th March 2014.

2. Citrate Functionalized Mn_3O_4 Nano-particle Based Sustainable Therapeutic Catalytic Agent for Hyperbilirubinemia

Indian Pat. Appl. (2014), 1267/KOL/2014 dated 4th December 2014.

3. A Solar Power Driven Wearable Cooling Kit.

Indian Pat. Appl. (2014), 1329/KOL/2014 dated 19th December 2014.

4. Expression of Interest on Bio-Templated Nanosensor for Mercury Detection in PPB Level.

Indian Pat. Appl. (2016), 201621004916 dated 11th Feb 2016.

5. Ultrasensitive Fluorescence-based Efficient Mercury Sensor.

Indian Pat. Appl. (2016), 201621005597 dated 17th Feb 2016.

**Publications are not included in the thesis*